UNIVERSITY OF OKLAHOMA

GRADUATE COLLEGE

SEARCHES FOR HEAVY RESONANCES IN THE $R \to WW \to \ell\nu\ell\nu$ DECAY CHANNEL USING pp COLLISIONS AT $\sqrt{s} = 13$ TEV WITH THE ATLAS DETECTOR AT THE LHC

A DISSERTATION

SUBMITTED TO THE GRADUATE FACULTY

in partial fulfillment of the requirements for the

Degree of

DOCTOR OF PHILOSOPHY

By

NATHAN ALLEN GRIESER
Norman, Oklahoma
2020

SEARCHES FOR HEAVY RESONANCES IN THE $R \to WW \to \ell\nu\ell\nu$ DECAY CHANNEL USING pp COLLISIONS AT $\sqrt{s} = 13$ TEV WITH THE ATLAS DETECTOR AT THE LHC

A DISSERTATION APPROVED FOR THE
HOMER L. DODGE DEPARTMENT OF PHYSICS
ASTRONOMY

BY THE COMMITTEE CONSISTING OF:

Dr. Michael Strauss, Chair

Dr. Howard Baer

Dr. Caleb Fulton

Dr. Alberto Marino

Dr. John Stupak

© Copyright by NATHAN ALLEN GRIESER 2020
All rights reserved.

Acknowledgements

I am extremely grateful to have received tremendous support during graduate school from my wife Victoria. Not only did you drop your plans to join this adventure with me, you continue to provide a listening ear and a calming presence in even the most difficult times.

"Who can find a capable wife? Her value is far more than that of corals."

– Proverbs 31:10

Special thanks to the many teachers and advisors over the years who supported my learning and instilled in me the love of science and mathematics. Specific thanks go to Dorothy Cott and Greg Janish, who first opened my intrigue into physics and mathematical challenges; to Mellita Caragiu, who encouraged me to think for myself and use my own talents to problem solve; to Mike Strauss, who continued to encourage and guide me even in unfavorable times.

"The mediocre teacher tells. The good teacher explains. The superior teacher demonstrates. The great teacher inspires."

– William Arthur Ward

Additionally, a very hearty thank you for all of my colleagues and supervisors in the Higgs WW working group who I worked so closely with over the past 3 years at CERN. Your constant willingness to discuss and troubleshoot issues with welcoming ears was vital to the completion of this thesis.

> *"It is the long history of humankind (and animal kind, too) that those who learned to collaborate and improvise most effectively have prevailed."*
>
> – Charles Darwin

For my children: Liam, Olivia, and Samson

May you always wonder about and examine the natural world that encompasses you with reverence, benevolence, and love.

Contents

List of Tables

List of Figures

Acronyms and Abbreviations

1. 2HDM - two Higgs-doublet model
2. AFII - Atlas Fast II
3. ALICE - A large ion collider experiment
4. ATLAS - **A** **T**oroidal **L**HC **A**pparatu**S**
5. BSM - beyond Standard Model
6. CDI - Calibration Data Interface
7. CL - Confidence level
8. CMS - Compact muon solenoid
9. CP - combined performance
10. CR - control region(s)
11. DY - Drell-Yan
12. eCal - electromagnetic calorimeter
13. ED - Extra dimension
14. ELM - effective Lagrangian model
15. FCTight - Fixed Cut Tight
16. (f)JVT - (forward) Jet Vertex Tagger
17. FSR - final state radiation
18. ggF - gluon–gluon fusion
19. GM - Georgi-Machacek
20. GRL - good runs lists
21. hCal - hadronic calorimeter
22. HLT - High Level Trigger
23. HVT - Heavy vector triplet
24. IBL - insertable *b*-layer
25. ID - inner detector
26. IP - interaction point
27. ISR - initial state radiation
28. JER - Jet energy resolution
29. JES - Jet energy scale
30. KK - Kaluza-Klein

31. L1 - Level 1 trigger
32. LAr - liquid argon
33. LHC - Large Hadron Collider
34. LHCb - Large Hadron Collider beauty
35. LO - leading order
36. MC - Monte-Carlo simulation
37. ME - Matrix element
38. MS - muon spectrometer
39. NF - normalization factor(s)
40. NLO - next-to-leading order
41. NNLO - next-to-next-to-leading order
42. N^3LO - next-to-next-to-next-to leading order
43. NWA - Narrow width approximation
44. OR - overlap removal
45. P4 - Four vector momentum
46. PFlow - particle flow
47. PMG - Physics Modeling Group
48. *pp* - proton–proton
49. PS - Proton synchotron
50. PS - Parton shower
51. PSB - Proton Synchotron Booster
52. PU - pile-up
53. PV - primary vertex
54. qqA - quark–quark annihilation
55. RF - radio frequency
56. RS - Randall-Sundrum
57. SCT - semiconductor tracker
58. SF - same-flavor
59. SF - scale factor
60. SM - Standard Model
61. SPS - Super proton synchotron
62. SR - signal region(s)
63. SUSY - supersymmetry
64. TRT - transition radiation tracker
65. TST - track-based soft term
66. VBF - Vector Boson Fusion
67. VEV - Vacuum expectation value
68. WP - working point(s)

Abstract

This thesis presents a search for a heavy Higgs-like resonance decaying in the $R \to WW^* \to \ell\nu\ell\nu$ channel using the ATLAS detector at the Large Hadron Collider. The search uses proton-proton collision data at a centre-of-mass energy of 13 TeV corresponding to an integrated luminosity of 139 fb^{-1}. Interpretations are given under the narrow-width approximation, Georgi-Machacek model, the radion particle of the Randall-Sundrum graviton model, a HVT model, and a spin-2 graviton of the Randall-Sundrum model.

Chapter 1

Introduction

The Higgs boson was initially predicted [92, 117] within the context of the Standard Model (SM) in the early 1960s. In the summer of 2012 the experimental discovery of the Higgs produced by proton-proton (pp) collisions was made by the ATLAS [16] and CMS [67] collaborations at the Large Hadron Collider (LHC) in Geneva, Switzerland. This discovery confirmed the existence of the Higgs field, which gives a particle mass and produces the Higgs boson through spontaneous symmetry breaking.

Even with the experimental discovery of the Higgs boson, the SM is still considered an incomplete theoretical model. A number of scenarios beyond the SM (BSM) have been proposed, such as an extended Higgs sector [83, 121] which predict additional heavy Higgs bosons, composite Higgs models [21, 101], and models with warped extra dimensions [134, 22, 32, 33] that predict additional tensor resonances and heavy vector bosons.

With this analysis a probe into the BSM space is conducted, where a search for a neutral heavy resonances decaying to a pair of W bosons is performed using the full Run-II dataset of the ATLAS detector corresponding to 139 fb^{-1} taken at a center-of-mass energy of $\sqrt{s}$ = 13 TeV. A previous search performed by ATLAS [14] was based on the partial dataset from Run 2 corresponding to 36 fb^{-1} from the 2015 and 2016 data taking years. The results were interpreted for seven scenarios: two which correspond to a heavy Higgs boson that had a narrow and large width compared to the experimental resolution, a scalar within the

Georgi-Machacek model, a two-Higgs doublet model (2HDM), a heavy vector triplet, a bulk Randall-Sundrum graviton model, and finally a spin-2 effective lagrangian model (ELM).

A theoretical overview of the SM and the BSM models used as benchmarks for the analysis is given in Chapter 2. The experimental apparatus at the LHC and the ATLAS detector is described in Chapter 3. An overview of the data and simulation samples used in the analysis is given in Chapter 4. The reconstruction definition of the physics objects and kinematic criteria of such objects is given in Chapter 5. Chapter 6 shares the optimization studies performed to select both signal and control regions to be used in the analysis. Chapter 7 highlights the event selection of the signal and control regions, and the relevant modeling in such regions. Chapter 8 gives the details of the systematic uncertainties that are consider in the analysis. An overview of the statistical analysis and the physics results achieved by the analysis are given in Chapter 9. Finally, Chapter 10 discusses the conclusions of the analysis while briefly discussing additional studies to come in the future.

The work perfomed as part of this thesis includes the analysis of experimental data, statistical analysis of the data, and production of the simulated detector data to model the observed data.

Chapter 2

The Standard Model and Beyond

In this chapter an overview of the Standard Model will be given in Section 2.1. A look at the phenomology of the Higgs boson, and it's interplay with pp collisions is given in Section 2.2. Finally, an overview of theoretical models beyond the Standard Model, and specifically the ones considered in this analysis, is given in Section 2.3.

2.1 Overview of the Standard Model of Particle Physics

The SM of particle physics [78] gives a description of three of the four fundamental forces in the known universe: the electromagnetic, weak, and strong interactions. Originally developed in the 1960's and 1970's, the SM is a quantum field theory which is based on categorically described fundamental particles, and gives a description of their interactions with one another. The SM gives a description of the electromagnetic interactions, given by quantum electrodynamics (QED), combined with the weak interactions to form electro-weak (EW) theory. The SM also includes a description of the strong interactions described by quantum chromodynamics (QCD). The gravitational force is much weaker than the scale of fundamental particles, and plays little role in the interactions of particle physics.

The SM is comprised of 49 fundamental particles (shown in Figure 2.1), each defined by its individual mass, charge, and spin. There are 12 spin-$\frac{1}{2}$ fermions which are subdivided into six quarks and six leptons. The quarks are commonly classifed into three generations, with the first generation defined as the up, u, and down, d, quarks, the second generation as the charm, c, and strange, s, quarks, and the third generation as the top, t, and bottom[1], b, quarks. The leptons subgroup, also commonly classified into three generations similar to the quarks, is comprised of electrons, e^-, muons, μ^-, and taus, τ^-, and their corresponding neutrinos, ν_e, ν_μ, ν_τ. Each of the fermions comes with a corresponding anti-particle of opposite charge, such as e^+, $\bar{t}$, and $\bar{\nu_\mu}$[2]. The mediation of the three fundamental interactions previously described is carried out by 12 spin-1 bosons. The QED interactions are mediated by the massless photon, γ. The weak interactions are mediated by the massive charged bosons, $W^\pm$ [143], and massive neutral boson, Z^0 [47]. The strong interactions are mediated by eight massless gluons, g. The last fundamental particle of the SM is the neutral scalar Higgs boson, H[3], whose field enables particles to obtain mass.

2.1.1 Quantum Chromodynamics

Quantum chromodynamics governs the strong interaction of quark and gluon fields of the standard model. The governing symmetry group of QCD is the $SU(3)_C$ gauge group, which gives rise to eight gluon fields $G^i_\mu, i = 1,..,8$. The quarks reside in color containing triplet fields and couple directly to gluon fields. All other particles in the SM are considered colorless and therefore do not couple to gluons directly. The QCD interactions are described by a Lagrangian shown as

$$\mathcal{L}_{QCD} = -\frac{1}{4}G^i_{\mu\nu}G^{i\mu\nu} + \sum_\alpha \bar{\Psi}^{(\alpha)}_a i\not{D}_{ab}\Psi^{(\alpha)}_b \tag{2.1}$$

where $\Psi^{(\alpha)}_a$ are the quark fields, α corresponds to the flavor $(u, d, s, ...)$ of the quarks, and a,b correspond to color indices. The gluon field strength tensor denoted can be further expanded

[1]The bottom quark is sometimes referred to as the beauty quark. Both are physically the same and can be used interchangeably.

[2]The anti-particle for fermions is denoted by either a bar over the particle ($\bar{t}$) or with the opposite charge (e^+))

[3]The SM Higgs is refered to with an uppercase H in the contect of only the SM. However, in the context of BSM (and the text to come) H refers to a heavy Higgs boson, where "h" refers to the SM Higgs with mass of 125 GeV

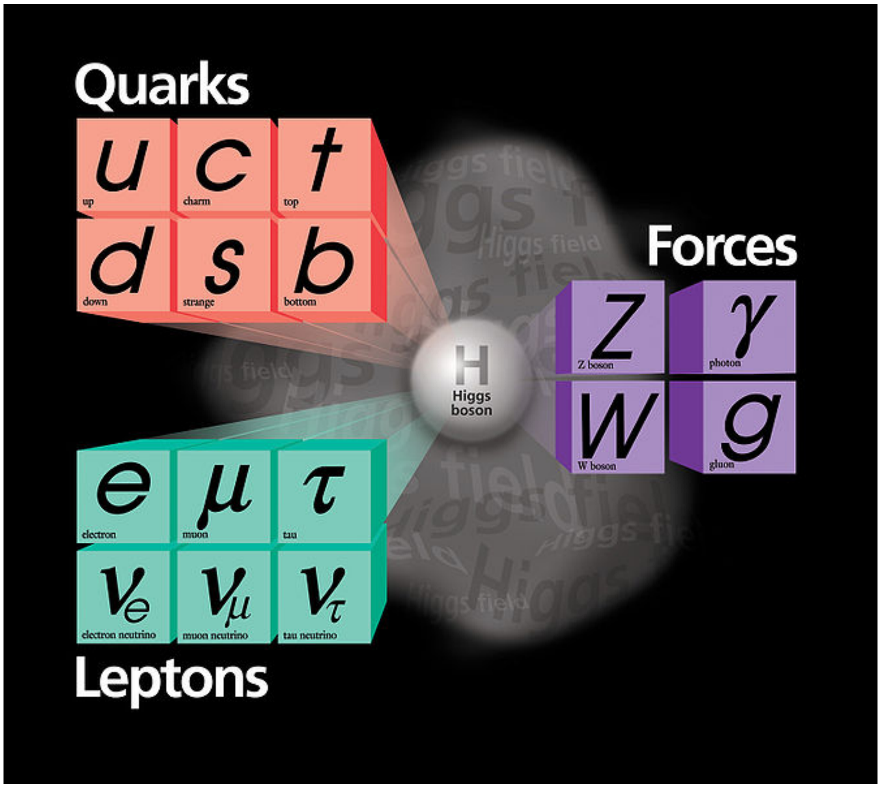

Figure 2.1: The fundamental particles of the Standard Model. [122]

as

$$G^i_{\mu\nu} = \partial_\mu G^i_\nu - \partial_\nu G^i_\mu - g_3 f^{ijk} G^j_\mu G^k_\nu \tag{2.2}$$

and the $SU(3)_C$ covariant derivated, $\not{D}_{ab} = \gamma^\mu D_{\mu ab}$, can be further expanded with

$$D_{\mu ab} = \partial_\mu \delta_{ab} + i g_3 \frac{\lambda^i_{ab}}{2} G^i_\mu \tag{2.3}$$

where g_3 is the $SU(3)_C$ coupling constant and λ^i are the eight $SU(3)_C$ group generators.

2.1.2 Electroweak Theory

The electroweak portion of the SM is comprised of the combination of the interactions governed by QED, with a $U(1)_Y$ symmetry, and the weak interactions. This combination which governs the fermion fields leads to the full EW symmetry of $SU(2)_L \times U(1)_Y$. The fermionic fields are described as a doublet, Ψ, whose transformation in the $SU(2)$ group can be described as

$$\Psi_L \rightarrow [1 - ig_2 T_i \alpha^i(x)]\Psi_L \tag{2.4}$$

where the subscript L refers to the left-handed chirality of the field, g_2 is the EW coupling strength, T_i are the group generators (such that $T_{1,2,3} = \sigma_{1,2,3}$, where σ are the Pauli spin matrices), and α is the phase of the infinitesimal transformation. Additionally, both left and right handed fermionic fields can transform under the $U(1)_Y$ group, described as

$$\Psi_{L,R} \rightarrow [1 - ig_1 Y \beta(x)]\Psi_{L,R} \tag{2.5}$$

where Y is the group generator and g_1 is the ED coupling strength. The gauge fields introudced by the $SU(2)_L$ group invariance are the three weak-isospin fields W^i_μ. The $U(1)_Y$ group invariance introduces a B_μ gauge field. The full Lagrangian of the $SU(2)_L \times U(1)_Y$ group for massless fermions can be written as

$$\mathcal{L}_{\mathrm{EW}} = -\frac{1}{4}W^i_{\mu\nu}W^{i\mu\nu} - \frac{1}{4}B^i_{\mu\nu}B^{i\mu\nu} + \bar{\Psi} i\gamma^\mu D_\mu \Psi \tag{2.6}$$

where W and B are the field strength tensors of the gauge fields previously discussed, and D_μ is the covariant derivative given by

$$D_\mu = \partial_\mu + ig_2 W^i_\mu T_i + ig_1 \frac{1}{2} B_\mu Y \tag{2.7}$$

Gauge fields in $SU(2)_L \times U(1)_Y$ do not directly correspond to the physical gauge bosons described in Section 2.1. To form the combined fields of the physical gauge bosons, these gauge fields are mixed by including an additional parameter, θ_W, known as the weak mixing angle[4]. The combined fields can then be produced by

$$\begin{aligned} W^{\pm}_{\mu} =& \frac{1}{\sqrt{2}}(W^1_{\mu} \mp iW^2_{\mu}) \\ Z_{\mu} =& \text{cos}\theta_W W^3_{\mu} - \text{sin}\theta_W B_{\mu} \\ A_{\mu} =& \text{sin}\theta_W W^3_{\mu} + \text{cos}\theta_W B_{\mu} \end{aligned} \tag{2.8}$$

where the $W^{\pm}_{\mu}$ fields correspond to the $W^{\pm}$ bosons, the Z_{μ} field corresponds to the neutral Z boson, and the A_{μ} field corresponds to the photon, γ. It has been shown experimentally that W and Z bosons are massive [143, 47], but an additional mass term for these fields in the Lagrangian in Equation 2.6 is forbidden, as the local $SU(2)_L \times U(1)_Y$ gauge symmetry would be broken. The solution to this problem is the introduction of the Higgs mechanism [117], which allows electroweak gauge field mixing and generates the boson masses through the spontaneous symmetry breaking of $SU(2)_L \times U(1)_Y$.

2.1.3 The Higgs Mechanism

A mathematical expression of where the W and Z bosons can be derived, first by following closely the process in a simple $U(1)$ gauge theory [81], known as the Abelian Higgs Model. To start, a simple Lagrangian is chosen as

$$\mathcal{L} = -\frac{1}{4}F_{\mu\nu}F_{\mu\nu} \tag{2.9}$$

where $F_{\mu\nu} = \partial_{\nu}A_{\mu} - \partial_{\mu}A_{\nu}$. To proceed, the local $U(1)$ gauge invariance is assumed, such that the Lagrangian is invariant under the transformation of $A_{\mu}(x) \rightarrow A_{\mu}(x) - \partial_{\mu}\eta(x)$. Adding a mass term to the Lagrangian results in

$$\mathcal{L} = -\frac{1}{4}F_{\mu\nu}F_{\mu\nu} + \frac{1}{2}m^2 A_{\mu}A^{\mu} \tag{2.10}$$

[4] θ_W Can be defined as a function of the coupling parameters of the $SU(2)_L \times U(1)_Y$ group: $\text{sin}\theta_W = \frac{g_2}{\sqrt{g_2^2+g_1^2}}$, $\text{cos}\theta_W = \frac{g_1}{\sqrt{g_2^2+g_1^2}}$

With this additional term, it can be seen that the Lagrangian is no longer invariant under the local $U(1)$ gauge symmetry. This gives confirmation that the $U(1)$ gauge boson must be massless.

An extension to the simple Lagrangian can be made by including a single complex scale field with charge $-e$ which directly couples to the gauge boson. The Lagrangian now takes the form of

$$\mathcal{L} = -\frac{1}{4}F_{\mu\nu}F_{\mu\nu} + |D_{\mu}\phi|^2 - V(\phi) \tag{2.11}$$

where $D_{\mu} = \partial_{\mu} - ieA_{\mu}$ and $V(\phi) = \mu^2|\phi|^2 + \lambda(|\phi|^2)^2$. $V(\phi)$ is the most general renormalizable potential that is allowed by the $U(1)$ gauge invariance. This Lagrangian is now invariant under local $U(1)$ gauge transformations.

There are two possibilities for characterizing μ in the theory: $\mu^2 > 0$ and $\mu^2 < 0$. The first gives rise to QED, with a massless gauge boson and a charged scalar field with mass μ. The latter results in the case where, when the potential is written as

$$V(\phi) = -|\mu^2||\phi|^2 + \lambda(|\phi|^2)^2 \tag{2.12}$$

no longer has the minimum energy state at $\phi = 0$. The minimum energy state is now $\langle\phi\rangle = \sqrt{-\frac{\mu^2}{2\lambda}} \equiv \frac{v}{\sqrt{2}}$. $\langle\phi\rangle$ is referred to as the vacuum expectation value (VEV) of ϕ. The VEV then gives rise to the breaking of the $U(1)$ symmetry. For further decomposition, it is useful to define ϕ in terms of real fields, χ and h, that do not have a VEV:

$$\phi \equiv \frac{1}{\sqrt{2}}e^{i\frac{\chi}{v}}(v + h) \tag{2.13}$$

Making the substitution of this definition of ϕ into the original Lagrangian at Equation 2.11

results in the following Lagrangian:

$$\begin{aligned}\mathcal{L} = &-\frac{1}{4}F_{\mu\nu}F_{\mu\nu} - evA_\mu\partial^\mu\chi + \frac{e^2v^2}{2}A_\mu A^\mu \\ &+ \frac{1}{2}(\partial_\mu h\partial^\mu h + 2\mu^2h^2) + \frac{1}{2}\partial_\mu\chi\partial^{\mu\chi} \\ &+ (h, \chi \text{ mixed terms})\end{aligned} \tag{2.14}$$

The new Lagrangian in 2.14 characterises a model with a gauge boson whose mass is $M_A = ev$, a scalar field h whose mass squared is $-2\mu^2 > 0$, and a massless scale field, χ. To allow for the removal of the not clearly understood χ–A mixing term, a gauge transformation of $A'_\mu \equiv A_\mu - \frac{1}{ev}\partial_\mu\chi$ can be made. This transformation removes the χ field completely, allowing the gauge boson to gain mass. This process is known as the Higgs mechanism, where the χ is commonly called a Goldstone boson, and the scalar field h is a Higgs boson. The conclusion of this exercise is that the spontaneous symmetry breaking of a gauge theory by non-zero VEV results in the transfer of a Goldstone boson into the longitudinal component of a massive gauge boson. Unfortunately, the $U(1)$ gauge bosons (γ) in nature are massless so not much is gained yet. However, the gauge bosons of $SU(2)_L \times U(1)_Y$ are not massless, and we can continue by applying the same mechanism to this group.

Beginning with the Lagrangian shown in Equation 2.6 with the fermionic fields removed, and now including a complex scalar $SU(2)$ doublet, $\Phi = \begin{pmatrix} \phi^+ \\ \phi- \end{pmatrix}$, that couples to the gauge fields. The scalar potential can then be written as

$$V(\Phi) = \mu^2|\Phi\Phi^\dagger| + \lambda(|\Phi^\dagger\Phi|)^2 \tag{2.15}$$

where $\lambda > 0$. Similar to the $U(1)$ example, the minimum energy state for the case $\mu^2 < 0$ gives rise to the scalar field having a VEV.

An arbitrary value for the VEV of the scalar field can be chosen as

$$\langle \Phi \rangle = \frac{1}{\sqrt{2}} \begin{pmatrix} 0 \\ v \end{pmatrix} \tag{2.16}$$

and with this selection the scalar doublet has a $U(1)_Y$ hypercharge of 1, retaining that the $U(1)$ symmetry is unbroken when introducing the scalar VEV.

The scalar doublet now gives an additional contribution to the EW Lagrangian:

$$\mathcal{L}_{\text{Scalar}} = (D^{\mu}\Phi)^{\dagger}(D_{\mu}\Phi) - V(\Phi) \tag{2.17}$$

As described in the Abelian Higgs Model, there are no longer Goldstone bosons and only the physical Higgs scalar remains after spontaneous symmetry breaking has taken place. Therefore, the scalar doublet can be written in the unitary gauge as

$$\Phi = \frac{1}{\sqrt{2}} \begin{pmatrix} 0 \\ v + h \end{pmatrix} \tag{2.18}$$

which gives an additional contribution to the EW Lagrangian of

$$\frac{1}{2}(0, v)(\frac{1}{4}g_2\sigma \cdot W_{\mu} + \frac{1}{2}g_1 B_{\mu})^2 \begin{pmatrix} 0 \\ v \end{pmatrix} \tag{2.19}$$

Combining the above with the physical gauge boson definitions Equation 2.8 gives rise to the mass of the gauge bosons through the Higgs mechanism, such that

$$\begin{aligned} M_W =& \frac{g_2 v}{2} \\ M_Z =& \frac{\sqrt{g_2^2 + g_1^2}}{2} \\ M_{\gamma} =& 0 \end{aligned} \tag{2.20}$$

confirms that $SU(2)_L \times U(1)_Y$ group allows for the massive vector bosons W and Z by means of the Higgs mechanism.

2.2 Phenomology of the Higgs Boson

The Higgs boson has four primary production modes. The first, and most abundant, production mode at the LHC is via gluon–gluon fusion (ggF), where two gluons combine to produce a Higgs boson through a virtual fermionic loop. The next common production mode is via vector boson fusion (VBF), where two quarks produce a pair of vector bosons, which, in turn, produces a Higgs boson. VBF topologies are often defined by the additional production of two or more energetic jets in the event. Two smaller associated production modes result in a Higgs boson, one in which a Higgs is produced in associated with a vector boson (VH), and another where the Higgs is produced with a pair of top quarks (ttH). The production cross sections (σ) of the m_H = 125 GeV SM Higgs boson can be seen in Figure 2.2 for the different $\sqrt{s}$ pp collisions of the LHC.

The decay modes of the Higgs bosons are highly dependent on the Higgs mass itself. The Higgs couplings are proportional to the decay products' mass, resulting in the largest branching ratio being the heaviest final state that is accessible kinematically for a specific Higgs mass. As can be seen in Figure 2.3, the decay mode of the Higgs is mostly dominated by $H \rightarrow b\bar{b}$ at the SM value of m_H =125 GeV. However, extending to higher masses of m_H allows for the decay mode to be dominated by the WW decay. As will be discussed in more detail in Section 2.3, the signal models considered in this analysis will often contain a heavy Higgs decaying to a pair of W bosons, alluding to strong sensitivity due to the high $\sigma \times BR$ shown here.

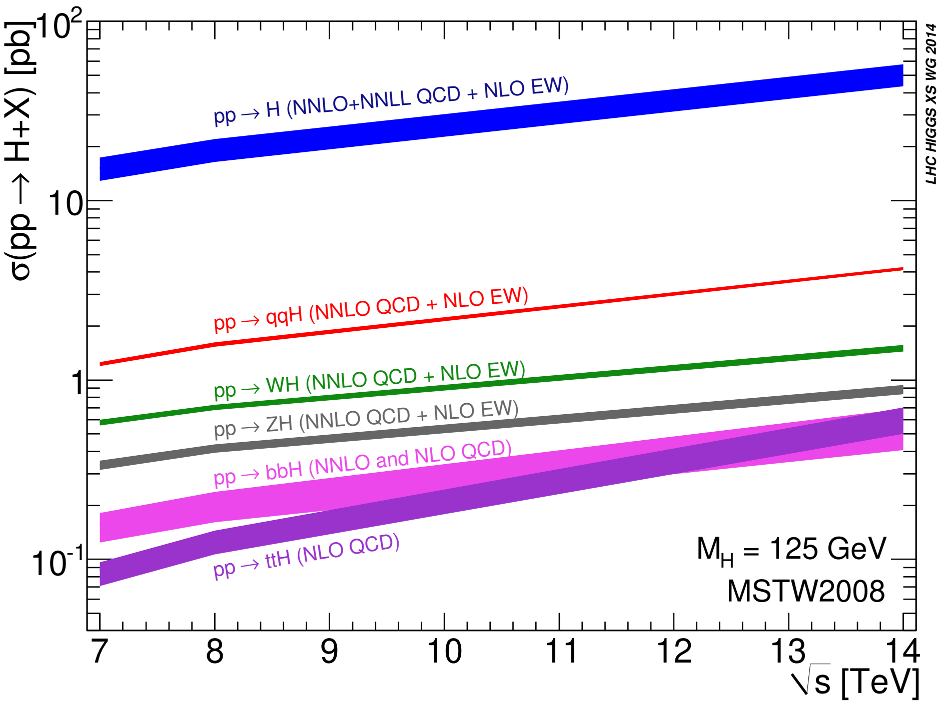

Figure 2.2: Production cross sections of each of the Higgs production modes for $m_H = 125$ GeV SM Higgs boson for the different $\sqrt{s}$ pp collisions of the LHC. [107]

2.3 Beyond the Standard Model

The SM perfectly describes all the particles presently discovered in the known universe. However, it is still thought to be an incomplete theory [91] due to some unexplained phenomena such as Dark Matter (DM), Lepton flavor violation, and unification of the gravitational force. With respect to the Higgs mechanism, current measurements leave a large hole that can be filled by BSM interpretations that allow for the existence of an extended Higgs sector, where the recently discovered SM Higgs boson is just one of multiple scalar bosons in such a theory. The remainder of this section will discuss in more detail for models specifically chosen for this analysis to probe this BSM space.

2.3.1 Specific BSM Models

BSM models span a wide range of theories and physics assumptions. Specific BSM models are often tested and searched for in large collider experiments to provide calculations and

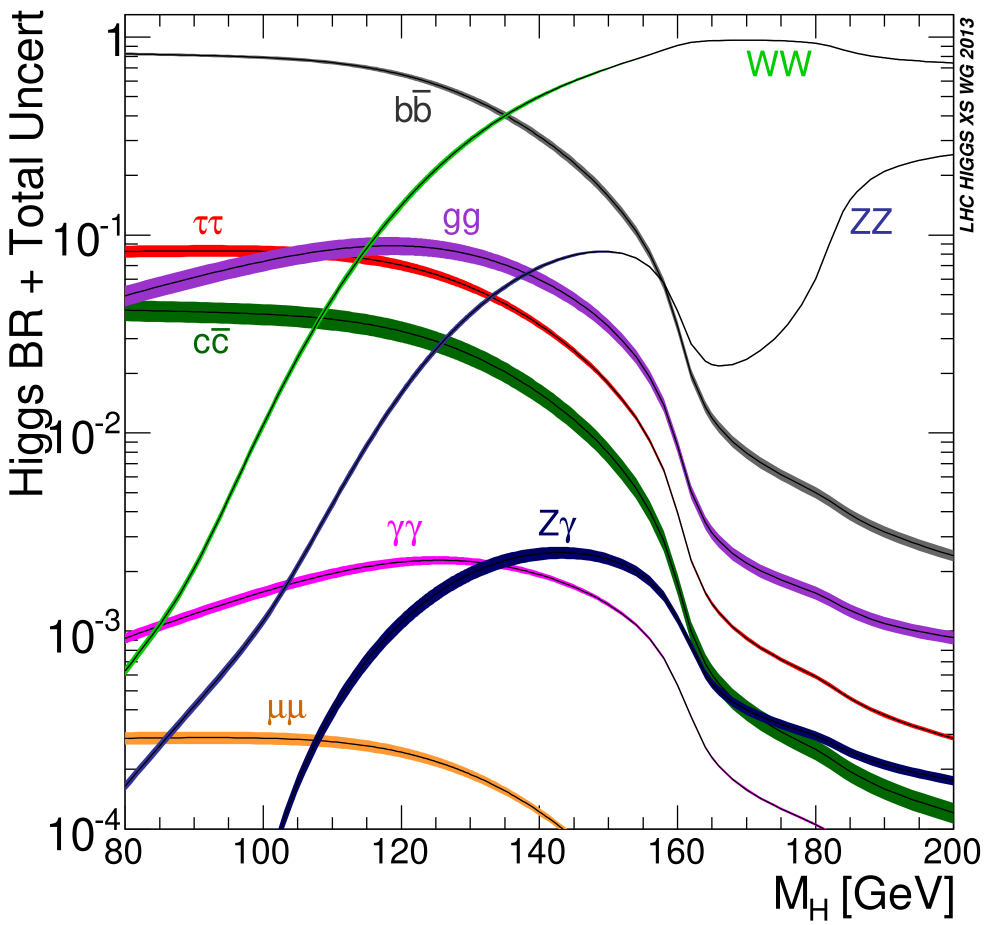

Figure 2.3: Branching ratios of the different Higgs boson decay modes as a function of Higgs mass. [107]

limitations on the chosen specific model. This subsection will describe the five resonance signals arising from four theoretical models that will be evaluated in this analysis.

Narrow Width Approximation

The first model considered is a Narrow Width Approximation (NWA) where the heavy scalar has a width that is much smaller than the detector resolution [87]. The width is taken to be identical to the SM Higgs boson width of 4 MeV. The NWA resonances behave very similarly to SM Higgs boson, allowing consideration of both ggF and VBF production modes in the analysis. The relevant NWA model Feynman diagrams are shown in Figure 2.4.

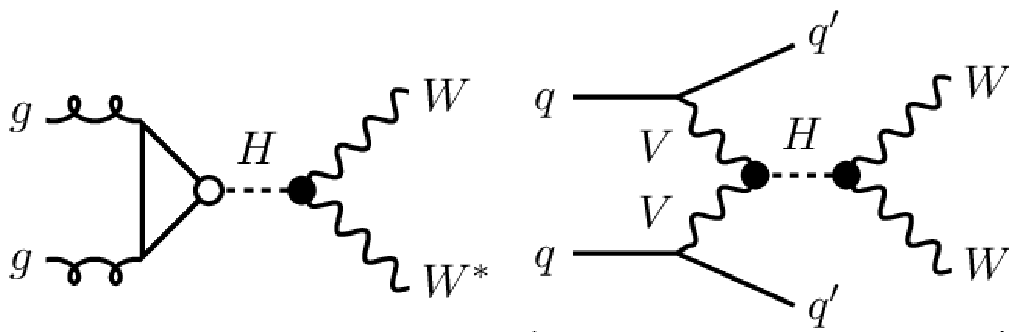

Figure 2.4: Feynman diagrams for the relevant Heavy-Higgs in the NWA for the ggF (left) and VBF (right) production modes.

Georgi-Machacek Model

A second scalar resonance considered in the analysis arises from the Georgi-Machacek (GM) model [100, 66]. The GM model has the Higgs sector extended by adding a real and complex $SU(2)_L$ triplet and has the SM value of $\rho = M_W^2/(M_Z^2 \cos^2\theta_W) = 1$ preserved at the tree level, where m_W and m_Z are the masses of the SM W and Z bosons and θ_W is the weak mixing angle. The five physical states present in the model combine to make the Higgs fiveplet and are uniquely identified by charge: H_5^0, $H_5^{\pm}$, $H_5^{\pm\pm}$. The members of the fiveplet have a preferential coupling to vector bosons [84], allowing the GM model to be less constrained in the VBF production mode [103]. A number of parameters are used to characterize this model [115, 144], however, significant dependence on the new heavy-Higgs boson's mass can lead to only the VBF production mode being possible (i.e. when $m_H > m_{H_5}$). Therefore, the cross section and branching ratio into VV are directly proportional to a single parameter, $\sin^2\theta_H$, which is used to characterise the amount the triplet Higgs fields generate the gauge boson masses. The analysis uses the H_5^0 resonance decay produced by VBF production as a reference model, and shares the same Feynman diagram as shown in Figure 2.4.

Bulk Randall-Sundrum Model

One spin-2 resonance is considered in this analysis rising from the Randall-Sundrum (RS) model. The RS model postulates the existence of a warped extra dimension in which only gravity propagates as in the original "RS1" scenario [134] or in which both gravity and all SM fields propagate as in the "bulk RS" or "RS2" scenario [22, 130]. Propagation in the extra dimension leads to a tower of Kaluza–Klein (KK) excitations of gravitons (denoted G_{KK}) and SM fields. In the bulk RS model considered in this analysis, KK gravitons are produced via both quark–antiquark annihilation and gluon–gluon fusion, with the latter dominating due to suppressed couplings to light fermions. It is also possible for these gravitons to be produced via vector boson fusion. The relevant Feynman diagrams for both productions are given in Figure 2.5. The strength of the couplings to the SM fields scale inversely to model parameter Λ_R, which can be expressed as:

$$\Lambda_R = \sqrt{g} \times k \times e^{-k\pi r_c} \times \sqrt{M_5^3/k^3} \tag{2.21}$$

where M_5 is the 5-dimensional Planck mass, k is the curvature factor for the extra dimension, and g is the 5-dimensional metric. The size of the extra dimension, $k\pi r_c$, is another free parameter of the model. Both the production cross section and decay width of the KK graviton scale as the square of k. For the value $k = 1$ used in this analysis, the G_{KK} resonance width relative to its mass is approximately 6%. The G_{KK} branching fraction is largest for decays into the $t\bar{t}$ final state, with values ranging from 42% for $m(G_{KK}) = 0.5$ TeV to 65% for $m(G_{KK})$ values above 1 TeV. Corresponding values for the WW (ZZ) final state range from 34% to 20% (18% to 10%). A summary of branching fractions for G_{KK} are given in Figure 2.6.

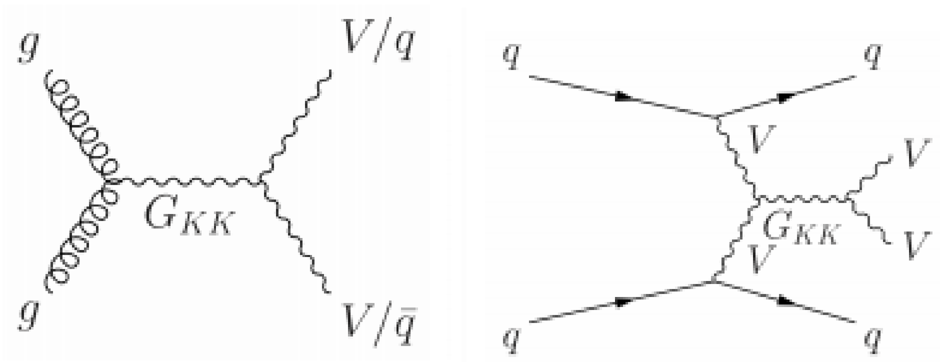

Figure 2.5: Feynman diagrams for the relevant Kaluza-Klein Graviton in the bulk RS model for the ggF (left) and VBF (right) production modes.

An additional scalar resonance is considered in this analysis that also comes from the RS model. In the RS model [134] the gravitional fluctuations in the single spatial extra dimension (ED) correspond to scalar fields, known as the radion [130], which to zeroth order are massless. One of the main issues in the original RS framework was a lack of a mechanism to stabilise the radius of the compactified ED, r_c. Introducing an additional scalar radion that propagates in the bulk is one solution to this problem, and would be produced by gluon-gluon fusion (ggF) with interactions localised at the two ends of the ED [104, 105]. This causes the radion field to acquire a mass term, and the coupling to SM fields scale inversely proportional to the model parameter Λ_R, similar to G_{KK} . The couplings of the radion to fermions are proportional to the masses of the fermions, while the couplings are proportional to the square of the masses for bosons. For radion mass above 1 TeV, the dominant decay mode is into pairs of bosons. The decay width of the radion is approximately 10% of its pole mass, resulting in observable mass peaks with a width comparable to the experimental resolution for the bosonic channels. The relevant Feynman diagrams for this process are shown in Figure 2.7.

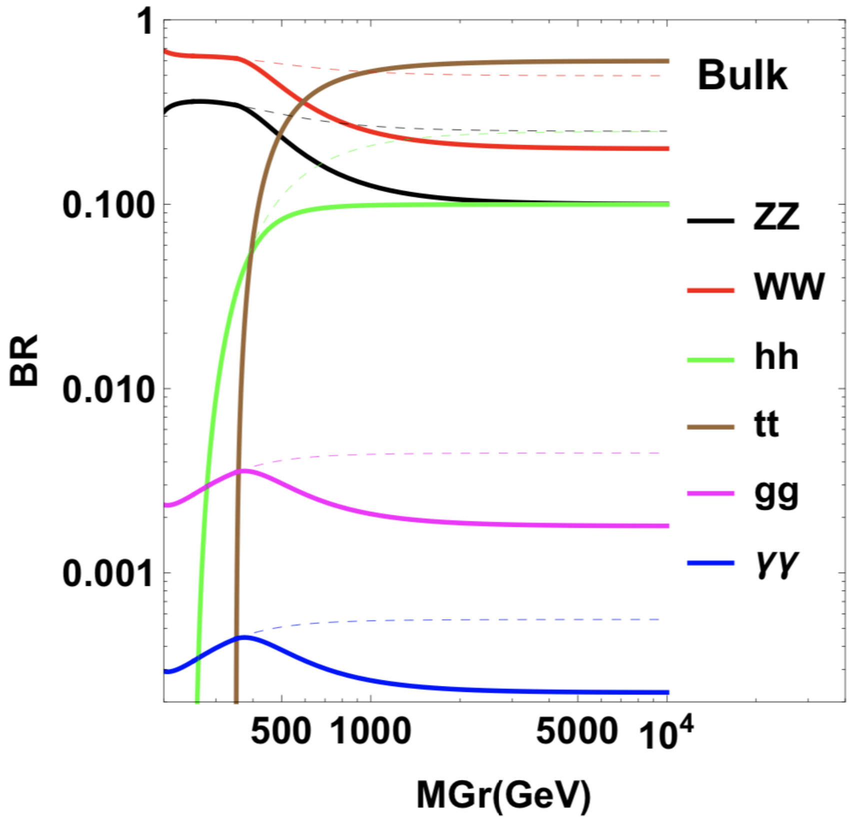

Figure 2.6: Branching ratios for the two body decay of the G_{KK} in the RS2 scenario. The solid and dashed lines show two hypotheses for fermion imbedding, where the solid line is the relevant value for this analysis. [130]

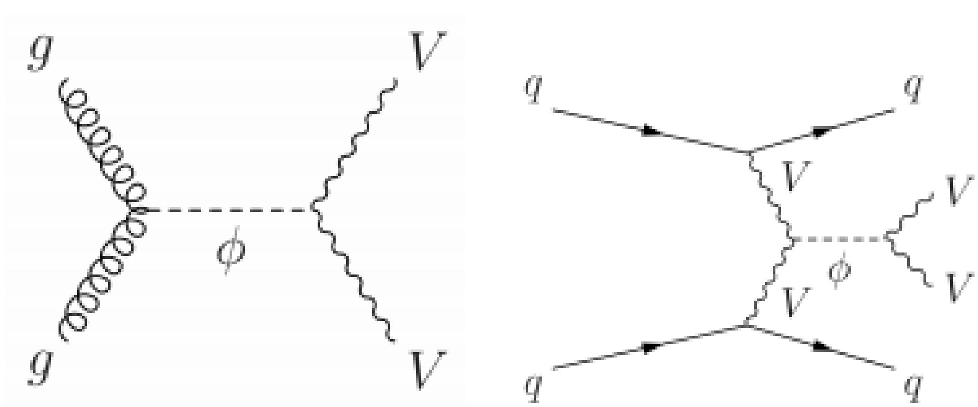

Figure 2.7: Feynman diagrams for the relevant Radion particle arising in the bulk RS model for the ggF (left) and VBF (right) production modes.

Heavy Vector Triplet

The last model considered in this analysis is a Heavy Vector Triplet (HVT) model, where the resonances considered are heavy neutral vector bosons, Z'. The HVT model provides a broad phenomenological framework [132, 82] that encompasses a range of different scenarios involving new heavy gauge bosons and their couplings to SM fermions and bosons. In this model, a triplet $\mathcal{W}$ of colorless vector bosons is introduced with zero hypercharge. This leads to a set of nearly degenerate charged, $W'^{\pm}$, and neutral, Z', states collectively denoted by V'. For the model used in this analysis, the W' and Z' masses are taken to be degenerate. The model is characterized by a number of different coupling strengths of those states to quarks, leptons, vector bosons, and Higgs bosons with the following interaction Lagrangian:

$$\mathcal{L}_{\mathcal{W}}^{\text{int}} = -g_q \mathcal{W}_\mu^a \bar{q}_k \gamma^\mu \frac{\sigma_a}{2} q_k - g_\ell \mathcal{W}_\mu^a \bar{\ell}_k \gamma^\mu \frac{\sigma_a}{2} \ell_k - g_H \left(\mathcal{W}_\mu^a H^\dagger \frac{\sigma_a}{2} i D^\mu H + \text{h.c.} \right), \tag{2.22}$$

where q_k and ℓ_k represent the left-handed quark and lepton doublets for fermion generation k ($k = 1, 2, 3$); H represents the Higgs doublet; σ_a ($a = 1, 2, 3$) are the Pauli matrices; and g_q, g_ℓ, and g_H correspond to the coupling strengths between the triplet field $\mathcal{W}$ and the quark, lepton, and Higgs fields, respectively.[5] Right-handed fermions do not participate in these interactions and the quark and lepton coupling terms can also be broken down further into specific first/second or third generation couplings for further interpretations. The triplet field interacts with the Higgs field and thus with the longitudinally polarized W and Z bosons by virtue of the equivalence theorem [77, 106, 65]. In this framework, the branching fractions for the decays $W' \to WZ$, $W' \to WH$, $Z' \to WW$, and $Z' \to ZH$, are equal for V' masses above 1.5 TeV and other neutral diboson final states are either suppressed or forbidden.

Two HVT scenarios are used as benchmark models for this analysis. The first is a Drell-Yan (DY) production mechanism while the second is produced via VBF, and the relevant

[5]The coupling constants g_H, g_f, g_q, and g_ℓ are used here. They are related to those in Ref. [132] as follows: the Higgs coupling $g_H = g_V c_H$ and the universal fermion coupling $g_f = g^2 c_F / g_V$, where g is the SM $\mathrm{SU}(2)_\mathrm{L}$ gauge coupling, while the c parameters and the coupling g_V are defined in Ref. [132]. Couplings specific to quarks and leptons are given by $g_q = g^2 c_q / g_V$ and $g_\ell = g^2 c_\ell / g_V$.

Feynman diagrams are shown in Figure 2.8. The DY scenario implements a strongly coupled scenario as in composite Higgs models [76] with $g_H = -2.9$ and $g_f = 0.14$. In terms of the coupling constants in the notation of Ref. [132], $g_V = 3$ is chosen. The V' resonances are broader than in a weakly coupled scenario (such as $g_V = 1$), but remain narrow relative to the experimental resolution at the LHC. The relative width, Γ/m, is below 5% over the parameter space considered for the DY HVT model in this analysis. The branching ratios for the DY produced V^0 are given in Figure 2.9. The VBF HVT production considers the case where the V' resonance couplings are set to $g_H = 1$ and $g_f = 0$. Therefore, the VBF HVT resides in a separate phase space domain and assumes no DY production.

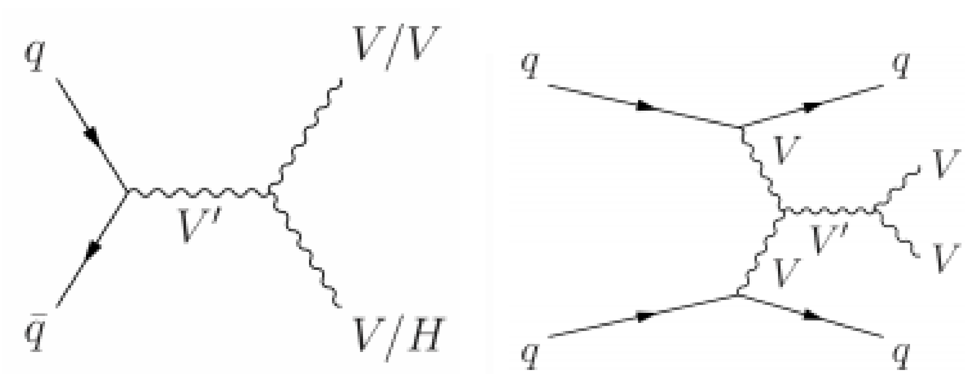

Figure 2.8: Feynman diagrams for the relevant Heavy Vector Boson in the HVT for the qqA (left) and VBF (right) production modes.

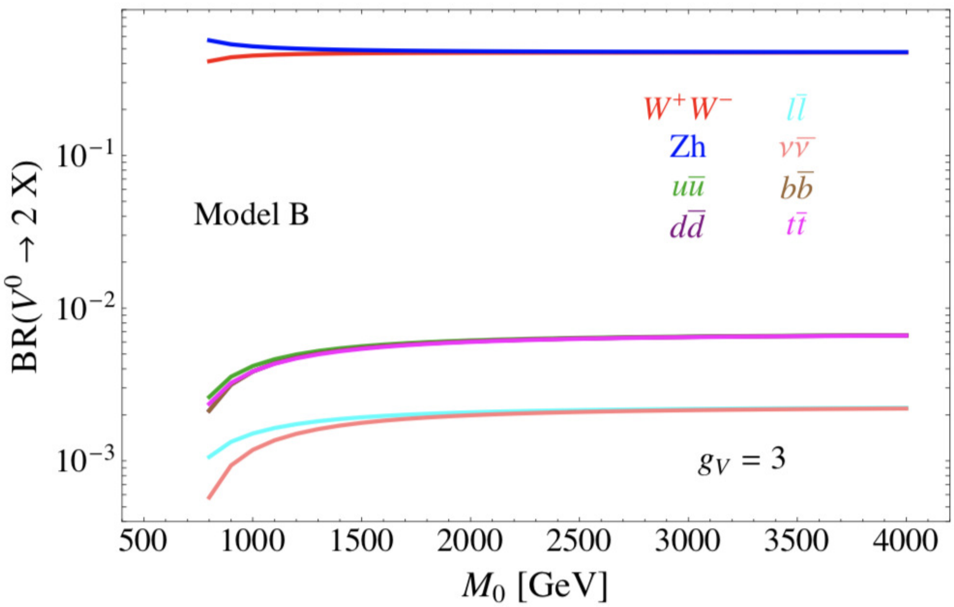

Figure 2.9: Branching ratios for the two-body decay of the HVT DY V^0. [132]

Chapter 3

The LHC and the ATLAS Detector

The Large Hadron Collider [55] is a 27 km circumference synchotron built about 100 m below the countryside near the city of Geneva, Switzerland. The LHC's main ring is home to four major collision points for the four main experiments located there: ATLAS [71], CMS [74], LHCb [75], and ALICE [18]. The LHC provides beams of proton clouds traveling in opposite directions, with individual protons carrying an average energy of 6.5 TeV. When the beams are collimated down at each collision point, the protons collide with a combined center of mass energy of $\sqrt{s} = 13$ TeV. The proton–proton collisions contain a diverse collection of collisions of the proton constituents, gluons and different quark flavors, which results in a vast array of physics processes to be observed and studied by the experiments. Section 3.1 will provide a brief overview of the LHC accelerator complex. Section 3.2 will provide a brief overview of the ATLAS experiment's detector components and data aquisition techniques.

3.1 The Large Hadron Collider

The LHC uses superconducting electromagnetic technology to accelerate and direct the particles to be used in collisions around it's 27 km circular path. Using roughly 1200 superconducting dipole magnets with field strengths of $\tilde{8}$ T, the accelarated particles (primarily protons, but also at times heavy ions) are steered around the near-circular path. To maintain the superconductive properties the magnets are constantly cooled to 1.9 K using superfluid helium. A cross-sectional of one of the cryodipole systems is shown in Figure 3.1.

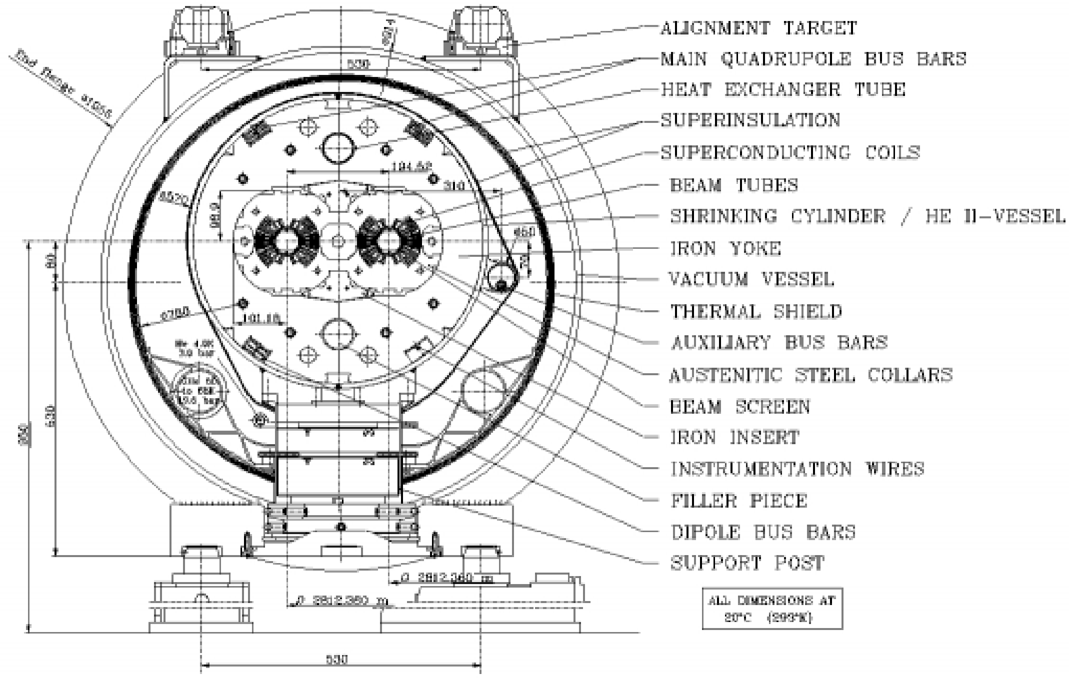

Figure 3.1: A cross-sectional view of one of the LHC cryodipole systems. [55]

At each collision point quadropole magnets are employed to focus the beams to ensure proton-proton collisions, up to roughly 40 million per second. The beam pipe is exceptionally maintained at near-perfect vacuum levels of 10^{-10} mbar to prevent the protons from interacting with any unwanted gas particles.

3.1.1 Accelerator Complex

In order to attain the desired center-of-mass energies for proton-proton collisions, the beams are accelarated in multiple stages. Prior to any acceleration, hydrogen atoms have their electrons removed by first adding an additional electron and bombarding the H^- ions with hydrogen gas to form a plasma which then has the electrons removed by a strong electric field. The Linac2 linear accelerator then uses radiofrequency (RF) cavities to push and pull the protons up to an energy of 50 MeV. After the Linac2, the protons enter the Proton Synchrotron Booster (PSB) which uses it's four superimposed synchrotron rings to accelerate the protons to 1.4 GeV to be sent to the Proton Synchrotron (PS). The 628 m circumference PS accelerates the protons to an energy of 25 GeV using 277 electromagnets. The protons are then sent off to the Super Proton Synchrotron (SPS), which accelerates the protons up to 450 GeV with its 1317 electromagnets. Finally the protons are injected to the LHC to reach their peak center-of-mass energy of 6.5 TeV. A full diagram of the LHC accelerator complex is shown in Figure 3.2.

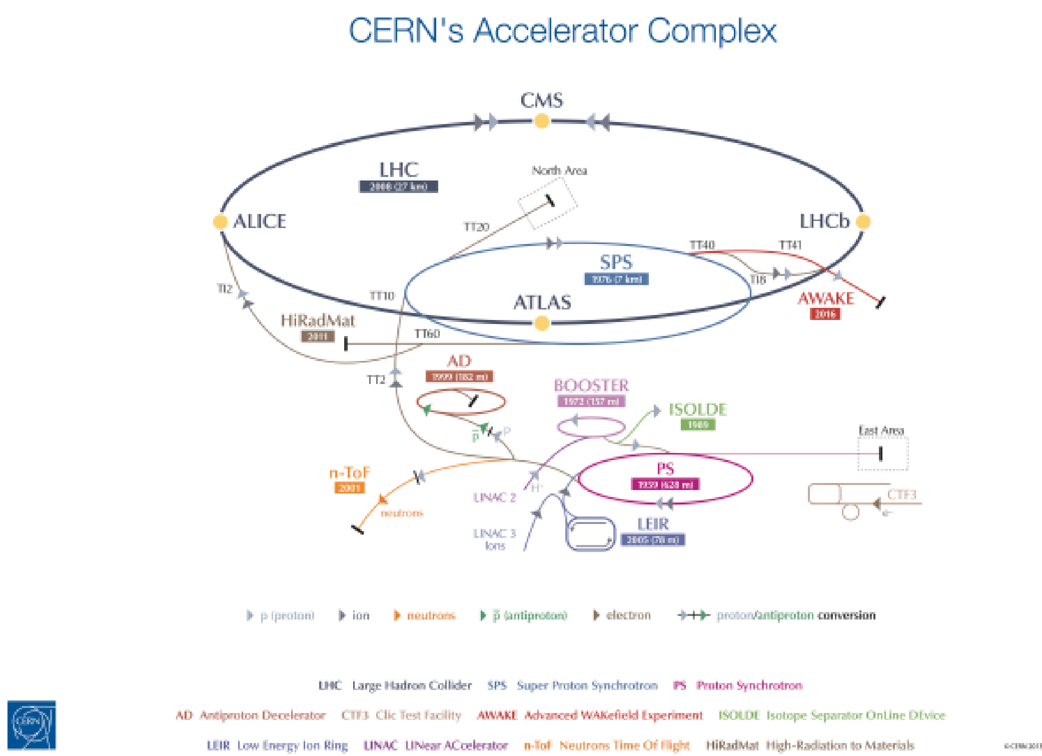

Figure 3.2: The accelerator complex of the LHC, with all the additional injection components leading to the main ring for the ATLAS experiment's data collection point. [55]

3.1.2 Luminosity Measurement

A measurement of the production of specific events generated by the LHC can be specifically calculated by:

$$N_{\text{event}} = \sigma_{\text{event}} \cdot \mathcal{L} \tag{3.1}$$

where N_{event} is the number of specific events generated, σ_{event} is the cross-section, or probability, of such an event being generated, and $\mathcal{L}$ is the integrated luminosity of collisions, which is defined as the number of particles passing through a given area integrated over time. More specifically, the machine luminosity for a Gaussian beam distribution can be defined as:

$$\mathcal{L} = \frac{N_b^2 n_b f_{\text{rev}} \gamma_r}{4\pi \epsilon_n \beta^*} \cdot F \tag{3.2}$$

where N_b is the number of particles per bunch, n_b is the number of bunches per beam, f_{rev} is the revolution frequency of the beam, γ_r is the relativistic gamma factor, ϵ_n is the normalized transverse beam emittance, and β^* is the beta function at the collision point [55]. The additional factor F is the geometric luminosity factor due to the crossing angle at the interaction point. By inspection, one can see the increase in measurable physics events by optimizing the transverse cross section and proton density of the collisions. Luminosity measurements of the LHC are taken periodically, with specific ATLAS measurements being performed using the LUCID-2 sub-detector [43]. The fully recorded ATLAS Run-II dataset corresponds to an integrated luminosity of 147 fb^{-1}, of which 139 fb^{-1} passed quality checks to be used for physics. The full scale of the collected integrated luminosity is shown in Figure 3.3.

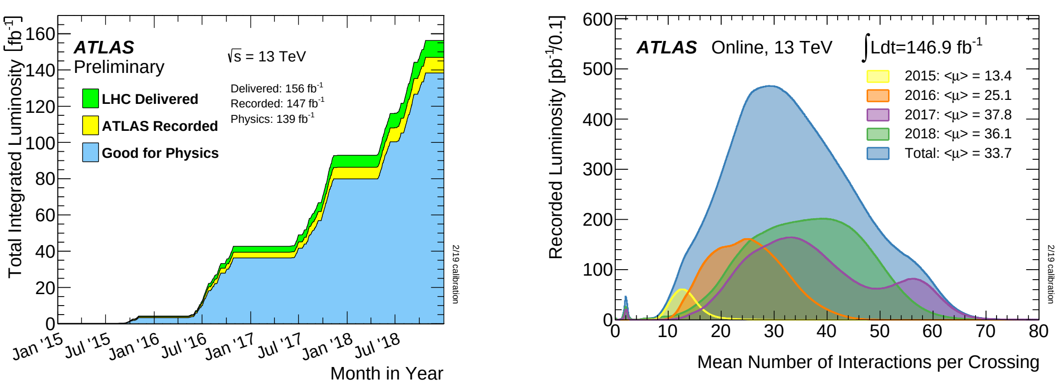

Figure 3.3: The integrated luminosity collected by the ATLAS experiment during Run-II (left) and the distributions of the mean number of interactions per crossing (right) for each data-taking year. [142]

3.2 The ATLAS Experiment

The ATLAS (**A** **T**oroidal **L**HC **A**pparatu**S**) experiment uses a general purpose particle detector located 100 m underground at LHC's point 1. The detector's original design optimization was for the search and measurement of the Higgs Boson and its related properties as well as for searching for evidence of supersymmetry (SUSY) and other BSM processes. The 7000 ton, 44 m long, 25 m diameter detector is cylindrical in shape and comprised of layers of sub-detectors radiating out from the center. Each of the sub-detectors is specifically designed for measurement of different fundamental properties of particles. Extending outwardly from the beampipe, the set of sub-detectors include an inner tracking detector (ID) surrounded by a superconducting solenoid, electromagnetic and hadronic calorimeters (eCal, hCal), and a muon spectrometer (MS). A full cut-out view of the ATLAS detector is shown in Figure 3.4.

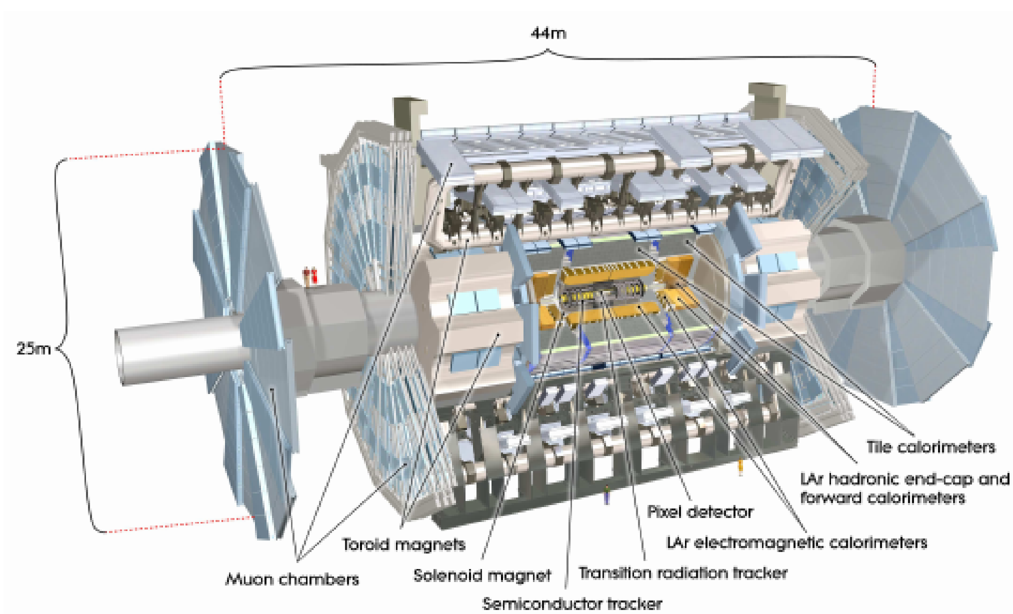

Figure 3.4: Cut-away view of the ATLAS detector, highlighting each of the components of the ID, the calorimetry system. Not shown are the encompassing MS systems. [71]

3.2.1 The ATAS Coordinate System

The ATLAS detector employs a right-handed Cartesian coordinate system, with the origin at the nominal interaction point (IP), the z-axis aligned along the beam pipe, and the x,y-plane transverse to the direction of the beam. The positive x direction points inwards of the LHC ring, and the positive y direction points upwards toward the surface of the earth. Additionally, cylindrical coordinates are employed in the transverse plane, with ϕ the angle from the positive x-axis, and θ the angle from the positive z-axis. Physical properties in the transverse plane are often used due to lack of conservation of energy information in the z direction. For example, the transverse momentum is defined as the projection of the momentum vector in the transverse plane, $\vec{p}_T = (p_x, p_y)$:

$$p_T \equiv \sqrt{p_x^2 + p_y^2} \tag{3.3}$$

A transformation of the polar angle, θ, is used to measure the separation between two particles and ensure that the quantity is Lorentz invariant. This is defined as the pseudorapidity, η:

$$\eta = -\ln\left(\tan\frac{\theta}{2}\right) \tag{3.4}$$

For massive objects, occasionally a more well-defined physics quantity of rapidity, y, can be used:

$$y = \frac{1}{2}\ln\left(\frac{E + p_z}{E - p_z}\right) \tag{3.5}$$

The separation of physics objects can be defined by a composite measurement of the pseudorapidity and the azimuthal angle, resulting in an angular distance of ΔR:

$$\Delta R \equiv \sqrt{(\Delta\eta)^2 + (\Delta\phi)^2} \tag{3.6}$$

3.2.2 Inner Tracking Detector (ID)

The center most portion of the ATLAS detector is the Inner Detector. It's primary purpose is to track charged particles' trajectories as they travel outwards from the collision point, while also measuring their momentum and the precise location of the primary vertex of the collision. Additionally, the ID components are used for displaced vertex measurements to aid in the identification of long-lived decays , such as used in heavy-flavor quark tagging. The ID consists of three major sub-detectors: the pixel detector, the semiconductor tracker (SCT), and the transition radiation tracker (TRT). Each sub-detector is divided into two portions: barrel, running parallel to the beam pipe covering the central region, and two end-caps, perpendicular to the beam pipe covering the forward regions. A solenoid magnet surrounds the ID, using a 2 T magnetic field to bend the trajectory of charge particles to use in charge identification and momentum measurements. A full visual overview of the ID can be seen in Figures 3.5 and 3.6. The ID was originally designed [71] for a momentum resolution defined as:

$$\frac{\sigma_{p_T}}{p_T} = 0.05\% \cdot p_T \cdot \text{GeV}^{-1} \tag{3.7}$$

Prior to collision and data taking, an intrinsic resolution in the limit of large values of p_T was calculated [72] using cosmic ray measurements as:

$$\frac{\sigma_p}{p} = (0.0483 \pm 0.016)\% \cdot p_T \cdot \text{GeV}^{-1} \tag{3.8}$$

With the addition of the insertable b-layer [60] at the beginning of LHC Run-II, no additional improvement of resolution was made in momentum resolution, but an improvement in the resolution of impact parameters d_0 and z_0 is seen.

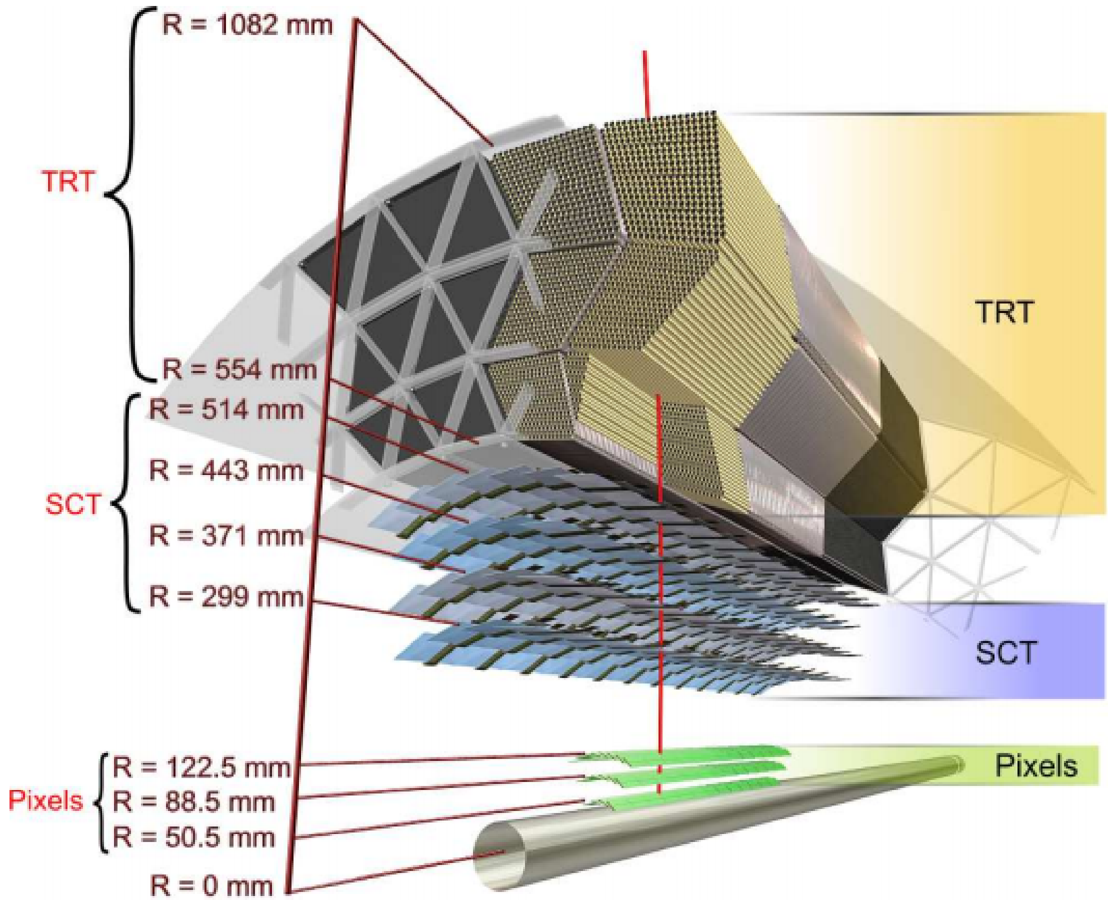

Figure 3.5: Drawing showing the trajectory of a charged particle traversing the different portions of the inner detector subsystems in the barrel region. [71] The IBL is missing from this depiction.

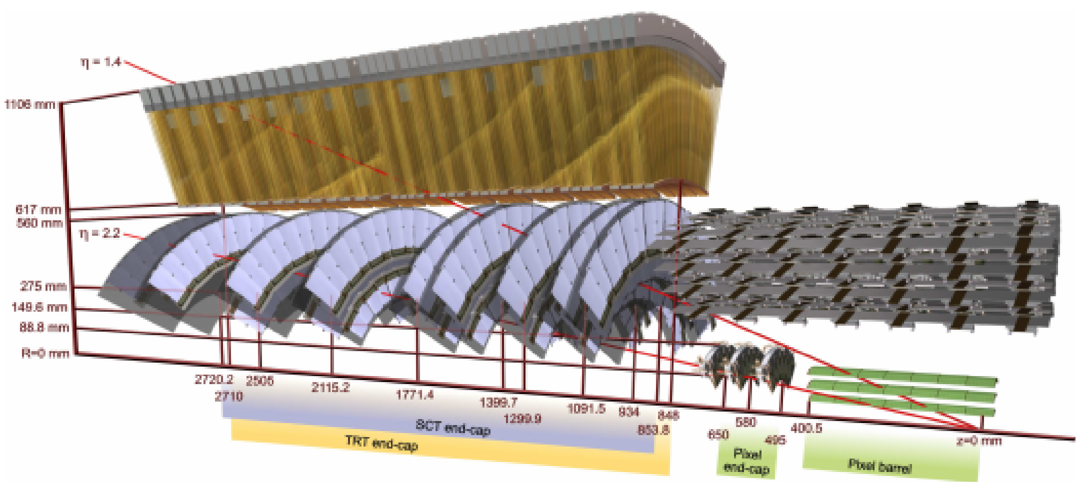

Figure 3.6: Drawing showing the trajectory of two charged particles with different η traversing the different portions of the inner detector subsystems in the endcap region. [71]

Pixel Detector

The pixel detector makes up the most inner layers of the ATLAS detector. The pixel detector gives a 3-dimensional measurements of the location of a charge particle as it traverses the medium in it's trajectory outwards from the IP. Nominally the pixel detector pixels have a dimension of 50 μm in the R-ϕ plane and 400 μm in the z direction. Prior to the beginning of the LHC Run-II in 2014, an additional layer of pixel detectors was added, referred to as the insertable b-layer (IBL), which has a slightly improved granularity in the z direction of 250 μm. Combined, the pixel layer has more than 90 million unique readout channels providing a track reconstruction resolution of 10 μm x 115 μm in the coverage range of $|\eta| < 2.5$. The fine granularity of the pixel detector allows for accurate impact parameter measurements, leading to improved b-tagging and vertex matching performance.

Semiconductor Tracker

Continuing outwards from the pixel detector is the semiconductor tracker. The SCT is made up of silicon strip detectors arranged in four double-layers in the barrel region, obtaining a spacial granularity of 17 μm x 580 μm in the R-ϕ and z directions. Each 80 μm wide, 6-13 cm long strip is arranged in a pair, with the strips rotated by 40 mrad with respect to each other to allow for an increased accuracy of measurement in the z-direction, despite the strips being much longer. Additionally, in the endcap regions another nine similar double-layers are arranged to give the SCT a coverage range of $|\eta| < 2.5$.

Transition Radiation Tracker

The outer layer of the ID is the transition radiation tracker. It is the largest of the ID sub-detectors, made up of almost 300,000 straw tubes measuring 4 mm in diameter and 144 (37) cm in length in the barrel (endcap) region. Each straw tube is filled with a Xenon-based gas mixture, allowing the gas to be ionized by charged particles traveling through. The excited electrons are then attracted to the conducting wire in the center, creating a signal to allow a timing calculation to determine the spatial location of the particle. The resolution of the TRT is about 130 μm in the R-ϕ plane, giving no additional information in the z direction. The TRT has a coverage range of $|\eta| < 2.0$.

3.2.3 Calorimetry System

Surrounding the ID and solenoid magent of the ATLAS detector is the calorimetry system. For the majority of the pseudorapidity coverage, it is subdivided radially into two sampling calorimeters: an electromagnetic calorimeter followed by a hadronic calorimeter. A full depicition of the calorimetry system can be seen in Figure 3.7. The caloriemetry system has a full coverage range of $|\eta| < 4.9$.

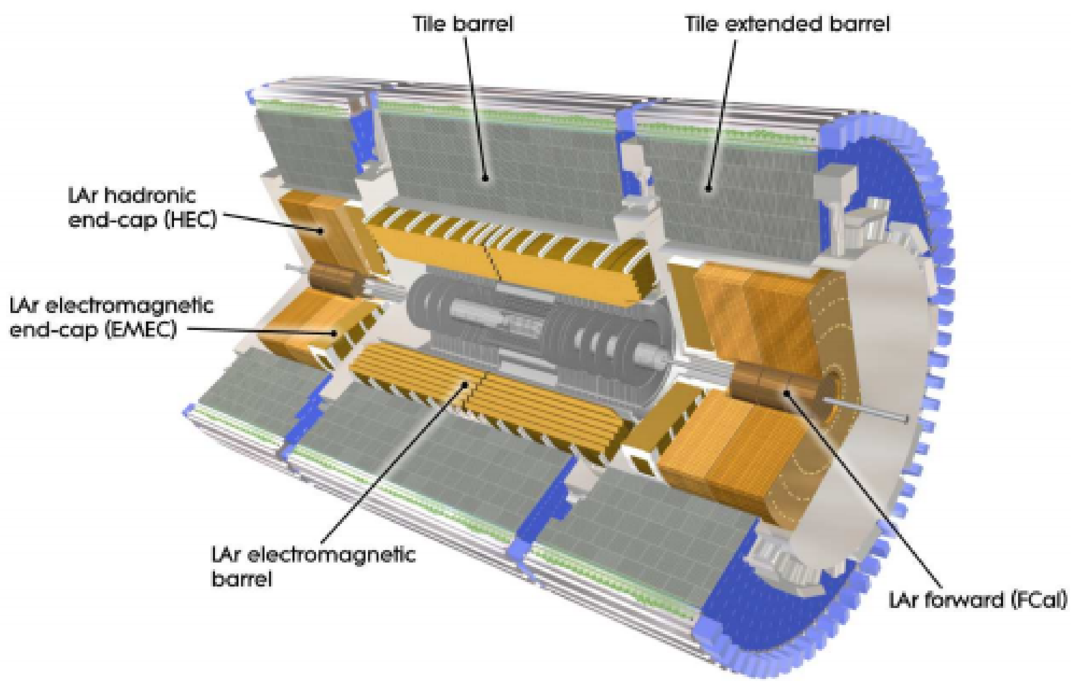

Figure 3.7: Cut-away view of the ATLAS detector's calorimetry system. [71]

Electromagnetic Calorimeter

The electromagnetic calorimeter is a sampling calorimeter using liquid-argon (LAr) as a scintillator and lead plates as absorbers. The eCal is split into a number of different portions depending on the psuedorapidity range. From $0 < |\eta| < 1.475$ consists of the barrel portion, with a granularity of 0.003 x 0.025 in η-ϕ space. The endcap portions cover the range from $1.375 < |\eta| < 3.20$ with a granularity of 0.1 x 0.1 in η-ϕ space. The eCal is split radially into four layers, with the first layer as a presampling layer only covering the range of $0 < |\eta| < 1.80$, which consists of no absorbing lead plates. The next three layers are sampling layers with the lead absorbers included. They provide differing granularity levels in η-ϕ space to improve the overall position resolution of the eCal. A diagram of the eCal layers in the barrel region can be seen in Figure 3.8. Due to the overlap of the barrel and endcap portions, a crack region exists between $1.37 < |\eta| < 1.52$ which leads to significantly reduced energy resolution for electrons and photons. Energy resolution calculations for the eCal can be given as:

$$\frac{\sigma_E}{E} = \frac{10\%}{\sqrt{E/\text{GeV}}} \tag{3.9}$$

Hadronic Calorimeter

The hadronic calorimeter resides outside the eCal, and consists of scinitillating tiles interleaved with steel plate absorbers in the barrel region, and LAr with copper absorbers in the endcap regions. The barrel region is subdivided into two layers, with a central part covering $0 < |\eta| < 1.0$, and two extended barrel parts covering $0.8 < |\eta| < 1.7$. The endcap region covers the range of $1.5 < |\eta| < 3.2$. Additionally, the hCal includes a forward calorimeter region covering the range of $3.1 < |\eta| < 4.9$, which employs a LAr-copper layer for electromagnetic measurements as well as two tungsten plates for hadronic measurements. A sample of the barrel and endcap portion of the hCal is shown in Figure 3.9. Energy resolution calculations

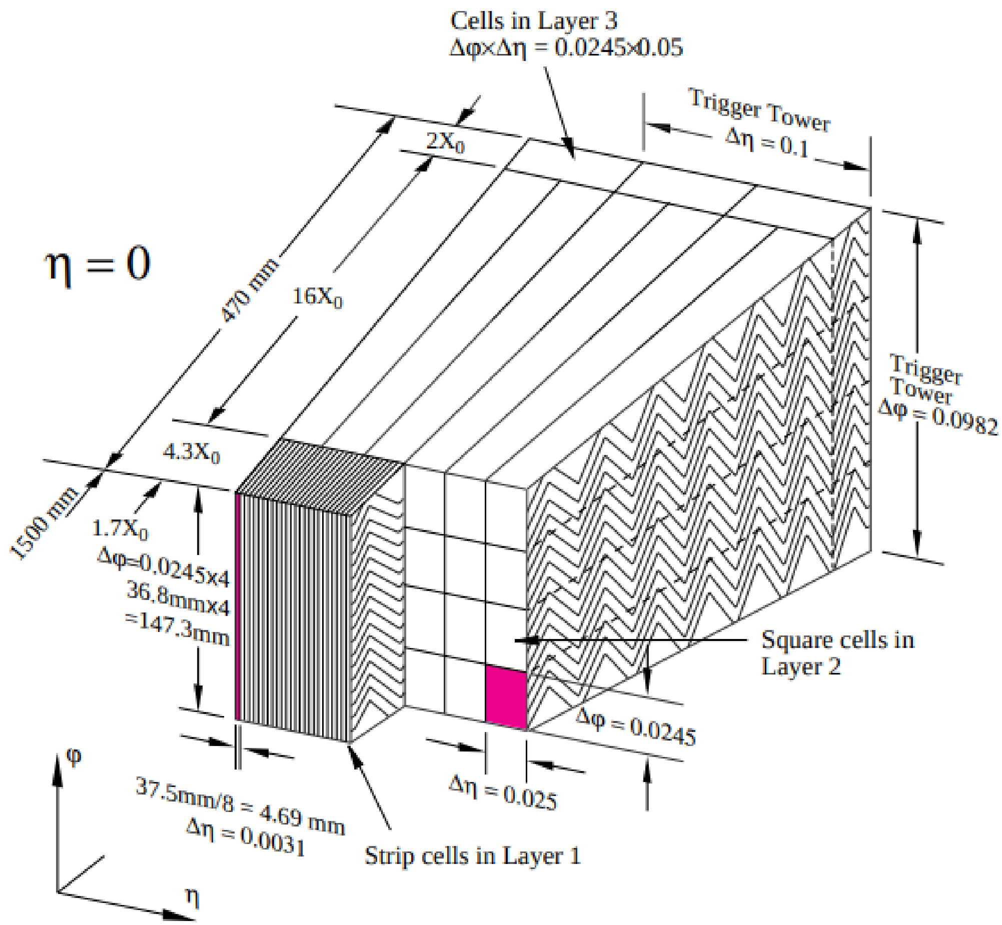

Figure 3.8: Display of the different radial layers of the electromagnetic calorimeter in the ATLAS detector's calorimetry system. [71]

for the hCal can be given as:

$$\frac{\sigma_E}{E} = \frac{50\%}{\sqrt{E/\text{GeV}}} \tag{3.10}$$

in the central and encap regions, and:

$$\frac{\sigma_E}{E} = \frac{100\%}{\sqrt{E/\text{GeV}}} \tag{3.11}$$

in the forward region.

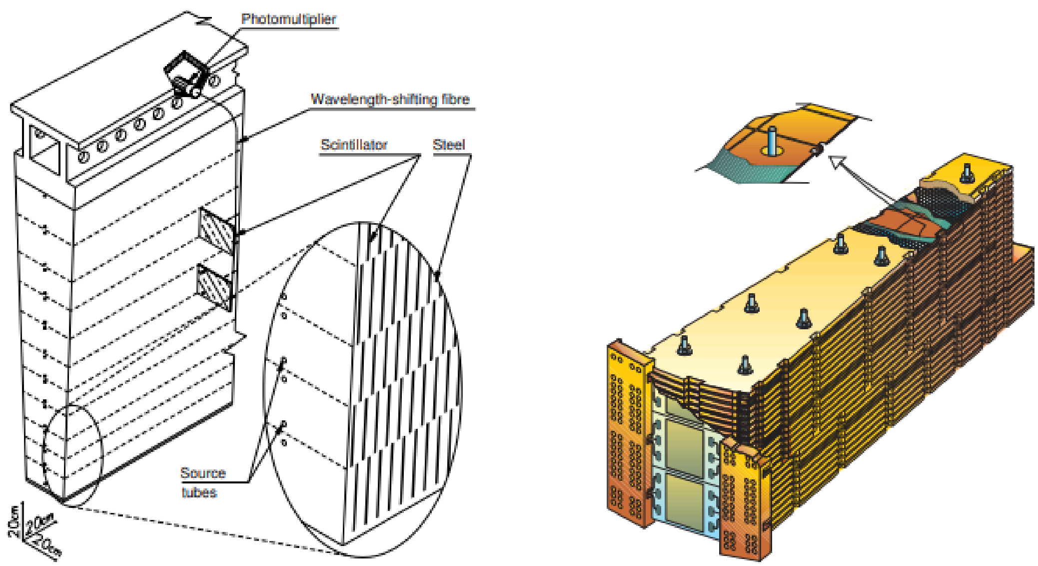

Figure 3.9: The scintillating tile schematics of the barrel portion of the hCal (left) and a cut-away view of a module of the end-cap portion of the hCal (right). [71]

3.2.4 Muon Spectrometer (MS)

Muons are the only particles to both have non-negligible interactions with the detector and regularly escape even the hCal. Due to this property, the outermost layer of the ATLAS detector is focused to measure muon momentum and trajectories. The muon spectrometer covers the range of $|\eta| < 2.7$, hosting three large magnets to bend the muon trajectory to allow for charge identification and momentum measurements.

The MS behaves similarly to the tracking portion of the ID, using multiple layers to track the trajectory of muons. Monitored drift tubes cover the range of $|\eta| < 2.7$, used for precision momentum measurements. The drift tubes are complemented with cathode strip containers covering the range of $2.0 < |\eta| < 2.7$. Resistive plate chambers and thin gap changes are installed between $0 < |\eta| < 1.0$ and $1.05 < |\eta| < 2.7$, respectively, to provide additional measurements with high temporal resolutions.

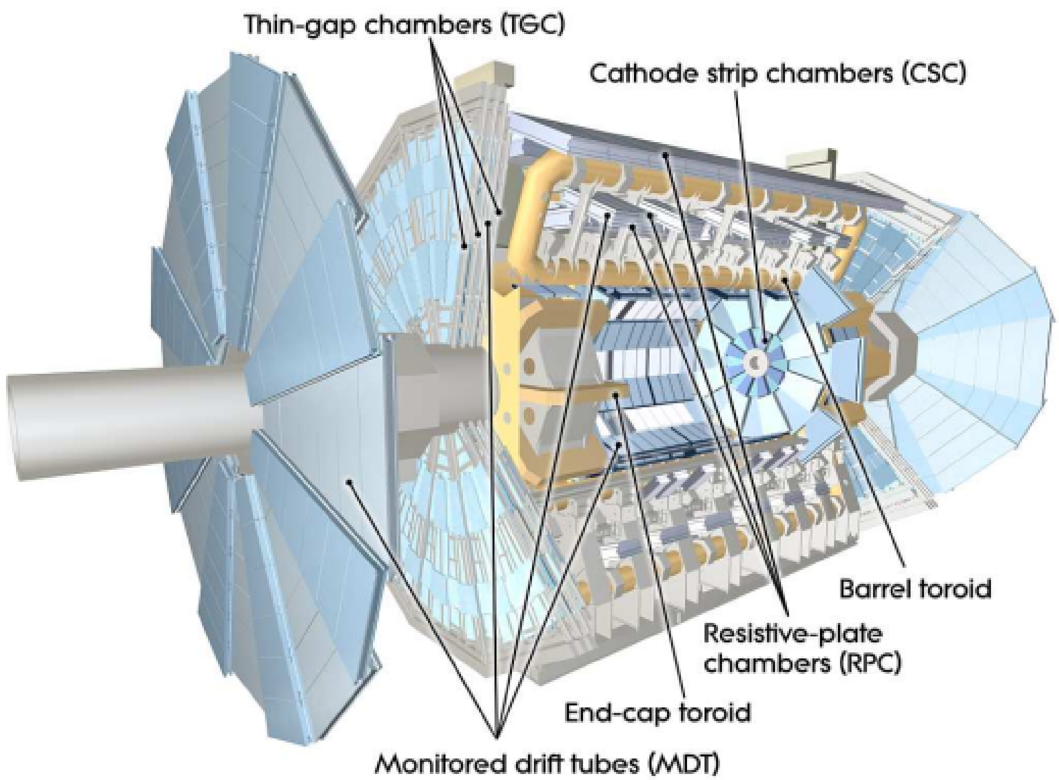

Figure 3.10: Cut-away view of the muon spectrometer system of the ATLAS detector. [71]

3.2.5 Trigger and Data Acquisition

With very little time (25ns) between the *pp* bunch crossings at the LHC, it is beyond the scope of possibility with current read-out technology to record every event's information. Not only this, but the high event rate (30-40MHz) would vastly exceed the CERN computing center's bandwidth and storage capabilities. Due to these limitations, a triggering strategy is employed to select events that become specifically interesting for physics analysis. ATLAS's triggering scheme uses a multi-layer trigger, with special focus to select signatures of events with cross sections many orders of magnitude lower than that of the nominal pp cross section. A full overview of the ATLAS Run-II trigger selection and scheme can be seen in Reference [31].

The first layer of the trigger is the "Level 1 trigger" (L1). The L1 trigger is implemented in custom electronic circuits in the MS and calorimetry systems with reduced granularity. The former portion is primarily used in selecting events with high p_T muons, and the latter is much more customizable, often used to select lepton signatures, highly energetic jets, and large amounts of missing transverse energy (E_T^{miss}). The frequency of the L1 trigger generally reduces the number of events to three orders of magnitude less than the collision rate.

The second layer of the trigger is the "High Level Trigger" (HLT). The HLT is implemented by software running on a dedicated computing farm with thousands of available CPU. The HLT uses reconstruction algorithms similar to the ones used in object reconstruction to make triggering decisions based on physical kinematics, with a number of different options (trigger chains) available to be satisfied. The HLT additionally reduces the events recorded to tape by a factor of 100 over the L1 trigger.

After an event successfully fires an HLT, the event is written to disk through one of the inclusive output streams dependent on which trigger chain has been fired. The output stream for the data processed in this thesis come from the "physics_Main" stream.

Chapter 4

Data and Monte-Carlo Simulation Samples

4.1 Data and MC Samples

The data that is used in this analysis corresponds to 139 fb^{-1} with an uncertainty of 1.7% and comes from the Physics Main stream[1] . The uncertainty calculation is discussed in detail in [43]. The data here corresponds to the full pp collision data collected between 2015 and 2018 at $\sqrt{s} = 13$ TeV with a bunch spacing of 25 ns, while also passing data quality checks. The Good-Runs-Lists[2] used for the data years are as follows:

- 2015: data15_13TeV.periodAllYear_DetStatus-v89-pro21-02_Unknown_PHYS_StandardGRL_All_Good_25ns.xml
- 2016: data16_13TeV.periodAllYear_DetStatus-v89-pro21-01_DQDefects-00-02-04_PHYS_StandardGRL_All_Good_25ns.xml
- 2017: data17_13TeV.periodAllYear_DetStatus-v99-pro22-01_Unknown_PHYS_StandardGRL_All_Good_25ns_Triggerno17e33prim.xml
- 2018: data18_13TeV.periodAllYear_DetStatus-v102-pro22-04_Unknown_PHYS_StandardGRL_All_Good_25ns_Triggerno17e33prim.xml

This analysis makes use of both flavor single lepton triggers, with an OR betweeen the triggers to try and maximise the total trigger efficiency. All of the triggers used for the specific data taking periods, along with their minimum transverse momentum (p_T) thresholds, are listed in Table 4.1.

[1] The ATLAS data production has a number of different data streams, which contain information pertinent to specific physics analyses. The 'Physics Main' stream is the most general stream used within the ATLAS experiment.

[2] The good runs lists (GRLs) are used in the data quality process with ATLAS. These lists contain the runs of the data-taking process where the quality of the data is deemed acceptable for physics analysis.

Lepton	Level-1 Trigger	High-Level Trigger (HLT)
Year 2015		
e	20 GeV	24M OR 60M OR 120L GeV
μ	15 GeV	20i OR 50 GeV
Year 2016-18		
e	20 GeV	26Ti OR 60M OR 140L GeV
μ	15 GeV	26i OR 50 GeV

Table 4.1: The minimum p_T requirement used at the different levels of triggers for each data year. Letters "T", "M", and "L" next to a minimum value correspond to lepton identification requirements Tight, Medium, and Loose, respectively. The letter "i" next to a minimum value indicates an isolation requirement lower or equal to the requirements used in the offline analysis.

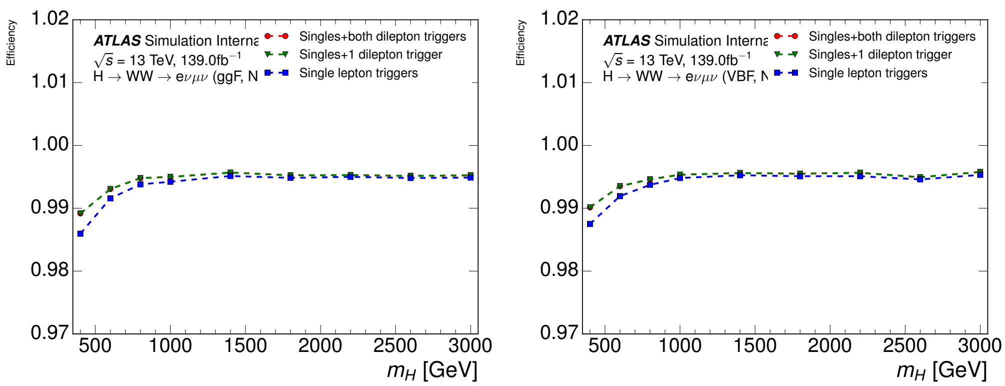

Figure 4.1: Trigger efficiency as a function of m_H for the baseline NWA signal model for ggF (left) and VBF (right) production modes. The single dilepton triggers corresponds to the average of using either the HLT_e17_lhloose_nod0_mu14 or HLT_e7_lhmedium_nod0_mu24 triggers. Preselection cuts on lepton p_T, quality, identification, and isolation are all applied prior to calculation.

In light of the single lepton trigger selection, a study was made to determine if there would be improvement by adding additional di-lepton triggers. The comparison of trigger efficiencies after lepton-based preselection for the baseline NWA sample for both ggF and VBF production modes is shown in Figure 4.1. There was very little efficiency gain to be seen for both production modes, so the single lepton triggers were chosen as the trigger selection.

4.1.1 Monte-Carlo Samples

Signal Samples

The analysis uses samples of simulated events to optimise the event selection and estimate the background contributions from SM processes. A summary of these and the generated mass points are shown in Table 4.2. The heavy Higgs NWA signal sample is produced using Powheg-Box 2.0 [127, 96, 24] where the ggF [25] and VBF [128] production mechanisms are calculated separately with matrix elements up to next-to-leading order (NLO) in quantum chromodynamics. It uses the CT10 NLO parton distribution function (PDF) set [123] and is interfaced with Pythia 8 (v8.186) [140] for the $H \to WW$ decays, for parton showering and hadronisation. A set of tuned parameters called the AZNLO tune [15] is used to describe the underlying event. The width of the NWA Higgs boson in these samples is set to 4 MeV.

The benchmark for the radion samples are generated using MadGraph5_aMC@NLO 2.6.1 [27] using the NNPDF2.0 PDF set [45] and interfaced with Pythia 8.230 [139] tuned to the A14 NNPDF2.0 parameter set [2]. The radion is a scalar field rising from the fluctuations of the extra dimension in the RS framework. Mass points for the radion samples are 300 GeV, 700 GeV, and 1 TeV to 6 TeV in 1 TeV intervals.

The benchmark samples of the GM are generated using MadGraph5_aMC@NLO 2.3.3 using the NNPDF30LO PDF set [44] and interfaced to Pythia 8 (v8.212) [139], tuned according to the A14 NNPDF2.0 parameter set [2]. The HVT samples are generated using the same generators and versions as for the GM samples, however, using the NNPDF2.0

Signal	Production Mode	Pole Masses [Step Size] in TeV
NWA	ggF	0.2, 0.25, 0.3-1.0 [0.1], 1.0-4.0 [0.2]
	VBF	0.2, 0.25, 0.3-1.0 [0.1], 1.0-4.0 [0.2]
Radion	ggF	0.3, 0.7, 1.0-6.0 [1.0]
	VBF	0.3, 0.7, 1.0-6.0 [1.0]
GM	ggF	x
	VBF	0.25, 0.3-1.0 [0.1]
HVT V'	qqA	0.3-1.0 [0.1], 1.0-3.0 [0.2], 3.0-5.0 [0.5], 5.0-8.0 [1.0]
	VBF	0.3-0.8 [0.1], 0.8, 1.0, 1.2, 1.5, 1.8, 2.0, 2.4, 2.6, 3.0, 3.5, 4.0
G_{KK}	ggF	0.6-2.0 [0.2]
	VBF	x

Table 4.2: Signals, production modes, and pole masses that MC samples were generated for.

PDF set for the hard scatter matrix element.

The benchmark for the bulk RS graviton samples are generated also with MadGraph5_$aMC@NLO$ 2.2.2 interfaced to Pythia 8.186 with the NNPDF23LO PDF set. The Kaluza-Klein excitations in this model give rise to excitations of the gravitational field that manifest as spin-2 gravitons (G_{KK}). By allowing the Standard Model field to propagate into the bulk (extra dimension), the couplings of G_{KK} to leptons and photons is significantly reduced, allowing the production to be dominated by gluon-gluon fusion. The G_{KK}gluon coupling is suppressed by a factor of $k/\bar{M}_{\text{Planck}}$ and $\bar{M}_{\text{Planck}}$ where is the reduced Planck mass, and is assumed to be 1.

SM Background Samples

The main sources of the SM background includes events from the production of top-quarks, dibosons, Z+jets, W+jets, and $V+\gamma$, where V stands for both vector bosons, W and Z, and Standard Model Higgs boson production.

Production of SM Higgs bosons via gluon fusion is simulated at next-to-next-to-leading-order (NNLO) accuracy in QCD using the Powheg NNLOPS program [109, 111, 26, 126, 97]. The simulation achieves NNLO accuracy for arbitrary inclusive $gg \to H$ observables by reweighting the Higgs boson rapidity spectrum in Hj-MiNLO [110, 59, 108] to that of HNNLO [63]. The PDF4LHC15 NLO PDF set [56] and the AZNLO tune [15] of PYTHIA 8 [138] is used. The gluon fusion prediction from the Monte Carlo samples is normalised to the next-to-next-to-next-to-leading order (N^{3}LO) cross section in QCD plus electroweak corrections at next-to-leading order (NLO) [83, 29, 30, 113, 114, 112, 131, 19, 20, 50]. Standard Model Higgs boson production via vector-boson fusion is generated with POWHEG-BOX [129, 26, 126, 97] and interfaced with PYTHIA 8 [138] for parton shower and non-perturbative effects. The POWHEG-BOX prediction is accurate to next-to-leading order (NLO) and tuned to match calculations with effects due to finite heavy-quark masses and soft-gluon resummations up to NNLL. The PDF4LHC15 PDF set [56] and the AZNLO tune [15] of PYTHIA 8 [138] are used. The Monte Carlo prediction is normalised to an approximate-NNLO QCD cross section with NLO electroweak corrections [68, 69, 49]. The normalisation of all SM Higgs boson samples accounts for the decay branching ratio calculated with HDECAY [88, 141, 89] and PROPHECY4F [54, 52, 53].

Samples of diboson final states ($VV = WW, WZ, ZZ$) are simulated with the SHERPA v2.2.1 or v2.2.2 [51] generator depending on the process, including off-shell effects and Higgs-boson contributions, where appropriate. Fully leptonic final states and semileptonic final states, where one boson decays leptonically and the other hadronically, are generated using matrix elements at NLO accuracy in QCD for up to one additional parton and at LO accuracy for up to three additional parton emissions. Samples for the loop-induced processes $gg \to VV$ are generated using LO-accurate matrix elements for up to one additional parton emission for both cases of fully leptonic and semileptonic final states. The matrix element calculations are matched and merged with the SHERPA parton shower based on Catani-Seymour dipole factorisation [102, 137] using the MEPS@NLO prescription [120, 118, 64, 119]. The virtual QCD correction are provided by the OPENLOOPS library [62, 86]. The NNPDF3.0NNLO set of PDFs is used [46], along with the dedicated set of tuned parton-shower parameters developed by the SHERPA authors. $V+\gamma$ events are generated using SHERPA 2.2.8 with NLO accuracy at 0- and 1-jet and LO accuracy at 2- and 3-jet matrix elements.

The production of $t\bar{t}$ events is modelled using the POWHEG-BOX [98, 126, 97, 26] v2 generator at NLO with the NNPDF3.0NLO [46] PDF set and the h_{damp} parameter[3] set to 1.5 m_{top} [36]. The events are interfaced to PYTHIA 8 (v8.230) [138] to model the parton shower, hadronisation, and underlying event, with parameters set according to the A14 tune [35] and using the NNPDF2.3LO set of PDFs [45]. The decays of bottom and charm hadrons are performed by EVTGEN v1.6.0 [125].

The associated production of top quarks with W bosons (tW) and the single-top s-channel production are modelled using the POWHEG-BOX v2 [135, 126, 97, 26] generator at NLO in QCD using the five-flavour scheme and the NNPDF3.0NLO set of PDFs [46]. For the single-top t-channel production [94, 126, 97, 26] the four-flavour scheme is used. The diagram removal scheme [95] is used to remove interference and overlap of tW with $t\bar{t}$ production. The related uncertainty is estimated by comparing with an alternative sample generated using the diagram subtraction scheme [95, 36] The events are interfaced to PYTHIA 8 (v8.230) [138] using the A14 tune [35] and the NNPDF2.3LO set of PDFs [45]. The decays of bottom and charm hadrons are again performed by EVTGEN v1.6.0 [125].

An additional NNLO reweighting is applied to $t\bar{t}$ to correct for mismodeling, and is discussed more in Section 7.2.2.

The production of Z+jets is simulated with the SHERPA v2.2.1 [51] generator using next-to-leading order (NLO) matrix elements (ME) for up to two jets, and leading order (LO) matrix elements for up to four jets calculated with the COMIX [102] and OPENLOOPS [62, 86] libraries. They are matched with the SHERPA parton shower [137] using the MEPS@NLO prescription [120, 118, 64, 119] using the set of tuned parameters developed by the SHERPA authors. The NNPDF3.0NNLO set of PDFs [46] is used and the samples are normalised to a next-to-next-to-leading order (NNLO) prediction [28].

To correctly model the effect of multiple pp interactions in the same and neighbouring

[3]The h_{damp} parameter is a resummation damping factor and one of the parameters that controls the matching of Powheg matrix elements to the parton shower and thus effectively regulates the high-p_T radiation against which the $t\bar{t}$ system recoils.

bunch crossings (pile-up), corrections need to be applied. The rate of these pile-up collisions are dependent on the luminosity and $\sqrt{s}$ energy of the collision, and takes two types: in-time (same bunch crossing) and out-of-time (neighbouring bunch crossing). The two types can be investigated using two observables: numbers of primary vertics N_{Vtx} which reflects the amount of in-time pile-up, and the average number of interactions per bunch crossing, μ. For the full run 2 sample, a rescaling of 1.03μ is made to correctly model the pile-up conditions. A comparison of the data to MC simulation of the two pile-up types are shown in Figure 4.2.

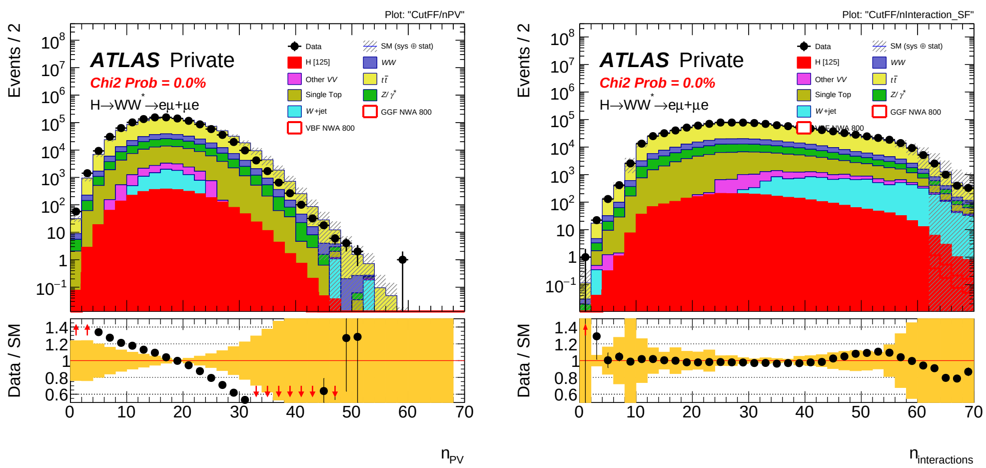

Figure 4.2: Data to MC comparison of N_{Vtx} (left) and Number of Interactions per Crossing (nIPC, right). For the nIPC plot, the average nIPC is used for mc16a, and for mc16d,e actual nIPC is used. The data rescaling factor of 1.03μ has also been applied.

Chapter 5

Physics Objects Reconstruction and Selection

Numerous physics objects are used in the analysis in both the reconstructed (reco) and object (truth) level definitions. Each of the sections in this chapter will briefly describe the different objects and how they are reconstructed with the available information obtained from the ATLAS detector. Section 5.1 will describe the minimum requirements for an event to be included in the reconstruction process. Section 5.2 will describe the reconstruction of the electrons from hits in the ID and energy deposits in the Ecal, and the analysis level criteria to define the electrons to be used in the event selection. Section 5.3 will describe the reconstruction of the electrons from hits in the ID and MS, and the analysis level criteria to define the muons to be used in the event selection. Section 5.4 will describe the reconstruction of the jet collections from hits in the ID and energy deposits in the Hcal, and the analysis level criteria to define the jets to be used in the event selection. Section 5.5 will describe the reconstruction of the missing transverse momentum (E_T^{miss}), and the analysis level criteria to define the E_T^{miss} to be used in the event selection. Section 5.6 describes the overlap removal (OR) process when multiple objects are spatially close to one another. Section 5.7 describes the kinematic variables constructed from intrinsic physics quantities of the different objects already described that will be used in the event selection. For overview, the object selection at a glance is highlighted in Table 5.1.

Electrons	Jets
Medium LH, $\|\eta\| < 2.5$, exclude crack region FixedCutTight Isolation: ptvarcone20_TightTTVA_pt1000/pT < 0.06	AntiKt4EMPFlow Jets, $p_T > 30$ GeV, JVT Tight WP BTagging: DL1r, 85% WP
Muons	Overlap Removal
Tight Quality, $\|\eta\| < 2.4$ FixedCutTight Isolation: ptvarcone30_TightTTVA_pt1000/pT < 0.04	b-tag aware OR: Prioritize keeping b-jets. e - ΔR 0.2 jet rejection, μ - ΔR 0.2 jet rejection + p_T dependence rejection

Table 5.1: Overview of the object selection criteria for the analysis.

5.1 Event Minimum Criteria

Events are required to have at least one primary vertex that has no less than two associated tracks[1], each with transverse momentum $p_T > 400$ MeV, where p_T is defined as the magnitude of the component of the momentum orthogonal to the beam axis. If there is more than one primary vertex reconstructed in the event, the one with the largest track Σp_T^2 is chosen as the hard-scatter primary vertex and is subsequently used for calculation of the main physics objects in this analysis: electrons, muons, jets, and E_T^{miss} .

5.2 Electrons

Electrons in the ATLAS detector [7] are reconstructed in four stages: seed-cluster reconstruction, track reconstruction, electron specific track fit, and electron candidate reconstruction. The seed-cluster reconstruction uses a sliding window with equivalent size of the granularity of the Ecal to search for cluster seeds with a transverse energy (E_T) greater than 2.5 GeV. Then a clustering algorithm [124] is used to remove duplicate energy deposits and to reconstruct cluster kinematics. Tracks are then reconstructed within the ID taking into account the energy loss due to the interactions with the material in the detector [8]. This allows for a possible 30% of energy to be lost at each transversal of the track with detector material due to possible bremsstrahlung radiation. A track seed, which consists of three hits in different layers of the silicon detectors, is then attempted to be reconstructed, requiring a

[1]The requirement of one primary vertex is needed to select a collision, while the track requirements are needed to ensure an accurate calculation of subsequently produced leptons.

p_T of more than 1 GeV. Then the track seed is extended to a full track which is required to have seven hits in the ID. A full track is then required to be matched to the cluster region of interest using a track fit which accounts for energy loss due to bremsstrahlung. Finally, an additional, stricter matching criteria is performed prior to the full electron reconstruction to remove any contribution from additional tracks.

All of this information, except for that related to track hits, is combined into a likelihood discriminant. The selection used combines the likelihood with the number of track hits and defines several working points (WP). This analysis uses the medium electron likelihood WP. Additionally, an isolation WP is also used to correctly select true electrons. This analysis uses the fixed cut tight (FCTight) WP, which corresponds to an Ecal isolation of topoetcone20/pT < 0.06 and a track isolation of ptvarcone20_TightTTVA_pt1000/pT < 0.06 [90].

5.3 Muons

Muons in the ATLAS detector [6] can be reconstructed in four different ways: combination of MS track with ID track, combination of tracks in the ID with a track segment in the MDT or CSC chambers, only a track in the MS, and the combination of tracks in the ID with energy deposits in the Ecal. The muons which are reconstructed using tracks in the MS, which make up the large majority of muons used in the analysis, use an algorithm called Chain 3 [73] to perform the reconstruction.

If a complete track is present in both the ID and the MS, a combined muon track is formed by a global fit using the hit information from both the ID and MS detectors (combined muon), otherwise the momentum is measured using the ID, and the MS track segment serves as identification (segment-tagged muon). The segment-tagged muon is limited to the center of the barrel region ($|\eta| < 0.1$) which has reduced MS geometrical coverage. Furthermore, in this central region an ID track with $p_T > 15$ GeV is identified as a muon if its calorimetric energy deposition is consistent with a minimum-ionising particle (calorimeter-tagged muon). In the forward region ($2.5 < |\eta| < 2.7$) with limited or no ID coverage, the MS track is either used alone (stand-alone muon) or combined with silicon hits, if found in the forward ID (combined muon). In software release 21, a set of changes were implemented in muon reconstruction aimed at reducing the fake tracks when extrapolating the tracks from the ID to MS; an example of this is presented in Ref. [17]. The ID tracks associated with the muons are required to have a minimum number of associated hits in each of the ID subdetectors to ensure good track reconstruction. The stand-alone muon candidates are required to have hits in each of the three MS stations they traverse. This analysis uses the tight muon quality WP. Similar to electrons, an additional isolation requirement is also used to help identify true muons. This analysis uses the FCTight WP, which corresponds to an Ecal isolation requirement of topoetcone20/pT < 0.15 and a track isolation of ptvarcone30_TightTTVA_pt1000/pT < 0.04 [90].

5.4 Jet Clusters and Identification

A jet is the manifestation of QCD objects in the detector in the form of energy deposits in the calorimeter. Progress has been made to include track information matched to calorimeter energy deposits to perform the jet reconstruction process. Jets are reconstructed using the anti-k_t algorithm [57] with a radius parameter $R = 0.4$ implemented in the FastJet package [58] Jets are required to pass basic requirements with $p_T > 30$ GeV and $|\eta|$ <4.5 and satisfying Jet Vertex Tagger (JVT) [4] requirements where applicable. For this analysis, JVT tight working point corresponding to JVT > 0.5 is used for EMPFlow jets between 20 <$p_T < 60$ GeV, and no forward-JVT (fJVT) requirements are yet used. The inputs to FastJet are the Particle Flow (PFlow) objects, which are the ensemble of positive energy topo-clusters surviving the energy subtraction step of the PFlow algorithm, within $|\eta| < 2.5$, and the selected tracks that are matched to a primary hard-scatter or pile-up vertex. Prior to jet-finding, the topo-cluster η and ϕ are recomputed with respect to the primary vertex (PV) position, rather than the detector origin. Outside the geometrical acceptance of the tracker, $|\eta| > 2.5$, only the calorimeter information is available. Hence, in the forward region, the topological clusters, formed from calorimeter cells with significant energy depositions, are used as inputs to jet reconstruction. More details on the particle flow algorithm in ATLAS can be found in Ref. [38]. After jets are built, a sequence of corrections are applied to calibrate the jets to the particle-level energy scale, as described in Ref. [37]. Due to the many interactions per crossing of proton bunch collisions, jets can be associated to an event which they did not originate from, which is called pile-up (PU). An in depth study of the validity of the $p_T > 30$ GeV requirement is carried out in the high statistics same-flavor (SF) VBF phase-space and documented in Ref. [93]. Kinematic studies of jets with $p_T > 30$ GeV along with PU dependencies is shown to have good agreement, validating the use of this lower p_T cut [93].

5.4.1 Tagging of Jets

Jets can originate from any QCD object. There is significant discriminatory power between different physics processes when one can identify which QCD objects a reconstructed jet originates from. The b-quark has longer lifetime than other SM quarks, making it able to be identified by looking for a displaced vertex in the ID. Numerous algorithms are available to take many of the different track kinematics to identify (tag) b-jets specifically. Jets containing b-hadrons in this analysis are identified using the DL1r b-tagging algorithm [9]. The b-jets are required to satisfy the requirements of the 85% efficiency determined by $t\bar{t}$ simulated events. The jets originating from b-hadron decays with $p_T \geq 20$ GeV and $|\eta| < 2.5$ are referred to as b-jets in this analysis. The March 11, 2020 calibration data interface (CDI) file produced by the ATLAS Flavor-tagging group is used as the baseline for jet identification criteria and scale factors.

5.5 Missing Transverse Momentum

The missing transverse momentum (E_T^{miss} is calculated as the negative of the vectorial sum of all the reconstructed objects (electrons, muons, and jets). Other tracks originating from the primary vertex, but not included in the other reconstructed objects, are also included. The track-based soft term E_T^{miss} , described in detail in Ref. [39], is used for all observable reconstruction and cuts in the analysis. An additional observable of the object-based E_T^{miss} Significance is used within the analysis based on it's ability to separate events where the E_T^{miss} is reconstructed from weakly interacting particles from events where the E_T^{miss} is reconstructed with large contributions coming from particle measurements, resolutions, and inefficiencies, with full details given in Ref. [11].

5.6 Overlap Removal

Overlap removal is used in the object selection of the analysis to remove the duplicate use of stimulations in the detector to reconstruct multiple objects and also as an additional isolation layer on close-by physics objects. The OR proceeds in three steps:

1. Electron – Muon : If a muon reconstructed by the ID and MS shares a track with an electron, the electron is removed. If a muon reconstructed by only the calorimeter deposits shares an ID track with an electron, the muon is removed.

2. Electron – Jet : A jet is removed if it is within a ΔR of 0.2 of an electron. For any jets outside this spatial selection, an additional p_T based criteria is used to remove an electron if the ΔR of the jet and electron is smaller than $\min(0.4, 0.04 + 10\text{GeV}/p_T^e)$.

3. Muon – Jet : A jet is removed if the jet is within ΔR of 0.2 of a muon AND the jet has less than three associated tracks with $p_T > 500$ MeV. Additionally a jet is removed if the p_T ratio of the muon and jet is larger than 0.5 (p_T^μ / $p_T^{jet} > 0.5$) and the ratio of the muon p_T to the sum of the p_T of tracks with $p_T > 500$ MeV associated to the

jet is greater than 0.7. For any jets outside this spatial selection, an additional p_T based criteria is used to remove a muon if the ΔR of the jet and muon is smaller than $\min(0.4, 0.04 + 10\text{GeV}/p_T^{\mu})$.

The OR requirements are chosen to allow for good spatial distance separation with respect to the resolution of the detector. This analysis makes use of an additional unofficial WP from the ATLAS Isolation and Fake Forum called "b-tag aware" OR. With this WP, the b-tagging DL1r algorithm is used on any jet in the event to give priority to jets which are b-tagged, removing any other physics object within a $\Delta R = 0.2$.

5.7 Composite Kinematic Observables

From the different truth and reconstructed objects composite kinematic observables can be created from the intrinsic quantities of the physics objects. These quantities are to be used in the event selection of the analysis. Within this section, j will be used to identify jet kinematics and ℓ will be used to identify one of the lepton (here only electrons and muons) kinematics.

- $m_{\ell\ell}$ – Invariant mass of the leading and subleading leptons in the event.
- $|\Delta\eta_{\ell\ell}|$ – Pseudorapidity separation of the leading and subleading leptons in the event.
- $\max(m_T^W)$ – The maximum value of the transverse mass of one of the two leptons, defined as:

$$m_T^W = \sqrt{2p_T^{\ell} E_T^{\text{miss}}(1 - \cos(\phi^{\ell} - \phi^{E_T^{\text{miss}}})} \tag{5.1}$$

- m_T – Transverse mass, defined as:

$$m_T = \sqrt{(E_T^{\ell\ell} + E_T^{\text{miss}})^2 - |p_T^{\ell\ell} + E_T^{\text{miss}}|^2} \tag{5.2}$$

- m_{jj} – Invariant mass of the leading and subleading jets in the event.

- $|\Delta\eta_{j\ell}|$ – Pseudorapidity separation of a jet and a lepton.

- $|\Delta y_{jj}|$ – Pseudorapidity separation of the leading and subleading jet in the event

Chapter 6

Optimization Studies

The signal region selections to be discussed in Section 7.1 and the control region selections to be discussed in Section 7.2 were carefully derived using multiple optimization techniques. This chapter describes the different studies performed, highlighting the intent of the optimization and also the impact on the final statistical analysis. The studies described in this chapter were all performed using the V19 PxAOD production (ATLAS Base Release 21.2.56) with EMTopo jet collection unless otherwise specifically stated. As a baseline selection, the analysis begins with a region selection identical to the previous 36 fb^{-1} analysis [14], and is shown for the control regions (CR) in Table 6.1 and for the signal regions (SR) in Table 6.2. Three main optimization methods were used: tighter selection cuts in SR and CR to eliminate SM background, using E_T^{miss} Significance cuts to purify the CR and increase signal significance in SR, and applying the common SR selection to the VBF CR to reduce extrapolation uncertainties. Additionally, cuts with ratios of mass-based kinematics were used to explore the possibility of further improving the sensitivity of the signal regions. And finally, a brief study on an alternative figure of merit for the signal regions was carried out.

6.1 Tighter Selection

The previous 36 fb^{-1} analysis [14] explored the possibility of using an optimized region selection using tighter cut selections. However, the limited statistics were insignificant to

<table>
<tr><td colspan="4">Pre-Selection</td></tr>
<tr><td colspan="4">Two Different Flavour, Opposite Sign Leptons, $p_T^\ell > 25$ GeV
Third lepton veto, $p_T^\ell > 15$ GeV</td></tr>
<tr><td>WW $\mathrm{CR}_{\mathrm{ggF}}$</td><td>Top $\mathrm{CR}_{\mathrm{ggF}}$</td><td>WW $\mathrm{CR}_{\mathrm{VBF1J}}$</td><td>Top $\mathrm{CR}_{\mathrm{VBF}}$</td></tr>
<tr><td>$N_{b-tag} = 0$
$|\Delta\eta_{\ell\ell}| > 1.8$</td><td>$N_{b-tag} = 1$
$|\Delta\eta_{\ell\ell}| < 1.8$</td><td rowspan="2">$N_{b-tag} = 0$
$(|\Delta\eta_{\ell\ell} > 1.8$ or
10 GeV $< m_{\ell\ell} <$ 55 GeV)</td><td rowspan="2">$N_{b-tag} \geq 1$
–
$m_{\ell\ell} > 10$ GeV</td></tr>
<tr><td colspan="2" rowspan="2">$m_{\ell\ell} > 55$ GeV
$p_T^{\ell,\mathrm{lead}} > 45$ GeV
$p_T^{\ell,\mathrm{sublead}} > 30$ GeV
$\max(m_T^W) > 50$ GeV</td></tr>
<tr><td colspan="2">$p_T^{\ell,\mathrm{lead}} > 25$ GeV
$p_T^{\ell,\mathrm{sublead}} > 25$ GeV
–</td></tr>
<tr><td colspan="2">Excluding VBF1/2J phase space</td><td>VBF1J phase space</td><td>VBF1/2J phase space</td></tr>
</table>

Table 6.1: Summary of all the selections used in the ggF and VBF WW and top-quark control regions in the $H \to WW$ resonance search made on 36 fb^{-1} in 2017.

<table>
<tr><td colspan="3">Pre-Selection</td></tr>
<tr><td colspan="3">Two Different Flavour, Opposite Sign Leptons, $p_T^\ell > 25$ GeV
Third lepton veto, $p_T^\ell > 15$ GeV</td></tr>
<tr><td>$\mathrm{SR}_{\mathrm{ggF}}$</td><td>$\mathrm{SR}_{\mathrm{VBF1J}}$</td><td>$\mathrm{SR}_{\mathrm{VBF2J}}$</td></tr>
<tr><td colspan="3">Common Selection</td></tr>
<tr><td colspan="3">$N_{b-tag} = 0$
$|\Delta\eta_{\ell\ell}| < 1.8$
$m_{\ell\ell} > 55$ GeV
$p_T^{\ell,\mathrm{lead}} > 45$ GeV
$p_T^{\ell,\mathrm{sublead}} > 30$ GeV
veto if $p_T^{\ell,\mathrm{other}} > 15$ GeV
$\max(m_T^W) > 50$ GeV</td></tr>
<tr><td>ggF phase space</td><td>VBF1J phase space</td><td>VBF1J phase space</td></tr>
<tr><td>Inclusive in N_{jet} but excluding VBF1J and VBF2J phase space</td><td>$N_{jet} = 1$ and $|\eta_j| > 2.4$,
$\min(|\Delta\eta_{j\ell}|) > 1.75$</td><td>$N_{jet} = 2$ and $m_{jj} > 500$ GeV, $|\Delta y_{jj}| > 4$</td></tr>
</table>

Table 6.2: Event selection for the three signal regions in the $H \to WW$ resonance search made on 36 fb^{-1} in 2017.

Kinematic	Cut Value
$m_{\ell\ell}$	$\geq$ 110 GeV
$\max(m_T^W)$	$\geq$ 100 GeV
$p_T^{\ell,\text{lead}}$	$\geq$ 70 GeV
$p_T^{\ell,\text{sublead}}$	$\geq$ 45 GeV
$\lvert\Delta\eta_{\ell\ell}\rvert$	$\leq$ 1.8

Table 6.3: Optimized cut values for "common" tighter selections from the Poisson significance gridscans. These cuts are applied on top of the baseline cuts already used for each CR and SR, with the exclusion of the VBF CR.

show any gain by going to a tighter cut selection. With the increase to the 139 fb^{-1} in the full Run-II dataset, a tighter selection cut optimization is explored. A gridscanning method is used to scan multiple cut values and search for an optimized selection in the signal regions.

Gridscanning processes were carried out for both ggF and VBF SR, scanning a combination of selection cuts of all the kinematic variables which are used to defined the "common" selection which is used for the quasi-inclusive CR and both ggF and VBF SR. The values obtained by optimizing multiple mass points to a maximimum value of Poisson significance are given in Table 6.3. The data vs. MC modeling of the CR regions (quasi-inclusive ggF) affected by this optimization are show in Figure 6.1. The modeling of NWA signal samples in the SR after applying the tighter cut selections are shown in Figure 6.2.

To fully understand the impact of the selection, the comparison of the 95% CLs limits produced by the full statistical analysis using only the statistical and detector uncertainties is used. A comparison of the limits produced for the tighter region selections vs. the baseline analysis region selections is shown in Figure 6.3. No gain is shown for the majority of mass points, with only a slight gain shown at the highest mass points. These results can be expected due to the SM background primarily being reduced in the lower m_T regime, where the signal models generally do not populate. Therefore, the tighter region selections are not applied.

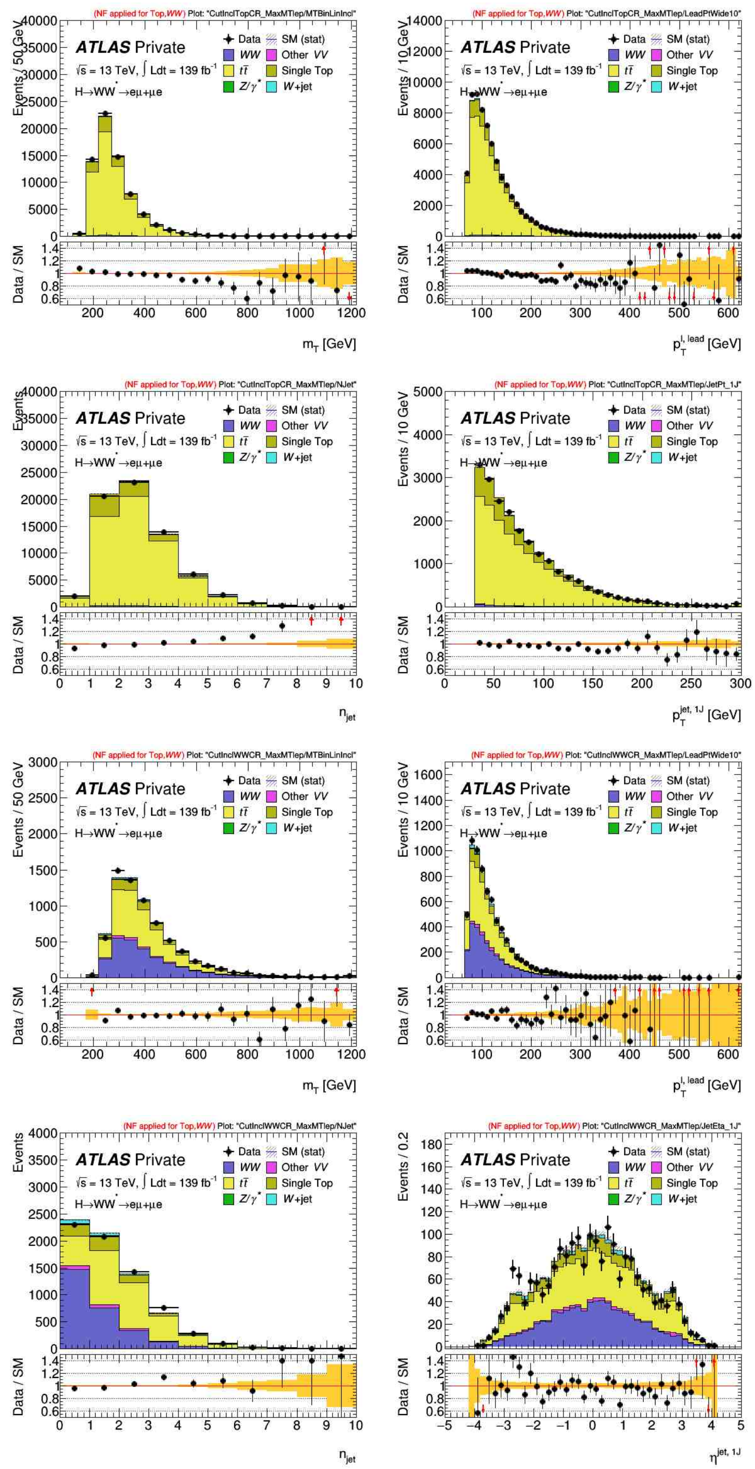

Figure 6.1: Modeling of significant kinematic variables in quasi-inclusive CR after applying a tighter cut selection: top CR (top two rows) and WW CR (bottom two rows). The yellow bands in the bottom pane correspond to the statistical uncertainties only. Top reweighting has not been applied. Normalization factors for WW and top have been applied for the tighter region selection.

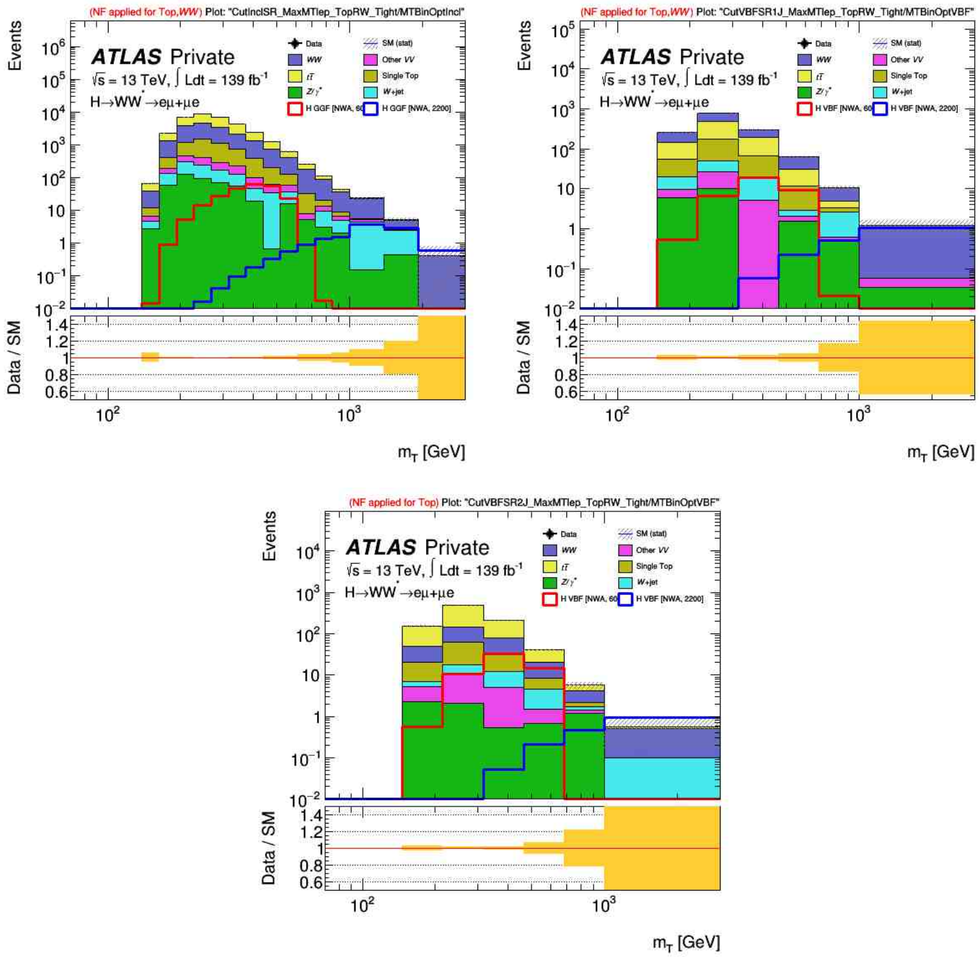

Figure 6.2: Modeling of the m_T variable in the individual SR: quasi-inclusive ggF (top left), VBF1J (top right), and VBF2J (bottom). The yellow bands in the bottom pane correspond to the statistical uncertainties only. Top reweighting has been applied. Normalization factors for WW and top have been applied for the tighter region selection.

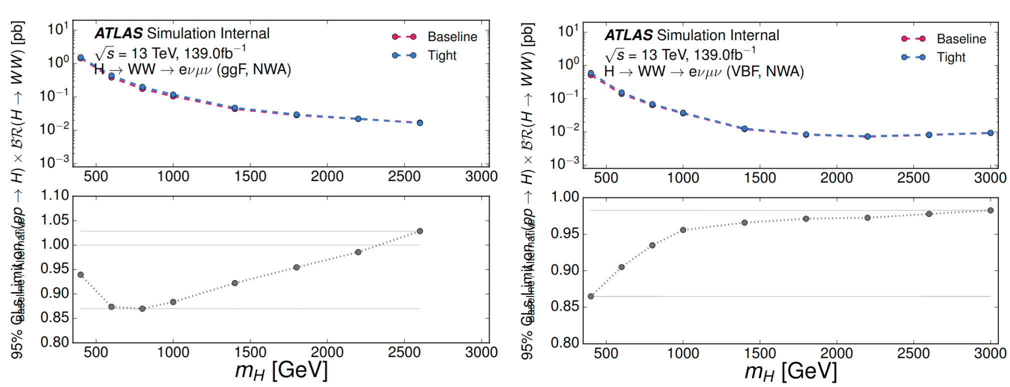

Figure 6.3: Comparison of expected limits between the baseline selection and the selection using tighter region selections for the NWA ggF (left) and VBF (right) samples. Missing mass points correspond to fit non-convergence.

6.2 Use E_T^{miss} Significance Cuts

With the move to Release 21, a new object-based E_T^{miss} Significance [11] became available. The variable nominally shows significant separating power of the major backgrounds that are present in this analysis. To begin an attempt to separate background channels that are not controlled with the CR in the analysis (Z+jets and non-prompt backgrounds, referred to as ddFakes) from the backgrounds that are controlled (top and WW). The modeling of the E_T^{miss} Significance can be seen in Figure 6.4 for each of the CR used. Because there is very little contamination of other backgrounds in the top CR, there seems to be no gain in applying a cut in this region. However, in the WW regions it can clearly be seen that the W+jets and Z/γ^* samples tend to lower values of E_T^{miss} Significance and could be exploited by a cut to try and increase the purity of WW in these CR.

Next the SR is examined to see if there is any separation of the NWA samples compared to SM background in the E_T^{miss} Significance distribution. The modeling of the E_T^{miss} Significance can be seen in Figure 6.5 for each of the SR used. It can be seen that the signal samples have a flatter slope in the distribution in comparison to the SM background spectrum. There seems to initially be the possibility to gain from a cut in the lower portion of the E_T^{miss} Significance distribution.

To select cuts to be used for the significance evaluation in the SR, Poisson significance [79] estimations are used to evaluate an optimized value of a cut. The E_T^{miss} Significance distribution is scanned, calculating a significance value using each integer value of E_T^{miss} Significance as a minimum. It is also important to consider the signal efficiency as well when applying this cut, so the efficiency of the cut is also compared in the same scanning fashion. The significance scans and the accompanying signal efficiency scans are shown for a low (m_H = 400 GeV), medium (m_H = 1000 GeV), and high (m_H = 2200 GeV) value of the searched resonance mass in Figures 6.6-6.8.

To select cuts to be used for the significance evaluation in the CR, a similar approach is used to scan over the E_T^{miss} Significance distribution. Because there is little gain using these

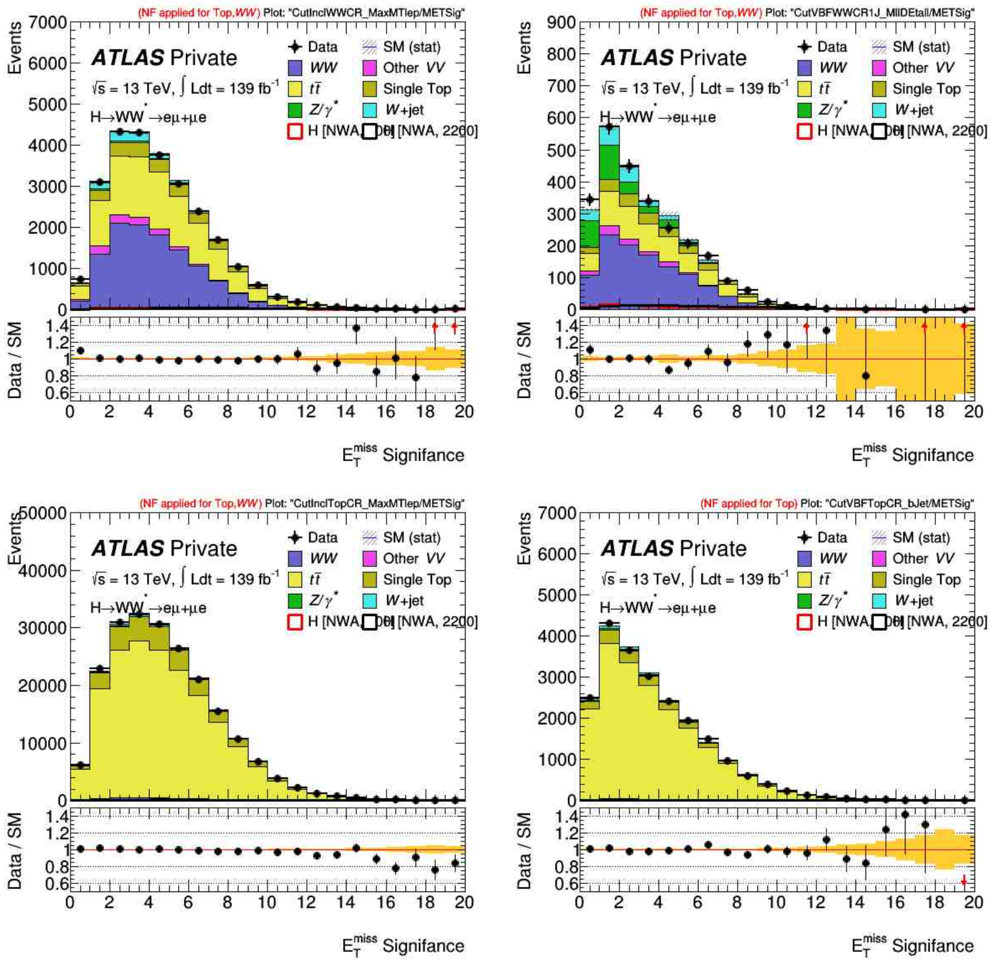

Figure 6.4: Modeling of the E_T^{miss} Significance variable in the individual CR: quasi-inclusive WW (top left), VBF1J WW (top right), quasi-inclusive top (bottom left), and VBF top (bottom right).

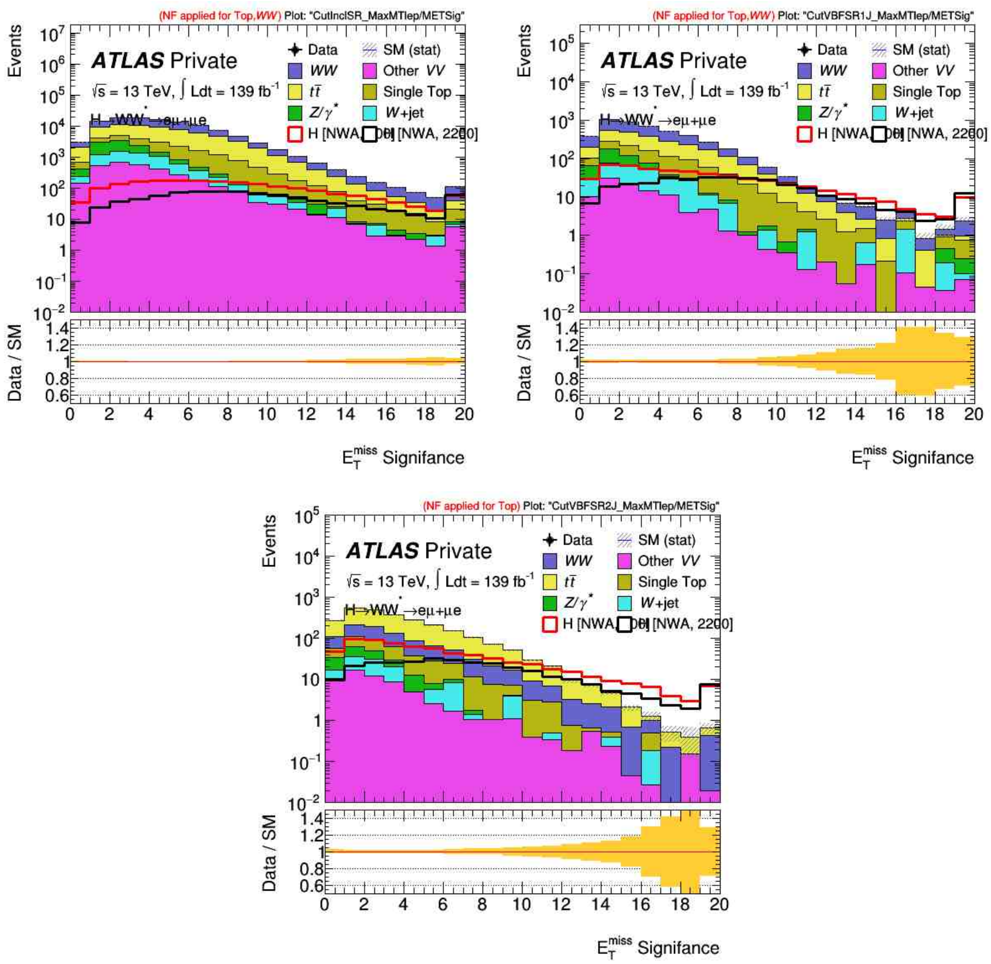

Figure 6.5: Modeling of the E_T^{miss} Significance variable in the individual SR: quasi-inclusive ggF (top left), VBF1J (top right), and VBF2J (bottom). Signal samples have been combined (VBF and ggF) to view the overall effect that would be had on the significance.

Region	E_T^{miss} Significance $\geq$
ggF SR	8
VBF1J SR	6
VBF2J SR	0
ggF WW CR	4
ggF Top CR	8
VBF WW CR	4
VBF Top CR	0

Table 6.4: Values of minimum E_T^{miss} Significance cuts used in each region to be used in the statistical analysis.

in the top CR, this is skipped to preserve the maximum statistics. For the VBF1J WW CR, the intended purpose is to try and maximize WW composition percentage while minimizing the composition percentage of the uncontrolled backgrounds (Z+jets and ddFakes). It is also important to consider the signal contamination percentage when looking for an optimal cut value. The compositional percentage scans are shown in Figure 6.9. From the significance scans shown in the VBF2J SR, it is seen that there is no gain when applying a cut in this region. In this sense, there is no need to explore a cut in the VBF top CR to maintain orthogonality between the regions. For the quasi-inclusive ggF CR, the WW region is scanned in a similar matter as the VBF1J CR. Also, because gain can be seen by applying a cut on the E_T^{miss} Significance in the quasi-inclusive SR, the signal contamination in the ggF top CR is also scanned to ensure this is not drastically changing when applying an orthogonal cut to the one to be used in the CR. These scans are shown in Figure 6.10.

Combining the results from the Poisson significance, efficiency, and composition scans, minimum value cuts are applied for five of the seven regions in the analysis as shown in Table 6.4 on top of the previous baseline cuts. Then the Asymptotic 95% CLs upper limits on the cross section times branching ratio are calculated for both the ggF and VBF NWA signal samples. A comparison of the results with respect to the same expected limits using the baseline cuts only are shown in Figure 6.11. It is clear that the addition of these cuts leads to worsened upper limits despite the gain shown in the Poisson estimate. Therefore, no minimum value cuts on E_T^{miss} Significance are applied in any region.

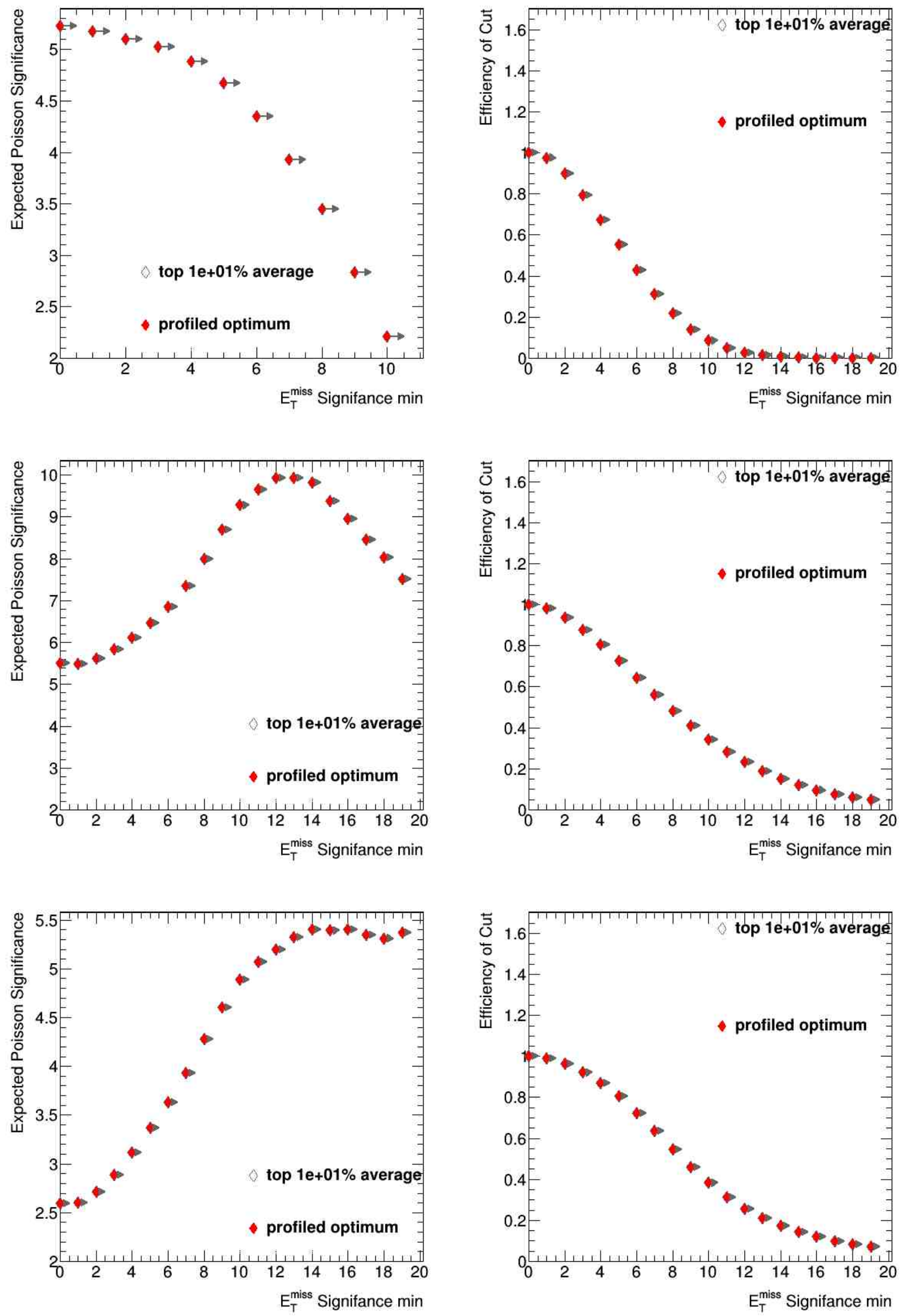

Figure 6.6: The expected Poisson Significance of the ggF produced NWA signals (left) compared to the signal efficiency of the cut (right) when making a minium cut on E_T^{miss} Significance in the ggF quasi-inclusive SR. Three mass points are shown: m_H = 400 GeV (Top), m_H = 1000 GeV (Middle), and m_H = 2200 GeV (Bottom).

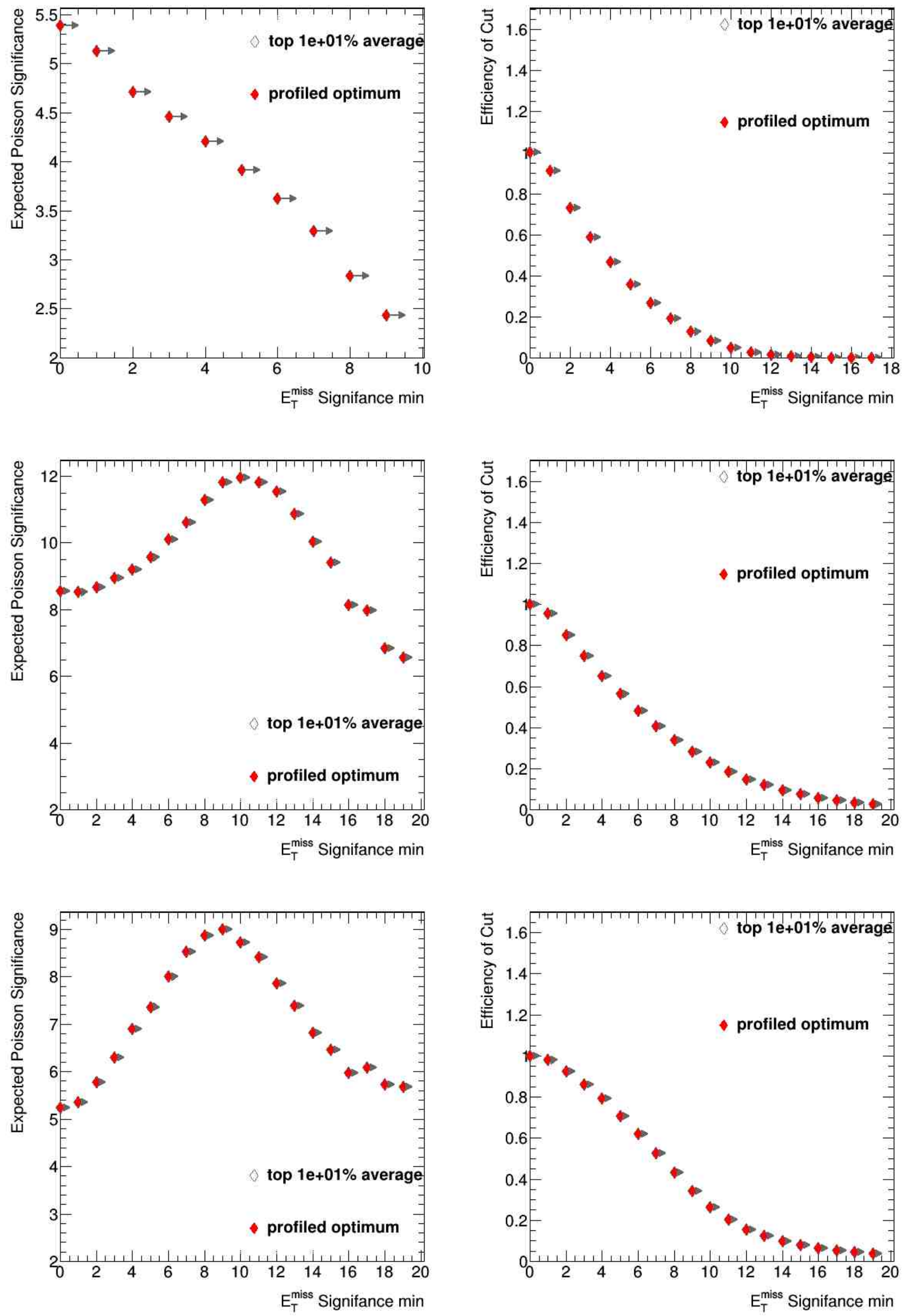

Figure 6.7: The expected Poisson Significance of the VBF produced NWA signals (left) compared to the signal efficiency of the cut (right) when making a minium cut on E_T^{miss} Significance in the VBF1J SR. Three mass points are shown: $m_H = 400$ GeV (Top), $m_H = 1000$ GeV (Middle), and $m_H = 2200$ GeV (Bottom).

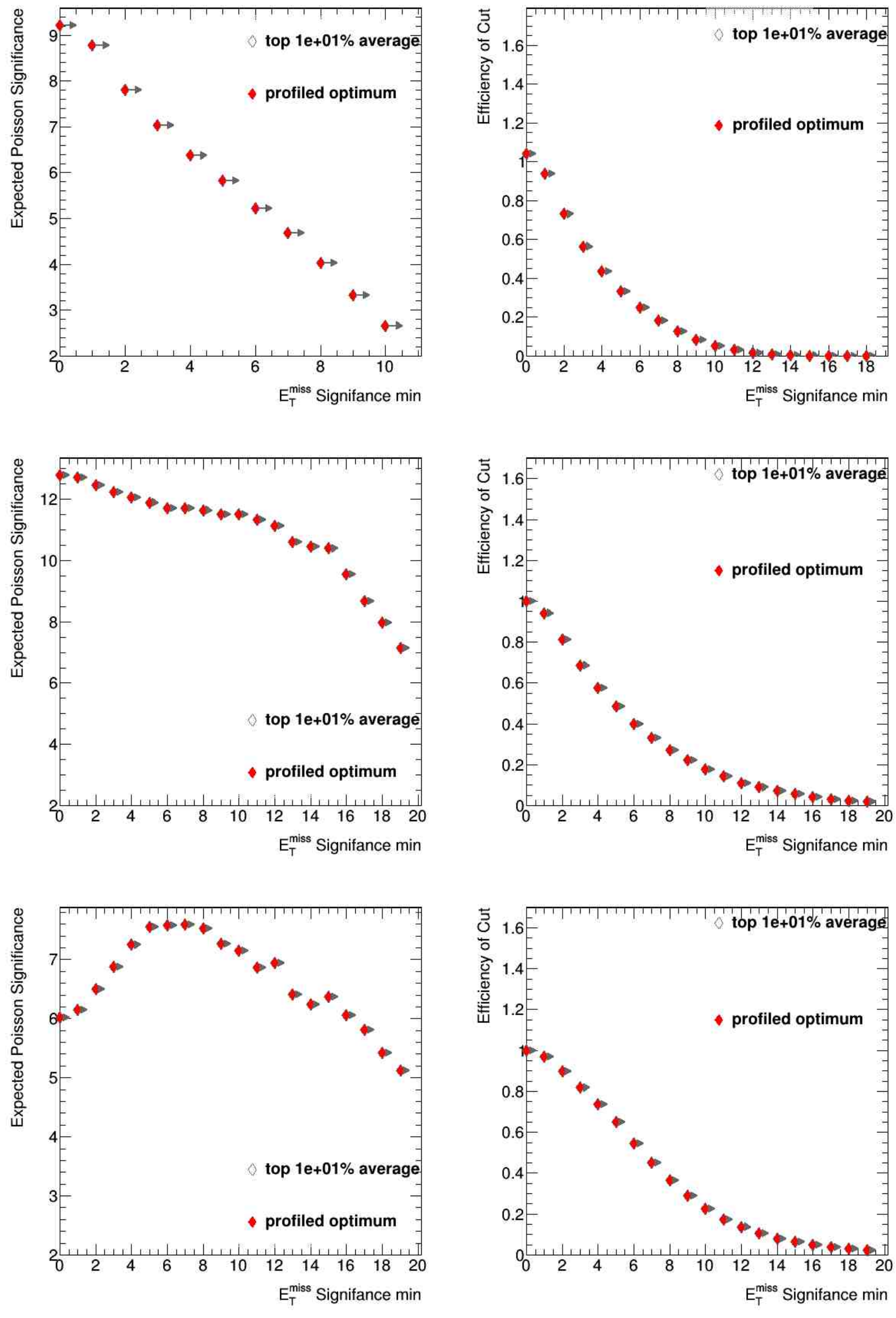

Figure 6.8: The expected Poisson Significance of the VBF produced NWA signals (left) compared to the signal efficiency of the cut (right) when making a minium cut on E_T^{miss} Significance in the VBF2J SR. Three mass points are shown: $m_H = 400$ GeV (Top), $m_H = 1000$ GeV (Middle), and $m_H = 2200$ GeV (Bottom).

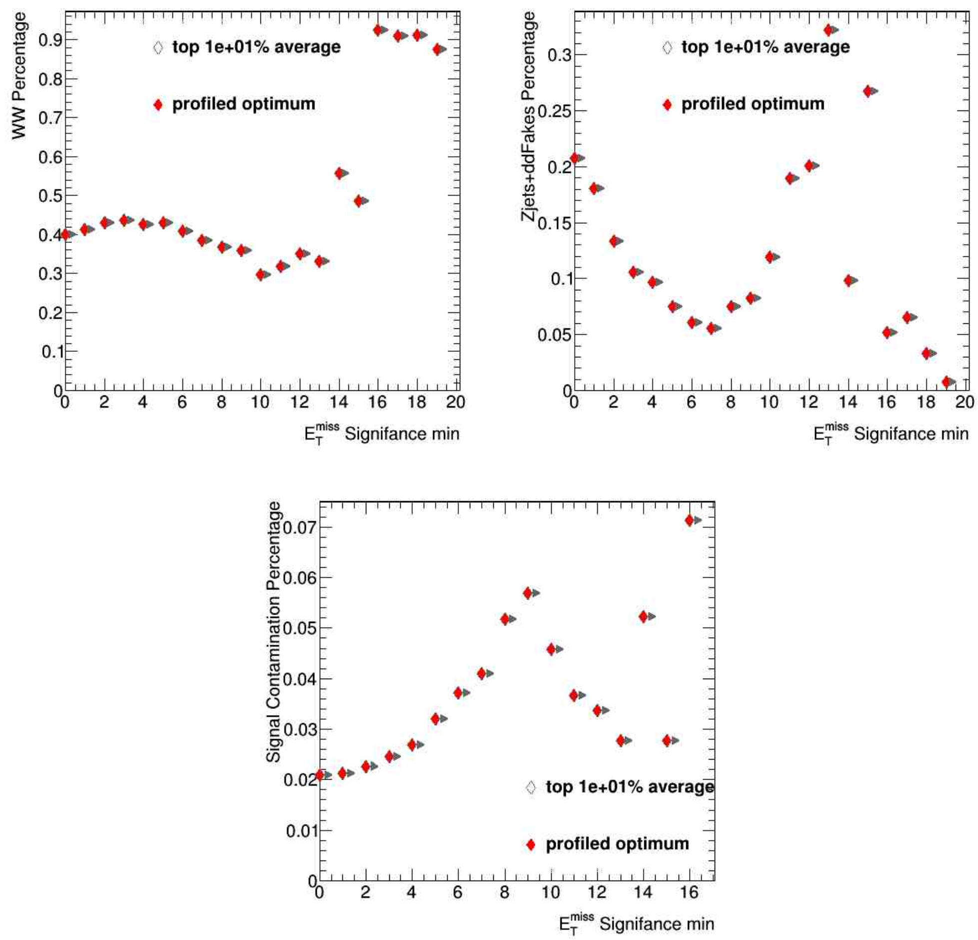

Figure 6.9: Sample composition of the VBF1J WW CR as a function of a minimum E_T^{miss} Significance cut: WW (top left), Z+Jets and ddFakes (top right), and $m_H = 400$ GeV VBF produced NWA signal (bottom).

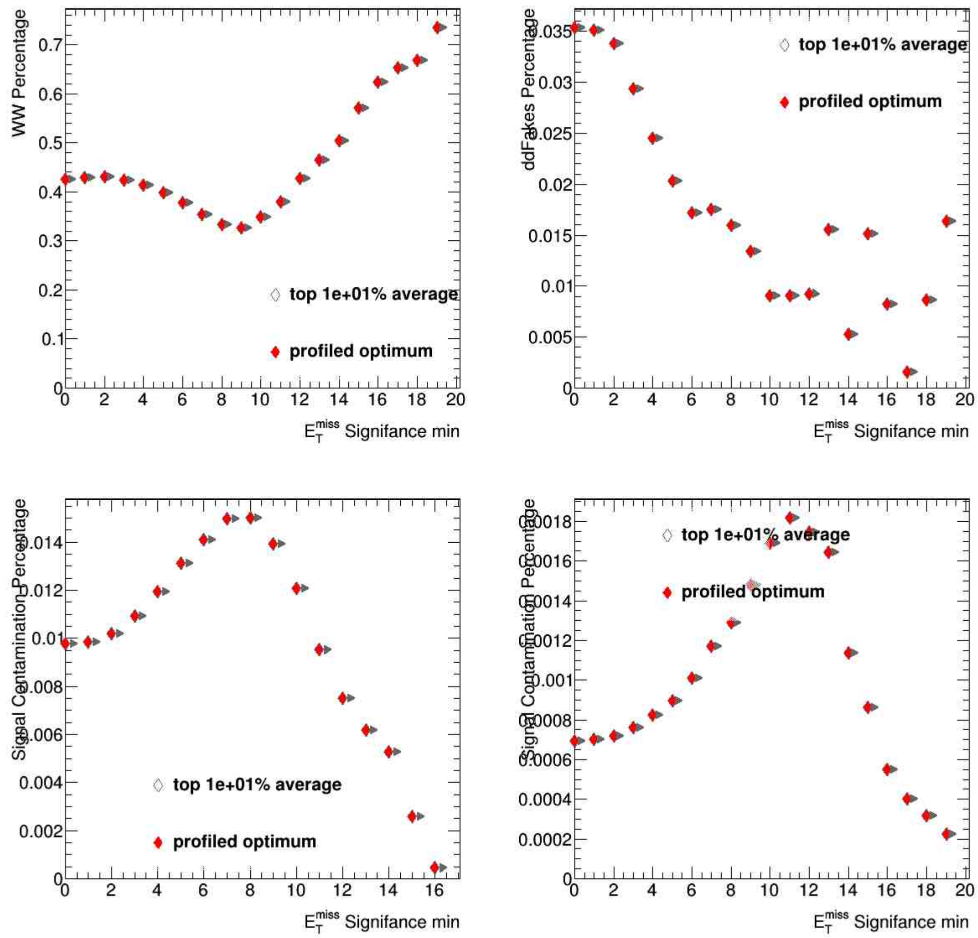

Figure 6.10: Sample composition of the quasi-inclusive ggF CR as a function of a minimum E_T^{miss} Significance cut: WW in WW CR (top left), Z+Jets and ddFakes in WW CR (top right), $m_H = 400$ GeV ggF produced NWA signal in WW CR (bottom left), and $m_H = 400$ GeV ggF produced NWA signal in Top CR (bottom right).

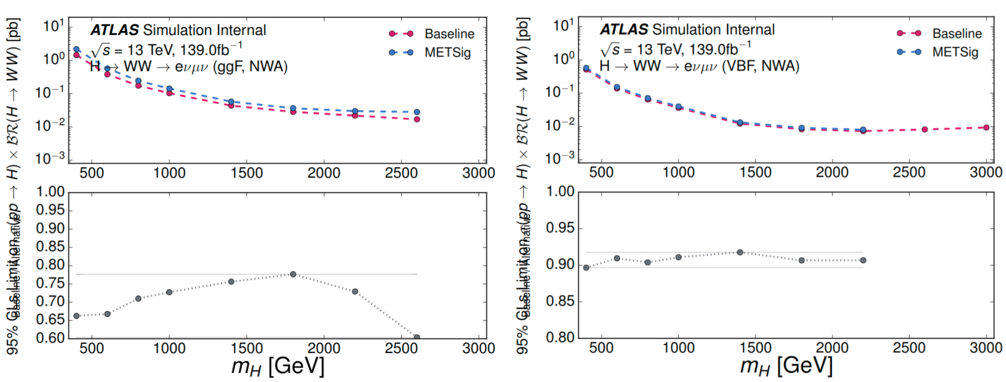

Figure 6.11: Comparison of expected limits between the baseline selection and the selection using cuts on E_T^{miss} Significance for the NWA ggF (left) and VBF (right) samples. Missing mass points correspond to fit non-convergence.

The application of the minimum value of the $E_T^{\rm miss}$ Significance cut applies a pseudo-cut on the $E_T^{\rm miss}$ itself. It is understood that this additional cut is why Poisson significance was improved, but when applied to the statistical analysis there was a worsened result. To try and counteract the $E_T^{\rm miss}$ pseudo-cut that is introduced when applying a minimum $E_T^{\rm miss}$ Significance, exploration of taking the ratio of the $E_T^{\rm miss}$ Significance and $E_T^{\rm miss}$ (METSigRatio) to remove the pseudo-cut is made. The modeling of such a composite variable can be seen in Figure 6.12. For simplicity, the VBF2J SR is not considered due to previously seeing little to no gain from using a cut on $E_T^{\rm miss}$ Significance.

In an attempt to increase WW purity in the quasi-inclusive ggF WW CR, a minimum cut value of the METSigRatio is taken to try and separate the WW events from top and Z+jets events while maintaining as much statistics as possible. For this, the minimum value of METSigRatio was taken as 0.8. For the VBF1J WW CR, no similar cut can be envisioned without significantly removing WW statistics from the region, which is already low in statistics.

After applying the METSigRatio cut in the quasi-inclusive ggF WW CR, the main background compositions are compared. Prior to the cut, the region contains 44.7% WW and 47.0% top. After the cut is applied, the region contains 59.0% WW and 32.0% top, showing a significant gain in purity. The modeling of major kinematic variables before and the METSigRatio cut is applied is shown in Figure 6.13. No significant change in the modeling of major kinematics is observed.

To measure the value of the increased purity in the quasi-inclusive ggF WW CR, Asymptotic 95% CLs upper limits on the cross section times branch ratio are once again calculated using the baseline and METSigRatio cut setups. Significant improvement was shown, and the METSigRatio cut is then applied to the quasi-inclusive ggF WW CR nominally.

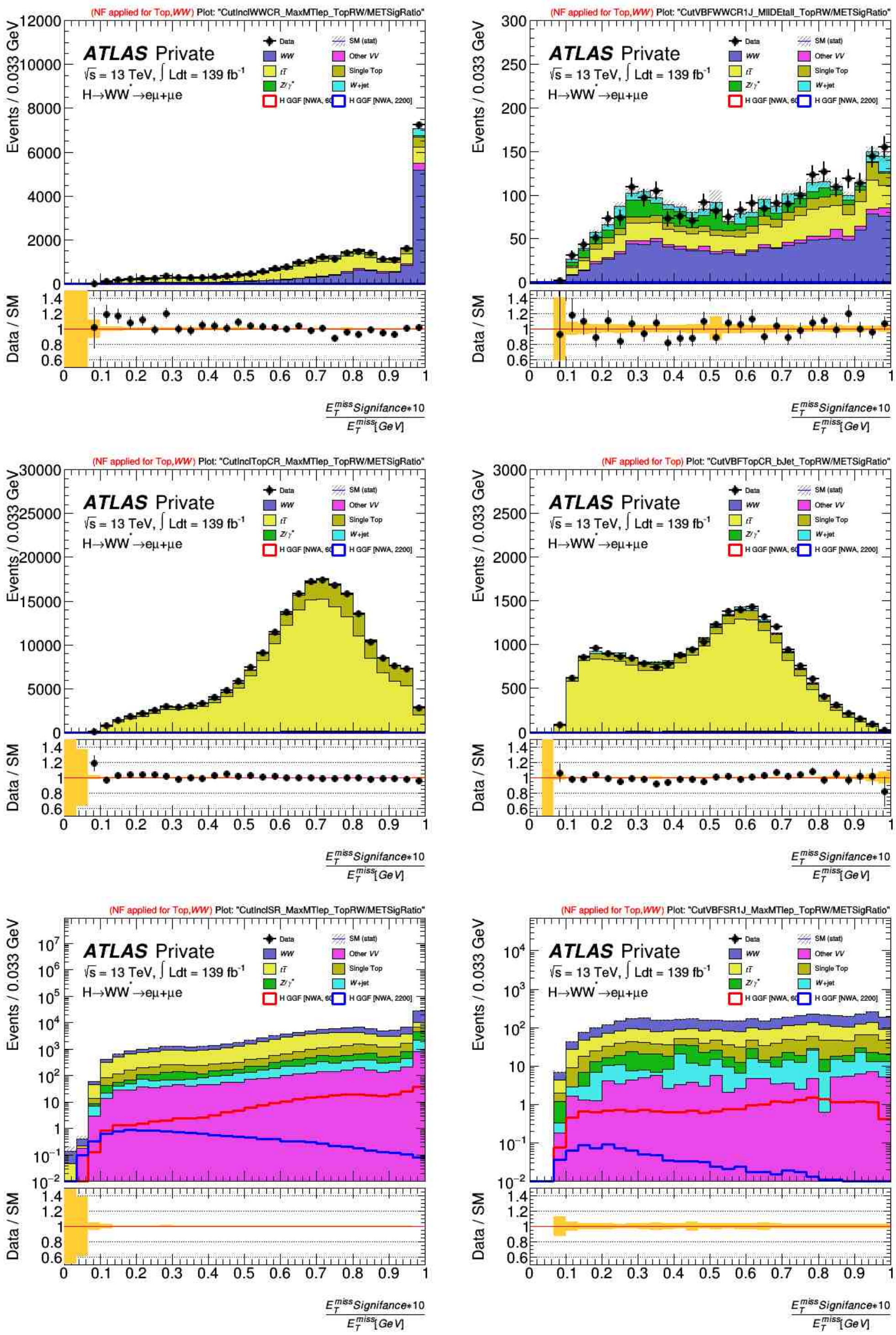

Figure 6.12: Modeling of the E_T^{miss} Significance divided by E_T^{miss} variable in the Regions: ggF WW (top left), VBF1J WW (top right), ggF top (middle left), VBF top (middle right), ggF SR (bottom left), VBF1J SR (bottom right). E_T^{miss} Significance has been multiplied by 10 to return a distribution roughly between 0 and 1.

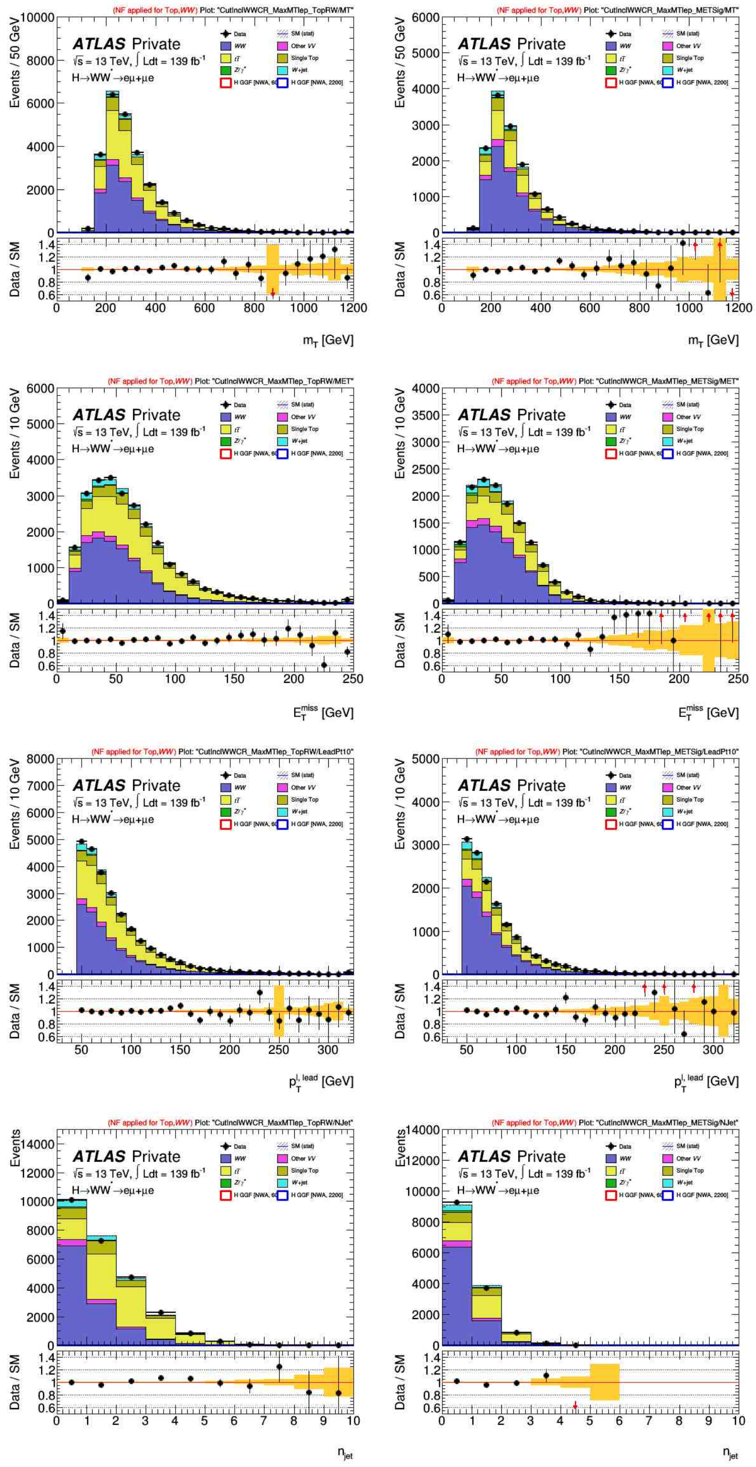

Figure 6.13: Modeling of the significant kinematics before (left) and after (right) applying the METSigRatio minimum cut of 0.8 in the quasi-inclusive ggF WW CR. Normalization factors are recalculated and applied after using the METSigRatio cut.

6.3 VBF Common Selection

An additional improvement over the previous 36 fb^{-1} analysis was explored. The previous VBF control region selections used looser kinematic selections than the common selections used to define the ggF control regions and signal regions. This loosening of selection was used to increase the statistics of control regions. With the move to 139 fb^{-1} with the full ATLAS Run-II dataset, an attempt was made to try and align the VBF control region selections with the signal region selections.

To begin the comparison, the common cut selection of signal regions ($m_{\ell\ell}$, $p_T^{\ell,\text{lead}}$, $p_T^{\ell,\text{sublead}}$, $\max(m_T^W)$) was applied to both the top and WW VBF control regions. To retain the control region orthogonality from the signal region, the b-jet veto is retained for the top control region, and the $|\Delta\eta_{\ell\ell}| < 1.8$ cut used in the signal region is reversed for the WW control region. A preliminary asimov-only statistical fit is then used to compare the tightened selection's impact on expected limits of the result. No significant change is observed from the lower statistics in the control regions.

To have a fuller understanding of the effect of the tightened selection, normalization factors are calculated for the regions, and the purity of the controlled background is examined before and after the tightened selection. For the top quark control region the normalization factor changes from 0.96±0.01 (stat.) to 0.94±0.01 (stat.), and the purity of top-quark backgrounds in the region changes from 97.5% to 98.3%. For the WW control region the normalization factor changes 1.08±0.05 (stat.) to 1.28±0.08 (stat.), and the purity of WW backgrounds in the region changes from 47.0% to 58.7%. No concerns arise from the change in the top-quark region, and therefore this tightened control region selection is applied.

The change in the normalization factor of the WW control region becomes quite concerning as the impact on the statistical analysis of this change is not included in an asimov fit. A comparison of the data to MC agreement is made in Figure 6.14, where it can be observed that the change in the normalization factor is coming from the orthogonal selection of the $|\Delta\eta_{\ell\ell}|$ distribution. The high values of the $|\Delta\eta_{\ell\ell}|$ tend to have a data excess, where the lower values have a data deficit. Because the goal of the control region is to accurately model our signal region (which is defined by the lower $|\Delta\eta_{\ell\ell}|$ selection), the modelling difference would not accurately give a normalization factor that is correct for the MC in this region. Therefore, it is chosen to remain with the previous 36 fb^{-1} analysis WW VBF control region selection.

6.4 Kinematic Ratio Cut Optimization

An additional study for optimizing the signal regions for the analysis is carried out by comparing the ratio of the m_T variable and it's constituent kinematics, and also some additional mass-based kinematics. Significance scans are used here rather than a gridscanning technique and statistical analysis comparison to allow for a simpler study. In the previous studies, no resonance mass dependence was included in the optimization, as gridscanner techniques showed very little difference in the cut selection used for multiple signal resonance mass points. However, with this study mass dependence is observed, and therefore the possible optimization is carried out for each individual mass point.

To begin this optimization study, a generic mass range was visited, looking at a low (m_H = 400 GeV), medium (m_H = 1000 GeV) and high (m_H = 2200 GeV) and the m_T constituent kinematics ($p_T^{\ell,\text{lead}}$, $p_T^{\ell,\text{sublead}}$, E_T^{miss}) were looked at with a ratio of m_T. Figures 6.15 - 6.17 show the significance scans of the different ratios for the three considered mass points for the quasi-inclusive ggF signal region. Only in the highest mass signal model were some improvements seen. However, to be discussed in further detail in Section 6.4.1, only the integrated significance is improved here, but not in an m_T region where this signal model is sensitive. Figures 6.18 - 6.20 show the same ratios for the VBF-enriched 1-jet signal region. Once again, only the highest mass point shows some possible significance improvement, but the significance gain is concentrated in the lower m_T range where there is little to no sensitivity of the signal model.

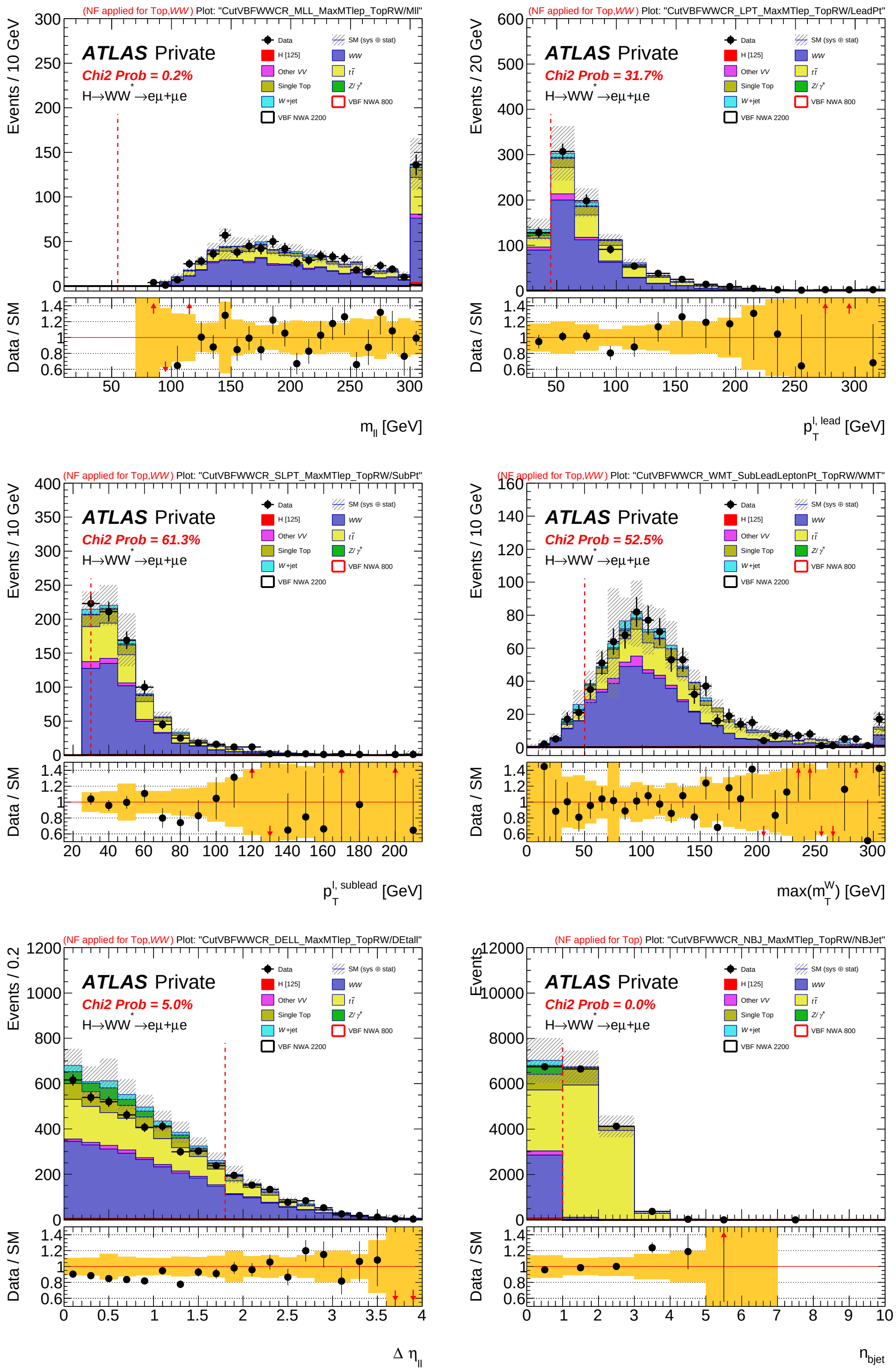

Figure 6.14: Comparison of data and MC in $N_{jet} = 1$ VBF WW control region, after the tightened control region selection,with one of the cuts on the selected distribution is removed: $m_{\ell\ell}$ (top left), $p_T^{\ell,\text{lead}}$ (top right), $p_T^{\ell,\text{sublead}}$ (middle left), $\max(m_T^W)$ (middle right), $|\Delta\eta_{\ell\ell}|$ (bottom left), N_{b-jet} (bottom right). The hatched band in the upper pane and the shaded band in lower pane show the combined statistical and experimental uncertainties on the predictions. The last bin contains the overflow. Normalization factors obtained from a comparison of data and MC have been applied for the top-quark and WW background. The reweighting for top-quark events has been applied. The red dashed vertical line indicates the cut value used in the region selection.

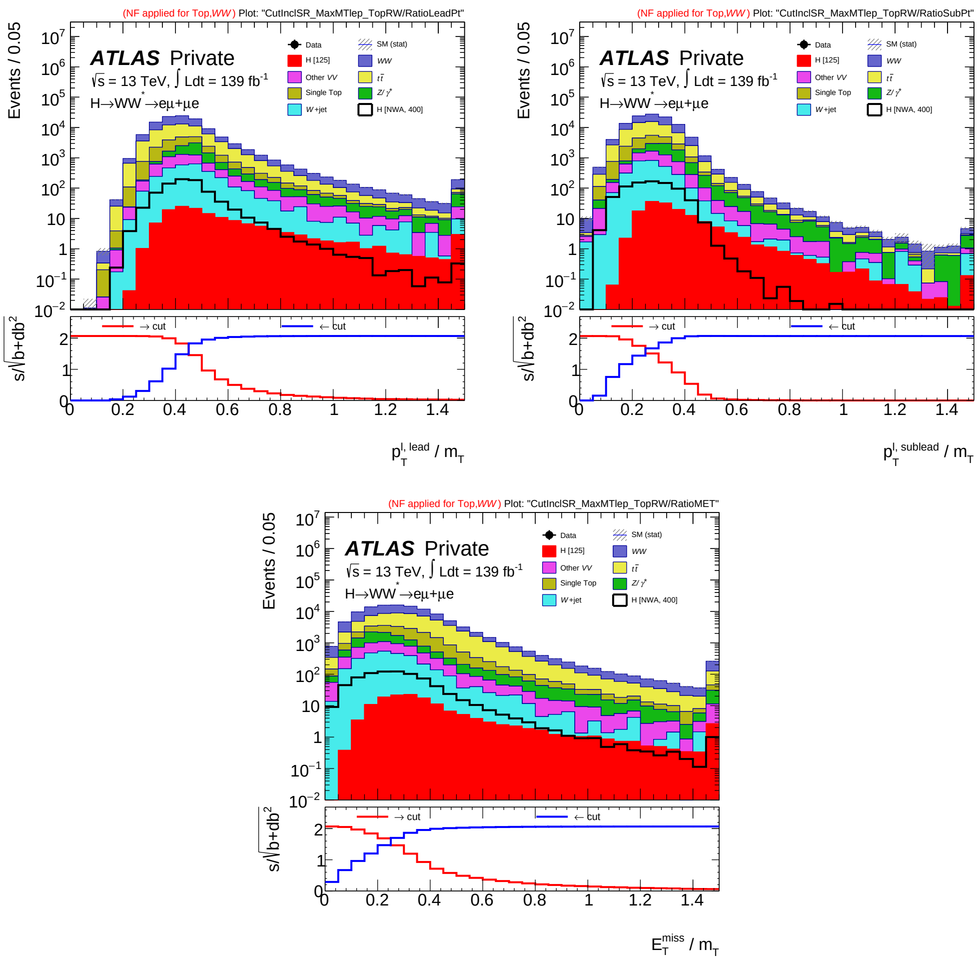

Figure 6.15: Significance scan of the $p_T^{\ell,\text{lead}}$ / m_T (top left), $p_T^{\ell,\text{sublead}}$ / m_T (top right), and E_T^{miss} / m_T (bottom) for the $m_H = 400$ GeV NWA ggF signal in the quasi-inclusive ggF signal region.

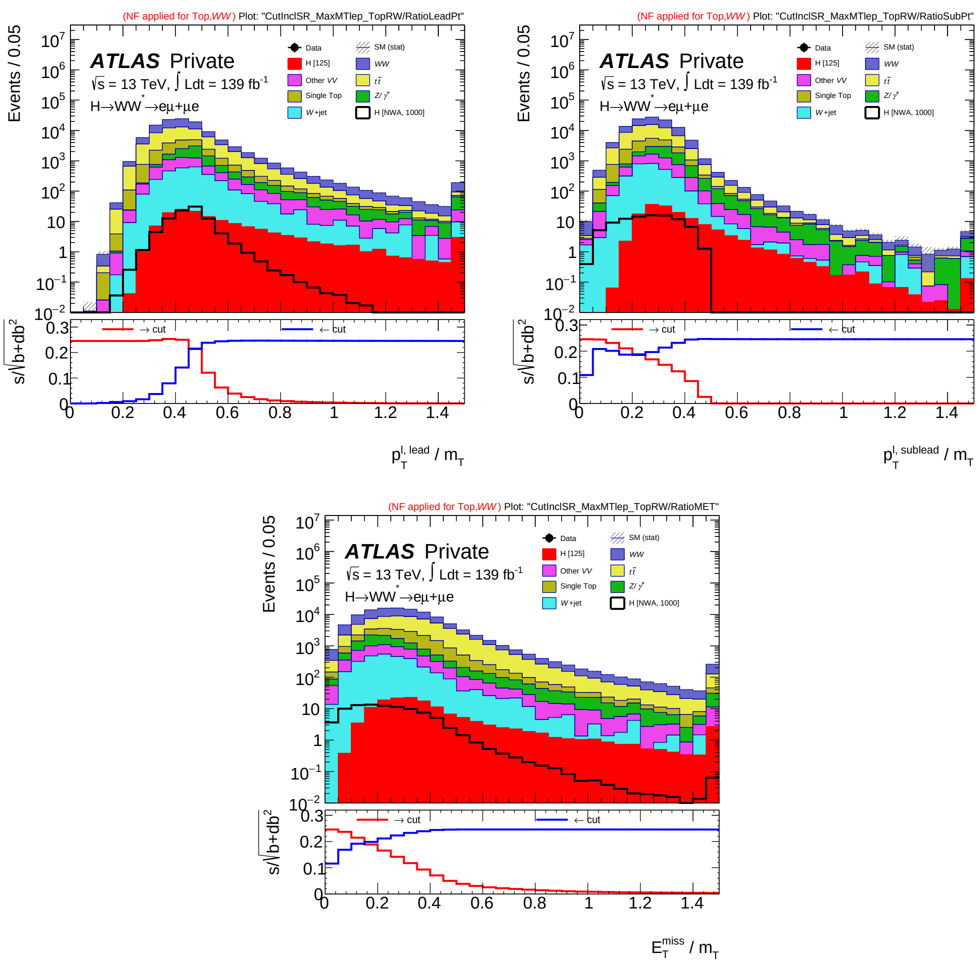

Figure 6.16: Significance scan of the $p_T^{\ell,\text{lead}}$ / m_T (top left), $p_T^{\ell,\text{sublead}}$ / m_T (top right), and E_T^{miss} / m_T (bottom) for the m_H = 1000 GeV NWA ggF signal in the quasi-inclusive ggF signal region.

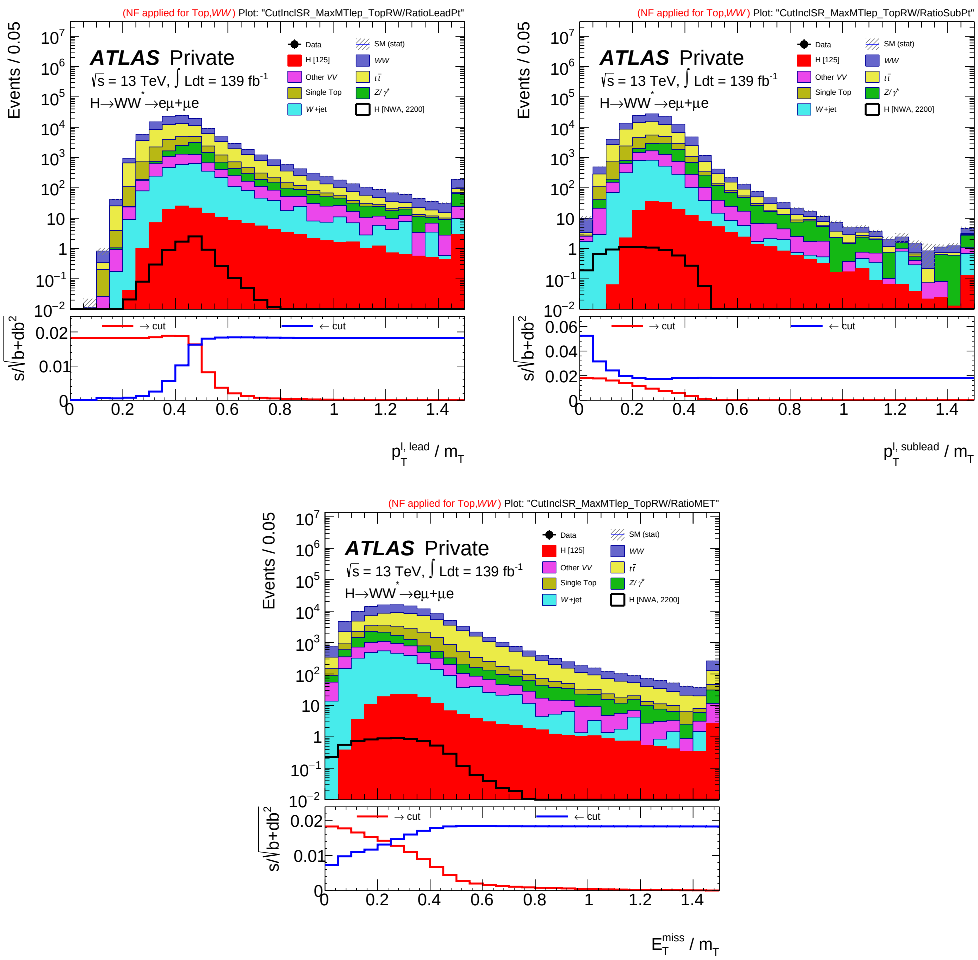

Figure 6.17: Significance scan of the $p_T^{\ell,\text{lead}}$ / m_T (top left), $p_T^{\ell,\text{sublead}}$ / m_T (top right), and E_T^{miss} / m_T (bottom) for the m_H = 2200 GeV NWA ggF signal in the quasi-inclusive ggF signal region.

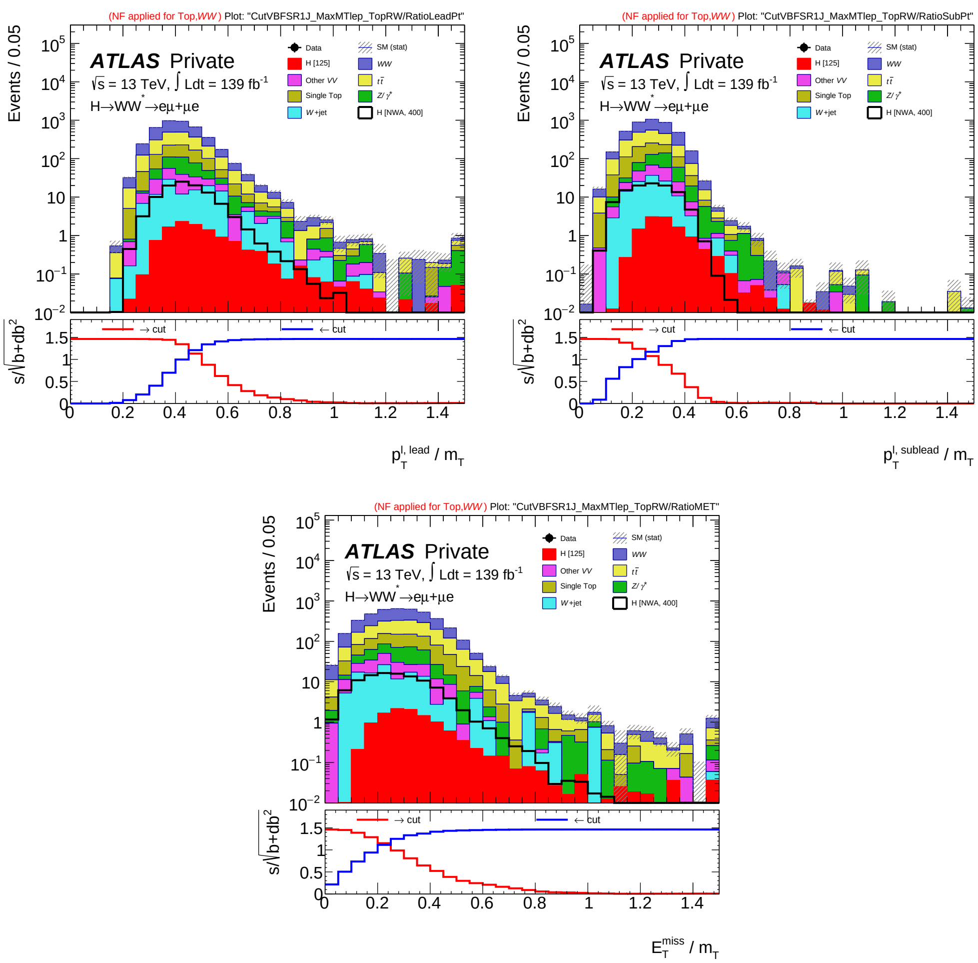

Figure 6.18: Significance scan of the $p_T^{\ell,\text{lead}}$ / m_T (top left), $p_T^{\ell,\text{sublead}}$ / m_T (top right), and E_T^{miss} / m_T (bottom) for the m_H = 400 GeV NWA VBF signal in the VBF 1-jet signal region.

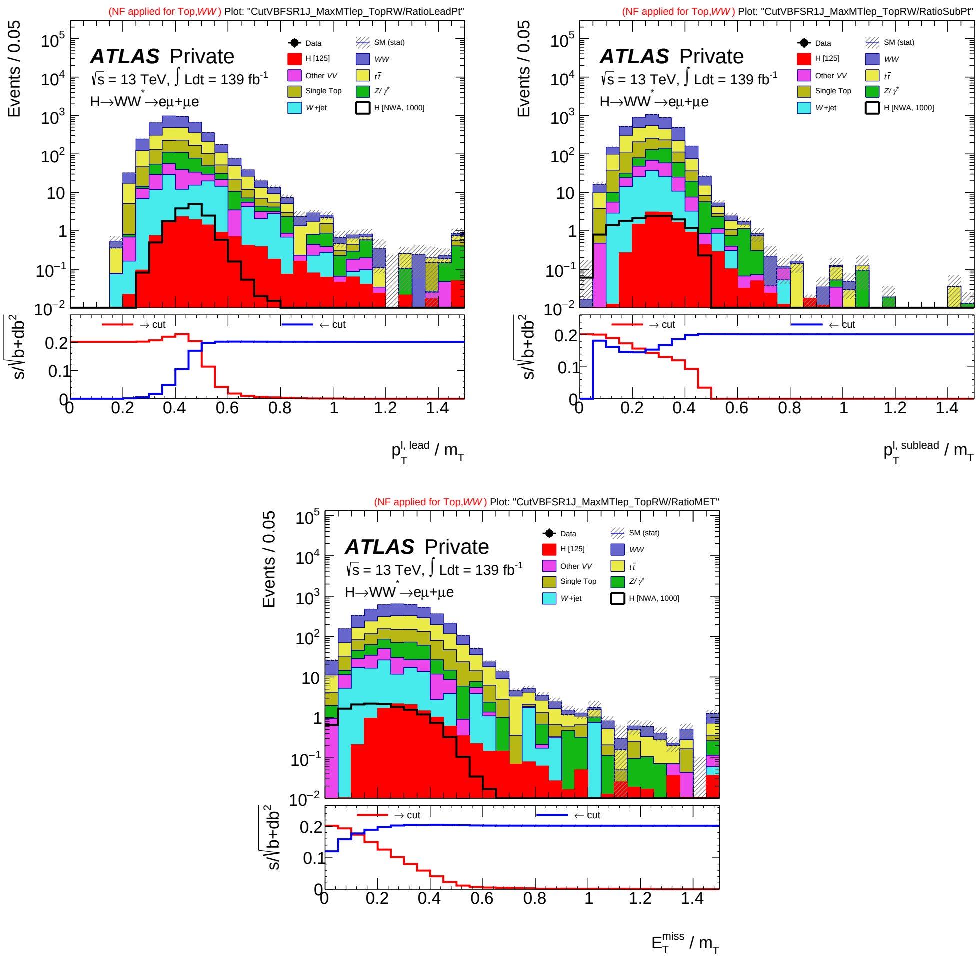

Figure 6.19: Significance scan of the $p_T^{\ell,\mathrm{lead}}$ / m_T (top left), $p_T^{\ell,\mathrm{sublead}}$ / m_T (top right), and E_T^{miss} / m_T (bottom) for the m_H = 1000 GeV NWA gGF signal in the VBF 1-jet signal region.

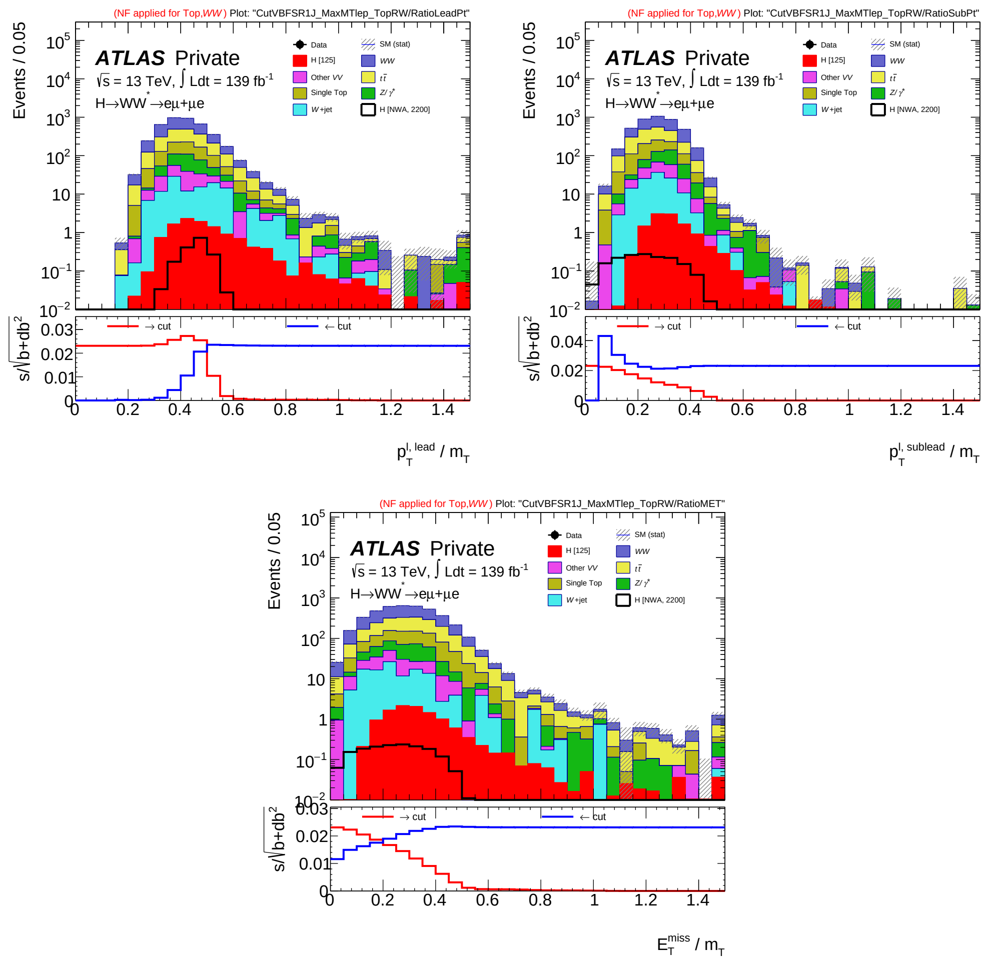

Figure 6.20: Significance scan of the $p_T^{\ell,\text{lead}}$ / m_T (top left), $p_T^{\ell,\text{sublead}}$ / m_T (top right), and E_T^{miss} / m_T (bottom) for the m_H = 2200 GeV NWA VBF signal in the VBF 1-jet signal region.

The same kinematic ratios are compared for the VBF-enriched 2+ jet signal region. Additionally, the kinematics used to select the VBF phase-space, m_{jj} and ΔY_{jj}, are compared with m_T in similar ratio fashion. Figures 6.21 - 6.23 show the significance scans of the different ratios for the three considered mass points for the VBF 2+ jet signal regions. No significance gain is observed from the previously considered m_T constituent kinematics. However, a strong significance gain is observed from the m_{jj} and ΔY_{jj} ratios even at intermediate masses.

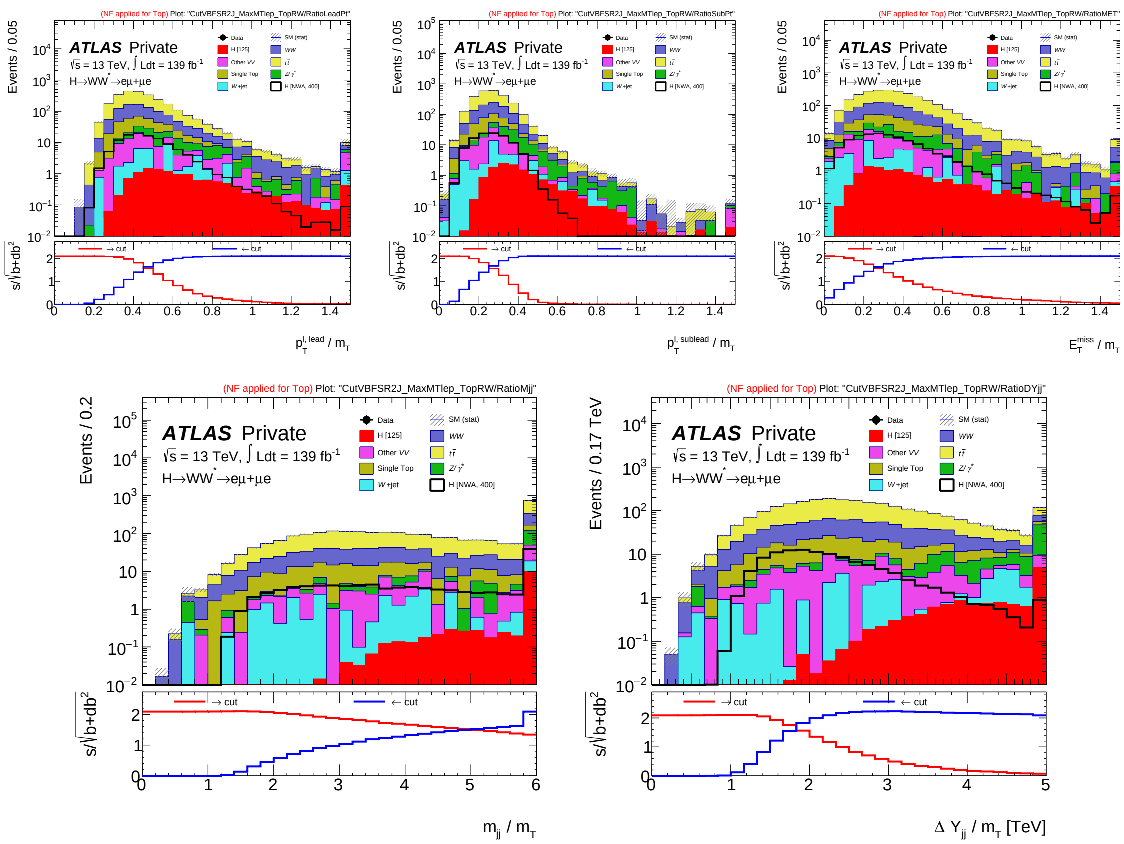

Figure 6.21: Significance scan of the $p_T^{\ell,\text{lead}}$ / m_T (top left), $p_T^{\ell,\text{sublead}}$ / m_T (top center), E_T^{miss} / m_T (top right), m_{jj} / m_T (bottom left), and $|\Delta y_{jj}|$ / m_T (bottom right) for the m_H = 400 GeV NWA VBF signal in the VBF 2+ jet signal region.

6.4.1 Optimization Challenges

Challenges exist when trying to do regional optimization within the analysis. Because of the wide range of resonance masses for the signal models considered (200 GeV - 6 TeV), a cut

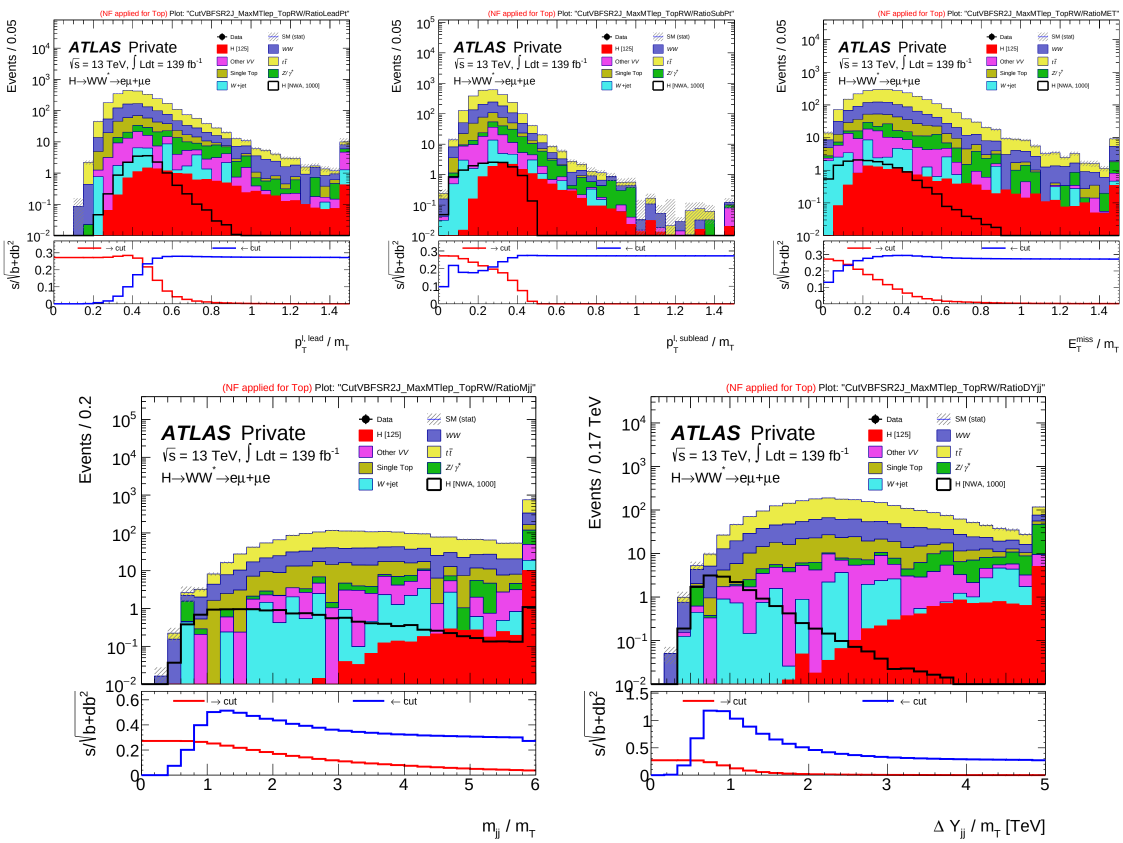

Figure 6.22: Significance scan of the $p_T^{\ell,\text{lead}}$ / m_T (top left), $p_T^{\ell,\text{sublead}}$ / m_T (top center), E_T^{miss} / m_T (top right), m_{jj} / m_T (bottom left), and $|\Delta y_{jj}|$ / m_T (bottom right) for the m_H = 1000 GeV NWA VBF signal in the VBF 2+ jet signal region.

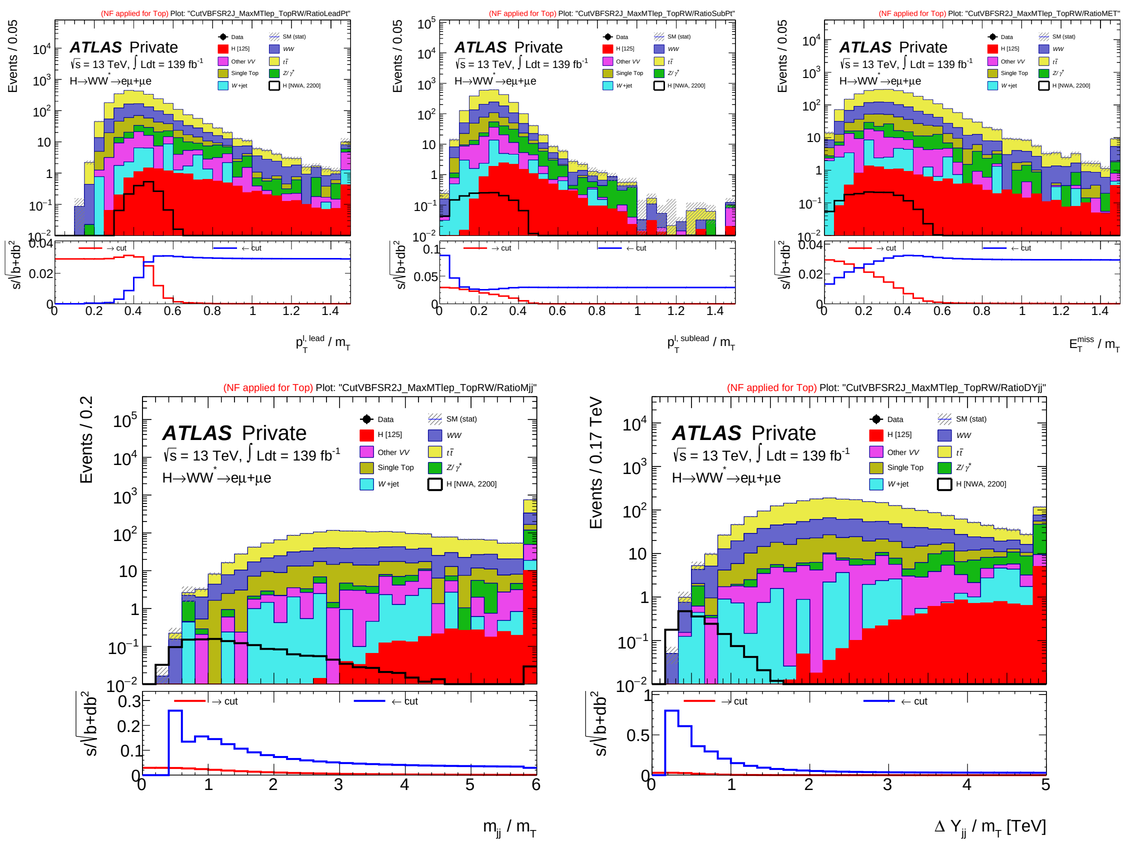

Figure 6.23: Significance scan of the $p_T^{\ell,\text{lead}}$ / m_T (top left), $p_T^{\ell,\text{sublead}}$ / m_T (top center), E_T^{miss} / m_T (top right), m_{jj} / m_T (bottom left), and $|\Delta y_{jj}|$ / m_T (bottom right) for the $m_H = 2200$ GeV NWA VBF signal in the VBF 2+ jet signal region.

selection which optimizes the entire range of regions is not simple. Additionally, the wide range of signal masses does not allow an easy implementation of multivariate analysis (MVA) techniques that are common place within the experimental high-energy physics community. This leaves a cut-based approach, which often uses kinematics that are strongly correlated to m_T, which is used as the statisticaly figure of merit in the analysis.

To highlight these challenges, a further study of the by-eye optimization values chosen from the studies in the main body of this section, specifically the m_{jj} / m_T and $|\Delta y_{jj}|$ / m_T cuts observed for the VBF-enriched 2+ jet region is shown. First, an observation on the two-dimensional distribution of m_T vs. m_{jj} / m_T is used to evaluate what range of m_T background events would be removed when a cut on the m_{jj} / m_T composite variable would be applied. Figure 6.24 shows that for the intermediate to higher resonance mass signals very little background in the sensitive m_T regions would be removed by such a cut.

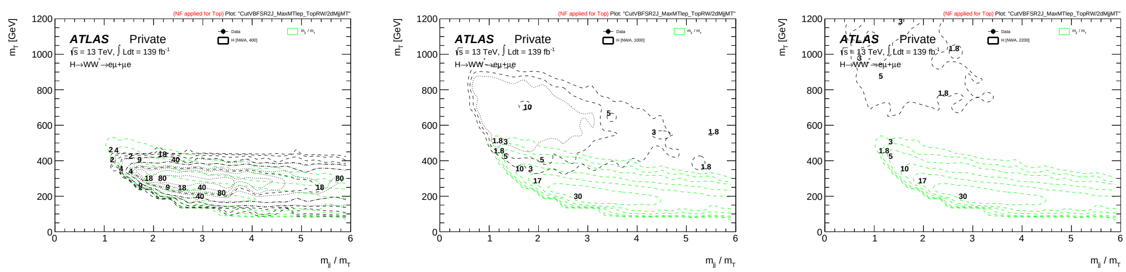

Figure 6.24: Two-dimensional plots of the m_T vs. m_{jj} / m_T distributions for the m_H = 400 GeV (left), m_H = 1000 GeV (center), and m_H = 2200 GeV (right) VBF NWA signal samples in the VBF 2+ jet signal regions.

In light of the unlikely improvement, a full comparison of the impact of applying the assumed improved significance is carried out in the VBF-enriched 2+ jet signal region. The cuts chosen are a m_{jj} / $m_T < 2$ and $|\Delta y_{jj}|$ / $m_T < 1.0$, applied independently, and considering only resonance masses of 1000 GeV or more. A bin-by-bin significance scan of the signal region before and after the cuts are applied for a selection of mass points is shown in Figures 6.25 - 6.27, where no improvement is shown over the nominal signal selection. Therefore, no kinematic ratios of m_T are included in the final cut selection.

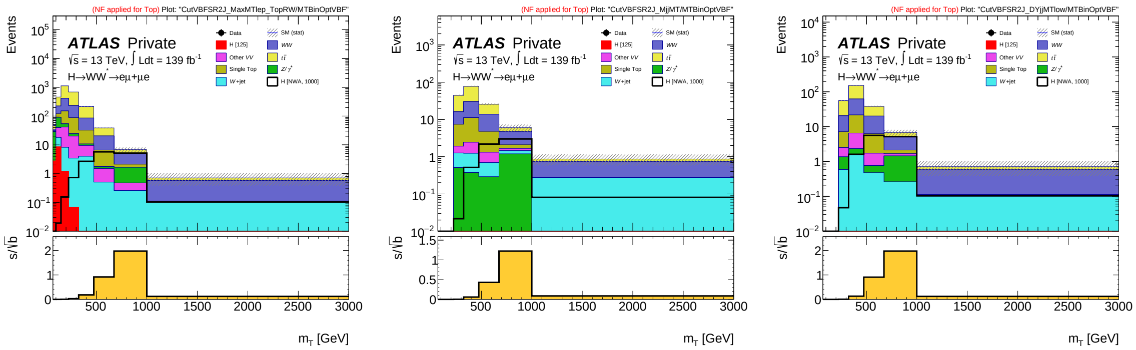

Figure 6.25: m_T distributions of VBF NWA $m_H = 1000$ GeV signal and SM background nominally (left), after applying a m_{jj} / $m_T < 2$ cut (center), and after applying a $|\Delta y_{jj}|$ / $m_T < 1.0$ (right) in the VBF 2+ jet signal regions. The bin-by-bin significance (s/$\sqrt{b}$) is shown in the bottom pane.

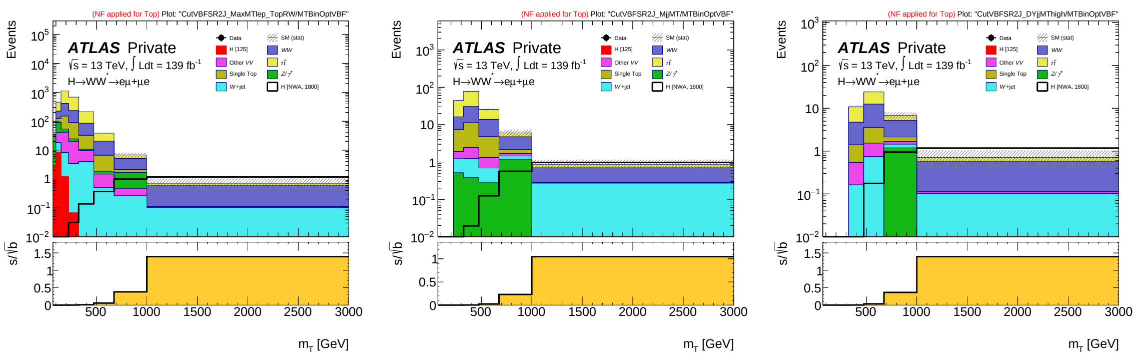

Figure 6.26: m_T distributions of VBF NWA $m_H = 1800$ GeV signal and SM background nominally (left), after applying a m_{jj} / $m_T < 2$ cut (center), and after applying a $|\Delta y_{jj}|$ / $m_T < 1.0$ (right) in the VBF 2+ jet signal regions. The bin-by-bin significance (s/$\sqrt{b}$) is shown in the bottom pane.

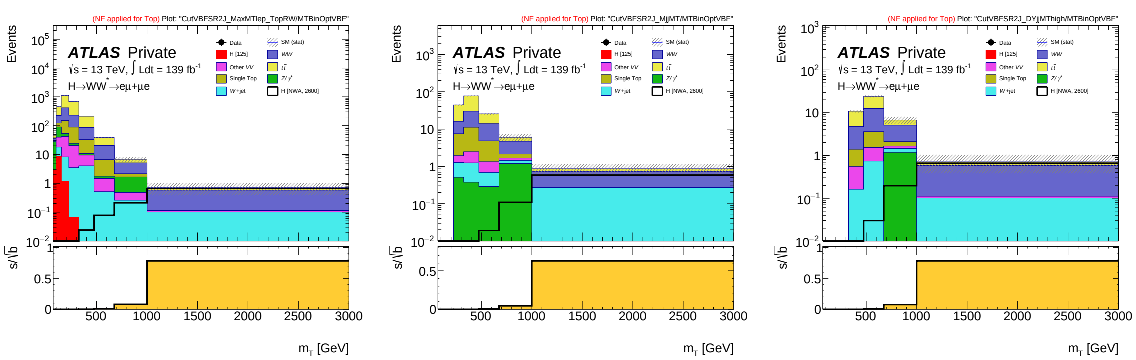

Figure 6.27: m_T distributions of VBF NWA $m_H = 2600$ GeV signal and SM background nominally (left), after applying a m_{jj} / $m_T < 2$ cut (center), and after applying a $|\Delta y_{jj}|$ / $m_T < 1.0$ (right) in the VBF 2+ jet signal regions. The bin-by-bin significance (s/$\sqrt{b}$) is shown in the bottom pane.

6.5 $m_{\tau\tau}$ Exploration

A final optimization study involves a possible use of the collinear mass, $m_{\tau\tau}$, as the figure of merit in the signal regions to be used in the statistical analysis. The observable $m_{\tau\tau}$ makes use of the Collinear Approximation Method [133] to make the assumption that the charged leptons seen are the products of the decay of a pair of τ leptons. In this case the neutrinos emitted are collinear with the charged leptons, and these neutrinos are the only source of the observed E_T^{miss} in the event. Therefore, the energy fractions of the neutrinos can be computed directly. The $m_{\tau\tau}$ distribution in each of the three signal regions is shown in Figure 6.28. Unfortunately no significant separation of the signal against the SM background is observed, and no use of this observable is included further in the analysis.

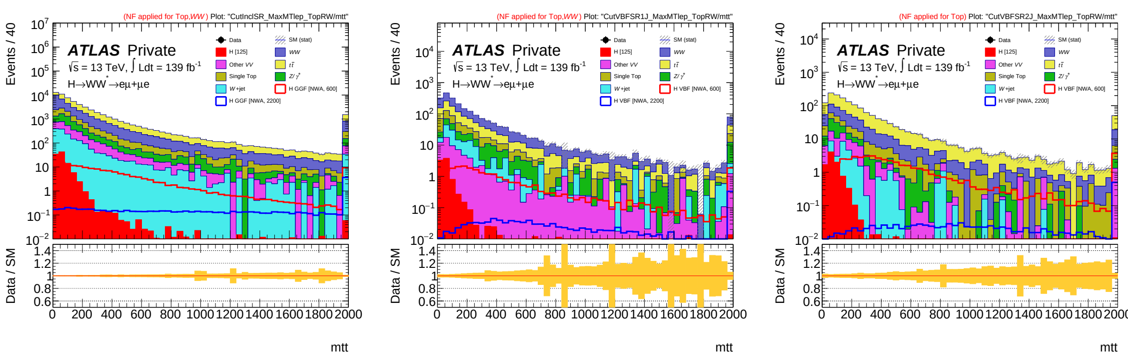

Figure 6.28: $m_{\tau\tau}$ distributions of select NWA signal productions and masses compared to the SM background in the quasi-inclusive ggF SR (left), VBF 1-jet SR (center), and VBF 2+ jet SR (right).

Chapter 7

Analysis Region Selection and Modelling

The analysis is optimized to select the proposed signals while minimizing the background processes. The analysis utilizes control regions to verify kinematic modelling of the data by the MC, extracting the difference as normalization factors (NF). All regions use a cut-based selection, with cuts specifically chosen for the optimal measurement of the different signal interpretations used within the analysis.

7.1 Event Selection

The selection requires two different flavor, opposite sign leptons surpassing a p_T threshold of 25 GeV[1]. The event is vetoed if it contains a third lepton with $p_T \geq 15$ GeV. Both leptons must satisfy the quality and isolation requirements from Chapter 5.

The event selection for each signal region (SR) has been optimized using a combination of gridscanning techniques and statistical procedures. Full detail on the methodology and results was given in Chapter 6. The resulting selection cuts for the pseudorapidity between the two leptons, $|\Delta\eta_{\ell\ell}|$, the invariant mass of the dilepton system, $m_{\ell\ell}$, the transverse momentum, p_T, of the leading and subleading leptons, and the maximum value of the transverse mass calculated for either of the two leptons with the E_T^{miss} are shown in Table 7.1. This

[1] Preselection thresholds are used to decrease the statistics of events being processed by further selection criteria, allowing for a faster processing of the dataset.

Pre-Selection		
Two Different Flavour, Opposite Sign Leptons, $p_T^\ell > 25$ GeV Third lepton veto, $p_T^\ell > 15$ GeV		
$\mathrm{SR_{ggF}}$	$\mathrm{SR_{VBF1J}}$	$\mathrm{SR_{VBF2J}}$
Common Selection		
$N_{b-tag} = 0$ $\|\Delta\eta_{\ell\ell}\| < 1.8$ $m_{\ell\ell} > 55$ GeV $p_T^{\ell,\mathrm{lead}} > 45$ GeV $p_T^{\ell,\mathrm{sublead}} > 30$ GeV $\max(m_T^W) > 50$ GeV		
ggF phase space	VBF1J phase space	VBF1J phase space
Inclusive in N_{jet} but excluding VBF1J and VBF2J phase space	$N_{jet} = 1$ and $\|\eta_j\| > 2.4$, $\min(\|\Delta\eta_{j\ell}\|) > 1.75$	$N_{jet} = 2$ and $m_{jj} > 500$ GeV, $\|\Delta y_{jj}\| > 4$

Table 7.1: Event selection for the three signal regions in the $H \to WW$ resonance search.

transverse mass value, m_T^W, is defined as

$$m_T^W = \sqrt{2p_T^\ell E_T^{\mathrm{miss}}(1 - \cos(\phi^\ell - \phi^{E_T^{\mathrm{miss}}})} \tag{7.1}$$

To suppress the top-quark background in the SR, an additional veto is applied on events with one or more b-tagged jets, $N_{b-\mathrm{jet}}$.

The analysis uses three event categories, two optimized for VBF production and a third optimized for ggF production of the heavy resonances. The VBF categories are separated into jet multiplicity (N_{jet}) bins, one with $N_{\mathrm{jet}} = 1$, and a second with $N_{\mathrm{jet}} \geq 2$. For the $N_{\mathrm{jet}} = 1$ VBF region, a selection on two discriminating kinematics variables is made to suppress the contribution of ggF signals: the pseudorapidity of the jet, $|\eta_j|$, and the minimum value of the pseudorapidity difference between the jet and the leptons, $\min(\Delta\eta_{j\ell})$. For the VBF $N_{\mathrm{jet}} \geq 2$ region, a selection on two other kinematic variables is used to suppress the contribution of the ggF signals: the transverse mass of the two leading jets, m_{jj}, and the difference in the rapidity of the two leading jets, Δy_{jj}. The ggF phase space is defined as events passing the common SR selection, while also not satisfying any of VBF region criteria, ensuring completely orthogonal regions. With these selections, the ggF category is mainly composed of the ggF produced signal samples, with a small contribution from the VBF produced signal samples. The overall acceptance times efficiency for all considered signal models is given in Figure 7.1. The acceptance is defined as the number of events remaining at preselection with respect to the number of events passing minimal selection (2 leptons - different flavor, overlap removal) requirements of the Processed xAOD (PxAOD) production, and the efficiency is defined as the number of events in the signal regions with respect to the events at preselection.

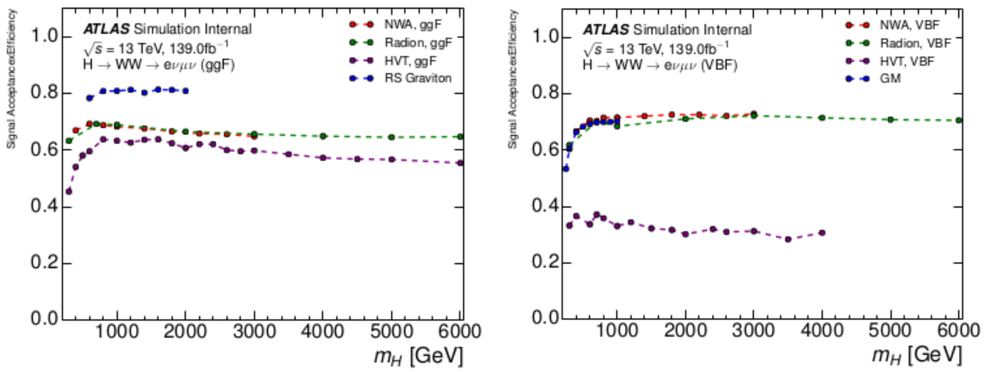

Figure 7.1: Signal acceptance times efficiency as a function of m_H for considered signal models for ggF (left) and VBF (right) production modes. The acceptance is defined as the ratio of the number of events after the preselection cuts and the number of events coming from the PxAOD. The efficiency is defined as the ratio of the combined number of events for all three signal regions and the preselection number of events. Both the acceptance and efficiency are defined on the reconstructed quantities.

7.2 SM Background Modelling

7.2.1 Background Composition for $e\nu\mu\nu$

The primary Standard Model background in this analysis comes from top-quark and WW processes. There is small, but not negligible, contributions also coming from W/Z+jets, multijets, and other diboson processes WZ, $V\gamma$, $V\gamma^*$, and ZZ. Both the top-quark and WW background processes are normalized to data in dedicated control regions which are defined by criteria similar, but orthogonal, to those used for the signal regions. The CR definitions are chosen by loosening or reversing signal region criteria to obtain a signal depleted region that has high purity of the primary background for the particular CR. The following subsections will describe in detail the methods used to estimate the most significant background processes: top-quark, WW, and W+jets. Due to the overall small contribution from the Drell-Yan and other diboson (Non-WW) processes in the selected regions, their prediction is taken from the available MC simulation. The small contribution from the SM Higgs boson with $m_H = 125$ GeV is also included. The comparison of the data and MC estimation prior to any region selection cuts, are applied can be seen in Figure 7.2. The full cutflow[2] of the control region selection for the primary backgrounds can be found in Table 7.7.

7.2.2 $t\bar{t}$ and Single Top Background

Top-quark events can be produced as a $t\bar{t}$ pair or singly in association with a W boson. In this analysis, contributions from $t\bar{t}$ and single-top (Wt) events are estimated together, with their relative contributions determined by the predicted cross sections and MC simulation due to the difficulty of separating the two processes kinematically and that the contribution from single top processes is relatively small.

The top-quark CR of the quasi-inclusive ggF category is defined with events having exactly one tagged b-jet and satisfying all other selection criteria of the ggF signal region (SR). The selection cuts are shown in Table 7.2. To observe the effect of each of the cuts applied in the region selection, the comparison of data and MC estimation is shown while removing each one of the cuts individually (NMinus), which can be seen in Figure 7.3. Due to the smaller statistics in the VBF categories, the CR for top background is merged for the two SR, with $p_T^{\ell,\text{lead}}$ and $p_T^{\ell,\text{sublead}}$ cuts relaxed, and the cuts on $m_{\ell\ell}$, $|\Delta\eta_{\ell\ell}|$, and $\max(m_T^W)$ cuts removed. The modelling of these kinematics is shown in Figure 7.4. NMinus cuts are also shown for the m_{jj} and $|\Delta Y_{jj}|$ distributions in Figure 7.5.

The normalization factor, the factor to correct the integral difference of data and MC

[2] A cutflow refers to the progressive selection provided by each of the kinematic selections that are used to define the regions in the analysis.

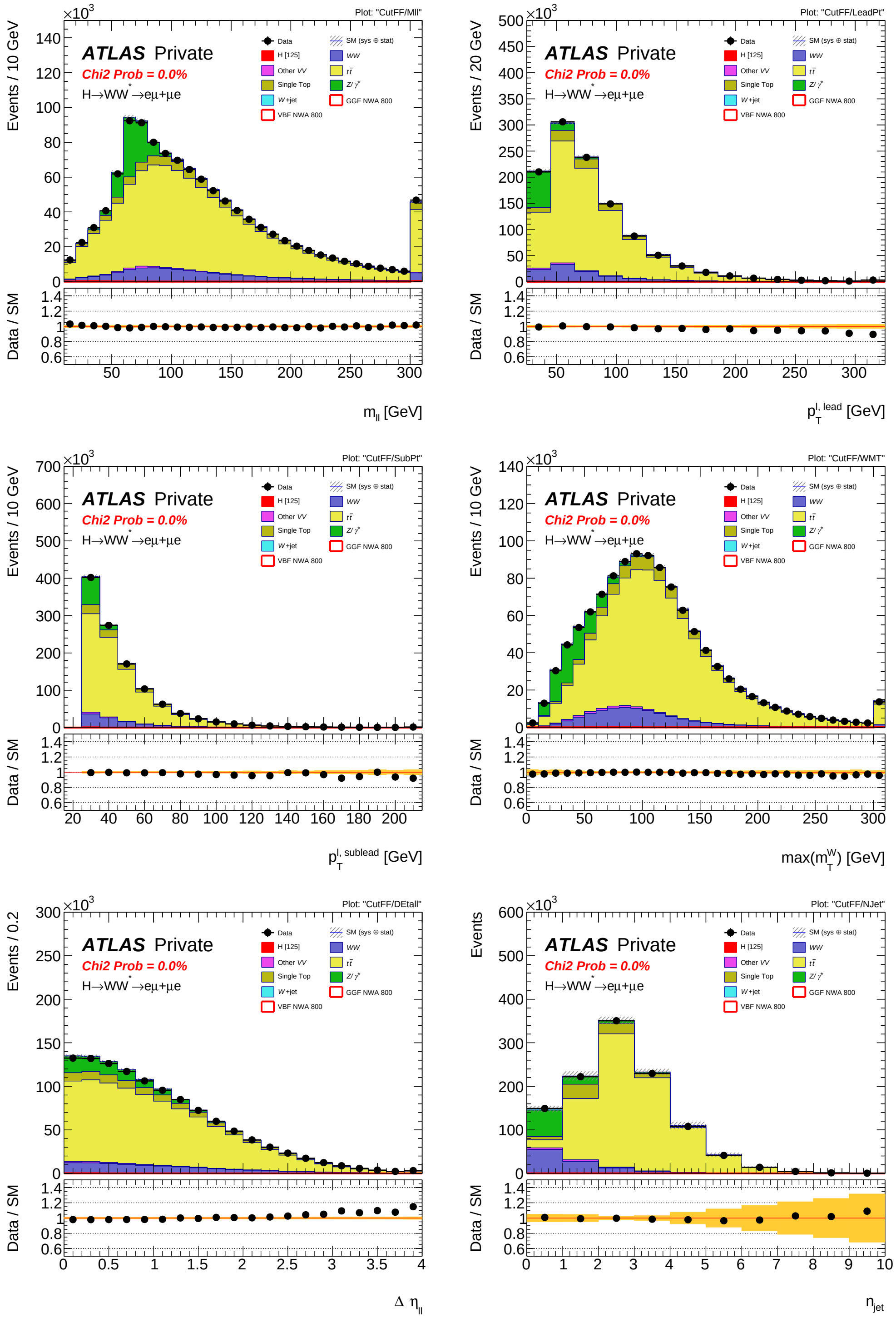

Figure 7.2: Comparison of data and MC at the event preselection level for the variables: $m_{\ell\ell}$ (top left), $p_T^{\ell,\text{lead}}$ (top right), $p_T^{\ell,\text{sublead}}$ (middle left), $\max(m_T^W)$ (middle right), $|\Delta\eta_{\ell\ell}|$ (bottom left), N_{jet} (bottom right). The hatched band in the upper pane and the shaded band in lower pane show the combined statistical and experimental uncertainties on the predictions. The last bin contains the overflow.

modelling, for the top background is calculated independently for each production mode CR. For the quasi-inculsive ggF category, the normalization factor is obtained by simultaneously fitting the top-quark and WW background in both the top and WW control regions. The normalization factor is calculated as 0.98±0.008 (stat). The normalization factor for the top-quark background in the VBF category is calculated by fitting the top-quark processes in the VBF Top CR. The normalization factor is calculated as 0.94±0.01 (stat). The purity in the ggF and VBF Top CR is 97.7% and 98.3%, respectively.

Top-quark p_T Mismodelling and Correction

From the $p_T^{\ell,\mathrm{lead}}$ distribution shown in Figure 7.3, one clearly observes a mismodeling of the data by the MC simulation in both the quasi-inclusive ggF and VBF Top CR. Prior to any correction, correction from NLO to NNLO QCD has been applied (TtbarNNLO reweighing) [10] by using TTbarNNLOReweighter package [1]. Significant studies on the impact of such a reweighting can be found in [23]. An in-situ correction (Fig. 7.12) is applied for both ggF and VBF regions. For the evaluation of the correction, the $p_T^{\ell,\mathrm{lead}}$ cut is relaxed from 45 GeV to 25 GeV and the $|\Delta\eta_{\ell\ell}|$ cut is removed entirely. The correction has been checked for each MC campaign (16a,d,e) independently (see Table 7.3) and was determined to apply the correction over the full dataset. Because the corrective values are similar between ggF and VBF regions, the former is chosen due to superior statistics. The correction is then applied to all top-quark samples in the analysis. Because the difference here is similar in nature to the uncertainties applied when comparing Matrix Element (ME) and parton shower (PS) uncertainties (see Section 8.2), no additional uncertainty is applied on this reweighting procedure.

Further validation of the need to apply this correction due to the inability of the MC generation to correctly model the data by is carried out by showing this effect is not isolated to the specific regions selected in this analysis. For these studies the focus will be primarily on the shape of the $p_T^{\ell,\mathrm{lead}}$ modelling, but the reader should be aware this also applies directly to

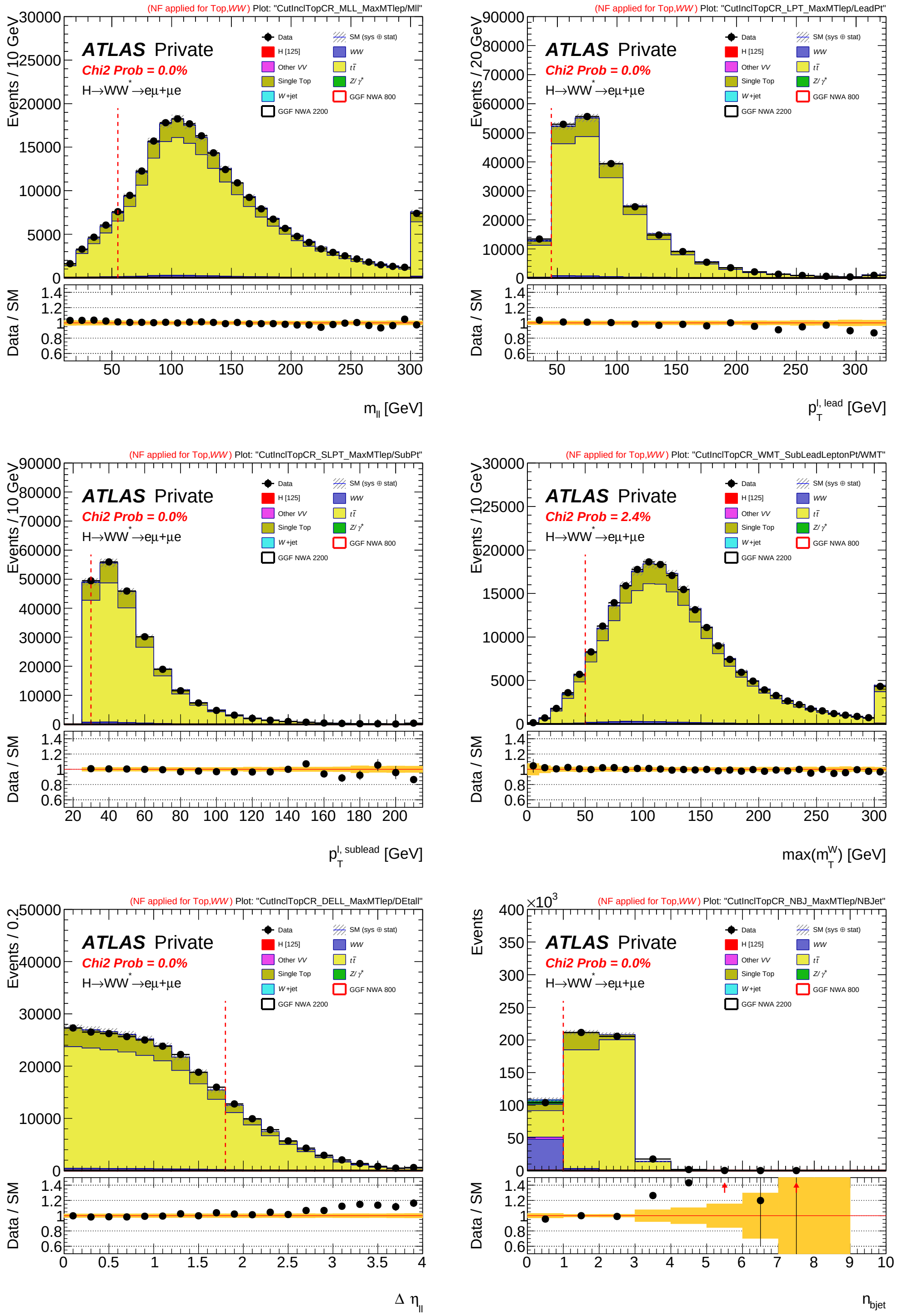

Figure 7.3: Comparison of data and MC in the ggF top-quark CR when one of these cuts is removed from the selection for the variables: $m_{\ell\ell}$ (top left), $p_T^{\ell,\text{lead}}$ (top right), $p_T^{\ell,\text{sublead}}$ (middle left), $\max(m_T^W)$ (middle right), $|\Delta\eta_{\ell\ell}|$ (bottom left), N_{b-jet} (bottom right). The hatched band in the upper pane and the shaded band in lower pane show the combined statistical and experimental uncertainties on the predictions. The last bin contains the overflow. Normalization factors obtained from a comparison of data and MC have been applied for the top-quark and WW background. The red dashed vertical line indicates the cut value used in the region selection.

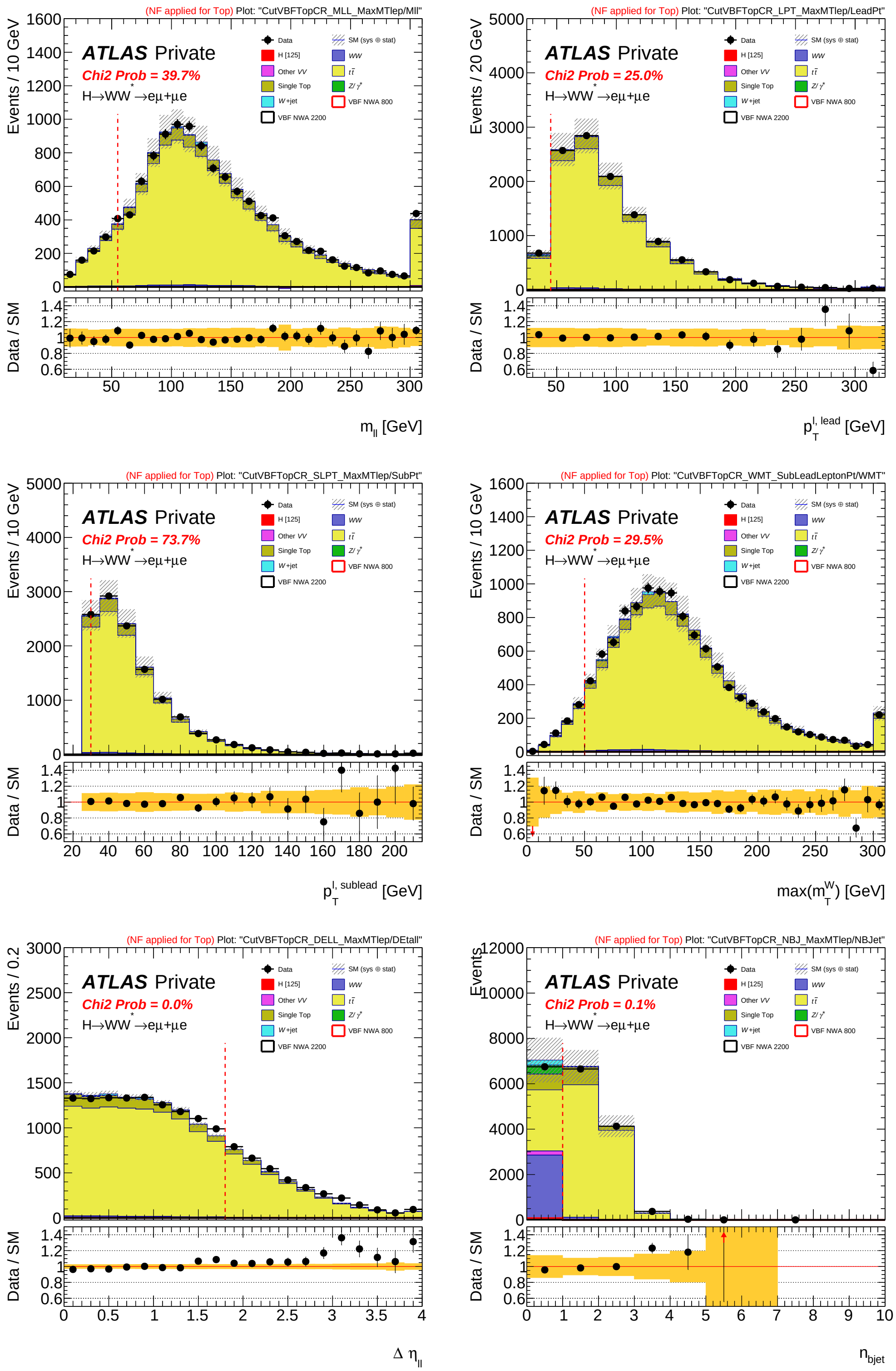

Figure 7.4: Comparison of data and MC in the VBF top-quark CR when one of these cuts is removed from the selection for the variables: $m_{\ell\ell}$ (top left), $p_T^{\ell,\text{lead}}$ (top right), $p_T^{\ell,\text{sublead}}$ (middle left), $\max(m_T^W)$ (middle right), $|\Delta\eta_{\ell\ell}|$ (bottom left), N_{b-jet} (bottom right). The hatched band in the upper pane and the shaded band in lower pane show the combined statistical and experimental uncertainties on the predictions. The last bin contains the overflow. Normalization factors obtained from a comparison of data and MC have been applied for the top-quark and WW background. The red dashed vertical line indicates the cut value used in the region selection.

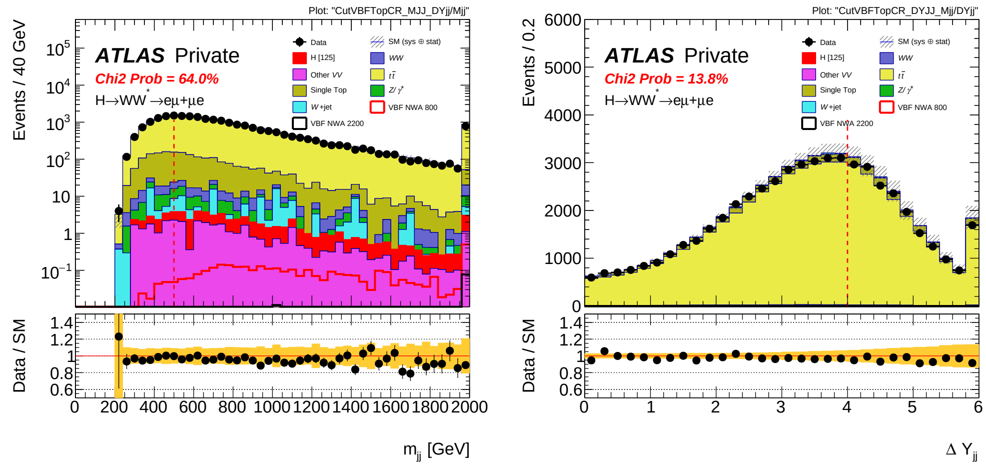

Figure 7.5: Comparison of data and MC in the VBF top-quark CR when one of these cuts is removed from the selection for the variables: m_{JJ} (left) and ΔY_{JJ} (right). The hatched band in the upper pane and the shaded band in lower pane show the combined statistical and experimental uncertainties on the predictions. The last bin contains the overflow. No normalization factors are applied. The red dashed vertical line indicates the cut value used in the region selection.

the m_T modelling by construction. A comparison of data to MC highlighting this discrepancy is shown in Figure 7.6 for the top control regions.

To see if the mismodeling is arising from the selection of b-jet in the top control regions, an additional comparison of the $p_T^{\ell,\text{lead}}$ modelling in both the WW control regions is made, shown in Figure 7.7. By observing the 1-dimensional polynomial fit slope, a comparison of the level of mismodeling between different regions cna be made. In the WW regions it is seen that this value is closer to zero than what was seen in the top regions, as would be expected due to the decreased top-quark background composition percentage in the WW regions. However, the negative slope is still clearly seen in the ggF control region, but absent in the more statistically limited VBF control region. From these findings, it can't definitely be confirmed that the modelling discrepancy is not from the b-jet tagged events, but gives a good hint that it is present regardless of b-jet selection.

The impact of jet multiplicity on the mismodeling of the $p_T^{\ell,\text{lead}}$ distribution is investigated. To avoid any sort of region selection bias a look at the modelling at the preselection level is made first. To study the jet multiplicity impact of the reweighting, the distributions are split into two bins based on the jet multiplicity: a 1- jet bin and a 2 or more (2+) jet bin. To ease

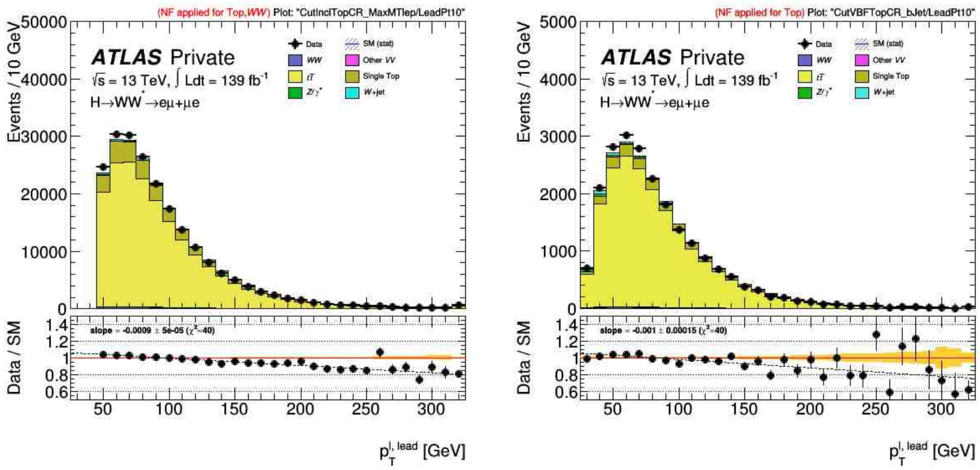

Figure 7.6: Data to MC comparison of the $p_T^{\ell,\text{lead}}$ distribution for the ggF (left) and VBF (right) top control regions. The hatched band in the upper pane and the shaded band in lower pane show the statistical uncertainties on the estimation. No normalization factors have been applied.

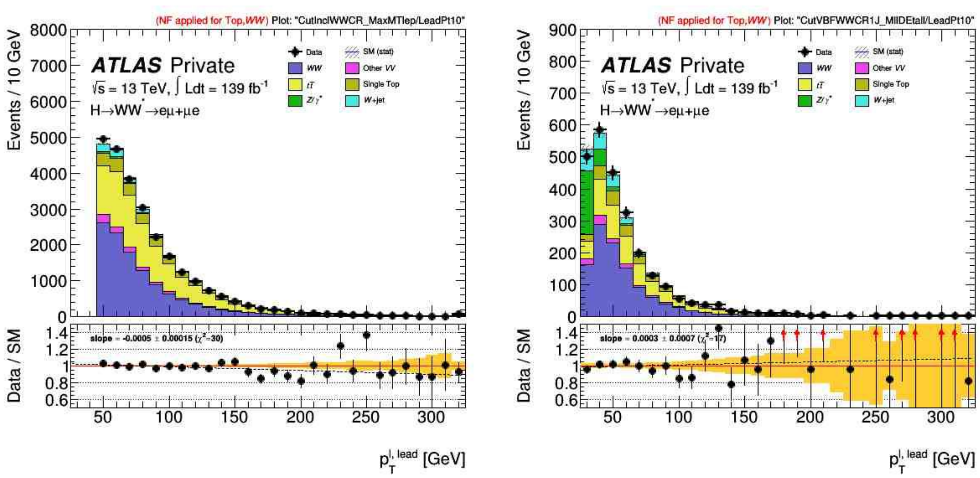

Figure 7.7: Data to MC comparison of the $p_T^{\ell,\text{lead}}$ distribution for the ggF (left) and VBF (right) WW control regions. The hatched band in the upper pane and the shaded band in lower pane show the statistical uncertainties on the estimation. No normalization factors have been applied.

the comparison of the mismodelling of the $p_T^{\ell,\text{lead}}$ distribution, a 1-dimensional polynomial is fit to the data vs. MC ratio in the bottom panes. Comparing the two jet multiplicity bins in Figure 7.8 shows no difference. To further study the jet multiplicity dependence, a comparison is made of the same jet multiplicity binned distributions for the ggF top and WW control regions in Figure 7.9. Again, no dependence of the mismodeling on the jet multiplicity bin is observed.

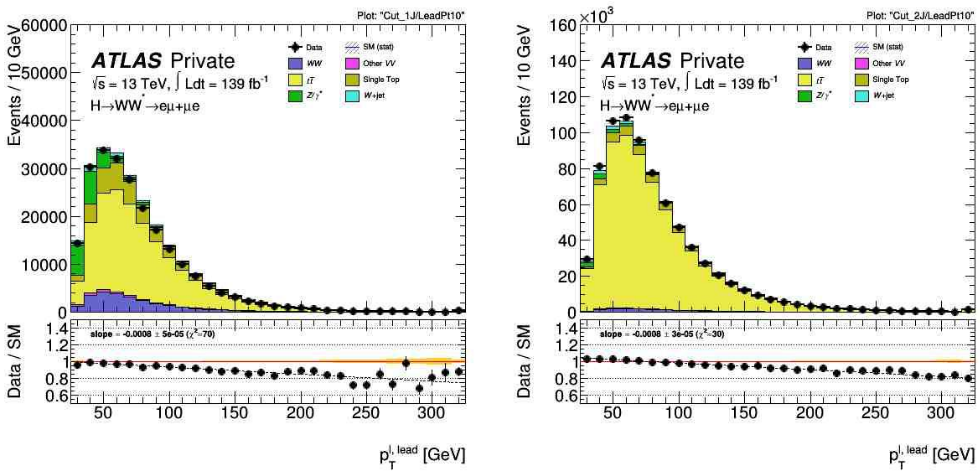

Figure 7.8: Data to MC comparison of the $p_T^{\ell,\text{lead}}$ distribution for the 1-jet (left) and 2+jet (right) bins at the preselection level. The hatched band in the upper pane and the shaded band in lower pane show the statistical uncertainties on the estimation. No normalization factors have been applied.

Because no kinematic dependence is shown for the $p_T^{\ell,\text{lead}}$ distribution mismodelling, the data-driven correction calculation is derived and applied to all top-quark originating events. In the previous 36 fb^{-1} analysis the uncertainty on this correction was the top-ranked systematic uncertainty in the ggF space, and the second ranked systematic uncertainty in the VBF space. However, this uncertainty is strongly conservative and, following the example of the $t\bar{t}$ cross section measurement analysis [42], no uncertainty is applied to this reweighting.

To validate not applying an uncertainty to the reweighting, a comparison is made between the data to MC modelling of the $p_T^{\ell,\text{lead}}$ distribution for the available alternative generators for the $t\bar{t}$ production. The different samples used are baseline Powheg+Pythia 8 sample, Herwig 7 sample, and MadGraph5_aMC@NLO sample. No alternative single top samples are used, as the contribution is much smaller than the $t\bar{t}$ background. As shown in Figure

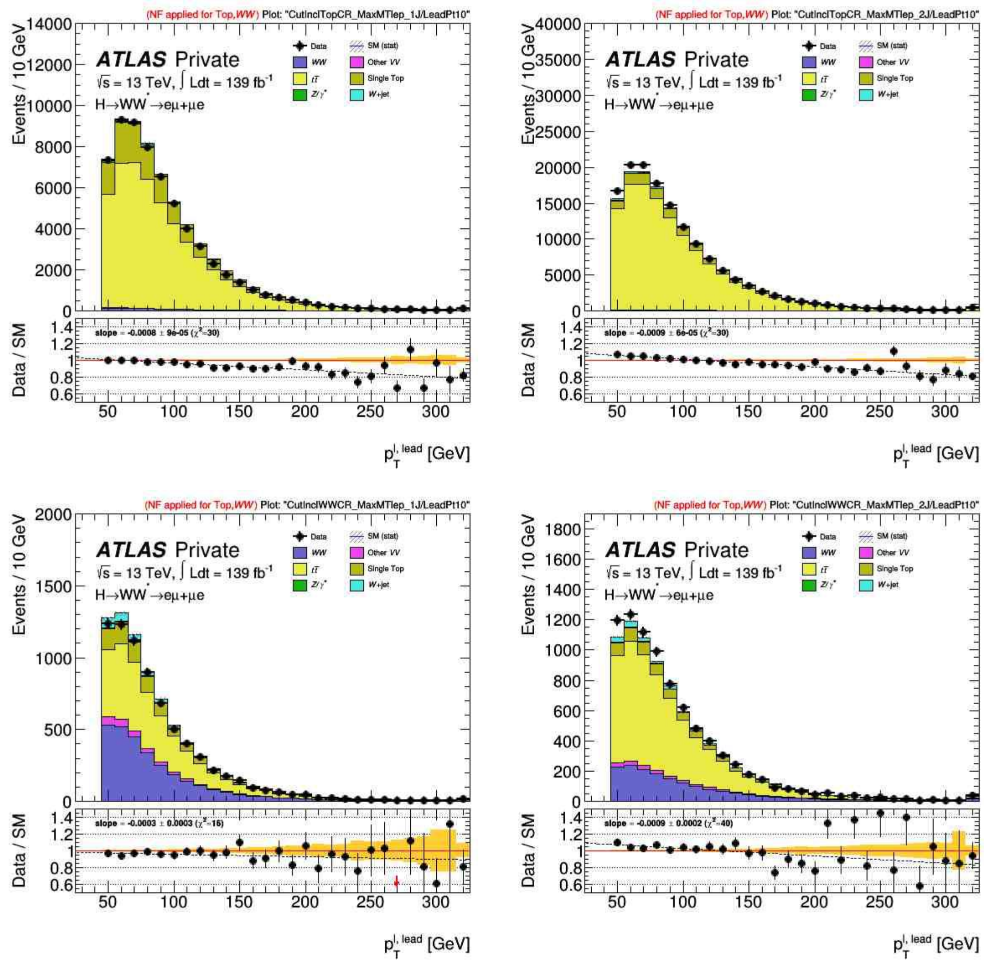

Figure 7.9: Data to MC comparison of the $p_T^{\ell,\text{lead}}$ distribution for the 1-jet (left) and 2+jet (right) bins in the ggF top control region (top) and ggF WW control region (bottom). The hatched band in the upper pane and the shaded band in lower pane show the statistical uncertainties on the estimation. No normalization factors have been applied.

7.10 no significant difference is seen between the baseline POWHEG+PYTHIA 8 sample and the HERWIG 7 sample in the top control regions. Only a small difference is observed between POWHEG+PYTHIA 8 and MADGRAPH5_aMC@NLO, but the mismodelling is still present for the MADGRAPH5_aMC@NLO sample. To further emphasize the similarities and need for the reweighting correction for all samples, the data-driven correction calculation is carried out for all $t\bar{t}$ generators in both the ggF and VBF top control regions. The results are shown in Figure 7.11, with no large differences observed.

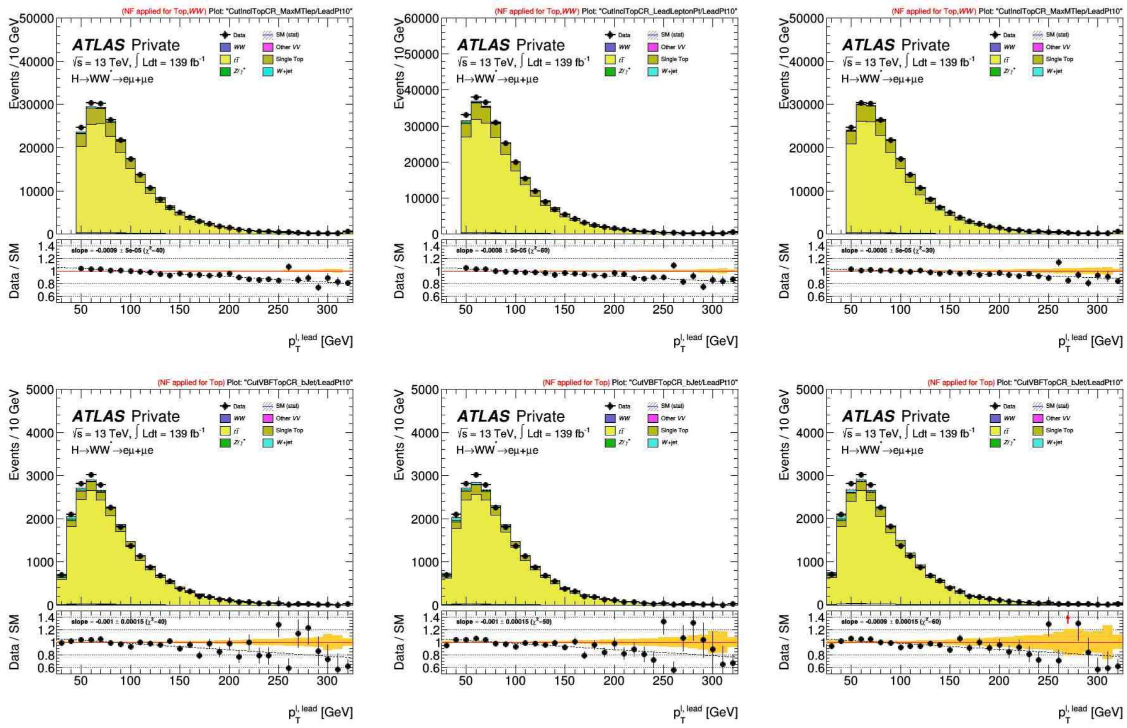

Figure 7.10: Data to MC comparison of the $p_T^{\ell,\mathrm{lead}}$ distribution in the ggF top control region (top) and VBF top control region (bottom). All three available $t\bar{t}$ generators are shown: baseline POWHEG+PYTHIA 8 (left), HERWIG 7 (middle), and MADGRAPH5_aMC@NLO (right). The hatched band in the upper pane and the shaded band in lower pane show the statistical uncertainties on the estimation. No normalization factors have been applied.

With no kinematic dependence observed and similar behavior shown between $t\bar{t}$ generators all further comparisons of data/MC modeling is made after applying the $p_T^{\ell,\mathrm{lead}}$ correction. The calculated values in the ggF and VBF top control regions are within the statistical uncertainty of the fits, so the ggF value is applied to all top-quark events due to the superior statistics in the region it was calculated. Finally, a small statistical uncertainty on the

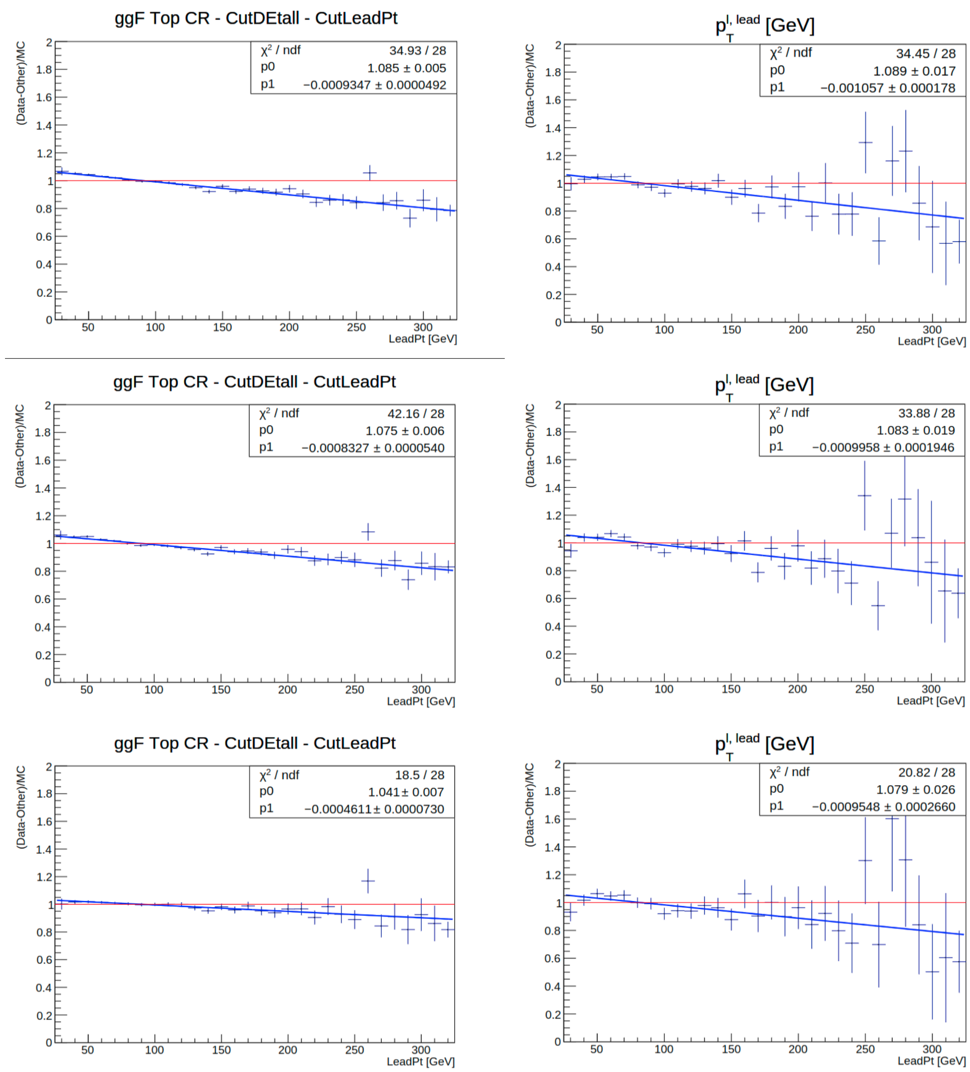

Figure 7.11: Data-driven calculation of the $p_T^{\ell,\text{lead}}$ correction in the ggF top control region with the $p_T^{\ell,\text{lead}}$ cut relaxed from 45 GeV to 25 GeV and the $|\Delta\eta_{\ell\ell}|$ cut removed (left) and VBF top control region (right). All three available $t\bar{t}$ generators are shown: baseline Powheg+Pythia 8 (top), Herwig 7 (middle), and MadGraph5_aMC@NLO (bottom). Uncertainty bars correspond to the statistical uncertainty in the corrected bin.

Pre-Selection			
Two Different Flavour, Opposite Sign Leptons, $p_T^{\ell} > 25$ GeV Third lepton veto, $p_T^{\ell} > 15$ GeV			
WW CR_{ggF}	Top CR_{ggF}	WW CR_{VBF1J}	Top CR_{VBF}
$N_{b-tag} = 0$	$N_{b-tag} = 1$	$N_{b-tag} = 0$	$N_{b-tag} \geq 1$
$\lvert\Delta\eta_{\ell\ell}\rvert > 1.8$	$\lvert\Delta\eta_{\ell\ell}\rvert < 1.8$	$(\lvert\Delta\eta_{\ell\ell} > 1.8$ or	$\lvert\Delta\eta_{\ell\ell}\rvert < 1.8$
$m_{\ell\ell} > 55$ GeV		10 GeV $< m_{\ell\ell} <$ 55 GeV)	$m_{\ell\ell} > 55$ GeV
$p_T^{\ell,\text{lead}} > 45$ GeV		–	$p_T^{\ell,\text{lead}} > 45$ GeV
$p_T^{\ell,\text{sublead}} > 30$ GeV		–	$p_T^{\ell,\text{sublead}} > 30$ GeV
$\max(m_T^W) > 50$ GeV		–	$\max(m_T^W) > 50$ GeV
METSigRatio > 0.8	–	–	
Excluding VBF1/2J phase space		VBF1J phase space	VBF1/2J phase space

Table 7.2: Summary of all the selections used in the ggF and VBF WW and top-quark control regions in the $H \to WW$ resonance search.

Campaign	p_0	p_1	$\frac{\chi^2}{\text{ndf}}$
MC16a	1.03 ± 9.31E-03	-3.43E-04 ± 9.16E-05	$\frac{18.06}{28}$
MC16d	1.04 ± 8.66E-03	-3.90E-04 ± 8.45E-05	$\frac{32.61}{28}$
MC16e	1.04 ± 7.60E-03	-4.53E-04 ± 7.40E-05	$\frac{24,64}{28}$
Full Run II	1.04 ± 4.87E-03	-3.97E-04 ± 4.76E-05	$\frac{21.61}{28}$

Table 7.3: Reweighting parameter values for the data-driven 1-dimensional fit for the correction on the $p_T^{\ell,\text{lead}}$ distribution for top-quark events for each individual MC campaign.

fitted parameters (0.5%) is observed, which is significantly smaller than the anticipated top modelling uncertainties, so it is reasonable to proceed without applying an uncertainty to the reweighting.

Figures 7.13, 7.14 shows the same distributions as Figures 7.3, 7.4 after the top-quark reweighting has been applied. Better data and MC agreement can be observed for all the distributions shown. Finally, in Figure 7.15 a comparison of the discriminating variable of the analysis, the transverse mass (m_T), is shown before and after the correction is applied in both the quasi-inclusive ggF and VBF Top CR.

7.2.3 WW Background

The WW CR for the ggF quasi-inclusive phase space uses the same selection cuts as the SR, with the reversal of the $\lvert\Delta\eta_{\ell\ell}\rvert$ cut to make the region orthogonal, and an additional cut

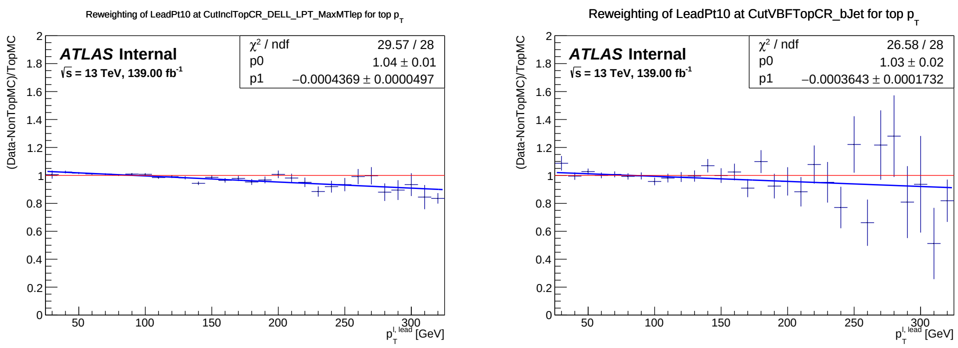

Figure 7.12: Fitted p_T correction for the leading lepton from top-quark background events in the ggF-like (left) and VBF-like (right) space. For the ggF-like space, the $p_T^{\ell,\text{lead}}$ cut has been relaxed from 45 GeV to 25 GeV and the $|\Delta\eta_{\ell\ell}|$ cut has been removed.

on the ratio of the E_T^{miss} Significance and E_T^{miss} (METSigRatio) to increase WW purity (see Chapter 6.2 for further details.) The cuts used in the region selection are shown in Table 7.2. The comparison of the data and the MC when removing one of the selection cuts at a time is shown in Figure 7.16. The normalization factor obtained from a simultaneous fit of top-quark and WW backgrounds in the ggF quasi-inclusive region is 1.11±0.02 (stat). The WW purity after the normalization is applied is 63.2%.

The WW CR for the 1-jet VBF phase space uses a loosened set of selection cuts compared with the SR (which is also shown in Table 7.2) in order to increase the statistics in the region. The comparison of data and MC when removing one of these cuts is shown in Figure 7.17. The normalization factor obtained from fitting the WW background in the 1-jet VBF WW CR is 1.08±0.05 (stat), where the uncertainty only includes the statistical contribution. The WW purity after the normalization is applied is 47.0%.

Figure 7.18 shows the m_T distributions in the ggF quasi-inclusive and 1-jet VBF WW CR. Normalization factors obtained from the top-quark CR as well as from the WW CR have been applied, along with the top $p_T^{\ell,\text{lead}}$ reweighting.

For the 2+ jet VBF phase space, the WW contribution is much smaller than in the other two regions. Because of the difficulty to isolate a kinematic region with high WW purity in this space, the prediction is taken from simulation.

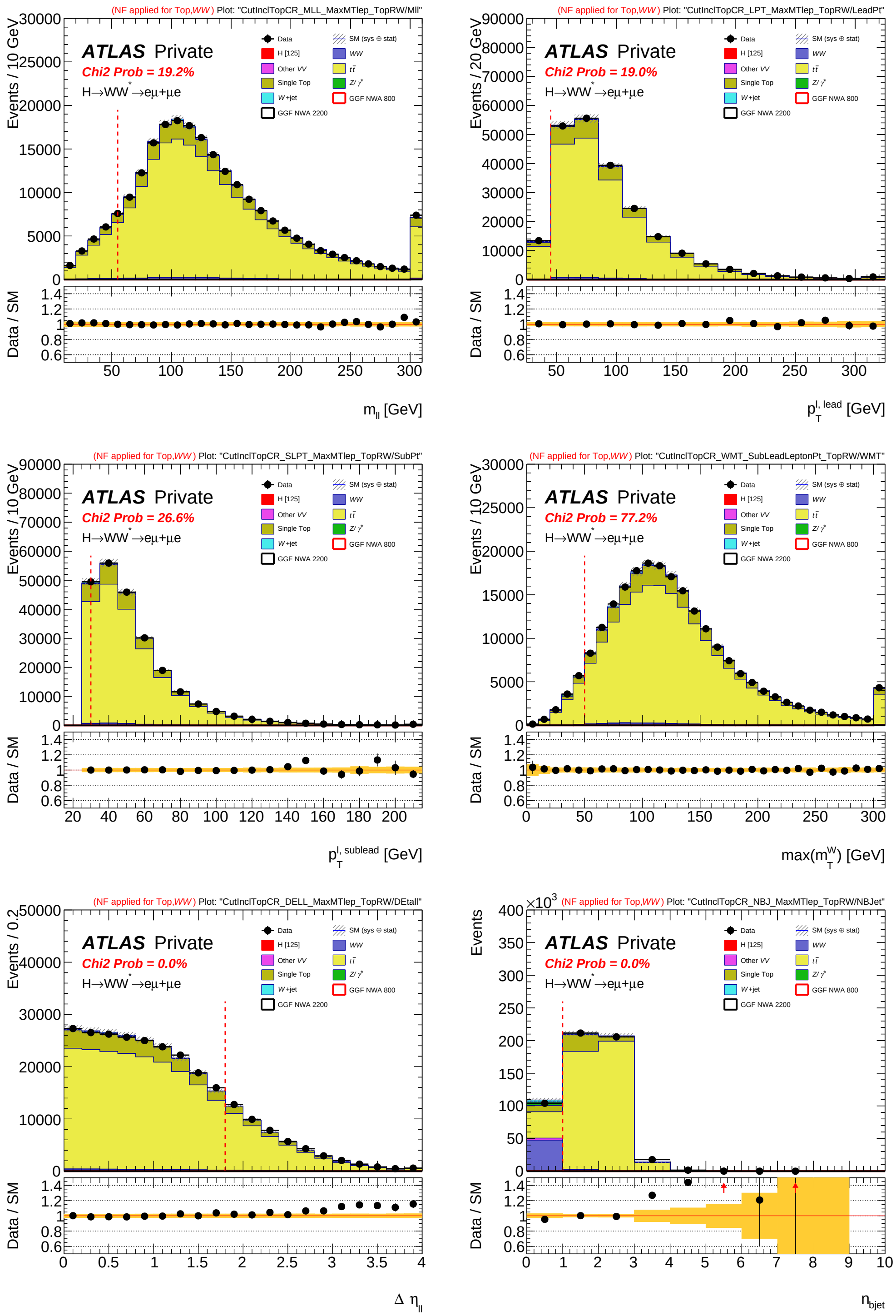

Figure 7.13: Comparison of data and MC in the ggF top-quark CR when one of these cuts is removed from the selection for the variables: $m_{\ell\ell}$ (top left), $p_T^{\ell,\text{lead}}$ (top right), $p_T^{\ell,\text{sublead}}$ (middle left), $\max(m_T^W)$ (middle right), $|\Delta\eta_{\ell\ell}|$ (bottom left), N_{b-jet} (bottom right). The hatched band in the upper pane and the shaded band in lower pane show the combined statistical and experimental uncertainties on the predictions. The last bin contains the overflow. Normalization factors obtained from a comparison of data and MC have been applied for the top-quark and WW background. The reweighting for top-quark events has been applied. The red dashed vertical line indicates the cut value used in the region selection.

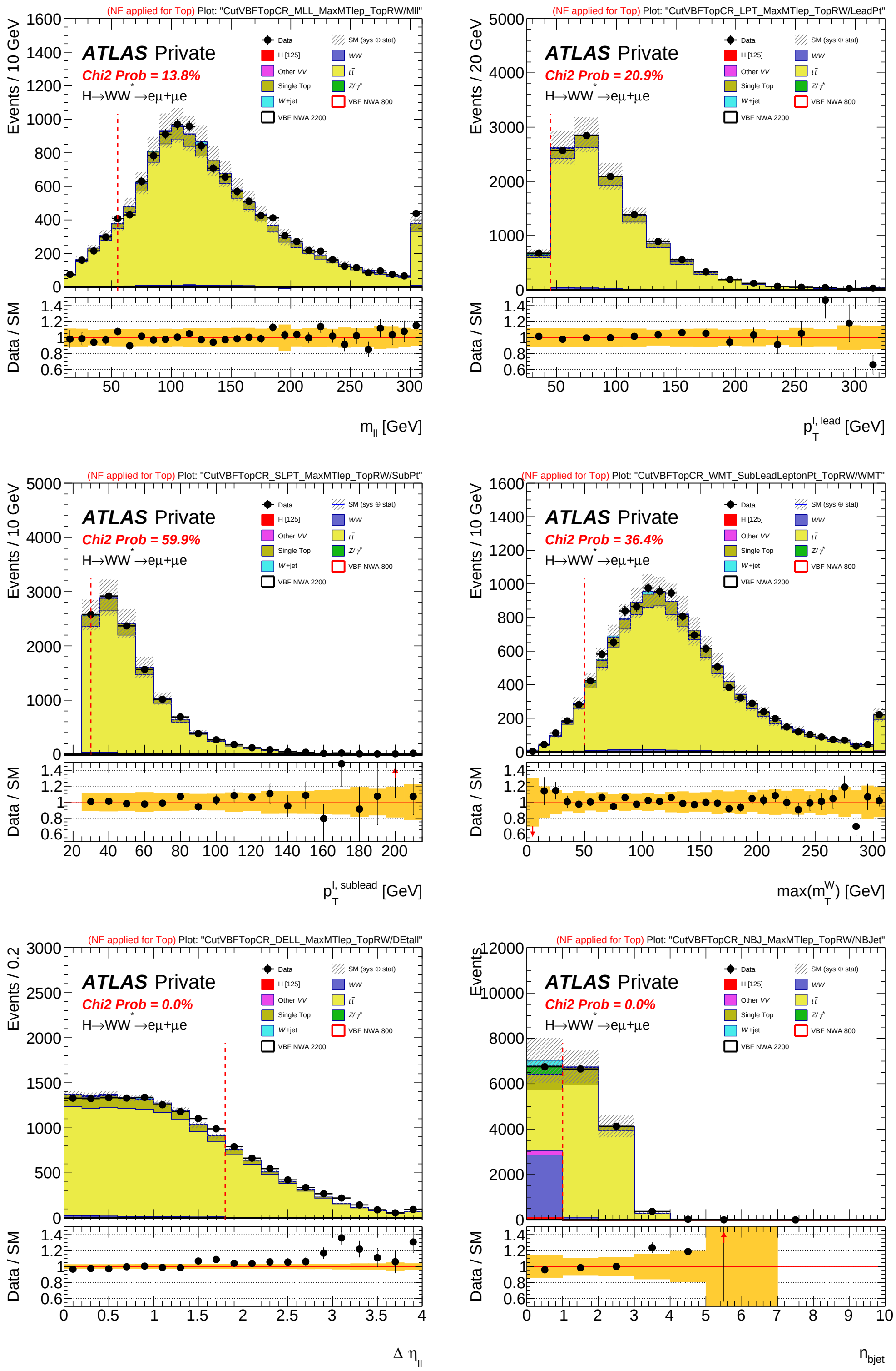

Figure 7.14: Comparison of data and MC in the VBF top-quark CR when one of these cuts is removed from the selection for the variables: $m_{\ell\ell}$ (top left), $p_T^{\ell,\mathrm{lead}}$ (top right), $p_T^{\ell,\mathrm{sublead}}$ (middle left), $\max(m_T^W)$ (middle right), $|\Delta\eta_{\ell\ell}|$ (bottom left), N_{b-jet} (bottom right). The hatched band in the upper pane and the shaded band in lower pane show the combined statistical and experimental uncertainties on the predictions. The last bin contains the overflow. Normalization factors obtained from a comparison of data and MC have been applied for the top-quark and WW background. The reweighting for top-quark events has been applied. The red dashed vertical line indicates the cut value used in the region selection.

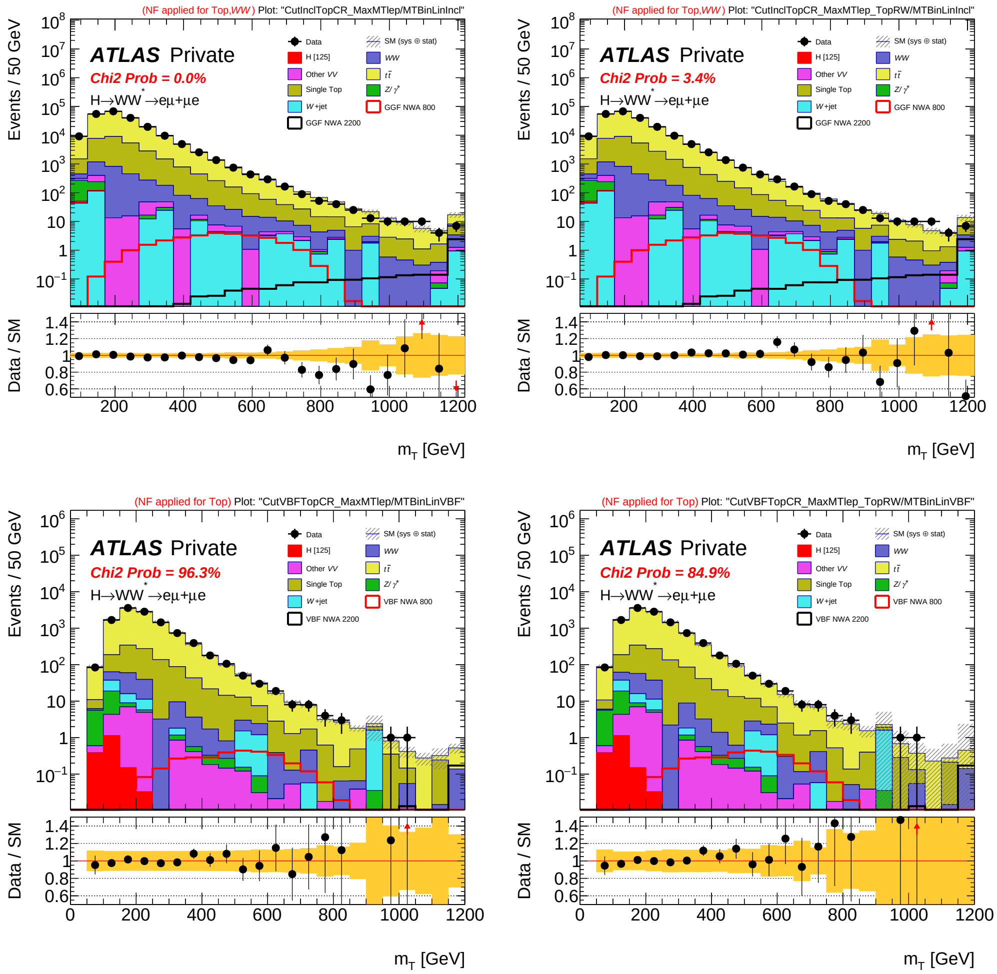

Figure 7.15: Comparison of the m_T distributions in the top CR for the ggF (top) and VBF (bottom) phase space before (left) and after (right) the reweighting of the top $p_T^{\ell,\text{lead}}$ distribution.

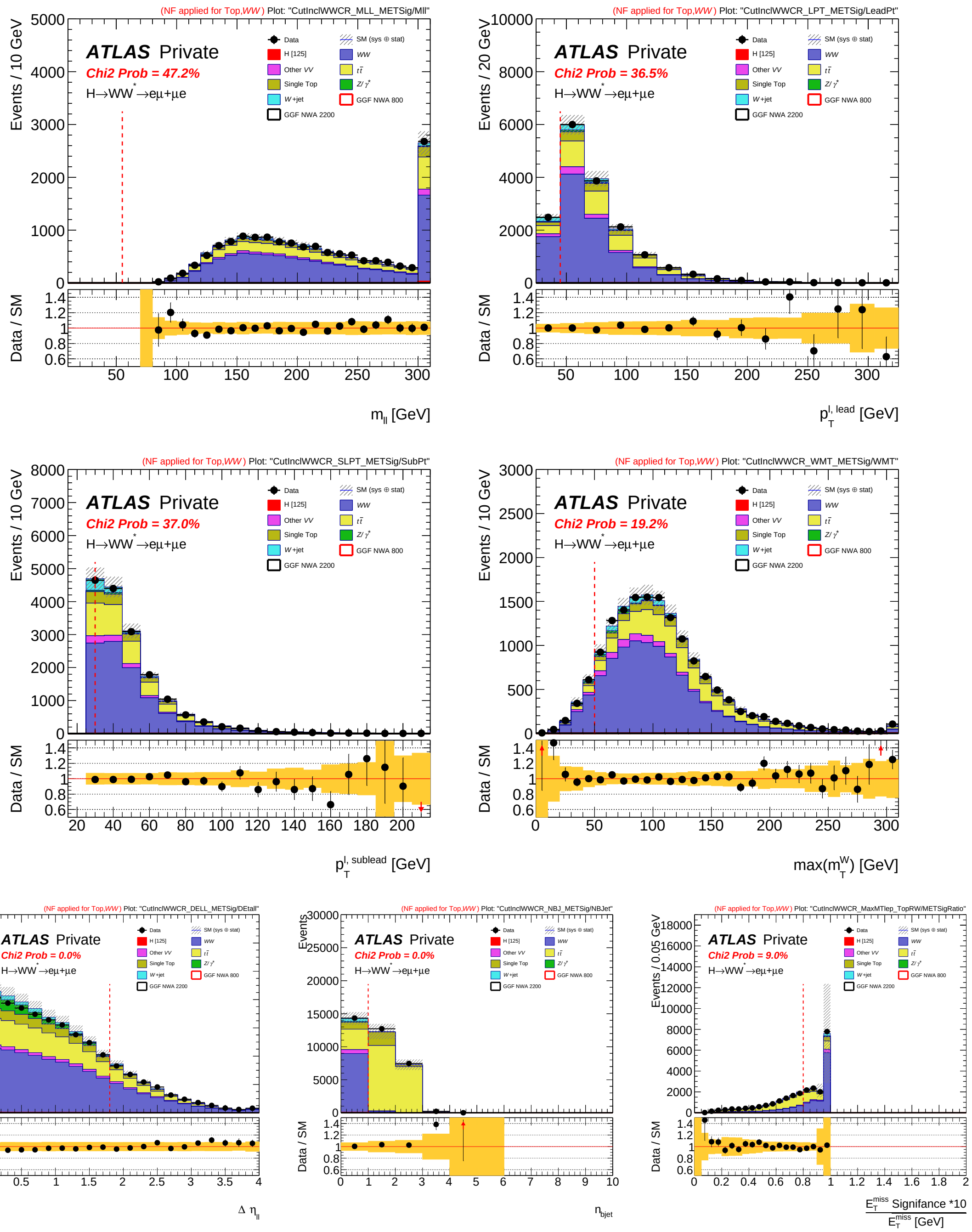

Figure 7.16: Comparison of data and MC in the ggF WW CR when one of these cuts is removed from the selection for the variables: $m_{\ell\ell}$ (top left), $p_T^{\ell,\text{lead}}$ (top right), $p_T^{\ell,\text{sublead}}$ (middle left), $\max(m_T^W)$ (middle right), $|\Delta\eta_{\ell\ell}|$ (bottom left), N_{b-jet} (bottom middle), and METSigRatio (bottom right). The hatched band in the upper pane and the shaded band in lower pane show the combined statistical and experimental uncertainties on the predictions. The last bin contains the overflow. Normalization factors obtained from a comparison of data and MC have been applied for the top-quark and WW background. The reweighting for top-quark events has been applied. The red dashed vertical line indicates the cut value used in the region selection.

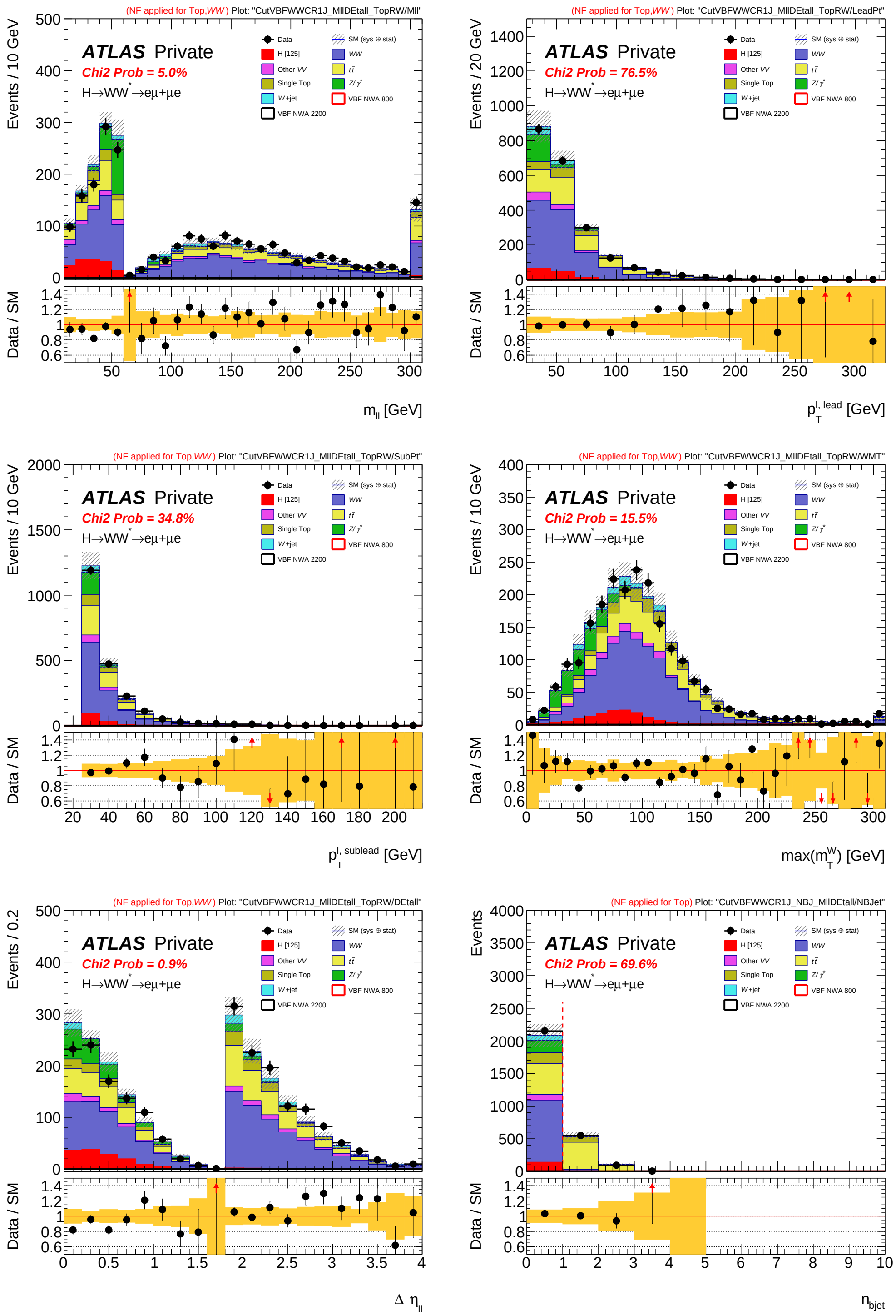

Figure 7.17: Comparison of data and MC in $N_{jet} = 1$ VBF WW control region with one of the cuts on the selected distribution is removed: $m_{\ell\ell}$ (top left), $p_T^{\ell,\text{lead}}$ (top right), $p_T^{\ell,\text{sublead}}$ (middle left), $\max(m_T^W)$ (middle right), $|\Delta\eta_{\ell\ell}|$ (bottom left), N_{b-jet} (bottom right). The hatched band in the upper pane and the shaded band in lower pane show the combined statistical and experimental uncertainties on the predictions. The last bin contains the overflow. Normalization factors obtained from a comparison of data and MC have been applied for the top-quark and WW background. The reweighting for top-quark events has been applied. The red dashed vertical line indicates the cut value used in the region selection.

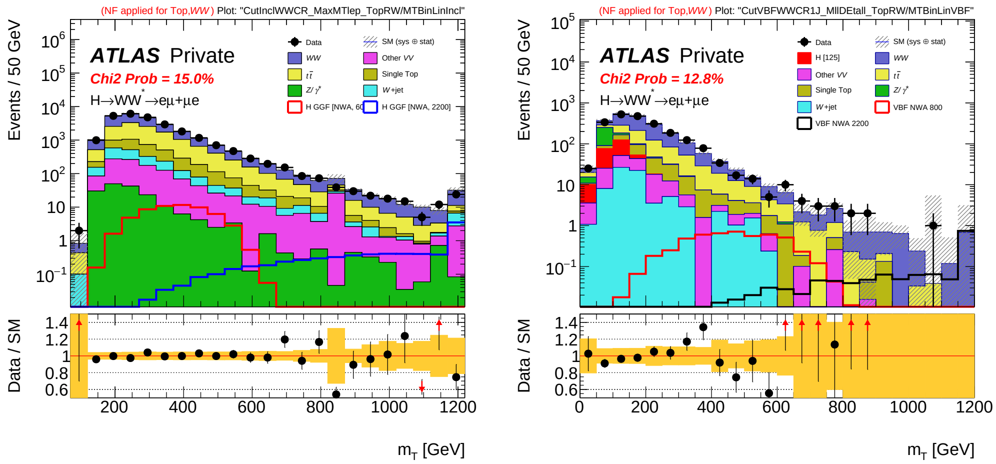

Figure 7.18: Comparison of data and MC in ggF WW CR (left) and $N_{jet} = 1$ VBF WW CR (right) of the m_T distribution. The hatched band in the upper pane and the shaded band in lower pane show the combined statistical and experimental uncertainties on the predictions. The last bin contains the overflow. Normalization factors obtained from a comparison of data and MC have been applied for the top-quark and WW background. The reweighting for top-quark events has been applied. The red dashed vertical line indicates the cut value used in the region selection.

7.2.4 Non-Prompt Background Estimate

The analysis also has some small contribution from non-prompt (fake) backgrounds, primarily coming from W+jets decays where one of the jets in the event is mis-identified as an electron or muon, or when a non-prompt lepton is produced in the jet evolution. These backgrounds are difficult to model correctly in simulations, so they are estimated with a data-driven fake factor method.

The number of events with misidentified leptons is estimated in a control selection where one or two leptons do not meet the lepton identification criteria but instead satisfy a looser set of criteria designed to select fake leptons. These criteria are called identified[3] (ID) and anti-identified (Anti-ID) and are listed in Table 7.4. The control region is optimized to be fairly pure in fake events, allowing it to be used to estimate the fake events in the signal region by applying an additional extrapolation factor F.

A mathematical derivation can be found in Ref. [70]. In the following equations of this

[3] The ID criteria of leptons in the fakes estimate matches the lepton identification criteria discussed in Sections 5.2 and 5.3

<table>
<tr><th colspan="2">Electron</th><th colspan="2">Muon</th></tr>
<tr><th>identified</th><th>anti-identified</th><th>identified</th><th>anti-identified</th></tr>
<tr><td colspan="2">p_T >25 GeV</td><td colspan="2">p_T >25 GeV</td></tr>
<tr><td colspan="2">$|\eta| < 2.47$,excluding $1.37 < |\eta| < 1.52$</td><td colspan="2">$|\eta| < 2.5$</td></tr>
<tr><td colspan="2">$|z_0 \sin\theta| < 0.5$ mm</td><td colspan="2">$|z_0 \sin\theta| < 0.5$ mm</td></tr>
<tr><td colspan="2">$|d_0|/\sigma(d_0) < 5$</td><td>$|d_0|/\sigma(d_0) < 3$</td><td>$|d_0|/\sigma(d_0) < 15$</td></tr>
<tr><td>Pass LHMedium
Pass FCTight
isolation</td><td>Pass LHLoose</td><td>Pass Quality Tight
Pass FCTight
isolation</td><td>Pass Quality Medium</td></tr>
<tr><td colspan="2">AUTHOR = 1</td><td></td><td></td></tr>
<tr><td></td><td>Veto against
identified electron</td><td></td><td>Veto against
identified muon</td></tr>
</table>

Table 7.4: Requirements for fully identified and anti-identified leptons.

section, the ID and Anti-ID selectons are denoted with a superscript "i" or "a". Using this definition the number of fakes in the ID-ID region[4] can be written as

$$N^{\mathrm{i,i}}_{>0\ \mathrm{fakes}} = F_2(N^{\mathrm{i,a}} - N^{\mathrm{i,a}}_{2\ \mathrm{prompt}}) + F_1(N^{\mathrm{a,i}} - N^{\mathrm{a,i}}_{2\ \mathrm{prompt}}) - F_1F_2(N^{\mathrm{a,a}} - N^{\mathrm{a,a}}_{2\ \mathrm{prompt}}). \quad (7.2)$$

Each variable N refers to a number of events. The superscripts indicate how each lepton is identified while the subscripts specify how many of these leptons are prompt leptons (i.e. non-fake). If no subscript is given, no selection based on truth information is applied. F_1 and F_2 are the fake factors for the first and second lepton (using the same ordering as the superscripts). On the right-hand side of equation (7.2), the event yields without index are measured in data. The number of events with 2 prompt leptons is sometimes and is simulated with MC. Because this term is subtracted, and is primarily composed of electroweak backgrounds, it is commonly referred to as electroweak subtraction. The first two terms in the sum estimate the contribution of single-fake events and the rightmost term, which has two fake factors applied, constitutes a correction due to the overcounting of double-fake events.

The fake factors F_1 and F_2 are applied independently for the two leptons. They are

[4]The ID-ID region refers to the space where both leptons in the event are identified. For this analysis this refers to the signal and control regions.

computed as functions of p_T and η of the lepton as they show significant dependency on the lepton topology. For this analysis, the fake factors are measured in a three-lepton selection targeting a leptonic Z-boson decay with an additional fake lepton. The fake factors are assumed to only have dependence on basic lepton kinematics, therefore allowing distributions of composite observables (such as m_T) of the fake events to be directly estimated from the control sample. An examination of the statistics and modelling of the different fake kinematics is made, with the statistics shown in Table 7.5, the m_T distributions of the fake-containing event in each of the SR shown in Figure 7.19, and the p_T distribution of the fake leptons shown in Figure 7.20.

$\sqrt{s}=13$ TeV, $\mathcal{L}=139\text{fb}^{-1}$		total bkg	Data	fakes	fake purity(%)
	Incl. SR	11005.42 ± 128.71	20548	9542.58 ± 192.65	46.44 ± 0.99
(eFakes)	VBF SR 1J	573.94 ± 37.46	936	362.06 ± 48.37	38.68 ± 5.32
	VBF SR 2J	267.51 ± 8.15	383	115.49 ± 21.20	30.15 ± 5.75
	Incl. SR	14258.99 ± 66.12	31126	16867.01 ± 188.41	54.19 ± 0.68
(mFakes)	VBF SR 1J	803.51 ± 17.33	1626	822.49 ± 43.89	50.58 ± 2.98
	VBF SR 2J	410.96 ± 7.65	601	190.04 ± 25.68	31.62 ± 4.46

Table 7.5: Fake estimation and purity in the control sample for the three signal regions for fake electrons and muons. Each entry corresponds to one subplot in Figure 7.19. The numbers are quoted as integrated over all bins. "Total bkg" refers to the MC yield. The fake yield is calculated as the difference between data and the total bkg. All uncertainties are statistical.

The fake factor method is built on the assumption that the fake lepton efficiency is independent of the remainder of the event[5]. With this assumption, the fake factor can be estimated in a three-lepton selection, where two leptons come from a Z-boson decay and the additional lepton is a fake candidate, and the validity of the estimate is conserved when moving to a two-lepton selection. The fake factor is measured as a ratio of events in the 3-lepton selection

$$F = \frac{N^{\text{i,i,i}} - N^{\text{i,i,i}}_{\text{non-}Z\text{+jets}}}{N^{\text{i,i,a}} - N^{\text{i,i,a}}_{\text{non-}Z\text{+jets}}}, \tag{7.3}$$

When being applied to equation (7.2), the terms with one Anti-ID lepton cancel out and the

[5]Because the lepton reconstruction only takes information from a small region in the detector, this is a reasonable assumption.

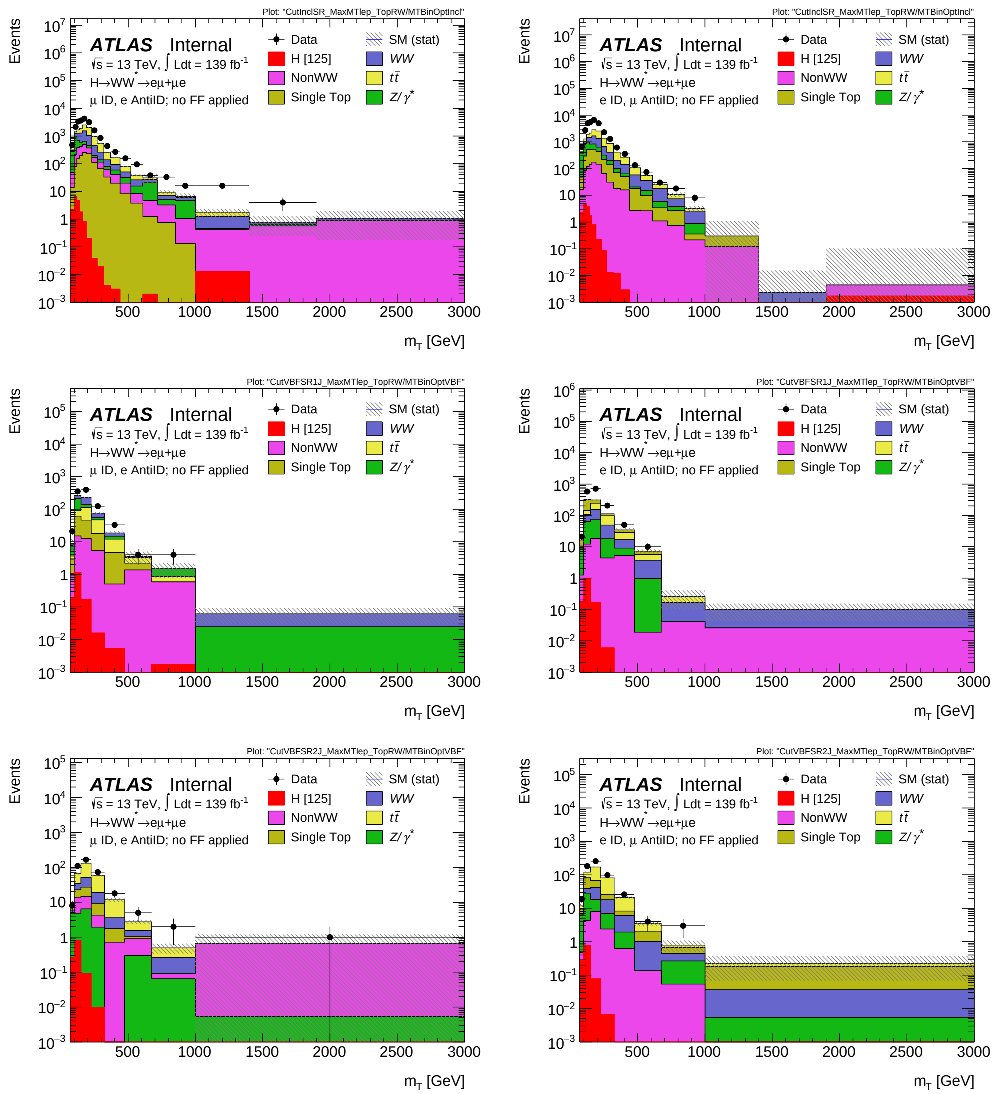

Figure 7.19: Transverse mass distributions in the control sample for electrons (left) and muons (right) in different signal regions (from top to bottom: Incl. SR, VBF SR 1J, VBF SR 2j). No fake factor is applied.

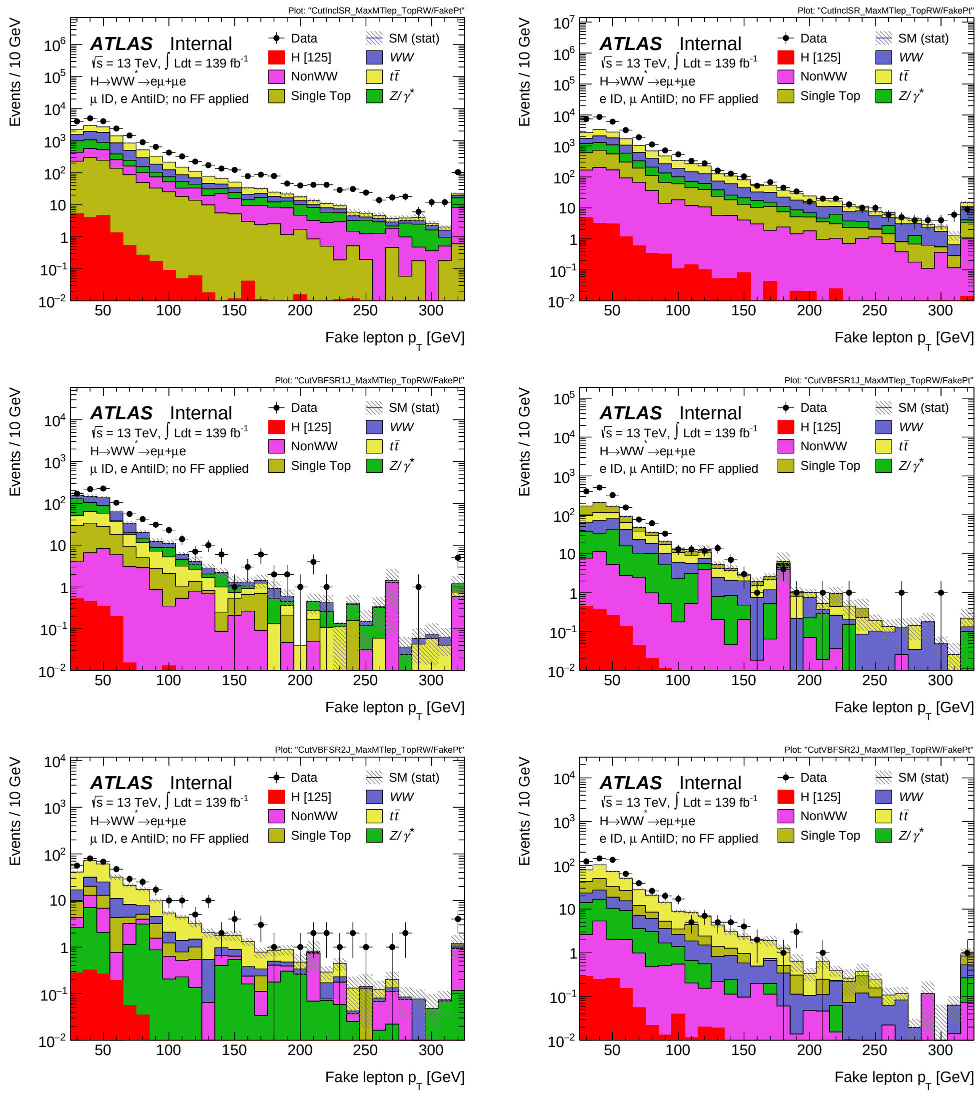

Figure 7.20: Fake lepton p_T distributions in the control sample for electrons (left) and muons (right) in different signal regions (from top to bottom: Incl. SR, VBF SR 1J, VBF SR 2j). No fake factor is applied.

yield with only ID leptons remains in the numerator.

Before equation 7.3 can be used, an analysis region has to be defined, which is sufficiently pure in Z+fake lepton. Events with three leptons with $p_T > 15$ GeV are considered. Two same flavor, oppositely charge leptons residing, for electrons, in an invariant-mass window of [80, 110] GeV, and for muons, in a window of [70, 110] GeV, are required to identify the Z boson in the event. They are identified with the same criteria as ID criteria in Table 7.4 with the exception that they only need to pass FCLoose isolation and a "loose-with-b-layer" electron or "medium" muon quality working point, allowing for an increase in statistics in Z+fake lepton region. Additionally, if at least one of the two leptons is matched to an object firing the single-lepton trigger, the leptons are accepted as Z-boson candidates. If multiple lepton combinations satisfy this requirement, the pair with the invariant mass closest to the Z boson is chosen. The remaining lepton in the event is the fake candidate. When applied to a Z+jets MC sample, this algorithm correctly assigns leptons to the Z boson in about 99% of all cases. The reconstructed Z-boson peak can be seen in Figure 7.21. To reject events with leptonic WZ decays, a cut on $m_T^W < 50$ GeV is applied. The pseudo-rapidity of the fake candidate is restricted to $|\eta| < 2.5$ for muons and $|\eta| < 2.47$ for electrons, which corresponds to the lepton acceptance region in the main analysis. Then, for each fake lepton type, electron and muon, two regions are constructed depending on whether the fake lepton passes the ID or Anti-ID cuts. The region above a m_T^W of 50 GeV, where the fake candidate is required to pass the ID criteria, is used as a control region for the WZ process. The region is very pure and a normalization factor of 0.99 ± 0.01 is extracted.

The fake factors commonly depend on lepton properties, such as lepton p_T and η. This can be exhibited in the lepton p_T distributions shown in Figure 7.22. Therefore, the fake factors are calculated in bins of p_T and η of the fake lepton, except in the case for the electrons where agreement between η bins was seen. Additional uncertainty on the fake factor calculation comes from the theoretical uncertainty on the EW background in the Z+fake lepton region. The electroweak subtraction uncertainty is calculated by taking theoretical variations on the

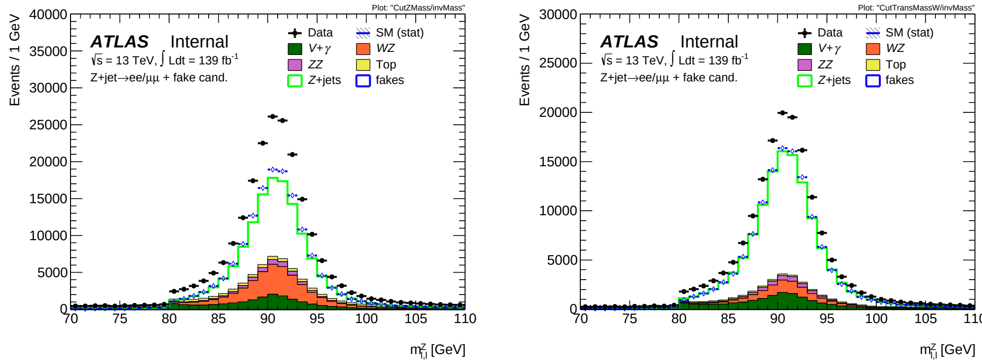

Figure 7.21: Distributions of the invariant mass of the reconstructed Z-boson candidate. The shape of the distribution agrees nicely between data and MC (compare the blue data points and the green MC estimate). At the stage of Z-boson identification, the normalization disagrees slightly. After applying a cut on the transverse mass $m_T^W < 50$ GeV the normalization agrees nicely. Normalization factors are not applied. The stacked histograms are background MC processes not including Z+fake. The measured data is shown in black datapoints. The blue datapoints are the data-driven Z+fake estimate. They are calculated by taking the difference between data and the stacked MC processes. They can be compared to the green Z+jets MC, which is not stacked on top of the other MC processes. The agreement between data and MC is seen by comparing the blue fake estimate to the green Z+jets MC.

major SM backgrounds (WZ, ZZ, and $Z+\gamma$) in the ID region only, as the Anti-ID region is quite pure in fakes and is not significantly impacted by variations in the background. The quantification of this uncertainty on the fake factor is shown alongside the nominal fake facotrs in Figure 7.23.

The fake factor method described so far implicitly assumes that the fake rates for identified and anti-identified leptons are identical in the Z+jets sample in which the fake factors are derived and the W+jets sample to which they are applied. An additional correction must be applied due to the fake lepton compositional difference observed between fakes coming from Z+jets decays (where we estimate the fake-factor) and W+jets decays (where we apply the fake-factor), which can be observed using the MC truth information shown in Figures 7.24 and 7.25. To account for potential sample dependence of the fake factor due to characteristics like jet flavor, a so-called *correction factor* is derived. The correction factor is used to scale the fake factor derived in the Z+jets sample, f_Z, to give the expected fake factor in a W+jets sample, f_W. It is derived by calculating the fake factors in W+jets and Z+jets

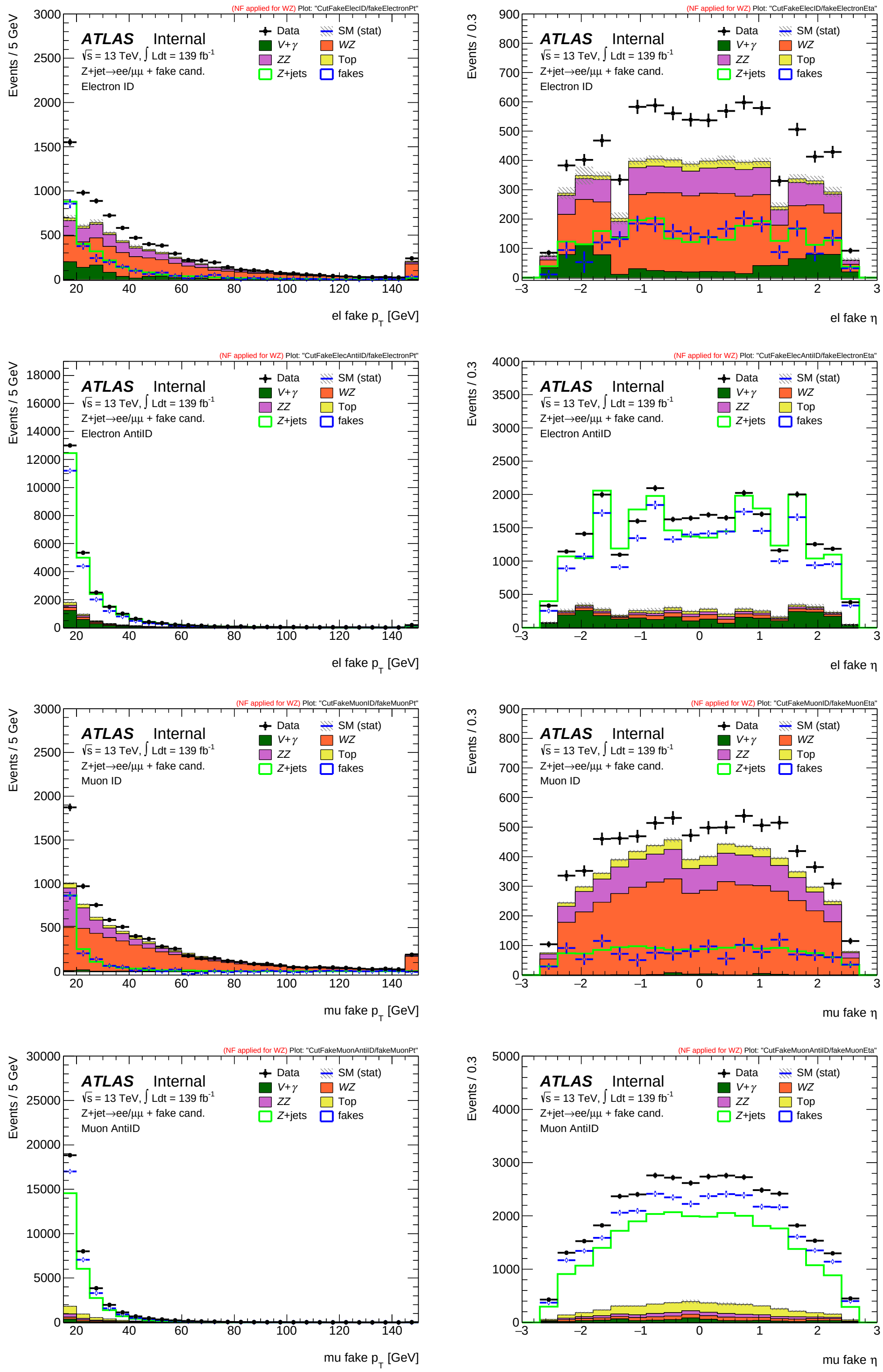

Figure 7.22: Kinematic distributions of the fake candidate. The top four plots are electron fake candidates and the bottom four muon fakes. Between these four plots, the top two show the ID selection and the bottom two show the Anti-ID selection. The transverse momentum is shown on the left and the pseudo-rapidity on the right side. A normalization factor of 0.993 is applied for WZ events.

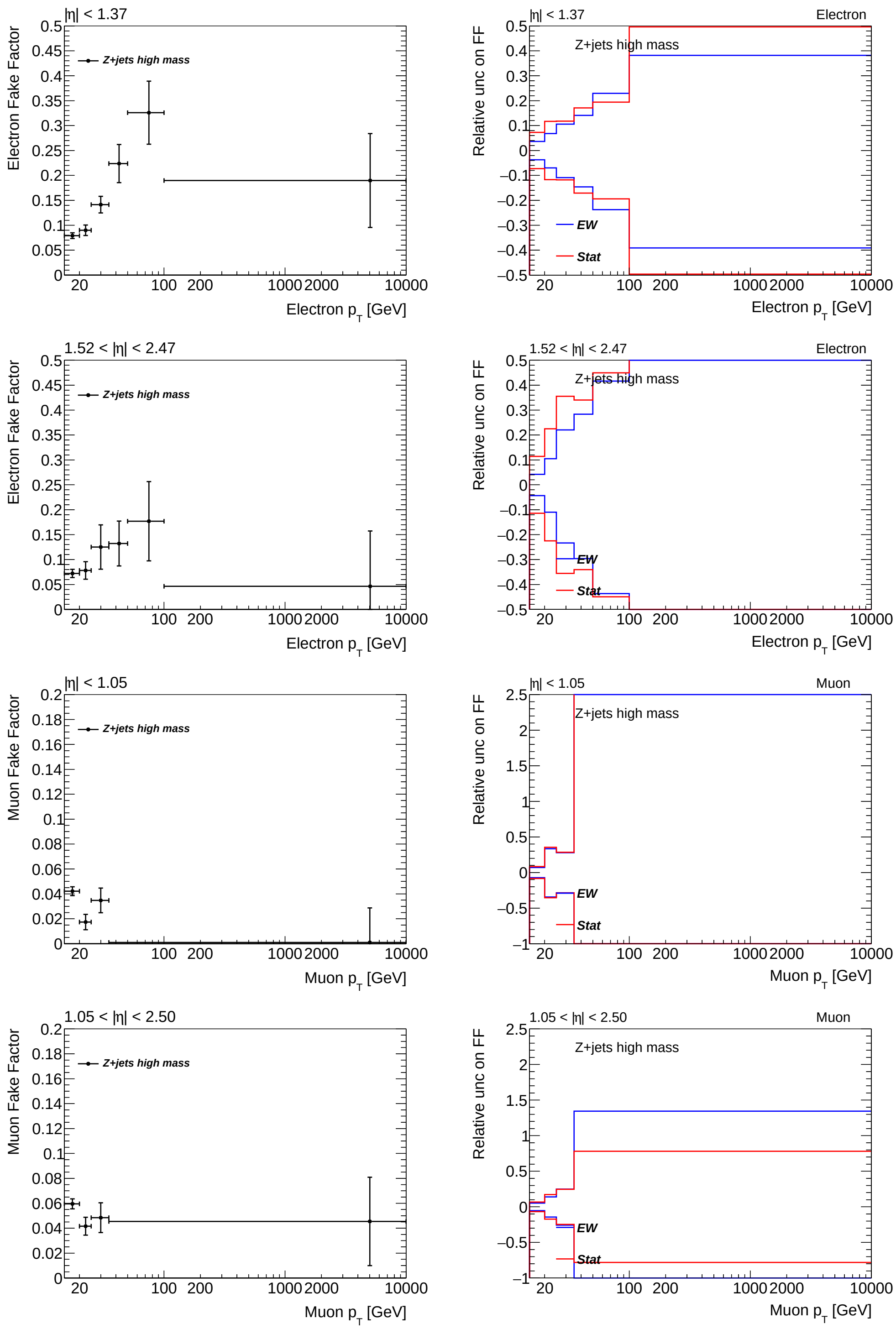

Figure 7.23: Fake factors derived in the three-lepton selection. The top four plots show the fake factor (left) and its relative uncertainties (right) for electrons, the bottom four for muons. Within each set of four plots, the top two plots show the muon fake factors in the low-η region and the bottom two plots the same in the high-η region. The relative uncertainty exceeds the scale, where the nominal fake factor is small. The values are also listed in Table 7.6

.

Monte Carlo simulations and taking the ratio,

$$CF = \frac{f^{\text{MC}}_{W+\text{jets}}}{f^{\text{MC}}_{Z+\text{jets}}} \tag{7.4}$$

The nominal correction factors are evaluated in samples generated with Powheg because it was found to have the best statistical precision. Since the sample flavor composition - and therefore the correction factor - can depend on the Monte Carlo generator, correction factors are also produced for samples generated with MadGraph5_aMC@NLO, and comparison with this alternate generator is used to assign the systematic uncertainty on the correction factor.

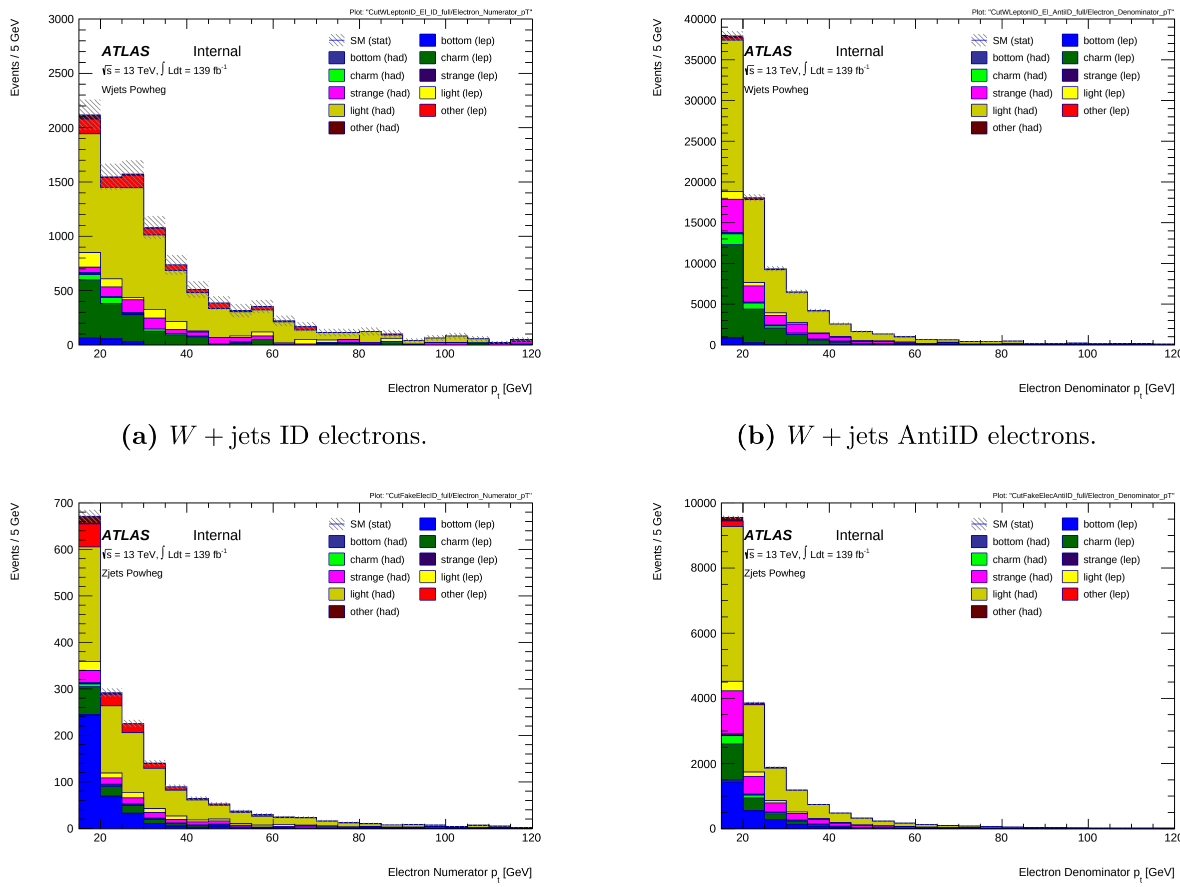

(a) $W+$jets ID electrons.

(b) $W+$jets AntiID electrons.

(c) $Z+$jets ID electrons.

(d) $Z+$jets AntiID electrons.

Figure 7.24: Flavor composition distributions of fake electrons in $W+$jets and $Z+$jets V21 Powheg MC.

The correction factors are produced in two bins from 25-35 GeV and above 35 GeV. The

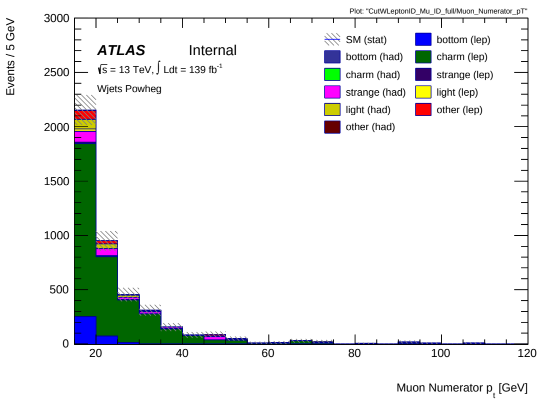

(a) $W+$jets ID muons.

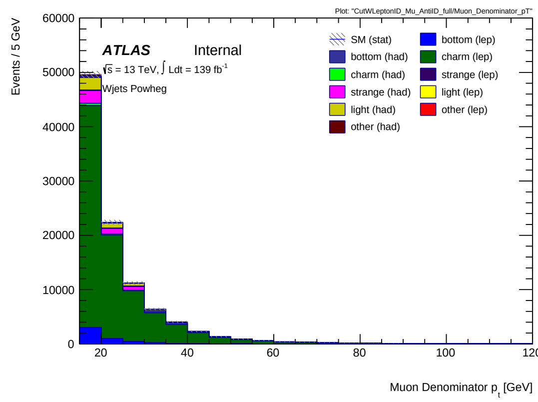

(b) $W+$jets AntiID muons.

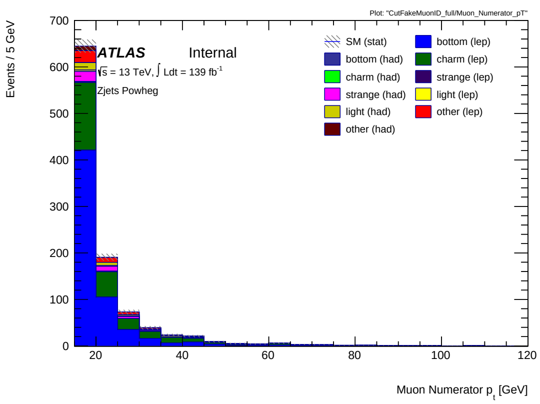

(c) $Z+$jets ID muons.

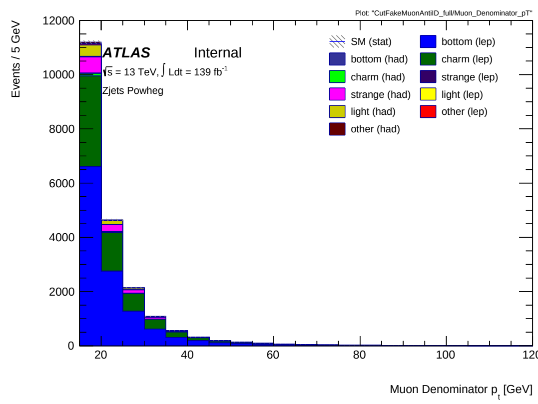

(d) $Z+$jets AntiID muons.

Figure 7.25: Flavor distributions of fake muons in $W+$jets and $Z+$jets V21 Powheg MC.

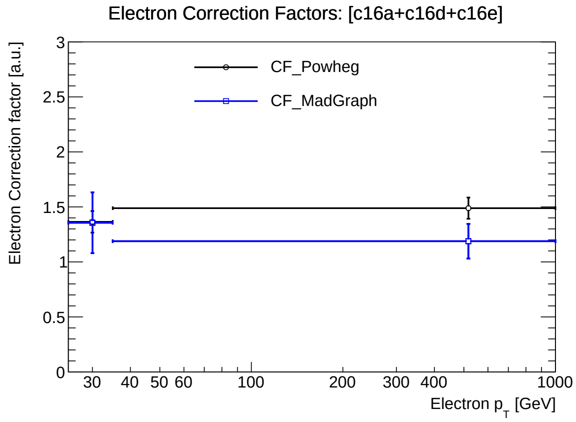

(a) Electron CF.

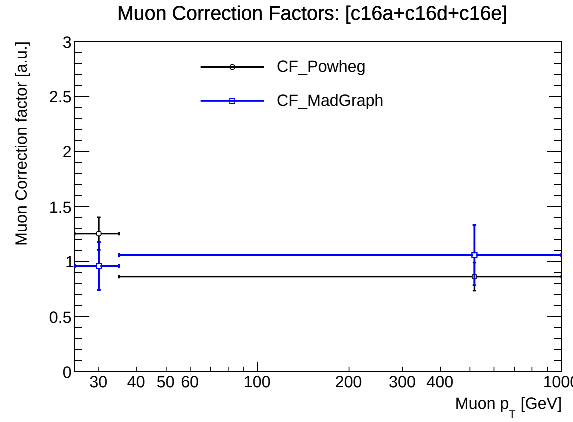

(b) Muon CF.

Figure 7.26: CFs derived in samples generated with POWHEG and MADGRAPH5_aMC@NLO. Uncertainties are statistical only.

correction factors above 35 GeV were found to be consistent, and this approach reduces the effect of statistical uncertainty in the highest p_T bins. The η dependence of the correction factors was also investigated and was found to be negligible, so the correction factors are produced inclusively in η. Distributions of the nominal correction factors are shown overlaid with the correction factors derived in the alternate generator MADGRAPH5_aMC@NLO in Figure 7.26.

A final correction to the fake factor method is necessary to account for the case where the Anti-ID lepton passes the Anti-ID criteria, but does not pass the criteria to fire the trigger (as the trigger criteria is tighter than the Anti-ID criteria), which results in the event not being recorded. Separate "triggered" fake factors are derived to account for this. To bias the anti-ID lepton selection during the fake-factor extraction in the same way as in the nominal analysis, the Anti-ID lepton is required to fire the trigger. Because this requirement reduces the statistics in the Z+jets selection significantly, triggered fake factors F^{T} are estimated in a dijets selection, using the definition

$$F^{\mathrm{T}} = \frac{N_{\mathrm{i}}}{N_{\mathrm{a^T}}} \tag{7.5}$$

where the superscript T indicates that a lepton fired the trigger. The triggered fake factors are then applied to events in which the Anti-ID lepton fires the trigger, while the nominal fake factors are applied to other events, yielding an unbiased estimate of the total fakes yield. The total yield can then be written as:

$$N^{\mathrm{i,i}} = F(N^{\mathrm{i^T,a^T}} + N^{\mathrm{i^T,a^{!T}}}) + F^{\mathrm{T}} N^{\mathrm{i^{!T},a^T}} \tag{7.6}$$

After all the corrections have been calculated, they are applied individually to events based on the p_T and η requirements of the fake leptons as described. A full overview of the nominal fake factor calculations and its associated uncertainty is given in Table 7.6.

7.3 Comparison of Data and Background Predictions in Signal Regions

This section describes the modelling of numerous kinematics for each of the three signal regions. Figure 7.27 shows the modelling of the major backgrounds and also selected NWA mass points in the ggF quasi-inclusive signal region. Figures 7.28 and 7.29 show a similar modelling of the major backgrounds and selected NWA mass points in the VBF 1-jet and VBF 2+ jet signal regions, respectively. The m_T distributions to be used in the statistical analysis are shown for each of the three signal regions in Figure 7.30. Table 7.8 shows the entire cutflow for each of the three signal regions.

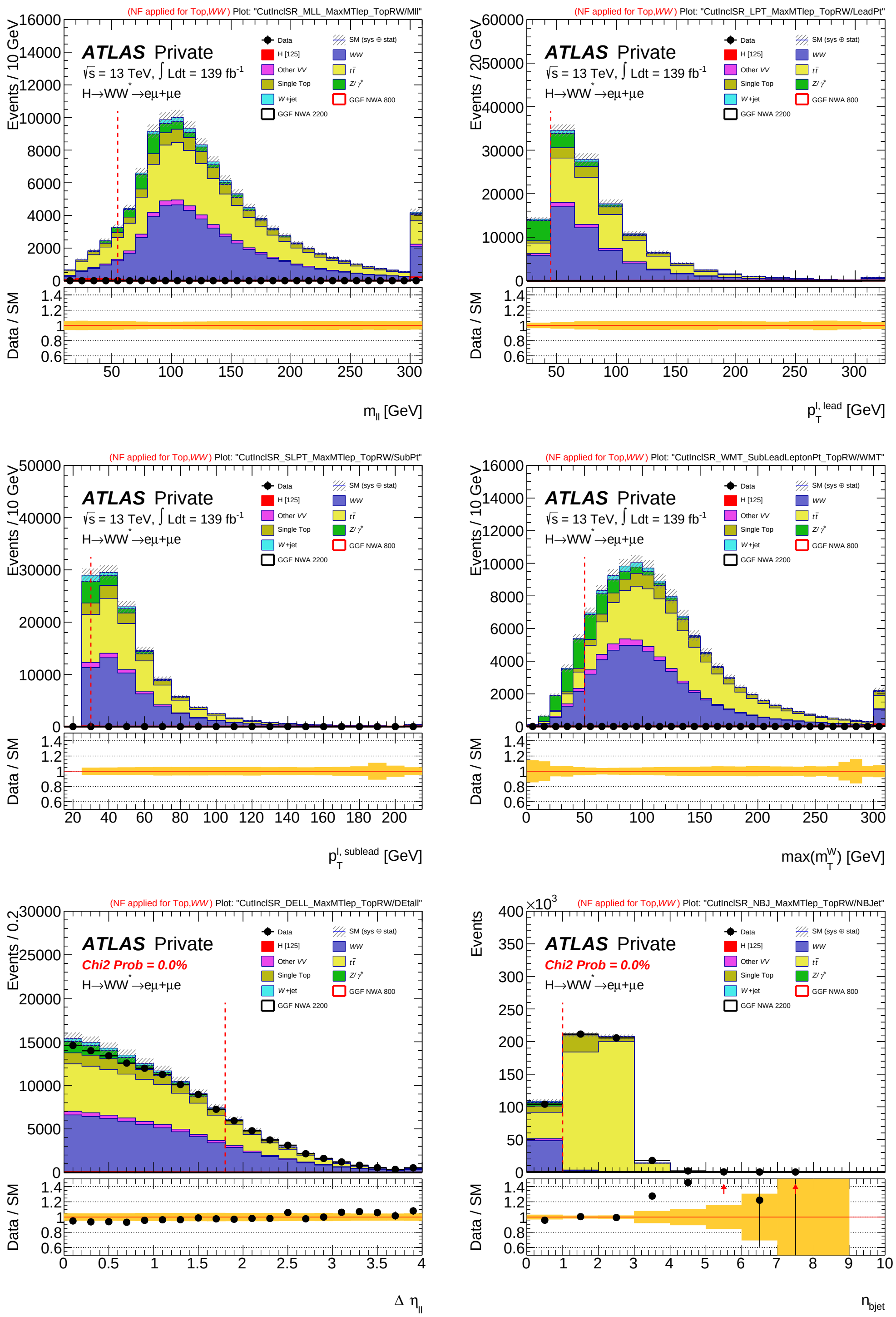

Figure 7.27: Comparison of signal (NWA) and background distributions in the quasi-inclusive ggF signal region for the variables: $m_{\ell\ell}$ (top left), $p_T^{\ell,\text{lead}}$ (top right), $p_T^{\ell,\text{sublead}}$ (middle left), $\max(m_T^W)$ (middle right), $|\Delta\eta_{\ell\ell}|$ (bottom left), N_{b-jet} (bottom right) The hatched band in the upper pane and the shaded band in lower pane show the statistical uncertainties on the predictions. The last bin contains the overflow.

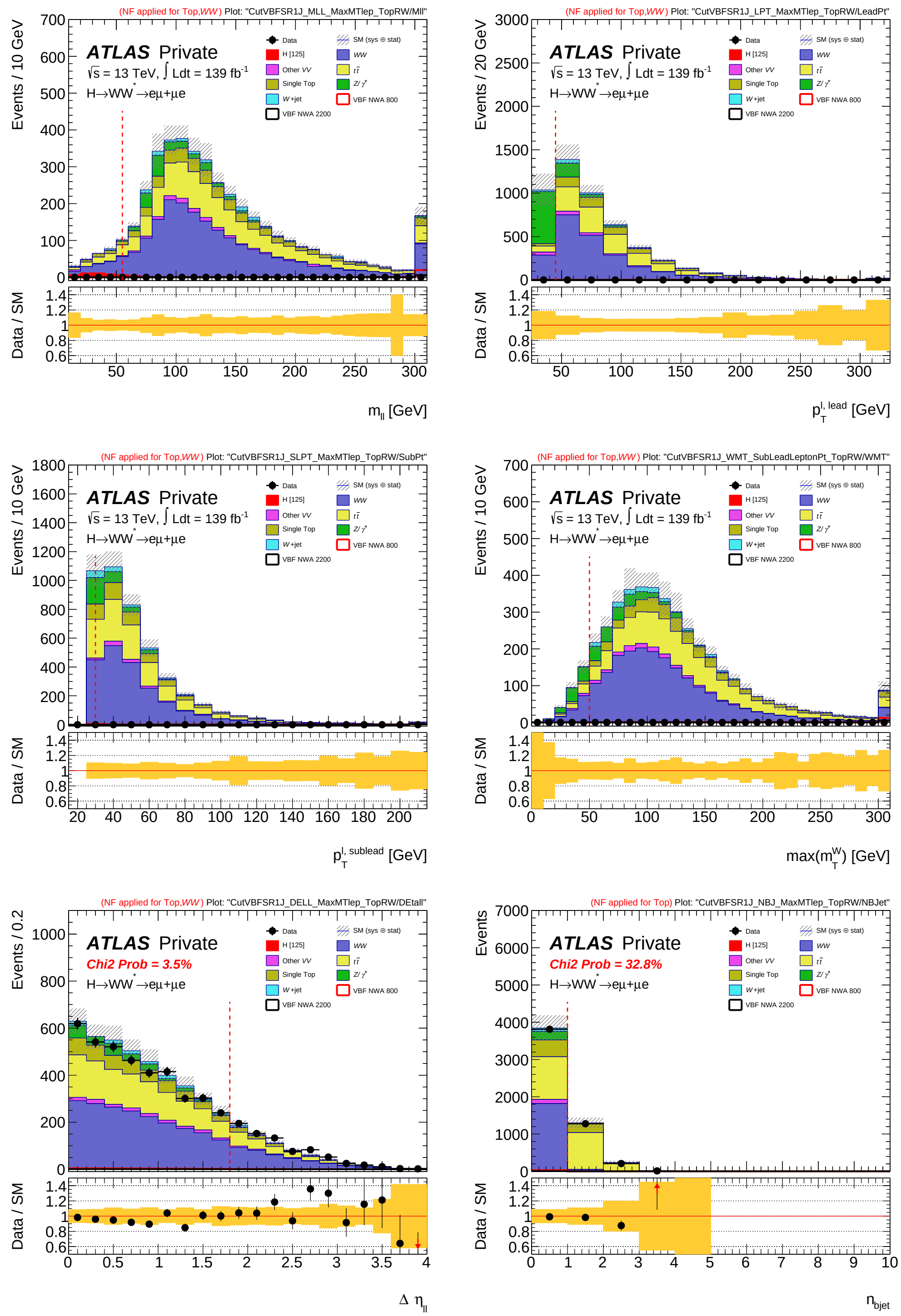

Figure 7.28: Comparison of signal (NWA) and background distributions in the VBF 1-jet signal region for the variables: $m_{\ell\ell}$ (top left), $p_T^{\ell,\text{lead}}$ (top right), $p_T^{\ell,\text{sublead}}$ (middle left), $\max(m_T^W)$ (middle right), $|\Delta\eta_{\ell\ell}|$ (bottom left), N_{b-jet} (bottom right). The hatched band in the upper pane and the shaded band in lower pane show the statistical uncertainties on the predictions. The last bin contains the overflow.

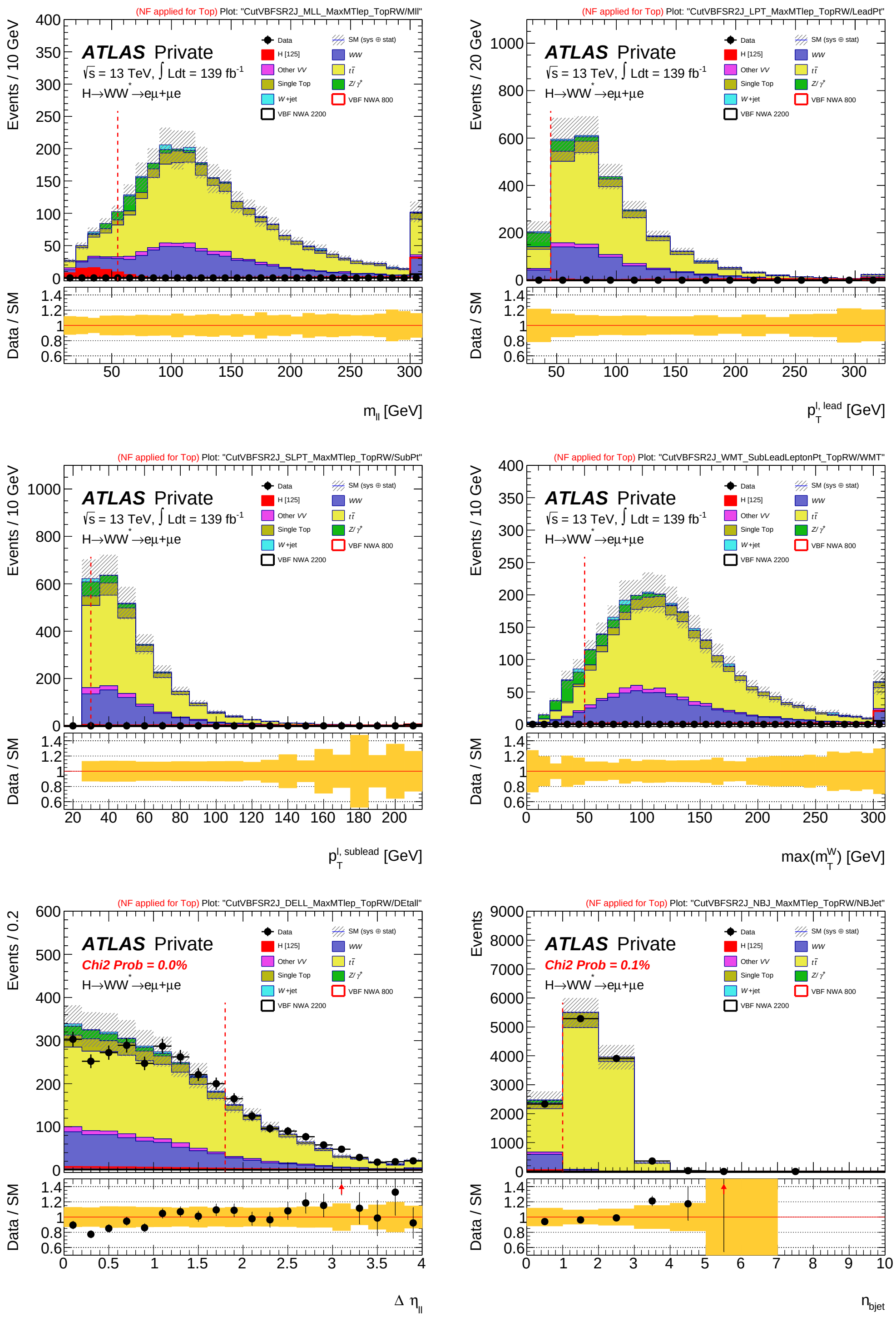

Figure 7.29: Comparison of signal (NWA) and background distributions in the VBF 2+ jet signal region for the variables: $m_{\ell\ell}$ (top left), $p_T^{\ell,\text{lead}}$ (top right), $p_T^{\ell,\text{sublead}}$ (middle left), $\max(m_T^W)$ (middle right), $|\Delta\eta_{\ell\ell}|$ (bottom left), N_{b-jet} (bottom right). The hatched band in the upper pane and the shaded band in lower pane show the statistical uncertainties on the predictions. The last bin contains the overflow.

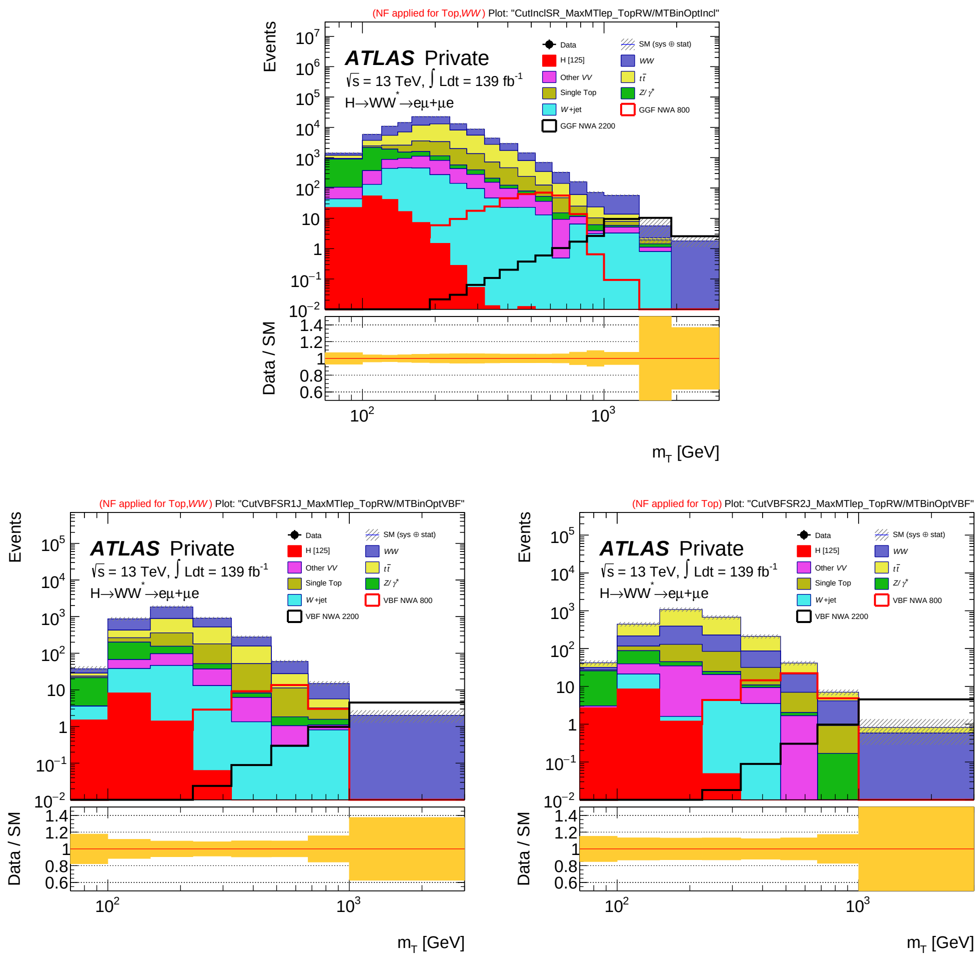

Figure 7.30: Comparison of signal (NWA) and background m_T distributions for each of the three : ggF quasi-inclusive (top), VBF 1-jet (bottom left), and VBF 2-jet (bottom right). The hatched band in the upper pane and the shaded band in lower pane show the combined statistical and experimental uncertainties on the predictions. The last bin contains the overflow. Normalization factors obtained from a comparison of data and MC have been applied for the top-quark and WW background where applicable.

Kinematic Region ($\|\eta\|$ and p_T range)	Value	Statistical	EW Subtraction	Sample Composition	Total
Electron:					
$0.0 < \|\eta\| < 1.5$					
$15.0 - 20.0$ GeV	0.079	7.3	3.7	7.5	11
$20.0 - 25.0$ GeV	0.090	12	6.9	31	34
$25.0 - 35.0$ GeV	0.14	12	11	7.4	18
$35.0 - 50.0$ GeV	0.22	17	14	21	31
$50.0 - 100.0$ GeV	0.33	19	23	21	37
$100.0 - \infty$ GeV	0.19	50	39	21	66
$1.5 < \|\eta\| < 2.5$					
$15.0 - 20.0$ GeV	0.072	11	4.3	7.5	14
$20.0 - 25.0$ GeV	0.078	22	11	31	40
$25.0 - 35.0$ GeV	0.13	36	23	7.4	43
$35.0 - 50.0$ GeV	0.13	34	29	21	50
$50.0 - 100.0$ GeV	0.18	45	43	21	66
$100.0 - \infty$ GeV	0.046	240	120	21	270
Muon:					
$0.0 < \|\eta\| < 1.05$					
$15.0 - 20.0$ GeV	0.042	8.4	7.1	8.1	14
$20.0 - 25.0$ GeV	0.017	35	34	11	50
$25.0 - 35.0$ GeV	0.035	28	28	26	48
$35.0 - \infty$ GeV	0.0010	2800	5100	27	5800
$1.05 < \|\eta\| < 2.5$					
$15.0 - 20.0$ GeV	0.060	6.7	5.3	8.1	12
$20.0 - 25.0$ GeV	0.042	17	14	11	25
$25.0 - 35.0$ GeV	0.048	25	25	26	44
$35.0 - \infty$ GeV	0.045	78	140	27	160

Table 7.6: Summary of the fake factors from the Z+jets estimate with uncertainties. All uncertainties are quoted in percent on the nominal value. *Value* denotes the nominal fake factor value. *Statistical* denotes the statistical uncertainties on the fake factors. *EW Subtraction* denotes the uncertainty due to the electroweak backgrounds that enter the Z+jets fake factor estimate. Some of these uncertainties look large, because they are quoted as relative uncertainties and the nominal values are small. *Sample Composition* denotes the uncertainty that accounts for differences in fake factors between Z+jets and W+jets processes, and includes both statistical and systematic uncertainty on the correction factors. The column *Total* sums all individual contributions in quadrature to give an overview of the total uncertainty of the fake factor.

$\sqrt{s} = 13TeV$, $\mathcal{L} = 139fb^{-1}$ (Full Run 2)	H GGF [NWA, 800]	H VBF [NWA, 800]	H [125]	WW	Other VV	Top	Z/γ^*	W+jet	Total Bkg.	Data	Data/Bkg
Channel Selection	507.75 ± 1.56	166.37 ± 0.78	6708.57 ± 8.16	132624.05 ± 121.47	21612.74 ± 228.69	1211681.61 ± 243.33	273092.83 ± 471.39	5095080.12 ± 4457.19	6740799.92 ± 4496.12	4374979	0.65 ± 0.00
Trigger Selection	507.05 ± 1.56	166.20 ± 0.78	6139.98 ± 7.80	128947.60 ± 119.81	19432.67 ± 206.17	1186870.45 ± 240.92	225883.95 ± 437.15	2693429.07 ± 4013.52	4260703.72 ± 4051.47	3358349	0.79 ± 0.00
Trigger Matching	505.10 ± 1.56	165.48 ± 0.78	5843.41 ± 7.53	126276.36 ± 118.03	18144.29 ± 195.36	1163780.46 ± 237.47	206556.63 ± 409.01	2765909.26 ± 3888.11	4286510.41 ± 3923.43	3275861	0.76 ± 0.00
Fake flavour split muon	505.10 ± 1.56	165.48 ± 0.78	5843.41 ± 7.53	126276.36 ± 118.03	18144.29 ± 195.36	1163780.46 ± 237.47	206556.63 ± 409.01	2437743.15 ± 3368.68	3958344.29 ± 3409.37	3275861	0.83 ± 0.00
Fake flavour split electron	505.10 ± 1.56	165.48 ± 0.78	5843.41 ± 7.53	126276.36 ± 118.03	18144.29 ± 195.36	1163780.46 ± 237.47	206556.63 ± 409.01	1781064.12 ± 2707.03	3301665.27 ± 2757.51	3275861	0.99 ± 0.00
Only two Leptons	503.84 ± 1.55	164.91 ± 0.78	5835.86 ± 7.53	126076.48 ± 117.98	16651.63 ± 193.66	1150215.32 ± 236.18	206232.13 ± 406.84	1778087.85 ± 2690.40	3283099.28 ± 2740.63	3251414	0.99 ± 0.00
$p_t^{lead} > 25$ GeV	503.83 ± 1.55	164.91 ± 0.78	5831.32 ± 7.52	126054.60 ± 117.97	16625.10 ± 193.37	1150071.58 ± 236.17	205672.55 ± 405.45	1765252.95 ± 2686.44	3269508.11 ± 2736.51	3243976	0.99 ± 0.00
$p_t^{\text{sublead}} > 25$	491.23 ± 1.54	160.43 ± 0.77	2912.83 ± 5.29	101538.05 ± 106.54	10015.44 ± 137.01	930848.04 ± 213.26	89710.95 ± 305.81	657415.50 ± 1947.64	1792440.81 ± 1990.59	1944267	1.08 ± 0.00
OS Leptons	491.23 ± 1.54	160.43 ± 0.77	2912.83 ± 5.29	101495.92 ± 103.29	9996.54 ± 132.64	930844.51 ± 213.26	89707.52 ± 299.29	655455.26 ± 1944.23	1790412.57 ± 1985.80	1942840	1.09 ± 0.00
$M_{\ell\ell} > 12/10$ GeV	491.23 ± 1.54	160.43 ± 0.77	2912.39 ± 5.29	101494.80 ± 103.29	9996.27 ± 132.64	930831.77 ± 213.26	89703.67 ± 299.29	655388.53 ± 1944.18	1790327.44 ± 1985.74	1942791	1.09 ± 0.00
Leptons ID	484.67 ± 1.53	158.28 ± 0.76	2881.05 ± 5.26	100284.15 ± 102.70	9929.74 ± 125.23	920299.03 ± 212.05	88741.98 ± 297.99	180982.95 ± 855.98	1303118.90 ± 944.84	1119100	0.86 ± 0.00
Apply fake factor	484.67 ± 1.53	158.28 ± 0.76	2881.05 ± 5.26	100284.15 ± 102.70	9929.74 ± 125.23	920299.03 ± 212.05	88741.98 ± 297.99	13257.30 ± 215.79	1135393.25 ± 454.52	1119100	0.99 ± 0.00
Scale factors				NF = 1.09 ± 0.02		NF = 0.97 ± 0.00			NFs Applied		
VBFVeto	432.88 ± 1.44	60.06 ± 0.48	2503.63 ± 5.01	102943.95 ± 108.97	9405.64 ± 120.77	868703.83 ± 203.23	84179.78 ± 292.60	12674.91 ± 211.51	1080411.75 ± 445.13	1081292	1.00 ± 0.00
VBFVeto: b-veto	393.86 ± 1.37	55.50 ± 0.46	2272.16 ± 4.77	97549.47 ± 107.15	8340.71 ± 116.53	88356.66 ± 71.98	80256.11 ± 288.57	8268.32 ± 146.36	285043.44 ± 367.37	271972	0.95 ± 0.00
Incl. WW CR: $\Delta\eta_{ll} > 1.8$	77.85 ± 0.61	11.95 ± 0.21	2.92 ± 0.17	19273.26 ± 49.37	1520.20 ± 36.98	15525.77 ± 30.02	813.79 ± 35.41	1628.27 ± 44.47	38764.22 ± 89.09	38376	0.99 ± 0.01
Incl. WW CR: $M_{ll} > 55$ GeV	77.85 ± 0.61	11.95 ± 0.21	2.92 ± 0.17	19273.15 ± 49.37	1520.20 ± 36.98	15525.69 ± 30.02	813.79 ± 35.41	1628.27 ± 44.47	38764.02 ± 89.09	38376	0.99 ± 0.01
Incl. WW CR: $p_T^{lead} > 45$ GeV	77.02 ± 0.61	11.83 ± 0.21	0.20 ± 0.04	14874.86 ± 43.21	1133.43 ± 28.22	13355.05 ± 27.79	275.82 ± 20.56	1109.08 ± 36.79	30748.44 ± 72.19	30453	0.99 ± 0.01
Incl. WW CR: $p_T^{sub-lead} > 30$ GeV	74.28 ± 0.60	11.42 ± 0.21	0.05 ± 0.02	13075.77 ± 40.75	975.57 ± 26.05	11627.43 ± 25.95	221.79 ± 14.56	795.19 ± 33.96	26695.79 ± 66.17	26569	1.00 ± 0.01
Incl. WW CR: $max(M_T^{\ell}) > 50$ GeV	73.16 ± 0.59	11.25 ± 0.21	0.03 ± 0.02	12036.84 ± 39.05	888.84 ± 25.49	10984.92 ± 25.25	170.31 ± 13.81	708.37 ± 32.65	24789.30 ± 63.79	24679	1.00 ± 0.01
Incl. WW CR: $\frac{E_T^{miss}\text{Significance}*10}{E_T^{miss}[GeV]} \geq 0.8$	34.25 ± 0.41	4.64 ± 0.14	0.02 ± 0.01	8919.43 ± 35.90	567.92 ± 22.61	4203.55 ± 16.70	127.06 ± 12.71	455.37 ± 24.87	14273.34 ± 53.47	14278	1.00 ± 0.01
VBFVeto: $n_{b-jets} = 1$	35.16 ± 0.42	4.33 ± 0.13	210.77 ± 1.45	5105.94 ± 19.83	1015.87 ± 30.27	372560.46 ± 137.96	3638.43 ± 47.88	2903.82 ± 108.42	385435.30 ± 185.45	389363	1.01 ± 0.00
Incl. Top CR: $\Delta\eta_{ll} < 1.8$	28.56 ± 0.38	3.51 ± 0.12	210.54 ± 1.45	4228.78 ± 17.74	823.63 ± 28.63	306113.10 ± 125.28	3602.55 ± 47.61	2384.15 ± 99.51	317362.77 ± 170.30	318631	1.00 ± 0.00
Incl. Top CR: $M_{ll} > 55$ GeV	28.56 ± 0.38	3.51 ± 0.12	39.63 ± 0.63	3620.97 ± 16.55	646.24 ± 23.17	262430.60 ± 115.95	2761.21 ± 45.65	1872.08 ± 90.77	271370.73 ± 156.77	271537	1.00 ± 0.00
Incl. Top CR: $p_T^{lead} > 45$ GeV	28.53 ± 0.38	3.50 ± 0.11	27.18 ± 0.52	3257.58 ± 15.35	537.56 ± 15.09	241899.15 ± 111.40	1117.52 ± 29.85	1522.67 ± 84.73	248361.66 ± 144.72	247924	1.00 ± 0.00
Incl. Top CR: $p_T^{sub-lead} > 30$ GeV	28.17 ± 0.38	3.45 ± 0.11	20.50 ± 0.45	2941.96 ± 14.62	480.24 ± 14.83	218095.45 ± 105.82	803.10 ± 27.76	1175.33 ± 80.35	223516.58 ± 137.32	223142	1.00 ± 0.00
Incl. Top CR: $max(M_T^{\ell}) > 50$ GeV	28.10 ± 0.37	3.44 ± 0.11	15.62 ± 0.40	2746.31 ± 14.05	423.78 ± 12.97	206657.90 ± 102.83	405.12 ± 25.61	1049.19 ± 77.25	211297.93 ± 132.53	211227	1.00 ± 0.00
Scale factors						NF = 0.94 ± 0.01			NF = 0.94 ± 0.01		
VBFLike	51.79 ± 0.50	98.21 ± 0.60	377.42 ± 1.61	5948.31 ± 23.99	524.10 ± 33.11	26717.51 ± 35.57	4562.20 ± 56.42	582.38 ± 42.77	38711.92 ± 89.18	37808	0.98 ± 0.01
VBFLike: b-veto	48.73 ± 0.48	94.40 ± 0.58	355.60 ± 1.57	5703.26 ± 23.64	494.73 ± 30.85	6008.74 ± 18.47	4382.94 ± 55.67	524.37 ± 35.06	17469.64 ± 78.63	16115	0.92 ± 0.01
Scale factors				NF = 1.04 ± 0.05		NF = 0.94 ± 0.01			NFs Applied		
VBFLike: $n_{jets} = 1$	30.58 ± 0.38	34.99 ± 0.36	181.07 ± 1.27	3691.73 ± 20.64	293.45 ± 25.14	2585.58 ± 13.01	2757.54 ± 40.14	384.76 ± 28.77	9894.14 ± 60.56	9275	0.94 ± 0.01
VBF WW CR 1J: $\Delta\eta_{ll} > 1.8$ OR $M_{ll} < 55$ GeV	3.72 ± 0.13	5.03 ± 0.14	139.75 ± 1.11	1001.80 ± 10.62	91.01 ± 16.63	626.65 ± 6.40	190.31 ± 9.52	109.14 ± 11.34	2158.66 ± 25.51	2148	1.00 ± 0.02
VBF Top CR: $n_{b-jets} \geq 1$	3.08 ± 0.12	3.85 ± 0.12	21.85 ± 0.37	247.53 ± 4.10	30.10 ± 13.08	20717.62 ± 30.43	179.54 ± 8.79	56.62 ± 24.49	21253.27 ± 42.32	21693	1.02 ± 0.01
VBF Top CR: $\Delta\eta_{ll} < 1.8$	2.56 ± 0.11	3.14 ± 0.11	21.81 ± 0.37	209.86 ± 3.75	23.34 ± 13.07	16059.32 ± 26.93	179.67 ± 8.71	45.14 ± 22.08	16539.15 ± 38.39	16514	1.00 ± 0.01
VBF Top CR: $M_{ll} > 55$ GeV	2.56 ± 0.11	3.14 ± 0.11	4.07 ± 0.16	175.35 ± 3.51	15.71 ± 12.83	13868.63 ± 25.03	144.65 ± 8.25	40.82 ± 20.24	14249.23 ± 35.79	14279	1.00 ± 0.01
VBF Top CR: $p_T^{lead} > 45$ GeV	2.56 ± 0.11	3.14 ± 0.11	2.83 ± 0.13	156.12 ± 3.10	13.49 ± 12.83	12861.38 ± 24.11	55.60 ± 4.66	29.84 ± 18.86	13119.26 ± 33.66	13107	1.00 ± 0.01
VBF Top CR: $p_T^{sub-lead} > 30$ GeV	2.53 ± 0.11	3.09 ± 0.11	2.19 ± 0.11	141.53 ± 2.95	8.53 ± 12.63	11602.00 ± 22.92	38.49 ± 3.98	31.37 ± 18.24	11824.12 ± 32.29	11811	1.00 ± 0.01
VBF Top CR: $max(M_T^{\ell}) > 50$ GeV	2.51 ± 0.11	3.08 ± 0.11	1.71 ± 0.10	133.82 ± 2.87	6.63 ± 12.63	10983.44 ± 22.28	24.03 ± 3.62	25.33 ± 17.65	11174.97 ± 31.44	11187	1.00 ± 0.01

Table 7.7: Full cutflow for the different top-quark and WW control regions used in the analysis. The quoted errors correspond to the statistical uncertainties only. The normalization factors quoted are applied to all the subsequent lines in the category and are calculating using the matrix inversion method. The heavy-Higgs signal sample for multiple mass points is taken from the NWA and is normalized to the previous 36 fb^{-1} observed upper limits.

$\sqrt{s} = 13TeV$, $\mathcal{L} = 139fb^{-1}$ (Full Run 2)	H GGF [NWA, 800]	H VBF [NWA, 800]	H [125]	WW	Other VV	Top	Z/γ^*	W+jet	Total Bkg.	Data	Data/Bkg
Channel Selection	507.75 ± 1.56	166.37 ± 0.78	6708.57 ± 8.16	132624.05 ± 121.47	21612.74 ± 228.69	1211681.61 ± 243.33	273092.83 ± 471.39	5095080.12 ± 4457.19	6740799.92 ± 4496.12	4374979	0.65 ± 0.00
Trigger Selection	507.05 ± 1.56	166.20 ± 0.78	6139.98 ± 7.80	128947.60 ± 119.81	19432.67 ± 206.17	1186870.45 ± 240.92	225883.95 ± 437.15	2693429.07 ± 4013.52	4260703.72 ± 4051.47	3358349	0.79 ± 0.00
Trigger Matching	505.10 ± 1.56	165.48 ± 0.78	5843.41 ± 7.53	126276.36 ± 118.03	18144.29 ± 195.36	1163780.46 ± 237.47	206556.63 ± 409.01	2765909.26 ± 3888.11	4286510.41 ± 3923.43	3275861	0.76 ± 0.00
Fake flavour split muon	505.10 ± 1.56	165.48 ± 0.78	5843.41 ± 7.53	126276.36 ± 118.03	18144.29 ± 195.36	1163780.46 ± 237.47	206556.63 ± 409.01	2437743.15 ± 3368.68	3958344.29 ± 3409.37	3275861	0.83 ± 0.00
Fake flavour split electron	505.10 ± 1.56	165.48 ± 0.78	5843.41 ± 7.53	126276.36 ± 118.03	18144.29 ± 195.36	1163780.46 ± 237.47	206556.63 ± 409.01	1781064.12 ± 2707.03	3301665.27 ± 2757.51	3275861	0.99 ± 0.00
GRL Selection	505.10 ± 1.56	165.48 ± 0.78	5843.41 ± 7.53	126276.36 ± 118.03	18144.29 ± 195.36	1163780.46 ± 237.47	206556.63 ± 409.01	1781064.12 ± 2707.03	3301665.27 ± 2757.51	3275861	0.99 ± 0.00
Jet Cleaning	505.10 ± 1.56	165.48 ± 0.78	5843.41 ± 7.53	126276.36 ± 118.03	18144.29 ± 195.36	1163780.46 ± 237.47	206556.63 ± 409.01	1781064.12 ± 2707.03	3301665.27 ± 2757.51	3275861	0.99 ± 0.00
Overlap: Vgamma/Vjets	505.10 ± 1.56	165.48 ± 0.78	5843.41 ± 7.53	126276.36 ± 118.03	18144.29 ± 195.36	1163780.46 ± 237.47	206556.63 ± 409.01	1781064.12 ± 2707.03	3301665.27 ± 2757.51	3275861	0.99 ± 0.00
Only two Leptons	503.84 ± 1.55	164.91 ± 0.78	5835.86 ± 7.53	126076.48 ± 117.98	16651.63 ± 193.66	1150215.32 ± 236.18	206232.13 ± 406.84	1778087.85 ± 2690.40	3283099.28 ± 2740.63	3251414	0.99 ± 0.00
$p_t^{lead} > 25$ GeV	503.83 ± 1.55	164.91 ± 0.78	5831.32 ± 7.52	126054.60 ± 117.97	16625.10 ± 193.37	1150071.58 ± 236.17	205672.55 ± 405.45	1765252.95 ± 2686.44	3269508.11 ± 2736.51	3243976	0.99 ± 0.00
$p_t^{\text{sublead}} > 25$	491.23 ± 1.54	160.43 ± 0.77	2912.83 ± 5.29	101538.05 ± 106.54	10015.44 ± 137.01	930848.04 ± 213.26	89710.95 ± 305.81	657415.50 ± 1947.64	1792440.81 ± 1990.59	1944267	1.08 ± 0.00
OS Leptons	491.23 ± 1.54	160.43 ± 0.77	2912.83 ± 5.29	101495.92 ± 103.29	9996.54 ± 132.64	930844.51 ± 213.26	89707.52 ± 299.29	655455.26 ± 1944.23	1790412.57 ± 1985.80	1942840	1.09 ± 0.00
$M_{\ell\ell} > 12/10$ GeV	491.23 ± 1.54	160.43 ± 0.77	2912.39 ± 5.29	101494.80 ± 103.29	9996.27 ± 132.64	930831.77 ± 213.26	89703.67 ± 299.29	655388.53 ± 1944.18	1790327.44 ± 1985.74	1942791	1.09 ± 0.00
Leptons ID	484.67 ± 1.53	158.28 ± 0.76	2881.05 ± 5.26	100284.15 ± 102.70	9929.74 ± 125.23	920299.03 ± 212.05	88741.98 ± 297.99	180982.95 ± 855.98	1303118.90 ± 944.84	1119100	0.86 ± 0.00
Apply fake factor	484.67 ± 1.53	158.28 ± 0.76	2881.05 ± 5.26	100284.15 ± 102.70	9929.74 ± 125.23	920299.03 ± 212.05	88741.98 ± 297.99	13257.30 ± 215.79	1135393.25 ± 454.52	1119100	0.99 ± 0.00
Scale factors				NF = 1.09 ± 0.02		NF = 0.97 ± 0.00			NFs Applied		
VBFVeto	432.88 ± 1.44	60.06 ± 0.48	2503.63 ± 5.01	102943.95 ± 108.97	9405.64 ± 120.77	868703.83 ± 203.23	84179.78 ± 292.60	12674.91 ± 211.51	1080411.75 ± 445.13	1081292	1.00 ± 0.00
VBFVeto: b-veto	393.86 ± 1.37	55.50 ± 0.46	2272.16 ± 4.77	97549.47 ± 107.15	8340.71 ± 116.53	88356.66 ± 71.98	80256.11 ± 288.57	8268.32 ± 146.36	285043.44 ± 367.37	271972	0.95 ± 0.00
Incl. SR: $\Delta\eta_{ll} < 1.8$	316.01 ± 1.23	43.55 ± 0.40	2269.25 ± 4.77	78276.21 ± 95.10	6820.51 ± 110.51	72830.89 ± 65.42	79442.32 ± 286.39	6640.06 ± 139.44	246279.22 ± 356.40	0	0.00
Incl. SR: $M_{ll} > 55$ GeV	315.97 ± 1.23	43.55 ± 0.40	549.56 ± 2.37	68353.59 ± 89.62	5600.24 ± 96.33	63326.71 ± 61.01	73185.54 ± 281.07	5905.87 ± 134.27	216921.50 ± 343.61	0	0.00
Incl. SR: $p_T^{lead} > 45$ GeV	315.51 ± 1.23	43.47 ± 0.40	278.44 ± 1.67	56545.45 ± 80.74	3962.75 ± 68.29	58592.14 ± 58.69	14083.38 ± 168.74	4626.61 ± 101.05	138088.76 ± 230.90	0	0.00
Incl. SR: $p_T^{sub-lead} > 30$ GeV	311.26 ± 1.22	42.88 ± 0.40	184.41 ± 1.35	51201.10 ± 76.67	3393.14 ± 61.91	53087.06 ± 55.87	9824.49 ± 152.54	3554.88 ± 93.88	121245.06 ± 211.94	0	0.00
Incl. SR: $max(M_{\mathrm{T}}^{\ell}) > 50$ GeV	310.29 ± 1.22	42.75 ± 0.40	144.17 ± 1.20	47191.56 ± 73.45	2994.50 ± 58.14	50533.63 ± 54.46	5381.01 ± 117.40	3223.91 ± 78.97	109468.78 ± 178.21	0	0.00
Scale factors						NF = 0.94 ± 0.01			NF = 0.94 ± 0.01		
VBFLike	51.79 ± 0.50	98.21 ± 0.60	377.42 ± 1.61	5948.31 ± 23.99	524.10 ± 33.11	26717.51 ± 35.57	4562.20 ± 56.42	582.38 ± 42.77	38711.92 ± 89.18	37808	0.98 ± 0.01
VBFLike: b-veto	48.73 ± 0.48	94.40 ± 0.58	355.60 ± 1.57	5703.26 ± 23.64	494.73 ± 30.85	6008.74 ± 18.47	4382.94 ± 55.67	524.37 ± 35.06	17469.64 ± 78.63	16115	0.92 ± 0.01
Scale factors				NF = 1.04 ± 0.05		NF = 0.94 ± 0.01			NFs Applied		
VBFLike: $n_{jets} = 1$	30.58 ± 0.38	34.99 ± 0.36	181.07 ± 1.27	3691.73 ± 20.64	293.45 ± 25.14	2585.58 ± 13.01	2757.54 ± 40.14	384.76 ± 28.77	9894.14 ± 60.56	9275	0.94 ± 0.01
VBF SR 1J: $\Delta\eta_{ll} < 1.8$	26.86 ± 0.36	29.96 ± 0.34	180.84 ± 1.27	3111.83 ± 18.85	249.38 ± 24.83	2227.02 ± 12.10	2730.64 ± 40.00	320.72 ± 27.55	8820.43 ± 58.98	0	0.00
VBF SR 1J: $M_{ll} > 55$ GeV	26.86 ± 0.36	29.96 ± 0.34	41.32 ± 0.62	2689.93 ± 17.70	202.44 ± 18.86	1965.28 ± 11.36	2567.24 ± 38.99	275.62 ± 26.44	7741.83 ± 54.93	0	0.00
VBF SR 1J: $p_T^{lead} > 45$ GeV	26.83 ± 0.36	29.93 ± 0.34	20.89 ± 0.43	2226.32 ± 16.07	124.42 ± 10.31	1806.82 ± 10.88	505.15 ± 21.46	224.78 ± 21.05	4908.39 ± 37.24	0	0.00
VBF SR 1J: $p_T^{sub-lead} > 30$ GeV	26.48 ± 0.36	29.55 ± 0.33	13.51 ± 0.34	2009.75 ± 15.31	102.92 ± 8.54	1629.36 ± 10.35	319.84 ± 15.70	163.31 ± 18.48	4238.69 ± 31.66	0	0.00
VBF SR 1J: $max(M_{\mathrm{T}}^{\ell}) > 50$ GeV	26.40 ± 0.36	29.46 ± 0.33	11.13 ± 0.31	1888.83 ± 14.81	93.36 ± 8.49	1563.94 ± 10.13	226.55 ± 14.31	157.24 ± 17.65	3941.06 ± 30.17	0	0.00
VBFLike: $n_{jets} \geq 2$	16.11 ± 0.28	58.72 ± 0.45	159.00 ± 0.83	1271.58 ± 8.07	144.53 ± 16.34	3140.73 ± 12.40	604.70 ± 17.00	100.27 ± 15.89	5420.80 ± 32.07	4990	0.92 ± 0.01
VBF SR 2J: $\Delta\eta_{ll} < 1.8$	13.01 ± 0.25	47.61 ± 0.41	158.85 ± 0.83	1060.00 ± 7.35	117.85 ± 16.07	2412.08 ± 10.93	598.47 ± 16.95	74.18 ± 14.65	4421.43 ± 30.56	0	0.00
VBF SR 2J: $M_{ll} > 55$ GeV	13.01 ± 0.25	47.60 ± 0.41	28.78 ± 0.36	850.52 ± 6.76	103.85 ± 11.95	2093.25 ± 10.16	429.71 ± 15.89	68.24 ± 13.37	3574.34 ± 26.89	0	0.00
VBF SR 2J: $p_T^{lead} > 45$ GeV	13.01 ± 0.25	47.53 ± 0.41	21.73 ± 0.31	777.44 ± 6.30	94.57 ± 11.91	1946.54 ± 9.78	221.69 ± 13.57	50.14 ± 11.69	3112.10 ± 24.45	0	0.00
VBF SR 2J: $p_T^{sub-lead} > 30$ GeV	12.84 ± 0.25	46.88 ± 0.41	17.19 ± 0.27	702.24 ± 6.00	80.27 ± 10.98	1761.97 ± 9.34	160.83 ± 12.50	43.96 ± 10.42	2766.46 ± 22.55	0	0.00
VBF SR 2J: $max(M_{\mathrm{T}}^{\ell}) > 50$ GeV	12.81 ± 0.25	46.80 ± 0.41	12.41 ± 0.23	661.91 ± 5.83	66.30 ± 8.04	1674.11 ± 9.09	87.21 ± 4.66	36.49 ± 9.88	2538.44 ± 17.34	0	0.00

Table 7.8: Full cutflow for the different signal regions used in the analysis. The quoted errors correspond to the statistical uncertainties only. The normalization factors quoted are applied to all the subsequent lines in the category and are calculating using the matrix inversion method. The heavy-Higgs signal sample for multiple mass points is taken from the NWA and is normalized to the previous 36 fb^{-1} observed upper limits.

Chapter 8

Systematic Uncertainties

Systematic uncertainties are considered to fully characterize the modelling of the SM background and the signal models considered in this analysis. The impact of these uncertainties are included in two ways: comparing the overall yield of the variation to the nominal (norm) and comparing the shape of the specific kinematic distribution being considered of the variation to the nominal (shape).

There are two source of systematic uncertainties considered in this chapter. Section 8.1 will cover the uncertainties related to the experimental apparatus coming from detector and reconstruction effects. Section 8.2 will cover the uncertainties related to theoretical predictions on the main SM background processes considered in the analysis.

8.1 Experimental Systematic Uncertainties

The evaluation of the experimental systematic uncertainties is performed by closely adhering to the recommendations of the individual combined performance (CP) groups of the ATLAS experiment. Each CP group is responsible for one or more of the reconstructed objects' calibrations and efficiency calculations. The analysis considers two distinct types of experimental systematic uncertainties:

1. Four-vector (P4) systematics - Uncertainties which are evaluated as $\pm 1\sigma$ variations on the four-momentum calculation of a reconstructed object.

2. Scale factor (SF) systematics - Uncertatines which are evaluated as $\pm 1\sigma$ variations on the weight applied to physics event, which are applied to either the unique reconstructed objects or the event as a whole.

A complete overview of all the systematic uncertainties considered is given in Table 8.1. Tables 8.2 - 8.4 list the pre-fit impact values of the experimental uncertainties on the dominant background samples and the baseline NWA signal samples.

8.1.1 Event Uncertainties

Two event-wide uncertainties are considered in this analysis. The first of these is the uncertainty on the integrated luminosity of the full ATLAS Run-II dataset. The uncertainty in the combined 2015–2018 integrated luminosity is 1.7 % [41], obtained using the LUCID-2 detector [43] for the primary luminosity measurements. The second of these is the uncertainty on the pileup reweighting data scale factor used to correctly model the pileup conditions observed in each data taking campaign of Run-II. The default value of the data scale factor for the pileup $<\mu>$ value rescaling is 1.0/1.03. To evaluate the systematics of the pileup $<\mu>$ value rescaling, the data scale factor are varied upward (1.0/0.99) and downward (1.0/1.07).

8.1.2 Electron and Muon Uncertainties

The uncertainties associated with the reconstruction, trigger, and selection (identification and isolation) efficiencies of leptons (muons and electrons) are corrected by applying scale factors to the reconstructed objects. Scale factors are derived from $Z \to \mu^+\mu^-/e^+e^-$ decays as functions of the lepton kinematics. The uncertainties are taken as variations on these scale factors, provided from the CP group. [73] [13]. Additionally, uncertainties are evaluated on the reconstructed four-momentum vectors by taking variations based on the energy scale and resolution of the reconstructed leptons. Uniquely applied to the muons is also an uncertainty related to the track-to-vertex-association (TTVA) impact parameter selection.

Systematic uncertainty	Short description
	Event
Luminosity	uncertainty on total integrated luminosity
Pileup Reweighting	uncertainty on pileup reweighting
	Electrons
EL_EFF_Trigger_Total_1NPCOR_PLUS_UNCOR	trigger efficiency uncertainty
EL_EFF_Reco_Total_1NPCOR_PLUS_UNCOR	reconstruction efficiency uncertainty
EL_EFF_ID_TotalCorrUncertainty	ID efficiency uncertainty
EL_EFF_ID_CorrUncertaintyNP (0 to 15)	ID efficiency uncertainty splits in 16 components
EL_EFF_ID_SIMPLIFIED_UncorrUncertaintyNP (0 to 17)	ID efficiency uncertainty splits in 18 components
EL_EFF_Iso_Total_1NPCOR_PLUS_UNCOR	isolation efficiency uncertainty
EG_SCALE_ALL EG_SCALE_AF2	energy scale uncertainty
EG_RESOLUTION_ALL	energy resolution uncertainty
	Muons
MUON_EFF_TrigStatUncertainty MUON_EFF_TrigSystUncertainty	trigger efficiency uncertainty
MUON_EFF_RECO_STAT MUON_EFF_RECO_SYS	reconstruction and ID efficiency uncertainty for muons with p_T ¿ 15 GeV
MUON_ISO_STAT MUON_ISO_SYS	isolation efficiency uncertainty
MUON_TTVA_STAT MUON_TTVA_SYS	track-to-vertex association efficiency uncertainty
MUON_ID	momentum resolution uncertainty from inner detector
MUON_MS	momentum resolution uncertainty from muon system
MUON_SCALE	momentum scale uncertainty
MUON_SAGITTA_RHO MUON_SAGITTA_RESBIAS	charge dependent momentum scale uncertainty
	Jets
JET_EffectiveNP_Detector (1 to 2) JET_EffectiveNP_Mixed (1 to 3) JET_EffectiveNP_Modelling (1 to 4) JET_EffectiveNP_Statistical (1 to 6)	energy scale uncertainty from the in situ analyses splits into 8 components
JET_EtaIntercalibration_Modeling	energy scale uncertainty on eta-intercalibration (modeling)
JET_EtaIntercalibration_TotalStat	energy scale uncertainty on eta-intercalibrations (statistics/method)
JET_EtaIntercalibration_NonClosure_highE JET_EtaIntercalibration_NonClosure_negEta JET_EtaIntercalibration_NonClosure_posEta	energy scale uncertainty on eta-intercalibrations (non-closure)
JET_Pileup_OffsetMu	energy scale uncertainty on pile-up (mu dependent)
JET_Pileup_OffsetNPV	energy scale uncertainty on pile-up (NPV dependent)
JET_Pileup_PtTerm	energy scale uncertainty on pile-up (pt term)
JET_Pileup_RhoTopology	energy scale uncertainty on pile-up (density ρ)
JET_Flavor_Composition	energy scale uncertainty on flavour composition
JET_Flavor_Response	energy scale uncertainty on samples' flavour response
JET_BJES_Response	energy scale uncertainty on b-jets
JET_PunchThrough_MC16	energy scale uncertainty for punch-through jets
JET_SingleParticle_HighPt	energy scale uncertainty from the behaviour of high-p_T jets
JET_JER_DataVsMC_MC16 JET_JER_EffectiveNP (1 to 11) JET_JER_EffectiveNP_12restTerm	energy resolution uncertainty, each for both MC and pseudo-data
JET_JvtEfficiency	JVT efficiency uncertainty
FT_EFF_Eigen_B FT_EFF_Eigen_C FT_EFF_Eigen_L	b-tagging efficiency uncertainties ("BTAG_MEDIUM"): 3 components for b jets, 3 for c jets and 4 for light jets
FT_EFF_Eigen_extrapolation	b-tagging efficiency uncertainty on the extrapolation to high-p_T jets
FT_EFF_Eigen_extrapolation_from_charm	b-tagging efficiency uncertainty on tau jets
	MET
MET_SoftTrk_ResoPara	track-based soft term related longitudinal resolution uncertainty
MET_SoftTrk_ResoPerp	track-based soft term related transverse resolution uncertainty
MET_SoftTrk_Scale	track-based soft term related longitudinal scale uncertainty

Table 8.1: Summary of the experimental sytematic uncertainties considered.

	Prefit Value [%]						
Source	Jet	Flavor Tagging	Pile-up	Muons	Electrons	MET	Total
ggF SR	3.517	7.609	2.538	1.01	0.298	0.050	8.821
VBF SR 1J	6.433	3.738	4.264	0.973	0.316	0.099	8.636
VBF SR 2J	9.853	6.686	4.128	1.082	0.301	0.010	12.652
ggF Top CR	1.267	1.821	0.911	0.987	0.300	0.058	2.611
ggF WW CR	9.462	6.509	7.408	1.192	0.358	1.713	13.829
VBF Top CR	9.806	1.519	4.133	0.973	0.282	0.111	10.797
VBF WW CR	6.703	3.615	4.102	1.113	0.381	0.000	8.729

Table 8.2: Relative prefit uncertainties (%) of dominant experimental sources on the event yields for the top-quark background processes in the three signal regions and four control regions. The last column shows the total uncertainty of the experimental uncertainties. Individual contributions to each category are summed in quadrature.

	Prefit Value [%]						
Source	Jet	Flavor Tagging	Pile-up	Muons	Electrons	MET	Total
ggF SR	1.257	0.409	0.940	1.040	0.328	0.106	1.957
VBF SR 1J	13.542	0.208	6.172	1.221	0.275	0.176	14.937
VBF SR 2J	14.402	0.739	9.486	0.942	0.327	0.140	17.290
ggF Top CR	-	-	-	-	-	-	-
ggF WW CR	3.769	0.218	2.465	1.182	0.314	1.313	4.852
VBF Top CR	-	-	-	-	-	-	-
VBF WW CR	13.428	0.209	6.518	0.932	0.343	0.000	14.960

Table 8.3: Relative prefit uncertainties (%) of dominant experimental sources on the event yields for the WW background processes in the three signal regions and four control regions. The top-quark control regions are omitted due to the very small contribution of the WW background in those regions. The last column shows the total uncertainty of the experimental uncertainties. Individual contributions to each category are summed in quadrature.

	Prefit Value [%]						
Source	Jet	Flavor Tagging	Pile-up	Muons	Electrons	MET	Total
	ggF Production						
ggF SR	1.359	0.580	0.743	1.088	0.863	0.014	2.159
VBF SR 1J	3.625	0.209	1.67	1.198	0.839	0.037	4.256
VBF SR 2J	9.996	0.677	5.013	1.464	0.856	0.030	11.330
	VBF Production						
ggF SR	3.773	0.462	1.902	1.324	0.857	0.037	4.533
VBF SR 1J	3.510	0.103	1.903	1.108	0.852	0.067	4.232
VBF SR 2J	4.635	0.320	2.265	1.020	0.897	0.022	5.344

Table 8.4: Relative prefit uncertainties (%) of dominant experimental sources on the event yields for the NWA $m_H = 800$ GeV signal processes in the three signal regions for both the ggF and VBF production modes. The last column shows the total uncertainty of the experimental uncertainties. Individual contributions to each category are summed in quadrature.

8.1.3 Jet Uncertainties

Jet systematic uncertainties can be broken into two subtypes: Systematics related to the energy scale of the reconstructed jets (JES) and the the jet energy resolution (JER). The JES uncertainties are treated with a category reduction scheme and are derived as a function of the p_T and η of the jet. Also, uncertainties related to the flavor of the jet and the pileup conditions are considered. The JES uncertainties are calculated via in-situ studies of dijet, Z+jet and γ+jet samples. [12] The JER uncertainties are evaluated with the full ATLAS JER scheme, which includes smearing of pseudo-data in addition to Monte-Carlo evaluations. These two formats are the combined into a single NP. An additional uncertainty is considered based on the scale factor variation of the application of the JVT working point as described in Section 5.4.

Flavor-Tagging Uncertainties

Because this analysis makes use of b-tagging in both a b-veto and b-jet selection, the variations on the b-tagging efficiencies and mistag rate is considered following the measurement procedure described in Ref. [3]. Individual uncertainties are taken for each of the jet flavors considered in the tagging process: b, c, and light jets. Two additional efficiency uncertainties are considered based on the extrapolation to high-p_T jets and τ-jets.

8.1.4 E_T^{miss} Uncertainties

Three uncertainties related to the calculation of the E_T^{miss} of the physics event are considered based on the calibrations found in Ref. [5]. Two are based on the resolution of the track-based soft term (TST) calculation, and the other is based on the variation of the energy scale of the TST.

8.2 Model Uncertainties on the Signal and Dominant Background Samples

This section discusses the modelling uncertainties arising from the parton showering (PS), choice of scale, and choice of the PDF set used in the generation of the major MC backgrounds: top-quark and WW. For top-quark backgrounds, modelling uncertainties are calculated for both $t\bar{t}$ and Wt production independently. For WW backgrounds, only the modelling uncertainties on the predominant contributing sample is considered, $qqWW$.

The $t\bar{t}$ modelling uncertainty pre-fit values are shown in Tables 8.5 and 8.6. The single-top (Wt) modelling uncertainty pre-fit values are shown in Tables 8.7 and 8.8. The WW ($qqWW$) modelling uncertainty pre-fit values are shown in Tables 8.9 and 8.10.

Each modelling uncertainty is evaluated as a comparison between the nominal process sample and an alternative generator at reconstructed object (reco) level, with the exclusion of a few WW uncertainties which are comparisons between truth object samples.

For $t\bar{t}$ and Wt, a comparison of the nominal (Powheg+Pythia 8) sample to one produced by an alternative generator (MadGraph5_aMC@NLO) and using an alternative showering (Herwig 7). Further comparison of variations on the initial state (ISR) and final state radiation (FSR) are made. Additionally, a comparison of the PDF is made by taking the standard deviation of NNPDF3.0 set. Lastly, an evaluation of the scale uncertainty is made by taking a 7-point envelope on the μR and μF scale variations. Full shape comparisons for $t\bar{t}$ modeling uncertainties can be see in Figures B.1 - B.6.

- All $t\bar{t}$ variations are taken at reco level following the PMG recommendations, with the nominal as the PowPy8 $t\bar{t}$ dilepton sample 410472, and calculated from the following variations:
  - **Generator** - Two-point comparison of AFII PowPy8 and aMC@NLO+Pythia8 generators, symmetrized.

- **Shower** - Two-point comparison of AFII PowPy8 and Powheg+Herwig generators, symmetrized.
- **Scale** - Bin-by-bin envelope calculation of 7-point μR and μF variations.
- **ISR** - Variation of strong coupling in initial shower using Var3c eigentune.
- **FSR** - Variation of μRfac (0.5,2.0) in the final state radiation.
- **PDF** - Standard deviation of NNPDF3.0 PDF set.

For Wt samples, we also evaluate interference effects by comparing to a specialized POWHEG+PYTHIA 8 DS sample. Full shape comparisons for Wt modeling uncertainties can be see in Figures B.7 - B.13.

- All Wt variations are taken at reco level following the PMG recommendations, with the nominal as the PowPy8 Wt dilepton samples 410648,9, and calculated from the following variations:
  - **Generator** - Two-point comparison of AFII PowPy8 and aMC@NLO+Pythia8 generators, symmetrized.
  - **Shower** - Two-point comparison of AFII PowPy8 and Powheg+Herwig generators, symmetrized.
  - **Scale** - Bin-by-bin envelope calculation of 7-point μR and μF variations.
  - **ISR** - Variation of strong coupling in initial shower using Var3c eigentune.
  - **FSR** - Variation of μRfac (0.5,2.0) in the final state radiation.
  - **PDF** - Standard deviation of NNPDF3.0 PDF set.
  - **Interference** - Two-point comparison of fullsim PowPy8 DR (nominal) and DS (variation) samples.

For $qqWW$ an evaluation of variations on the nominal (SHERPA) samples is made at reco level by comparing the 7-point envelope on the μR and μF scale variations, the standard deviation of NNPDF3.0 set, and variations on the α_S scale. Additionally, truth level comparisons are made by comparing the nominal sample to alternative showering variations in CKKW, QSF, and and CSSKIN generator options. Full shape comparisons for $qqWW$ modeling uncertainties can be see in Figures B.14 - B.20.

- WW uncertainties are taken only on $qqWW$, following the PMG recommendations, with the nominal as the Sherpa $qqWW$ dilepton sample 364254, and calculated from the following variations:
  - **PDF** - Standard deviation of NNPDF3.0 PDF set.
  - **Scale** - Bin-by-bin envelope calculation of 7-point μR and μF variations.
  - α_S - Variation of the fine-structure constant compared to the nominal PDF set.
  - **Shower** - Two-point comparison of truth PowPy8 to Powheg+Herwig7, symmetrized.
  - **CKKW** - Variation of the CKKW matching scale on the Sherpa generation at truth level.
  - **QSF** - Variation of the resummation scale on the Sherpa generation at truth level.
  - **CSSKIN** - Two-point comparison of truth Sherpa with variations on the parton shower recoil scheme, symmetrized.

	Impact high / low [%]			
Systematic	ggF Top CR	ggF WW CR	ggF Incl SR	$\Delta\alpha$ [%]
Shower	±6.9	±6.2	±8.4	±1.4
Generator	±9.6	±8.9	±13.7	±3.8
Scale	11.6 / -11.6	13.6 / -13.2	11.7 / -11.6	0.1 / -0.1
ISR	-0.2 / 0.2	-0.8 / 0.7	-0.2 / 0.2	-0.0 / 0.0
FSR	-0.9 / 1.2	-4.9 / 9.1	-4.0 / 6.4	-3.2 / 5.2
PDF	±1.5	±1.6	±1.6	±0.4

Table 8.5: The major modeling uncertainties for $t\bar{t}$ events in the ggF regions. $\Delta\alpha$ is calculated as $\Delta\alpha = \frac{N_{SR}^{var}/N_{CR}^{var}}{N_{SR}^{nom}/N_{CR}^{nom}}$

Systematic	Impact high / low [%] VBF Top CR	VBF WW CR	VBF 1J SR	VBF 2J SR	$\Delta\alpha$ [%] (1J)	$\Delta\alpha$ [%] (2J)
Shower	±10.1	±6.0	±3.5	±13.9	±6.0	±3.4
Generator	±16.6	±17.9	±20.6	±17.9	±3.5	±1.2
Scale	14.5 / -13.1	14.0 / -13.2	11.6 / -11.6	13.8 / -13.8	2.5 / -2.5	0.6 / -0.6
ISR	1.9 / -1.7	-1.3 / 1.2	-1.0 / 0.9	2.7 / -2.5	-2.8 / 2.7	0.8 / -0.8
FSR	2.3 / -3.2	-2.3 / 2.9	-1.5 / 4.0	-0.6 / 0.6	-3.7 / 7.4	-2.8 / 3.9
PDF	±1.6	±1.6	±1.6	±2.1	±0.2	±1.0

Table 8.6: The major modeling uncertainties for $t\bar{t}$ events in the VBF regions. $\Delta\alpha$ is calculated as $\Delta\alpha = \frac{N_{SR}^{var}/N_{CR}^{var}}{N_{SR}^{nom}/N_{CR}^{nom}}$

Systematic	Impact high / low [%] ggF Top CR	ggF WW CR	ggF Incl SR	$\Delta\alpha$ [%]
Shower	±12.0	±20.5	±25.4	±11.9
Generator	±11.2	±15.5	±17.1	±5.2
Scale	4.4 / -4.5	4.3 / -4.4	4.4 / -4.4	0.4 / -0.4
ISR	-0.4 / 0.4	-0.8 / 0.8	4.4 / -4.4	-0.3 / 0.1
FSR	0.6 / -0.4	-3.2 / 3.1	-2.8 / 4.5	-3.4 / 5.0
Interference	±1.9	±2.5	±0.0	±1.6
PDF	±1.9	±1.9	±1.9	±0.3

Table 8.7: The major modeling uncertainties for single-top events in the ggF regions. $\Delta\alpha$ is calculated as $\Delta\alpha = \frac{N_{SR}^{var}/N_{CR}^{var}}{N_{SR}^{nom}/N_{CR}^{nom}}$

Systematic	Impact high / low [%] VBF Top CR	VBF WW CR	VBF 1J SR	VBF 2J SR	$\Delta\alpha$ [%] (1J)	$\Delta\alpha$ [%] (2J)
Shower	±10.3	±14.3	±14.8	±29.7	±4.1	±17.6
Generator	±19.8	±24.5	±22.6	±28.4	±2.3	±7.2
Scale	5.2 / -5.0	5.1 / -5.0	4.3 / -4.4	4.9 / -4.8	2.1 / -2.1	0.5 / -0.5
ISR	2.9 / -2.6	-0.0 / 0.4	-0.4 / 0.3	2.6 / -2.1	-3.3 / 3.0	-0.3 / 0.6
FSR	1.6 / -4.5	-3.2 / 2.9	-1.5 / -0.8	0.4 / 0.7	-3.1 / 3.9	-1.2 / 5.4
Interference	±2.5	±6.8	±6.4	±2.6	±9.1	±5.7
PDF	±1.9	±1.8	±1.9	±2.3	±0.3	±1.0

Table 8.8: The major modeling uncertainties for single-top events in the VBF regions. $\Delta\alpha$ is calculated as $\Delta\alpha = \frac{N_{SR}^{var}/N_{CR}^{var}}{N_{SR}^{nom}/N_{CR}^{nom}}$

Systematic	Impact high / low [%] ggF Top CR	ggF WW CR	ggF Incl SR	$\Delta\alpha$ [%]
PDF	±1.0	±1.9	±1.5	±0.7
Scale	20.00 / -14.9	3.1 / 3.9	7.5 / -6.8	4.9 / -4.9
α_S	2.1 / -2.1	1.2 / -1.2	1.4 / -1.4	0.1 / -0.1
Shower	±8.3	±3.8	±3.5	±0.4
CKKW	0.4 / 0.6	-1.2 / 0.4	-2.1 / 0.9	-0.9 / 0.5
QSF	-1.1 / 0.2	0.2 / 2.2	-1.0 / 1.9	-1.2 / -0.2
CSSKIN	±0.0	±1.9	±0.6	±0.2

Table 8.9: The major modeling uncertainties for WW events in the ggF regions. $\Delta\alpha$ is calculated as $\Delta\alpha = \frac{N_{SR}^{var}/N_{CR}^{var}}{N_{SR}^{nom}/N_{CR}^{nom}}$

	Impact high / low [%]					
Systematic	VBF Top CR	VBF WW CR	VBF 1J SR	VBF 2J SR	$\Delta\alpha$ [%] (1J)	$\Delta\alpha$ [%] (2J)
PDF	±1.1	±1.4	±1.4	±1.0	±0.3	±1.0
Scale	20.1 / -14.9	6.9 / -6.5	5.8 / -5.7	21.8 / -15.4	1.1 / -1.1	15.3 / -15.3
α_S	1.9 / -1.9	1.4 / -1.4	1.4 / -1.4	2.0 / -2.0	-0.1 / 0.1	0.6 / -0.6
Shower	±9.8	±13.0	±12.6	±13.6	±0.5	±30.6
CKKW	-10.4 / 11.9	-6.5 / 3.2	-3.3 / 2.0	-12.6 / 9.0	3.4 / -1.2	-6.5 / 5.7
QSF	-7.6 / 6.5	2.3 / 1.6	-1.1 / -0.9	-1.9 / 3.3	-3.3 / -2.5	-4.1 / 1.7
CSSKIN	±0.0	±8.7	±0.0	±0.0	±6.2	±6.1

Table 8.10: The major modeling uncertainties for WW events in the VBF regions. $\Delta\alpha$ is calculated as $\Delta\alpha = \frac{N_{SR}^{var}/N_{CR}^{var}}{N_{SR}^{nom}/N_{CR}^{nom}}$

Chapter 9

Statistical Analysis

The methodlogy used to derive the statistical results is described in detail in Ref. [34]. A likelihood function, $\mathcal{L}$, is defined using the distributions of the discriminating variable, m_T, in the signal regions of the the three analysis categories: quasi-inclusive ggF, $N_{\text{jet}} = 1$ and $\geq$ 2-jet VBF categories. The likelihood function is a product of Poisson functions over the bins of the m_T distribution in the signal regions and ones describing the total yield in each of the four control regions. The systematic uncertainties are parameterized as individual nuisance parameters, θ, modelled by a Gaussian function.

9.1 General Implementation

This analysis uses the m_T distribution as the discriminating value. The m_T distibution is divided into 18 bins in the ggF quasi-inclusive SR and 8 bins in the two VBF SR for each of the various model and mass hypotheses. The binning retains the optimization performed in the previous 36 fb^{-1} analysis [40], but has been slightly modified to give general values to avoid any specific bias being applied to a specific bin. The binning is varied, with increasing widths moving to higher masses to reflect the increasing width of the expected signal distributions as they increase with mass. The bin boundaries are shown in Table 9.1. All four control regions in the analysis combine the m_T distribution into a single bin per region.

Prior to building the workspace, nuisance parameters are split into shape and rate por-

Inclusive ggF SR									
70	100	120	140	165	195	225	270	315	375
440	525	610	725	850	1000	1400	1900	3000	

$N_{jet} = 1$ and ≥ 2 VBF SRs								
70	100	150	215	315	465	675	1000	3000

Table 9.1: Bin boundaries of the m_T [GeV] distribution for the ggF quasi-inclusve SR (top) and the VBF SRs (bottom).

tions independently. A pruning is applied to remove any rate nuisance parameter that does not have more than a 1% pre-fit contribution of the uncertainty to a specific channel in a specific regions used in the final fit. A similar pruning is applied to remove any shape portion of a nuisance parameter by performing a χ^2 calculation in each signal region and removing all nuisance parameters with a χ^2 p-value below 0.05 in a specific channel in a specific region.

The modified frequentist method for obtaining confidence level (CL) intervals [136], known as CLs, combined with an asymptotic approximation [80], is used to compute 95% confidence level upper limits on $\sigma_R \times \mathrm{BR}(H \to WW)$. The method uses a test statistic, q_μ, a function of the signal strength μ which is defined as the ratio of $\sigma_R \times \mathrm{BR}(R \to WW)$ to that of the prediction[1]. The test statistic is defined as a ratio of likelihood functions:

$$q_\mu = -2\ln\left(\frac{\mathcal{L}(\mu;\hat{\theta}_\mu)}{\mathcal{L}(\hat{\mu};\hat{\theta})}\right) \tag{9.1}$$

where θ refers to individual nuisance parameters and $\mathcal{L}$ refers to the likelihood functions. The quantities $\hat{\mu}$ and $\hat{\theta}$ are the values of μ and θ that unconditionally maximize $\mathcal{L}$. The values $\hat{\theta}_\mu$ are the values of individual nuisance parameters that maximise $\mathcal{L}$ for a given value of μ. The general form of the likelihood function for each m_T bin in each region is given as:

$$\mathcal{L}(\mu,\mu_b) = P(N|\mu_s + \mu_b b^{\mathrm{exp}}_{\mathrm{SR}}) \times P(M|\mu_b b^{\mathrm{exp}}_{\mathrm{CR}}) \tag{9.2}$$

where N and M are the number of data events in the signal and control regions respectively,

[1]The previously derived limits, where available, are used for the prediction normalization. Specifically for Radion samples, the normalization is taken from Ref. [61]

s is the expected signal yield in the signal region, $b_{\mathrm{SR}}^{\mathrm{exp}}$ and $b_{\mathrm{CR}}^{\mathrm{exp}}$ are expected background yields in the signal and control regions, respectively, μ is the signal strength parameters, μ_b is the strength for the background b.

9.2 Statistical Treatment of Uncertainties on Background Estimation and Signal Prediction

Statistical uncertainties apply to each m_T bin in each signal region and to the single bin control regions. Systematic uncertainties of both shape and rate are applied depending on the type of background channel being considered:

- **Standard Model WW :** Systematic uncertainties of both shape and rate apply. As can be seen from tables in Appendix A, the experimental systematics have similarities between signal and control regions, allowing for strong cancellations. In the $N_{\mathrm{jet}} \geq 2$ VBF category, the normalization is taken from the MC prediction and shape and rate uncertainties apply.

- **$t\bar{t}$ and Wt:** In the quasi-inclusive ggF and $N_{\mathrm{jet}} \geq 2$ VBF categories, the normalization is constrained from control regions, so that shape and rate uncertainties apply, but again most experimental systematics show large cancellations between signal and control regions.

- **W+jets :** The data-driven method, described in detail in Chapter 7.2.4. Systematic uncertainties are applied specifically to this sample and procedure, and contain both shape and rate components.

- **Z/γ+jets, Non-WW diboson, SM Higgs :** These small backgrounds are estimated purely by MC techniques, so that uncertainties of shape and rate apply normally. However, for simplification of the fit, the shape portion of these small backgrounds is removed to avoid large impacts from statistical fluctuations in the high m_T bins where these backgrounds contribute very little.

- **Signal samples :** All signal models are predicted purely by MC techniques, so that uncertainties of shape and rate apply.

Further optimization of nuisance parameters is required for the theoretical uncertainties outlined in Chapter 8.2. First and foremost, the individual NPs are decorrelated across the VBF-GGF phase-space, such that two nuisance parameters for each uncertainty are included in the fit construction. Additionally, due to the low statistics at the high m_T region in the VBF space, the Wt theoretical unceraintes have their shape portion removed. Similar to the Non-WW diboson, SM Higgs, and Z/γ+jets background above, this removes the spurious impact of statistical fluctuations that could arise in these low stat regions.

9.3 Statistical Results

Figure 9.1 shows the 95% confidence level upper limits on $\sigma_H \times \text{BR}(H \to WW)$ as a function of m_H for a Higgs boson in the NWA scenario for each production mode (ggF and VBF) separately. Figure 9.3 shows the 95% confidence level upper limits on $\sigma_R \times \text{BR}(H \to WW)$ as a function of m_H for the bulk RS Kaluza-Klein Graviton and the Heavy-Higgs in the Georgi-Machacek model, respectively. Figure 9.4 shows the 95% confidence level upper limits on $\sigma_R \times \text{BR}(H \to WW)$ as a function of m_R for a resonant boson in the HVT model for each production mode (ggF and VBF) separately. Figure 9.2 shows the 95% confidence level upper limits on $\sigma_\phi \times \text{BR}(H \to WW)$ as a function of m_ϕ for a resonant radion in the RS model for each production mode (ggF and VBF) separately. The pull[2] for all nuisance parameters surviving the pruning stage and their corresponding contribution to the uncertainty on μ is given in Figure 9.5 for the $m_H = 800$ GeV NWA model. The contribution on the total

[2] A pull refers to the deviation of a parameter away from its central value. An in-depth look at pulls can be found in [85]

uncertainty is calculated as the quadratic difference of the uncertainty of the signal strength μ in a fit using only all uncertainties and a fit where the nuisance parameter concerned is removed [48]. Figure 9.6 shows the post-fit correlation matrices for the $m_H = 800$ GeV NWA model. Figures 9.7 and 9.8 show the same pull and correlation plots for the $m_H = 2200$ GeV NWA model.

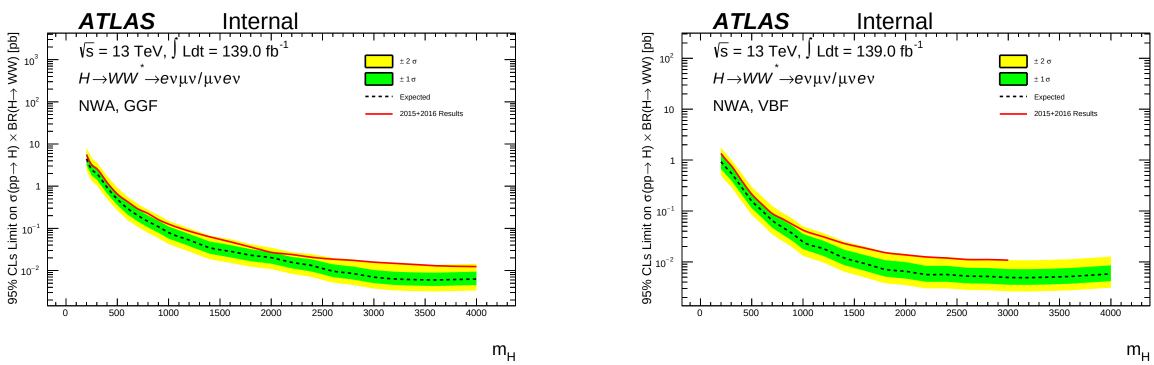

Figure 9.1: 95% CL$_s$ upper limits on the Higgs production cross section times branching ratio $\sigma \times \mathrm{BR}(H \to WW)$ for a signal with the narrow-width approximation for the ggF production mode (left) and the VBF production mode (right). The green and yellow bands correspond to the $\pm 1\sigma$ and $\pm 2\sigma$ uncertainties on the expected limit calculation.

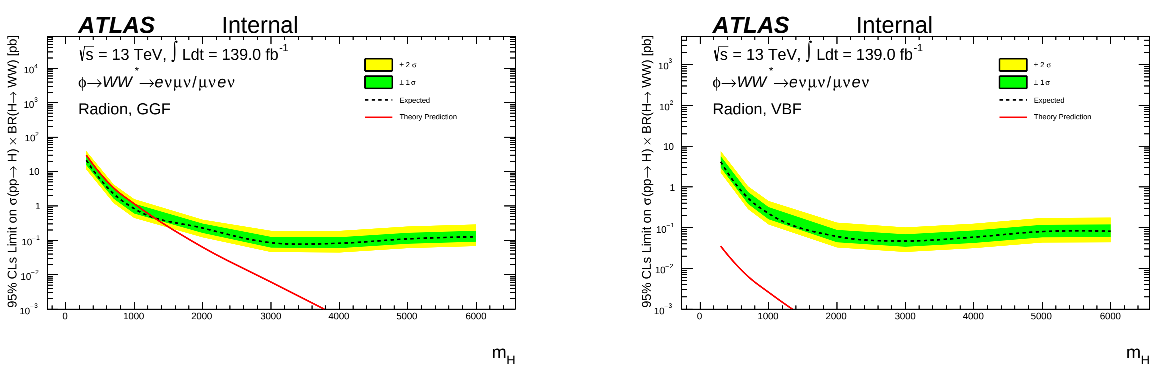

Figure 9.2: 95% CL$_s$ upper limits on the resonant boson production cross section times branching ratio $\sigma \times \mathrm{BR}(H \to WW)$ for a signal from the Radion particle for the ggF production mode (left) and the VBF production mode (right). The green and yellow bands correspond to the $\pm 1\sigma$ and $\pm 2\sigma$ uncertainties on the expected limit calculation. The red line corresponds to the theoretical cross section prediction.

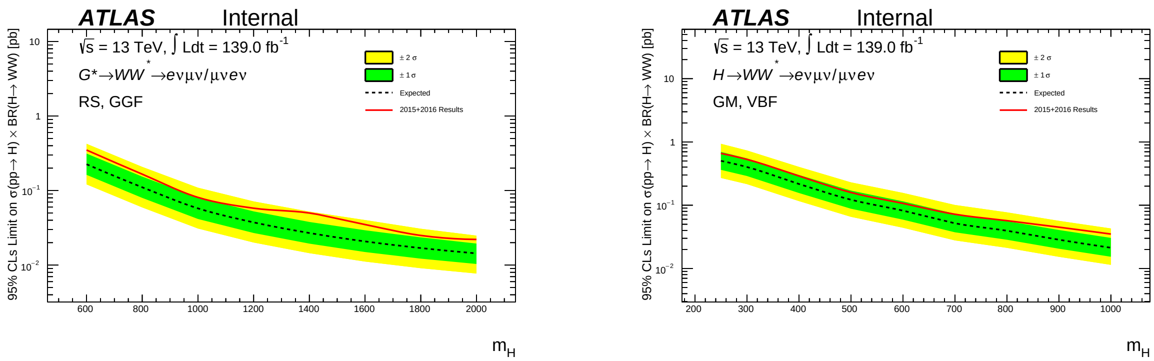

Figure 9.3: 95% CL_s upper limits on the Higgs production cross section times branching ratio $\sigma \times \mathrm{BR}(H \to WW)$ for a Kaluza-Klein Graviton in the bulk RS model with ggF production mode (left) and the Heavy-Higgs boson arising from the Georgi-Machacek model with VBF production mode (right). The green and yellow bands correspond to the $\pm 1\sigma$ and $\pm 2\sigma$ uncertainties on the expected limit calculation.

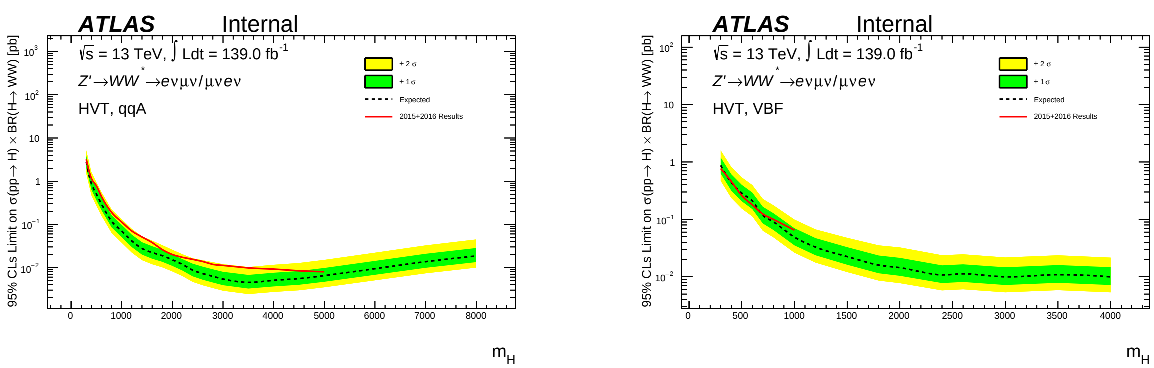

Figure 9.4: 95% CL_s upper limits on the resonant boson production cross section times branching ratio $\sigma \times \mathrm{BR}(H \to WW)$ for a signal from the Heavy Vector Triplet model for the qqA production mode (left) and the VBF production mode (right). The green and yellow bands correspond to the $\pm 1\sigma$ and $\pm 2\sigma$ uncertainties on the expected limit calculation.

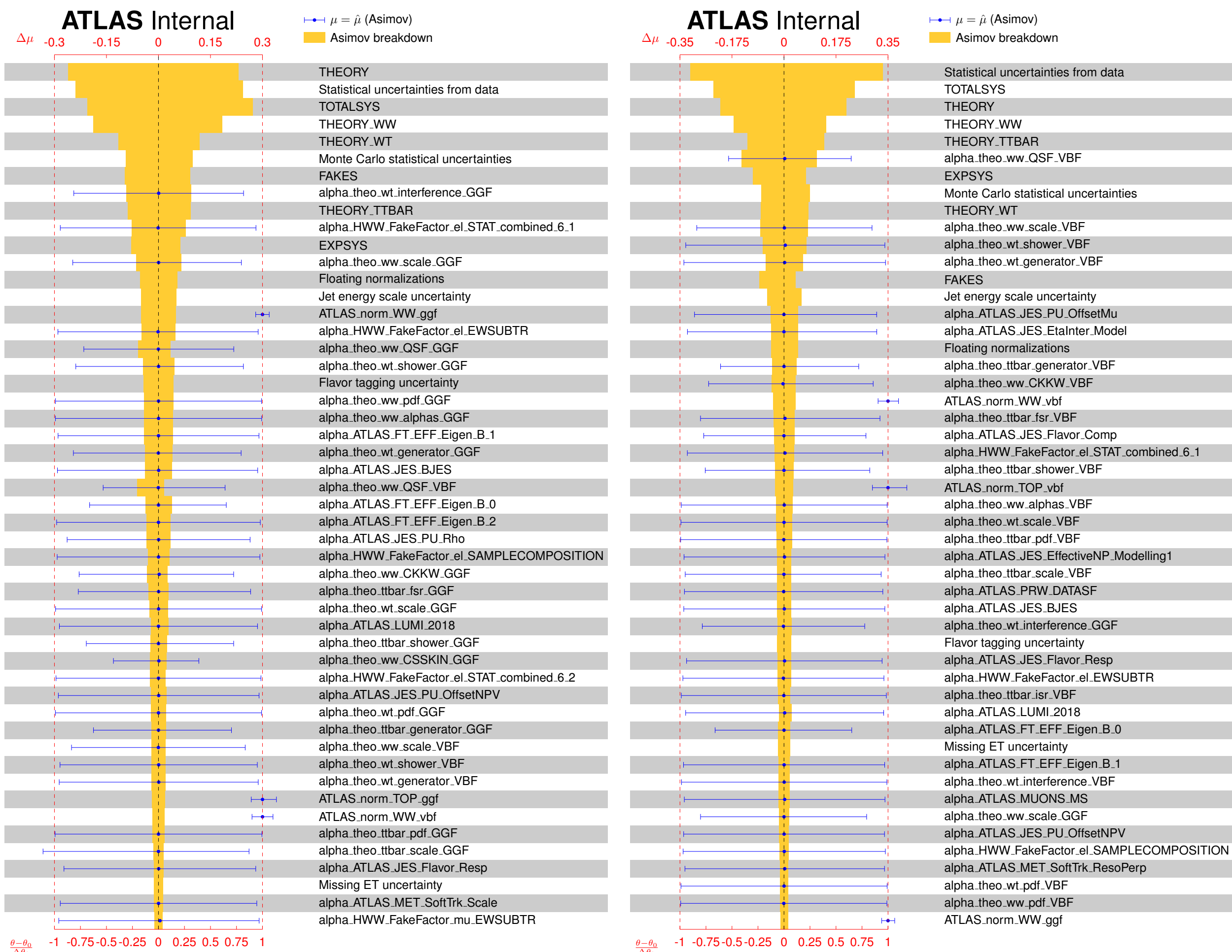

Figure 9.5: The pull distributions and post-fit uncertainties of the nuisance parameters for the $\mu = \hat{\mu}$ for the $m_H = 800$ GeV fit for the ggF production mode (left) and the VBF production mode (right). Only the largest 50 groupings or NPs are shown.

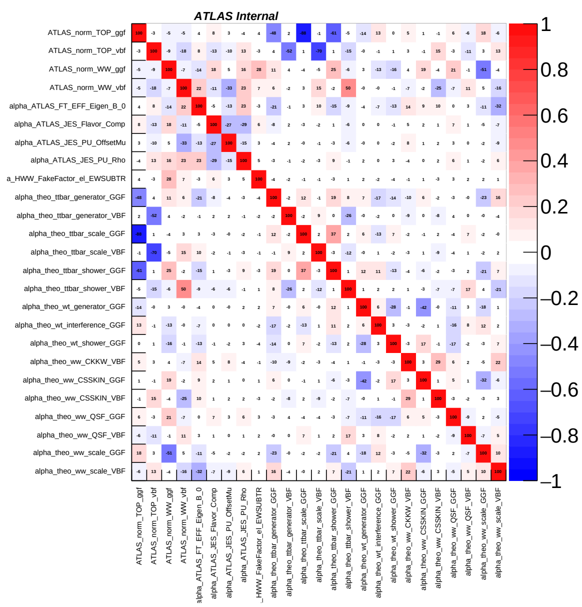

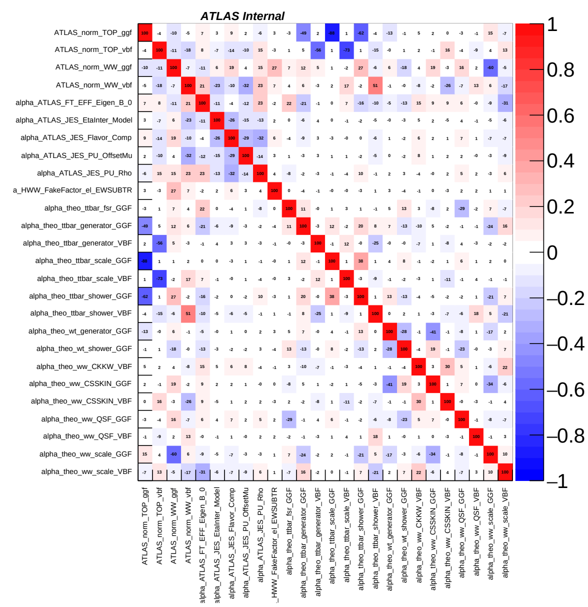

Figure 9.6: Correlation matrices for the $m_H = 800$ GeV fit for the ggF production mode (left) and the VBF production mode (right). The top plot shows all nuisance parameters with correlations larger than 25%, and the bottom plot shows the full correlation matrix of all nuisance parameters that are not skimmed away prior to the fit.

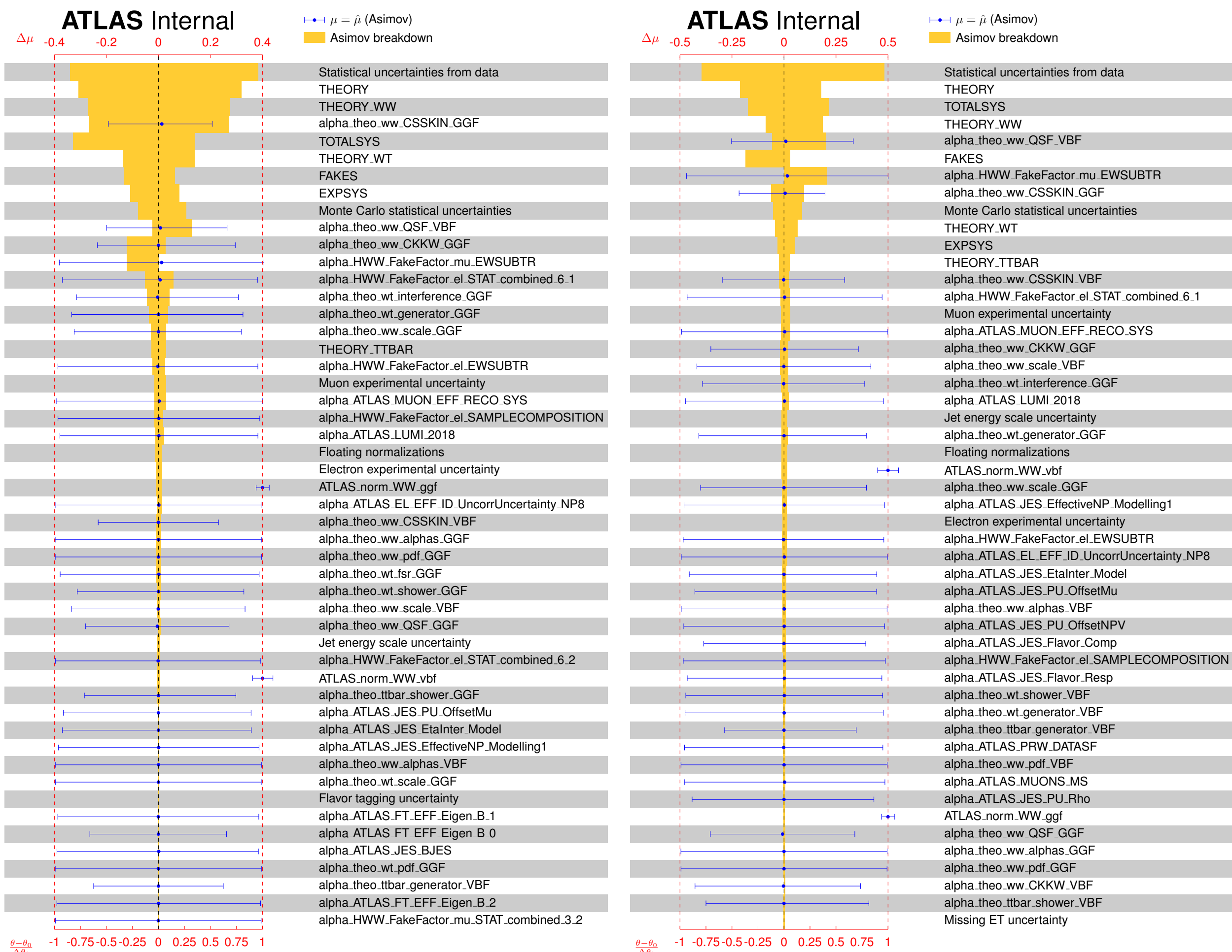

Figure 9.7: Fitted values of the nuisance parameters for the $\mu = \hat{\mu}$ for the $m_H = 2200$ GeV fit for the ggF production mode (left) and the VBF production mode (right). Only the largest 50 groupings or NPs are shown.

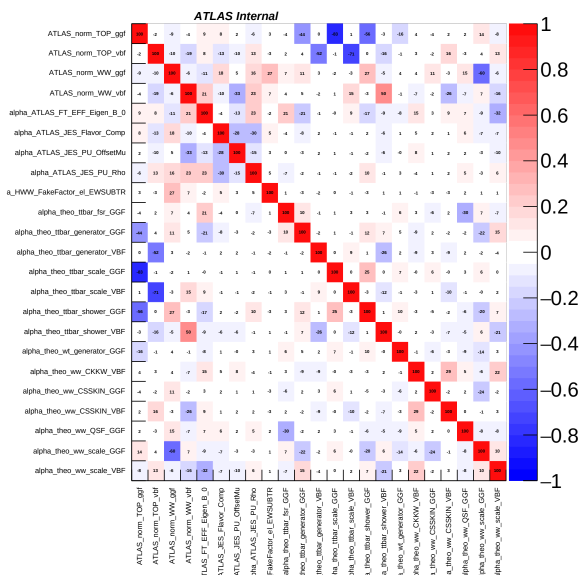

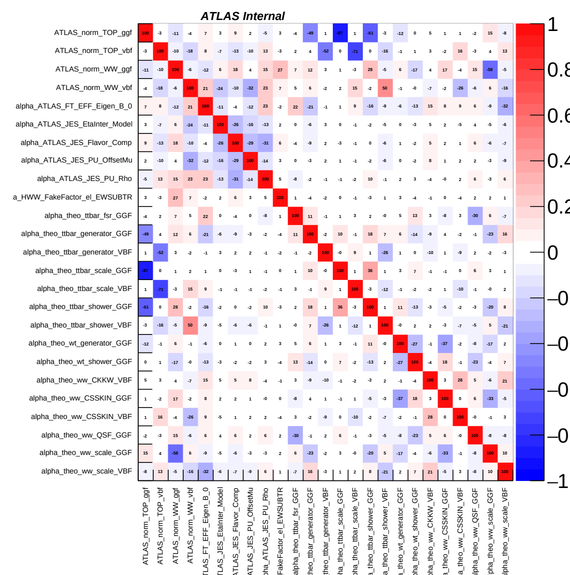

Figure 9.8: Correlation matrices for the $m_H = 2200$ GeV fit for the ggF production mode (left) and the VBF production mode (right). The top plot shows all nuisance parameters with correlations larger than 25%, and the bottom plot shows the full correlation matrix of all nuisance parameters that are not skimmed away prior to the fit.

Chapter 10

Conclusions

A search for a neutral heavy resonance decaying in the $R \to WW \to \ell\nu\ell\nu$ decay channel was performed using 139 fb^{-1} of LHC pp collision data recorded by the ATLAS dector at a center-of-mass energy of $\sqrt{s} = 13$ TeV. No significant deviation from the SM background-only prediction is observed. Therefore, upper limits on $\sigma_R \times \mathrm{BR}\,(R \to WW)$ are set on the resonances described in Chapter 2.3.1 for each production mode and as a function of the resonance mass, m_R. The results show significant improvement over the previous 36 fb^{-1} analysis in both cross-section times branching ratio limits and mass range explored.

The interpretations considered in this thesis look to provide answers to some of the missing pieces of the SM. For instance, the RS model uses extra dimensions to try and solve the hierarchy problem, the heavy vector triple model provides a probe into the heavier generations of vector bosons, and the Georgi-Machacek model gives explanation to neutrino masses. While non-discovery in these interpretations does not give a clear solution, it allows for a narrowing down of physical regions that physicists and theorists can use to continue to probe the BSM space.

Additional searches in the high-mass space continue to be performed, such as those to be included in the heavy-resonance combination analysis performed by ATLAS. [116] Additional improvements to the $R \to WW \to \ell\nu\ell\nu$ search continue to be explored, such as the inclusion of the same-flavor lepton final state [99], which looks to improve the sensitivity of the current results by a factor of $\sqrt{2}$. Additionally, the ATLAS detector to continues its upgrade program to prepare for the LHC Run-3 data-taking campaign, which hopes to reach a center-of-mass energy of $\sqrt{s} = 14$ TeV, allowing for production of high mass decays at a higher frequency.

References

Bibliography

[1] TTbarNNLOReweighter package. https://gitlab.cern.ch/lserkin/TTbarNNLOReweighter.

[2] ATLAS Pythia 8 tunes to 7 TeV datas. Technical Report ATL-PHYS-PUB-2014-021, CERN, Geneva, Nov 2014.

[3] Calibration of b-tagging using dileptonic top pair events in a combinatorial likelihood approach with the ATLAS experiment. Technical Report ATLAS-CONF-2014-004, CERN, Geneva, Feb 2014.

[4] Tagging and suppression of pileup jets with the ATLAS detector. Technical Report ATLAS-CONF-2014-018, CERN, Geneva, May 2014.

[5] Expected performance of missing transverse momentum reconstruction for the ATLAS detector at $\sqrt{s} = 13$ TeV. Technical Report ATL-PHYS-PUB-2015-023, CERN, Geneva, Jul 2015.

[6] Muon reconstruction performance in early $\sqrt{s} = 13$ TeV data. Technical Report ATL-PHYS-PUB-2015-037, CERN, Geneva, Aug 2015.

[7] Electron efficiency measurements with the ATLAS detector using the 2015 LHC proton-proton collision data. Technical Report ATLAS-CONF-2016-024, CERN, Geneva, Jun 2016.

[8] Electron and photon reconstruction and performance in ATLAS using a dynamical, topological cell clustering-based approach. Technical Report ATL-PHYS-PUB-2017-022, CERN, Geneva, Dec 2017.

[9] Identification of Jets Containing b-Hadrons with Recurrent Neural Networks at the ATLAS Experiment. Technical Report ATL-PHYS-PUB-2017-003, CERN, Geneva, Mar 2017.

[10] Top-pair production at the LHC through NNLO QCD and NLO EW. *J. High Energ. Phys.*, 10:186, 2017.

[11] Object-based missing transverse momentum significance in the ATLAS detector. Technical Report ATLAS-CONF-2018-038, CERN, Geneva, Jul 2018.

[12] M. Aaboud, G. Aad, B. Abbott, J. Abdallah, O. Abdinov, B. Abeloos, S. Abidi, O. AbouZeid, N. Abraham, H. Abramowicz, and et al. Jet energy scale measurements and their systematic uncertainties in proton-proton collisions at $\sqrt{s} = 13$tev with the atlas detector. *Physical Review D*, 96(7), Oct 2017.

[13] M. Aaboud, G. Aad, B. Abbott, J. Abdallah, O. Abdinov, B. Abeloos, O. S. AbouZeid, N. L. Abraham, H. Abramowicz, and et al. Electron efficiency measurements with the atlas detector using 2012 lhc proton–proton collision data. *The European Physical Journal C*, 77(3), Mar 2017.

[14] M. Aaboud et al. Search for heavy resonances decaying into WW in the $e\nu\mu\nu$ final state in pp collisions at $\sqrt{s} = 13$ TeV with the ATLAS detector. *Eur. Phys. J. C*, 78(1):24, 2018.

[15] G. Aad, B. Abbott, J. Abdallah, S. Abdel Khalek, O. Abdinov, R. Aben, B. Abi, M. Abolins, O. S. AbouZeid, and et al. Measurement of the z/γ * boson transverse momentum distribution in pp collisions at $\sqrt{s} = 7$ tev with the atlas detector. *Journal of High Energy Physics*, 2014(9), Sep 2014.

[16] G. Aad et al. Observation of a new particle in the search for the Standard Model Higgs boson with the ATLAS detector at the LHC. *Phys. Lett. B*, 716:1–29, 2012.

[17] G. Aad et al. Muon reconstruction performance of the ATLAS detector in proton–proton collision data at $\sqrt{s}$ =13 TeV. *Eur. Phys. J. C*, 76(5):292, 2016.

[18] e. a. Aamodt, K. The ALICE experiment at the CERN LHC. A Large Ion Collider Experiment. *JINST*, 3:S08002. 259 p, 2008. Also published by CERN Geneva in 2010.

[19] S. Actis, G. Passarino, C. Sturm, and S. Uccirati. NLO Electroweak Corrections to Higgs Boson Production at Hadron Colliders. *Phys. Lett. B*, 670:12–17, 2008.

[20] S. Actis, G. Passarino, C. Sturm, and S. Uccirati. NNLO Computational Techniques: The Cases H to gamma gamma and H to g g. *Nucl.Phys.*, B811:182–273, 2009.

[21] K. Agashe, R. Contino, and A. Pomarol. The Minimal composite Higgs model. *Nucl. Phys. B*, 719:165–187, 2005.

[22] K. Agashe, H. Davoudiasl, G. Perez, and A. Soni. Warped Gravitons at the LHC and Beyond. *Phys. Rev.*, D76:036006, 2007.

[23] A. Aggarwal, S. Argyropoulos, M. J. Basso, A. K. Becker, C. Bertella, C. D. Burgard, D. Duda, D. Du, A. Farilla, F. Filthaut, A. Gavrilyuk, N. A. Grieser, R. Gugel, R. L. Hayes, C. Hays, P.-h. J. Hsu, C.-t. Huang, Y.-c. Huang, G. Iakovidis, B. P. Jaeger, C. Kitsaki, K. Koeneke, A. Kotwal, K. Lehmann, H.-c. Lin, K. Lohwasser, Y.-J. Lu, A. Montalbano, T. H. Park, F. Pasquali, E. Ramakoti, C. Schmitt, S. Sen, D. R. Shope, H. A. Smith, J. Strandberg, M. Strauss, I. Tsukerman, S. Wang, B. T. Winter, and G. Zemaityte. Measurements of the Higgs boson production cross section via ggF and VBF in $H\to WW^*\to \ell\nu\ell\nu$ with 139 fb^{-1} of data collected with the ATLAS detector at $\sqrt{s}$ = 13 TeV. Technical Report ATL-COM-PHYS-2020-302, CERN, Geneva, May 2020.

[24] S. Alioli, K. Hamilton, P. Nason, C. Oleari, and E. Re. Jet pair production in powheg. *Journal of High Energy Physics*, 2011(4), Apr 2011.

[25] S. Alioli, P. Nason, C. Oleari, and E. Re. Nlo higgs boson production via gluon fusion matched with shower in powheg. *Journal of High Energy Physics*, 2009(04):002–002, Apr 2009.

[26] S. Alioli, P. Nason, C. Oleari, and E. Re. A general framework for implementing NLO calculations in shower Monte Carlo programs: the POWHEG BOX. *JHEP*, 06:043, 2010.

[27] J. Alwall, R. Frederix, S. Frixione, V. Hirschi, F. Maltoni, O. Mattelaer, H.-S. Shao, T. Stelzer, P. Torrielli, and M. Zaro. The automated computation of tree-level and next-to-leading order differential cross sections, and their matching to parton shower simulations. *Journal of High Energy Physics*, 2014(7), Jul 2014.

[28] C. Anastasiou, L. J. Dixon, K. Melnikov, and F. Petriello. High precision QCD at hadron colliders: Electroweak gauge boson rapidity distributions at NNLO. *Phys. Rev. D*, 69:094008, 2004.

[29] C. Anastasiou, C. Duhr, F. Dulat, E. Furlan, T. Gehrmann, F. Herzog, A. Lazopoulos, and B. Mistlberger. High precision determination of the gluon fusion Higgs boson cross-section at the LHC. *JHEP*, 05:058, 2016.

[30] C. Anastasiou, C. Duhr, F. Dulat, F. Herzog, and B. Mistlberger. Higgs Boson Gluon-Fusion Production in QCD at Three Loops. *Phys. Rev. Lett.*, 114:212001, 2015.

[31] A. R. M. and. The run-2 ATLAS trigger system. *Journal of Physics: Conference Series*, 762:012003, oct 2016.

[32] O. Antipin, D. Atwood, and A. Soni. Search for RS gravitons via W(L)W(L) decays. *Phys. Lett. B*, 666:155–161, 2008.

[33] O. Antipin and A. Soni. Towards establishing the spin of warped gravitons. *JHEP*, 10:018, 2008.

[34] ATLAS Collaboration. Combined search for the Standard Model Higgs boson in pp collisions at $\sqrt{s} = 7\,\mathrm{TeV}$ with the ATLAS detector. *Phys. Rev. D*, 86:032003, 2012.

[35] ATLAS Collaboration. ATLAS Pythia 8 tunes to 7 TeV data. ATL-PHYS-PUB-2014-021, 2014.

[36] ATLAS Collaboration. Studies on top-quark Monte Carlo modelling for Top2016. ATL-PHYS-PUB-2016-020, 2016.

[37] ATLAS Collaboration. Jet energy scale measurements and their systematic uncertainties in proton–proton collisions at $\sqrt{s} = 13\,\mathrm{TeV}$ with the ATLAS detector. *Phys. Rev. D*, 96:072002, 2017.

[38] ATLAS Collaboration. Jet reconstruction and performance using particle flow with the ATLAS Detector. *Eur. Phys. J. C*, 77:466, 2017.

[39] ATLAS Collaboration. Performance of missing transverse momentum reconstruction with the ATLAS detector using proton–proton collisions at $\sqrt{s} = 13\,\mathrm{TeV}$. *Eur. Phys. J. C*, 78:903, 2018.

[40] ATLAS Collaboration. Search for heavy resonances decaying into WW in the $e\nu\mu\nu$ final state in pp collisions at $\sqrt{s} = 13\,\mathrm{TeV}$ with the ATLAS detector. *Eur. Phys. J. C*, 78:24, 2018.

[41] ATLAS Collaboration. Luminosity determination in pp collisions at $\sqrt{s} = 13\,\mathrm{TeV}$ using the ATLAS detector at the LHC. ATLAS-CONF-2019-021, 2019.

[42] ATLAS Collaboration. Measurements of top-quark pair differential and double-differential cross-sections in the ℓ+jets channel with pp collisions at $\sqrt{s} = 13\,\mathrm{TeV}$ using the ATLAS detector. 2019.

[43] G. Avoni, M. Bruschi, G. Cabras, D. Caforio, N. Dehghanian, A. Floderus, B. Giacobbe, F. Giannuzzi, F. Giorgi, P. Grafström, V. Hedberg, F. Lasagni Manghi, S. Meneghini, J. Pinfold, E. Richards, C. Sbarra, N. Semprini Cesari, A. Sbrizzi, R. Soluk, G. Ucchielli, S. Valentinetti, O. Viazlo, M. Villa, C. Vittori, R. Vuillermet, and A. Zoccoli. The new LUCID-2 detector for luminosity measurement and monitoring in ATLAS. *JINST*, 13(07):P07017. 33 p, 2018.

[44] R. D. Ball, V. Bertone, S. Carrazza, C. S. Deans, L. Del Debbio, S. Forte, A. Guffanti, N. P. Hartland, J. I. Latorre, and et al. Parton distributions for the lhc run ii. *Journal of High Energy Physics*, 2015(4), Apr 2015.

[45] R. D. Ball et al. Parton distributions with LHC data. *Nucl. Phys. B*, 867:244–289, 2013.

[46] R. D. Ball et al. Parton distributions for the LHC Run II. *JHEP*, 04:040, 2015.

[47] M. Banner et al. Observation of Single Isolated Electrons of High Transverse Momentum in Events with Missing Transverse Energy at the CERN anti-p p Collider. *Phys. Lett. B*, 122:476–485, 1983.

[48] N. Berger. Lecture on ATLAS Statistical Analysis Methods. https://cds.cern.ch/record/2285058/files/ATL-PHYS-SLIDE-2017-797.pdf.

[49] P. Bolzoni, F. Maltoni, S.-O. Moch, and M. Zaro. Higgs production via vector-boson fusion at NNLO in QCD. *Phys. Rev. Lett.*, 105:011801, 2010.

[50] M. Bonetti, K. Melnikov, and L. Tancredi. Higher order corrections to mixed QCD-EW contributions to Higgs boson production in gluon fusion. *Phys. Rev. D*, 97(5):056017, 2018. [Erratum: Phys.Rev.D 97, 099906 (2018)].

[51] E. Bothmann et al. Event Generation with Sherpa 2.2. *SciPost Phys.*, 7(3):034, 2019.

[52] A. Bredenstein, A. Denner, S. Dittmaier, and M. Weber. Precise predictions for the Higgs-boson decay H to WW/ZZ to 4 leptons. *Phys.Rev.*, D74:013004, 2006. 42 pages, LaTeX, 38 postscript figures, references updated, some typos corrected, version to appear in Phys. Rev. D Report-no: MPP-2005-24, PSI-PR-06-05.

[53] A. Bredenstein, A. Denner, S. Dittmaier, and M. Weber. Precision calculations for the Higgs decays H —¿ ZZ/WW —¿ 4 leptons. *Nucl. Phys. B Proc. Suppl.*, 160:131–135, 2006.

[54] A. Bredenstein, A. Denner, S. Dittmaier, and M. Weber. Radiative corrections to the semileptonic and hadronic Higgs-boson decays H to W W / Z Z to 4 fermions. *JHEP*, 0702:080, 2007. 29 pages, LaTeX, 30 postscript figures.

[55] O. S. Brüning, P. Collier, P. Lebrun, S. Myers, R. Ostojic, J. Poole, and P. Proudlock. *LHC Design Report*. CERN Yellow Reports: Monographs. CERN, Geneva, 2004.

[56] J. Butterworth et al. PDF4LHC recommendations for LHC Run II. *J. Phys. G*, 43:023001, 2016.

[57] M. Cacciari, G. P. Salam, and G. Soyez. The anti-k_t jet clustering algorithm. *JHEP*, 04:063, 2008.

[58] M. Cacciari, G. P. Salam, and G. Soyez. FastJet user manual. *Eur. Phys. J. C*, 72:1896, 2012.

[59] J. M. Campbell, R. Ellis, R. Frederix, P. Nason, C. Oleari, and C. Williams. NLO Higgs Boson Production Plus One and Two Jets Using the POWHEG BOX, MadGraph4 and MCFM. *JHEP*, 07:092, 2012.

[60] M. Capeans, G. Darbo, K. Einsweiller, M. Elsing, T. Flick, M. Garcia-Sciveres, C. Gemme, H. Pernegger, O. Rohne, and R. Vuillermet. ATLAS Insertable B-Layer

Technical Design Report. Technical Report CERN-LHCC-2010-013. ATLAS-TDR-19, Sep 2010.

[61] A. Carvalho. Gravity particles from warped extra dimensions, predictions for lhc, 2014.

[62] F. Cascioli, P. Maierhofer, and S. Pozzorini. Scattering Amplitudes with Open Loops. *Phys. Rev. Lett.*, 108:111601, 2012.

[63] S. Catani and M. Grazzini. An NNLO subtraction formalism in hadron collisions and its application to Higgs boson production at the LHC. *Phys. Rev. Lett.*, 98:222002, 2007.

[64] S. Catani, F. Krauss, R. Kuhn, and B. Webber. QCD matrix elements + parton showers. *JHEP*, 11:063, 2001.

[65] M. S. Chanowitz and M. K. Gaillard. The TeV physics of strongly interacting W's and Z's. *Nucl. Phys. B*, 261:379, 1985.

[66] M. S. Chanowitz and M. Golden. Higgs boson triplets with mw=mzcos θw. *Physics Letters B*, 165(1):105 – 108, 1985.

[67] S. Chatrchyan et al. Observation of a New Boson at a Mass of 125 GeV with the CMS Experiment at the LHC. *Phys. Lett. B*, 716:30–61, 2012.

[68] M. Ciccolini, A. Denner, and S. Dittmaier. Strong and electroweak corrections to the production of Higgs + 2jets via weak interactions at the LHC. *Phys. Rev. Lett.*, 99:161803, 2007.

[69] M. Ciccolini, A. Denner, and S. Dittmaier. Electroweak and QCD corrections to Higgs production via vector-boson fusion at the LHC. *Phys. Rev. D*, 77:013002, 2008.

[70] A. Collaboration. Tools for estimating fake/non-prompt lepton backgrounds in ATLAS. https://cds.cern.ch/record/2686919.

[71] A. Collaboration. The ATLAS experiment at the CERN large hadron collider. *Journal of Instrumentation*, 3(08):S08003–S08003, aug 2008.

[72] A. Collaboration. he ATLAS Inner Detector commissioning and calibration. *Eur. Phys. J*, 70:787–821, 2010.

[73] A. Collaboration. Measurement of the muon reconstruction performance of the ATLAS detector using 2011 and 2012 LHC proton–proton collision data. *The European Physical Journal C*, 74:3130, 2012.

[74] C. Collaboration. Overview of the cms detector performance in lhc run ii. *EPJ Web of Conferences*, 164(07023), dec 2017.

[75] T. L. Collaboration. The LHCb detector at the LHC. *Journal of Instrumentation*, 3(08):S08005–S08005, aug 2008.

[76] R. Contino, D. Marzocca, D. Pappadopulo, and R. Rattazzi. On the effect of resonances in composite Higgs phenomenology. *JHEP*, 10:081, 2011.

[77] J. M. Cornwall, D. N. Levin, and G. Tiktopoulos. Derivation of gauge invariance from high-energy unitarity bounds on the S matrix. *Phys. Rev. D*, 10:1145, 1974.

[78] W. N. Cottingham and D. A. Greenwood. *An Introduction to the Standard Model of Particle Physics*. Cambridge University Press, 2 edition, 2007.

[79] R. D. Cousins, J. T. Linnemann, and J. Tucker. Evaluation of three methods for calculating statistical significance when incorporating a systematic uncertainty into a test of the background-only hypothesis for a poisson process. *Nuclear Instruments and Methods in Physics Research Section A: Accelerators, Spectrometers, Detectors and Associated Equipment*, 595(2):480–501, Oct 2008.

[80] G. Cowan, K. Cranmer, E. Gross, and O. Vitells. Asymptotic formulae for likelihood-based tests of new physics. *The European Physical Journal C*, 71(2), Feb 2011.

[81] S. Dawson. Introduction to electroweak symmetry breaking. In *ICTP Summer School in High-Energy Physics and Cosmology*, pages 1–83, 6 1998.

[82] J. de Blas, J. M. Lizana, and M. Perez-Victoria. Combining searches of Z' and W' bosons. *JHEP*, 01:166, 2013.

[83] D. de Florian et al. Handbook of LHC Higgs Cross Sections: 4. Deciphering the Nature of the Higgs Sector. 2/2017, 10 2016.

[84] C. Degrande, K. Hartling, H. E. Logan, A. D. Peterson, and M. Zaro. Automatic predictions in the georgi-machacek model at next-to-leading order accuracy. *Physical Review D*, 93(3), Feb 2016.

[85] L. Demortier and L. Lyons. Everything you always wanted to know about pulls. Technical report, 2002.

[86] A. Denner, S. Dittmaier, and L. Hofer. Collier: a fortran-based Complex One-Loop LIbrary in Extended Regularizations. *Comput. Phys. Commun.*, 212:220–238, 2017.

[87] S. Dittmaier et al. Handbook of LHC Higgs Cross Sections: 1. Inclusive Observables. 1 2011.

[88] A. Djouadi, J. Kalinowski, and M. Spira. Hdecay: A program for higgs boson decays in the standard model and its supersymmetric extension. *Comput. Phys. Commun.*, 108:56–74, 1998.

[89] A. Djouadi, M. M. Muhlleitner, and M. Spira. Decays of supersymmetric particles: The Program SUSY-HIT (SUspect-SdecaY-Hdecay-InTerface). *Acta Phys. Polon.*, B38:635–644, 2007.

[90] O. Ducu. Recommended isolation working points. `https://twiki.cern.ch/twiki/bin/view/AtlasProtected/RecommendedIsolationWPs`.

[91] J. R. Ellis. Limits of the Standard Model. Technical Report hep-ph/0211168. CERN-TH-2002-320, CERN, Geneva, Nov 2002.

[92] F. Englert and R. Brout. Broken symmetry and the mass of gauge vector mesons. *Phys. Rev. Lett.*, 13:321–323, Aug 1964.

[93] A. G. et al. Data/mc comparisons for (vbf) $h/h \to ww^{(*)} \to \ell\nu\ell\nu$ channel with the complete 2015-2018 year dataset with the v20 pxaod samples. ATL-COM-PHYS-2019-1331.

[94] R. Frederix, E. Re, and P. Torrielli. Single-top t-channel hadroproduction in the four-flavour scheme with POWHEG and aMC@NLO. *JHEP*, 09:130, 2012.

[95] S. Frixione, E. Laenen, P. Motylinski, B. R. Webber, and C. D. White. Single-top hadroproduction in association with a W boson. *JHEP*, 07:029, 2008.

[96] S. Frixione, P. Nason, and C. Oleari. Matching nlo qcd computations with parton shower simulations: the powheg method. *Journal of High Energy Physics*, 2007(11):070–070, Nov 2007.

[97] S. Frixione, P. Nason, and C. Oleari. Matching NLO QCD computations with parton shower simulations: the POWHEG method. *JHEP*, 11:070, 2007.

[98] S. Frixione, P. Nason, and G. Ridolfi. A Positive-weight next-to-leading-order Monte Carlo for heavy flavour hadroproduction. *JHEP*, 09:126, 2007.

[99] A. Gavrilyuk, E. Ramakoti, and I. Tsukerman. Jet ISJVTPU flag and MC study of (VBF) $h/H \to WW^{(*)} \to \ell\nu\ell\nu$ channel with the complete 2015-2018 year dataset with the v20 CAF version. Technical Report ATL-COM-PHYS-2020-042, CERN, Geneva, Jan 2020. Draft 0.

[100] H. Georgi and M. Machacek. Doubly charged higgs bosons. *Nuclear Physics B*, 262(3):463 – 477, 1985.

[101] G. Giudice, C. Grojean, A. Pomarol, and R. Rattazzi. The Strongly-Interacting Light Higgs. *JHEP*, 06:045, 2007.

[102] T. Gleisberg and S. Höche. Comix, a new matrix element generator. *JHEP*, 12:039, 2008.

[103] S. Godfrey and K. Moats. Exploring Higgs Triplet Models via Vector Boson Scattering at the LHC. *Phys. Rev. D*, 81:075026, 2010.

[104] W. D. Goldberger and M. B. Wise. Modulus stabilization with bulk fields. *Phys. Rev. Lett.*, 83:4922–4925, 1999.

[105] W. D. Goldberger and M. B. Wise. Phenomenology of a stabilized modulus. *Phys. Lett.*, B475:275–279, 2000.

[106] G. J. Gounaris, R. Kogerler, and H. Neufeld. Relationship between longitudinally polarized vector bosons and their unphysical scalar partners. *Phys. Rev. D*, 34:3257, 1986.

[107] H. X. W. Group. Lhchxswgcrosssectionsfigures, 2016.

[108] K. Hamilton, P. Nason, C. Oleari, and G. Zanderighi. Merging H/W/Z + 0 and 1 jet at NLO with no merging scale: a path to parton shower + NNLO matching. *JHEP*, 05:082, 2013.

[109] K. Hamilton, P. Nason, E. Re, and G. Zanderighi. NNLOPS simulation of Higgs boson production. *JHEP*, 10:222, 2013.

[110] K. Hamilton, P. Nason, and G. Zanderighi. MINLO: Multi-Scale Improved NLO. *JHEP*, 10:155, 2012.

[111] K. Hamilton, P. Nason, and G. Zanderighi. Finite quark-mass effects in the NNLOPS POWHEG+MiNLO Higgs generator. *JHEP*, 05:140, 2015.

[112] R. V. Harlander, H. Mantler, S. Marzani, and K. J. Ozeren. Higgs production in gluon fusion at next-to-next-to-leading order QCD for finite top mass. *Eur. Phys. J. C*, 66:359–372, 2010.

[113] R. V. Harlander and K. J. Ozeren. Finite top mass effects for hadronic Higgs production at next-to-next-to-leading order. *JHEP*, 11:088, 2009.

[114] R. V. Harlander and K. J. Ozeren. Top mass effects in Higgs production at next-to-next-to-leading order QCD: Virtual corrections. *Phys. Lett. B*, 679:467–472, 2009.

[115] K. Hartling, K. Kumar, and H. E. Logan. GMCALC: a calculator for the Georgi-Machacek model. 12 2014.

[116] D. Hayden, K. Terashi, B. Dong, R. Les, T. Hryn'ova, Y. Takubo, P. J. Falke, C. Vergis, E. Dreyer, E. Kajomovitz, A. Honle, M. I. Abreu Juliao Ochoa De Castro, M. Lu, W. Su, N. A. Grieser, L. Zhang, H. De la Torre, T. Farooque, T. Poulsen, S. Calvet, K. S. Krowpman, M. Pinamonti, R. Yuan, U. Klein, E. Kay, M. W. O'Keefe, G. J. Facini, A. Picazio, D. Duda, W. C. Fisher, and G. Halladjian. Combination of searches for heavy resonances using 139 fb^{-1} of proton–proton collision data at $\sqrt{s}$ = 13 TeV with the ATLAS detector. Technical Report ATL-COM-PHYS-2020-222, CERN, Geneva, Mar 2020.

[117] P. W. Higgs. Broken symmetries and the masses of gauge bosons. *Phys. Rev. Lett.*, 13:508–509, Oct 1964.

[118] S. Höche, F. Krauss, M. Schönherr, and F. Siegert. QCD matrix elements + parton showers: The NLO case. *JHEP*, 04:027, 2013.

[119] S. Höche, F. Krauss, S. Schumann, and F. Siegert. QCD matrix elements and truncated showers. *JHEP*, 05:053, 2009.

[120] S. Hoeche, F. Krauss, M. Schonherr, and F. Siegert. A critical appraisal of NLO+PS matching methods. *JHEP*, 09:049, 2012.

[121] I. P. Ivanov. Building and testing models with extended Higgs sectors. *Prog. Part. Nucl. Phys.*, 95:160–208, 2017.

[122] F. N. A. Laboratory. Standard model from fermi lab, 2008.

[123] H.-L. Lai, M. Guzzi, J. Huston, Z. Li, P. M. Nadolsky, J. Pumplin, and C.-P. Yuan. New parton distributions for collider physics. *Phys. Rev. D*, 82:074024, 2010.

[124] W. Lampl, S. Laplace, D. Lelas, P. Loch, H. Ma, S. Menke, S. Rajagopalan, D. Rousseau, S. Snyder, and G. Unal. Calorimeter Clustering Algorithms: Description and Performance. Technical Report ATL-LARG-PUB-2008-002. ATL-COM-LARG-2008-003, CERN, Geneva, Apr 2008.

[125] D. J. Lange. The EvtGen particle decay simulation package. *Nucl. Instrum. Meth. A*, 462:152, 2001.

[126] P. Nason. A new method for combining NLO QCD with shower Monte Carlo algorithms. *JHEP*, 11:040, 2004.

[127] P. Nason. A new method for combining nlo qcd with shower monte carlo algorithms. *Journal of High Energy Physics*, 2004(11):040–040, Nov 2004.

[128] P. Nason and C. Oleari. Nlo higgs boson production via vector-boson fusion matched with shower in powheg. *Journal of High Energy Physics*, 2010(2), Feb 2010.

[129] P. Nason and C. Oleari. NLO Higgs boson production via vector-boson fusion matched with shower in Powheg. *JHEP*, 02:037, 2010.

[130] A. Oliveira. Gravity particles from Warped Extra Dimensions, predictions for LHC. 2014.

[131] A. Pak, M. Rogal, and M. Steinhauser. Finite top quark mass effects in NNLO Higgs boson production at LHC. *JHEP*, 02:025, 2010.

[132] D. Pappadopulo, A. Thamm, R. Torre, and A. Wulzer. Heavy Vector Triplets: Bridging Theory and Data. *JHEP*, 09:060, 2014.

[133] T. Plehn, D. Rainwater, and D. Zeppenfield. Method for identifying h$\rightarrow$ $\tau\tau$ $\rightarrow$e$\pm\mu\pm p_T$ at the cern lhc. *Physical Review D*, 61(9), Apr 2000.

[134] L. Randall and R. Sundrum. A Large mass hierarchy from a small extra dimension. *Phys. Rev. Lett.*, 83:3370–3373, 1999.

[135] E. Re. Single-top Wt-channel production matched with parton showers using the POWHEG method. *Eur. Phys. J. C*, 71:1547, 2011.

[136] A. L. Read. Presentation of search results: theCLstechnique. *Journal of Physics G: Nuclear and Particle Physics*, 28(10):2693–2704, sep 2002.

[137] S. Schumann and F. Krauss. A parton shower algorithm based on Catani–Seymour dipole factorisation. *JHEP*, 03:038, 2008.

[138] T. Sjöstrand, S. Ask, J. R. Christiansen, R. Corke, N. Desai, P. Ilten, S. Mrenna, S. Prestel, C. O. Rasmussen, and P. Z. Skands. An introduction to PYTHIA 8.2. *Comput. Phys. Commun.*, 191:159, 2015.

[139] T. Sjöstrand, S. Ask, J. R. Christiansen, R. Corke, N. Desai, P. Ilten, S. Mrenna, S. Prestel, C. O. Rasmussen, and P. Z. Skands. An introduction to pythia 8.2. *Computer Physics Communications*, 191:159–177, Jun 2015.

[140] T. Sjöstrand, S. Mrenna, and P. Skands. A brief introduction to pythia 8.1. *Computer Physics Communications*, 178(11):852–867, Jun 2008.

[141] M. Spira. QCD effects in Higgs physics. *Fortsch. Phys.*, 46:203–284, 1998.

[142] E. Torrence. Luminosity Public Results Run2. https://twiki.cern.ch/twiki/bin/view/AtlasPublic/LuminosityPublicResultsRun2.

[143] UA1. Experimental observation of isolated large transverse energy electrons with associated missing energy at s=540 gev. *Physics Letters B*, 122(1):103 – 116, 1983.

[144] M. Zaro and H. Logan. Recommendations for the interpretation of LHC searches for H_5^0, $H_5^{\pm}$, and $H_5^{\pm\pm}$ in vector boson fusion with decays to vector boson pairs. Apr 2015.

Appendices

Appendix A

Experimental Uncertainty Values

Each individual reconstructed object has several sources of uncertainties arising from detector capabilities, each of which are evaluated separately. The methods to do this follow the latest available recommendations from the combined performance (CP) groups of the ATLAS experiment. The leading experimental uncertainties for all channels comes from jet energy scale (JES) and resolution (JER) and on the b-tagging efficiency. A summary of experimental uncertainties corresponding to variations in the scale and resolution of the reconstructed objects is shown in Tables A.1, A.2 for the top-quark background and Tables A.3, A.4 for the ggF quasi-inclusive and VBF regions, respectively. A similar summary is shown in Tables A.5, A.6 for the 600 GeV NWA ggF and VBF signals, respectively. A summary of the experimental uncertainties corresponding to the efficiency corrections of the reconstructed objects is shown in Tables A.7 - A.12. For these types of uncertainties we see that the dominant sources of uncertainty is associated with b-jet tagging in top control regions, and b-jet veto in the WW control regions and signal regions. In all tables a comparison to the uncertainty arising from the limited MC statistics in the different regions is included at the bottom.

Systematic	TopCRIncl	WWCRIncl	SRIncl
EG_RESOLUTION_ALL	± 0.01	± 0.01	± 0.02
EG_SCALE_AF2	± 0.00	± 0.00	± 0.00
EG_SCALE_ALL	± 0.07	± 0.11	± 0.06
JET_BJES_Response	± 0.26	± 1.16	± 1.12
JET_EffectiveNP_Detector1	± 0.01	± 0.04	± 0.03
JET_EffectiveNP_Detector2	± 0.00	± 0.00	± 0.00
JET_EffectiveNP_Mixed1	± 0.00	± 0.02	± 0.01
JET_EffectiveNP_Mixed2	± 0.02	± 0.06	± 0.05
JET_EffectiveNP_Mixed3	± 0.01	± 0.03	± 0.02
JET_EffectiveNP_Modelling1	± 0.26	± 0.88	± 0.79
JET_EffectiveNP_Modelling2	± 0.02	± 0.07	± 0.06
JET_EffectiveNP_Modelling3	± 0.02	± 0.07	± 0.06
JET_EffectiveNP_Modelling4	± 0.00	± 0.01	± 0.01
JET_EffectiveNP_Statistical1	± 0.00	± 0.01	± 0.01
JET_EffectiveNP_Statistical2	± 0.03	± 0.11	± 0.10
JET_EffectiveNP_Statistical3	± 0.00	± 0.00	± 0.00
JET_EffectiveNP_Statistical4	± 0.00	± 0.02	± 0.01
JET_EffectiveNP_Statistical5	± 0.01	± 0.02	± 0.02
JET_EffectiveNP_Statistical6	± 0.00	± 0.01	± 0.01
JET_EtaIntercalibration_Modelling	± 0.33	± 0.91	± 0.85
JET_EtaIntercalibration_NonClosure_highE	± 0.00	± 0.00	± 0.00
JET_EtaIntercalibration_NonClosure_negEta	± 0.00	± 0.02	± 0.01
JET_EtaIntercalibration_NonClosure_posEta	± 0.00	± 0.01	± 0.01
JET_EtaIntercalibration_TotalStat	± 0.06	± 0.21	± 0.19
JET_Flavor_Composition	± 0.38	± 0.80	± 0.65
JET_Flavor_Response	± 0.36	± 1.05	± 1.03
JET_Pileup_OffsetMu	± 0.23	± 0.56	± 0.54
JET_Pileup_OffsetNPV	± 0.24	± 0.79	± 0.73
JET_Pileup_PtTerm	± 0.03	± 0.09	± 0.07
JET_Pileup_RhoTopology	± 0.68	± 2.36	± 2.16
JET_PunchThrough_MC16	± 0.00	± 0.00	± 0.00
JET_SingleParticle_HighPt	± 0.00	± 0.00	± 0.00
MET_SoftTrk_ResoPara	± 0.04	± 0.06	± 0.06
MET_SoftTrk_ResoPerp	± 0.03	± 0.06	± 0.05
MET_SoftTrk_Scale	± 0.04	± 0.08	± 0.04
MUON_ID	± 0.16	± 0.39	± 0.21
MUON_MS	± 0.21	± 0.17	± 0.20
MUON_SCALE	± 0.06	± 0.09	± 0.06
MUON_SAGITTA_RHO	± 0.00	± 0.00	± 0.00
MUON_SAGITTA_RESBIAS	± 0.60	± 0.81	± 0.63
Total	± 1.24	± 3.49	± 3.18
MC Stat.	± 0.07	± 3.43	± 1.61

Table A.1: Relative experimental uncertainties in % related to the lepton, jets, and missing transverse energy scale and resolution on the top quark background in the ggF top-quark CR (2nd column), ggF WW CR (3rd column) and ggF quasi-inclusive SR (4th column). All uncertainties have been symmetrized by taking the average up and down variation for simplicity. The "Total" row refers to the quadrature sum of all variations. The final row "MC Stat." shows for comparison the statistical uncertainty from MC samples.

Systematic	TopCRVBF	WWCRVBF	SRVBF1J	SRVBF2J
EG_RESOLUTION_ALL	± 0.01	± 0.05	± 0.06	± 0.04
EG_SCALE_AF2	± 0.00	± 0.00	± 0.00	± 0.00
EG_SCALE_ALL	± 0.07	± 0.19	± 0.12	± 0.07
JET_BJES_Response	± 0.98	± 2.48	± 2.65	± 1.30
JET_EffectiveNP_Detector1	± 0.06	± 0.03	± 0.03	± 0.07
JET_EffectiveNP_Detector2	± 0.01	± 0.00	± 0.02	± 0.01
JET_EffectiveNP_Mixed1	± 0.06	± 0.02	± 0.03	± 0.09
JET_EffectiveNP_Mixed2	± 0.11	± 0.08	± 0.08	± 0.14
JET_EffectiveNP_Mixed3	± 0.04	± 0.04	± 0.05	± 0.05
JET_EffectiveNP_Modelling1	± 1.03	± 1.21	± 1.16	± 1.00
JET_EffectiveNP_Modelling2	± 0.03	± 0.12	± 0.07	± 0.02
JET_EffectiveNP_Modelling3	± 0.01	± 0.11	± 0.10	± 0.09
JET_EffectiveNP_Modelling4	± 0.02	± 0.01	± 0.03	± 0.02
JET_EffectiveNP_Statistical1	± 0.01	± 0.02	± 0.03	± 0.01
JET_EffectiveNP_Statistical2	± 0.13	± 0.16	± 0.14	± 0.11
JET_EffectiveNP_Statistical3	± 0.00	± 0.01	± 0.00	± 0.01
JET_EffectiveNP_Statistical4	± 0.01	± 0.04	± 0.03	± 0.04
JET_EffectiveNP_Statistical5	± 0.02	± 0.04	± 0.05	± 0.06
JET_EffectiveNP_Statistical6	± 0.02	± 0.00	± 0.06	± 0.03
JET_EtaIntercalibration_Modelling	± 4.28	± 2.20	± 1.94	± 4.60
JET_EtaIntercalibration_NonClosure_highE	± 0.00	± 0.00	± 0.00	± 0.00
JET_EtaIntercalibration_NonClosure_negEta	± 0.05	± 0.02	± 0.08	± 0.10
JET_EtaIntercalibration_NonClosure_posEta	± 0.06	± 0.01	± 0.05	± 0.09
JET_EtaIntercalibration_TotalStat	± 0.48	± 0.12	± 0.08	± 0.53
JET_Flavor_Composition	± 6.10	± 2.95	± 2.65	± 7.20
JET_Flavor_Response	± 2.27	± 1.28	± 1.17	± 2.42
JET_Pileup_OffsetMu	± 3.72	± 2.07	± 2.07	± 3.93
JET_Pileup_OffsetNPV	± 0.95	± 0.70	± 1.01	± 0.84
JET_Pileup_PtTerm	± 0.10	± 0.05	± 0.02	± 0.18
JET_Pileup_RhoTopology	± 1.86	± 3.32	± 3.26	± 1.18
JET_PunchThrough_MC16	± 0.00	± 0.00	± 0.00	± 0.00
JET_SingleParticle_HighPt	± 0.00	± 0.00	± 0.00	± 0.00
MET_SoftTrk_ResoPara	± 0.00	± 0.00	± 0.03	± 0.06
MET_SoftTrk_ResoPerp	± 0.00	± 0.00	± 0.08	± 0.07
MET_SoftTrk_Scale	± 0.00	± 0.00	± 0.07	± 0.01
MUON_ID	± 0.21	± 0.18	± 0.14	± 0.20
MUON_MS	± 0.21	± 0.23	± 0.23	± 0.12
MUON_SCALE	± 0.04	± 0.10	± 0.06	± 0.07
MUON_SAGITTA_RHO	± 0.00	± 0.00	± 0.00	± 0.00
MUON_SAGITTA_RESBIAS	± 0.61	± 0.86	± 0.68	± 0.69
Total	± 9.01	± 6.29	± 6.09	± 10.02
MC Stat.	± 0.21	± 1.47	± 0.94	± 0.80

Table A.2: Relative experimental uncertainties in % related to the lepton, jets, and missing transverse energy scale and resolution on the top quark background in the VBF top-quark CR (2nd column), VBF WW CR (3rd column), VBF 1J SR (4th column), and VBF 2J SR (5th column). All uncertainties have been symmetrized by taking the average up and down variation for simplicity. The "Total" row refers to the quadrature sum of all variations. The final row "MC Stat." shows for comparison the statistical uncertainty from MC samples.

Systematic	WWCRIncl	SRIncl
EG_RESOLUTION_ALL	± 0.14	± 0.13
EG_SCALE_AF2	± 0.00	± 0.00
EG_SCALE_ALL	± 0.04	± 0.13
JET_BJES_Response	± 0.01	± 0.01
JET_EffectiveNP_Detector1	± 0.02	± 0.01
JET_EffectiveNP_Detector2	± 0.00	± 0.00
JET_EffectiveNP_Mixed1	± 0.01	± 0.00
JET_EffectiveNP_Mixed2	± 0.03	± 0.02
JET_EffectiveNP_Mixed3	± 0.02	± 0.01
JET_EffectiveNP_Modelling1	± 0.20	± 0.19
JET_EffectiveNP_Modelling2	± 0.02	± 0.01
JET_EffectiveNP_Modelling3	± 0.01	± 0.01
JET_EffectiveNP_Modelling4	± 0.00	± 0.00
JET_EffectiveNP_Statistical1	± 0.00	± 0.00
JET_EffectiveNP_Statistical2	± 0.03	± 0.02
JET_EffectiveNP_Statistical3	± 0.00	± 0.00
JET_EffectiveNP_Statistical4	± 0.00	± 0.00
JET_EffectiveNP_Statistical5	± 0.00	± 0.00
JET_EffectiveNP_Statistical6	± 0.01	± 0.00
JET_EtaIntercalibration_Modelling	± 0.48	± 0.53
JET_EtaIntercalibration_NonClosure_highE	± 0.00	± 0.00
JET_EtaIntercalibration_NonClosure_negEta	± 0.01	± 0.01
JET_EtaIntercalibration_NonClosure_posEta	± 0.02	± 0.01
JET_EtaIntercalibration_TotalStat	± 0.09	± 0.07
JET_Flavor_Composition	± 0.60	± 0.75
JET_Flavor_Response	± 0.25	± 1.05
JET_Pileup_OffsetMu	± 0.48	± 0.53
JET_Pileup_OffsetNPV	± 0.16	± 0.79
JET_Pileup_PtTerm	± 0.02	± 0.01
JET_Pileup_RhoTopology	± 0.37	± 0.40
JET_PunchThrough_MC16	± 0.00	± 0.00
JET_SingleParticle_HighPt	± 0.00	± 0.00
MET_SoftTrk_ResoPara	± 0.10	± 0.04
MET_SoftTrk_ResoPerp	± 0.04	± 0.08
MET_SoftTrk_Scale	± 0.08	± 0.08
MUON_ID	± 0.42	± 0.24
MUON_MS	± 0.14	± 0.21
MUON_SCALE	± 0.10	± 0.07
MUON_SAGITTA_RHO	± 0.00	± 0.00
MUON_SAGITTA_RESBIAS	± 0.74	± 0.68
Total	± 1.38	± 1.92
MC Stat.	± 0.34	± 0.16

Table A.3: Relative experimental uncertainties in % related to the lepton, jets, and missing transverse energy scale and resolution on the WW background in the ggF WW CR (2nd column) and ggF quasi-inclusive SR (3rd column). All uncertainties have been symmetrized by taking the average up and down variation for simplicity. The "Total" row refers to the quadrature sum of all variations. The final row "MC Stat." shows for comparison the statistical uncertainty from MC samples.

Systematic	WWCRVBF1J	SRVBF1J
EG_RESOLUTION_ALL	± 0.04	± 0.10
EG_SCALE_AF2	± 0.00	± 0.00
EG_SCALE_ALL	± 0.14	± 0.10
JET_BJES_Response	± 0.01	± 0.03
JET_EffectiveNP_Detector1	± 0.11	± 0.11
JET_EffectiveNP_Detector2	± 0.01	± 0.01
JET_EffectiveNP_Mixed1	± 0.04	± 0.04
JET_EffectiveNP_Mixed2	± 0.18	± 0.23
JET_EffectiveNP_Mixed3	± 0.07	± 0.07
JET_EffectiveNP_Modelling1	± 1.59	± 1.86
JET_EffectiveNP_Modelling2	± 0.13	± 0.12
JET_EffectiveNP_Modelling3	± 0.03	± 0.02
JET_EffectiveNP_Modelling4	± 0.00	± 0.02
JET_EffectiveNP_Statistical1	± 0.01	± 0.02
JET_EffectiveNP_Statistical2	± 0.22	± 0.32
JET_EffectiveNP_Statistical3	± 0.01	± 0.01
JET_EffectiveNP_Statistical4	± 0.02	± 0.01
JET_EffectiveNP_Statistical5	± 0.02	± 0.02
JET_EffectiveNP_Statistical6	± 0.01	± 0.01
JET_EtaIntercalibration_Modelling	± 6.72	± 6.29
JET_EtaIntercalibration_NonClosure_highE	± 0.00	± 0.00
JET_EtaIntercalibration_NonClosure_negEta	± 0.16	± 0.21
JET_EtaIntercalibration_NonClosure_posEta	± 0.17	± 0.15
JET_EtaIntercalibration_TotalStat	± 1.00	± 0.94
JET_Flavor_Composition	± 8.03	± 8.03
JET_Flavor_Response	± 1.86	± 2.17
JET_Pileup_OffsetMu	± 5.54	± 5.84
JET_Pileup_OffsetNPV	± 1.38	± 1.51
JET_Pileup_PtTerm	± 0.21	± 0.09
JET_Pileup_RhoTopology	± 3.06	± 3.30
JET_PunchThrough_MC16	± 0.00	± 0.00
JET_SingleParticle_HighPt	± 0.00	± 0.00
MET_SoftTrk_ResoPara	± 0.00	± 0.18
MET_SoftTrk_ResoPerp	± 0.00	± 0.12
MET_SoftTrk_Scale	± 0.00	± 0.10
MUON_ID	± 0.16	± 0.16
MUON_MS	± 0.12	± 0.33
MUON_SCALE	± 0.13	± 0.08
MUON_SAGITTA_RHO	± 0.00	± 0.00
MUON_SAGITTA_RESBIAS	± 0.37	± 0.91
Total	± 12.61	± 12.72
MC Stat.	± 1.06	± 0.78

Table A.4: Relative experimental uncertainties in % related to the lepton, jets, and missing transverse energy scale and resolution on the WW background in the VBF WW 1J CR (2nd column) and VBF 1J SR (3rd column). All uncertainties have been symmetrized by taking the average up and down variation for simplicity. The "Total" row refers to the quadrature sum of all variations. The final row "MC Stat." shows for comparison the statistical uncertainty from MC samples.

Systematic	SRIncl	SRVBF1J	SRVBF2J
EG_RESOLUTION_ALL	± 0.01	± 0.06	± 0.04
EG_SCALE_AF2	± 0.01	± 0.03	± 0.00
EG_SCALE_ALL	± 0.01	± 0.03	± 0.01
JET_BJES_Response	± 0.03	± 0.02	± 0.00
JET_EffectiveNP_Detector1	± 0.00	± 0.02	± 0.09
JET_EffectiveNP_Detector2	± 0.00	± 0.01	± 0.04
JET_EffectiveNP_Mixed1	± 0.00	± 0.04	± 0.08
JET_EffectiveNP_Mixed2	± 0.02	± 0.03	± 0.30
JET_EffectiveNP_Mixed3	± 0.01	± 0.01	± 0.09
JET_EffectiveNP_Modelling1	± 0.24	± 0.38	± 1.69
JET_EffectiveNP_Modelling2	± 0.01	± 0.03	± 0.09
JET_EffectiveNP_Modelling3	± 0.01	± 0.04	± 0.04
JET_EffectiveNP_Modelling4	± 0.00	± 0.04	± 0.04
JET_EffectiveNP_Statistical1	± 0.00	± 0.04	± 0.04
JET_EffectiveNP_Statistical2	± 0.03	± 0.04	± 0.41
JET_EffectiveNP_Statistical3	± 0.00	± 0.01	± 0.00
JET_EffectiveNP_Statistical4	± 0.00	± 0.02	± 0.04
JET_EffectiveNP_Statistical5	± 0.00	± 0.01	± 0.04
JET_EffectiveNP_Statistical6	± 0.00	± 0.04	± 0.04
JET_EtaIntercalibration_Modelling	± 2.03	± 0.91	± 4.75
JET_EtaIntercalibration_NonClosure_highE	± 0.00	± 0.00	± 0.00
JET_EtaIntercalibration_NonClosure_negEta	± 0.00	± 0.02	± 0.04
JET_EtaIntercalibration_NonClosure_posEta	± 0.01	± 0.09	± 0.08
JET_EtaIntercalibration_TotalStat	± 0.08	± 0.11	± 0.95
JET_Flavor_Composition	± 0.38	± 1.92	± 5.83
JET_Flavor_Response	± 0.28	± 0.40	± 2.18
JET_Pileup_OffsetMu	± 0.42	± 1.48	± 3.81
JET_Pileup_OffsetNPV	± 0.24	± 0.33	± 1.56
JET_Pileup_PtTerm	± 0.02	± 0.02	± 0.11
JET_Pileup_RhoTopology	± 0.51	± 0.80	± 2.79
JET_PunchThrough_MC16	± 0.00	± 0.00	± 0.00
JET_SingleParticle_HighPt	± 0.00	± 0.00	± 0.00
MET_SoftTrk_ResoPara	± 0.02	± 0.04	± 0.06
MET_SoftTrk_ResoPerp	± 0.00	± 0.06	± 0.01
MET_SoftTrk_Scale	± 0.02	± 0.01	± 0.01
MUON_ID	± 0.22	± 0.22	± 0.28
MUON_MS	± 0.16	± 0.18	± 0.45
MUON_SCALE	± 0.02	± 0.02	± 0.06
MUON_SAGITTA_RHO	± 0.00	± 0.00	± 0.00
MUON_SAGITTA_RESBIAS	± 0.72	± 0.78	± 1.14
Total	± 2.34	± 2.91	± 9.58
MC Stat.	± 0.40	± 1.41	± 2.18

Table A.5: Relative experimental uncertainties in % related to the lepton, jets, and missing transverse energy scale and resolution on the NWA ggF signal with mass 600 GeV in the ggF quasi-inclusive SR (2nd column), VBF 1J SR (3rd column) and VBF 2J SR (4th column). All uncertainties have been symmetrized by taking the average up and down variation for simplicity. The "Total" row refers to the quadrature sum of all variations. The final row "MC Stat." shows for comparison the statistical uncertainty from MC samples.

Systematic	SRIncl	SRVBF1J	SRVBF2J
EG_RESOLUTION_ALL	± 0.02	± 0.06	± 0.03
EG_SCALE_AF2	± 0.03	± 0.01	± 0.01
EG_SCALE_ALL	± 0.01	± 0.03	± 0.02
JET_BJES_Response	± 0.01	± 0.00	± 0.03
JET_EffectiveNP_Detector1	± 0.05	± 0.08	± 0.05
JET_EffectiveNP_Detector2	± 0.01	± 0.00	± 0.01
JET_EffectiveNP_Mixed1	± 0.04	± 0.06	± 0.03
JET_EffectiveNP_Mixed2	± 0.09	± 0.16	± 0.08
JET_EffectiveNP_Mixed3	± 0.05	± 0.07	± 0.04
JET_EffectiveNP_Modelling1	± 0.63	± 0.62	± 0.77
JET_EffectiveNP_Modelling2	± 0.06	± 0.08	± 0.05
JET_EffectiveNP_Modelling3	± 0.03	± 0.06	± 0.03
JET_EffectiveNP_Modelling4	± 0.01	± 0.04	± 0.02
JET_EffectiveNP_Statistical1	± 0.01	± 0.04	± 0.02
JET_EffectiveNP_Statistical2	± 0.11	± 0.17	± 0.12
JET_EffectiveNP_Statistical3	± 0.01	± 0.00	± 0.01
JET_EffectiveNP_Statistical4	± 0.01	± 0.00	± 0.01
JET_EffectiveNP_Statistical5	± 0.01	± 0.00	± 0.01
JET_EffectiveNP_Statistical6	± 0.03	± 0.06	± 0.03
JET_EtaIntercalibration_Modelling	± 2.17	± 1.42	± 2.49
JET_EtaIntercalibration_NonClosure_highE	± 0.00	± 0.00	± 0.00
JET_EtaIntercalibration_NonClosure_negEta	± 0.04	± 0.02	± 0.01
JET_EtaIntercalibration_NonClosure_posEta	± 0.01	± 0.08	± 0.07
JET_EtaIntercalibration_TotalStat	± 0.31	± 0.26	± 0.37
JET_Flavor_Composition	± 2.85	± 2.46	± 3.73
JET_Flavor_Response	± 0.77	± 0.97	± 1.06
JET_Pileup_OffsetMu	± 1.16	± 0.85	± 1.46
JET_Pileup_OffsetNPV	± 0.51	± 0.53	± 0.63
JET_Pileup_PtTerm	± 0.05	± 0.14	± 0.06
JET_Pileup_RhoTopology	± 1.41	± 1.44	± 1.64
JET_PunchThrough_MC16	± 0.00	± 0.00	± 0.00
JET_SingleParticle_HighPt	± 0.00	± 0.00	± 0.00
MET_SoftTrk_ResoPara	± 0.02	± 0.03	± 0.04
MET_SoftTrk_ResoPerp	± 0.01	± 0.00	± 0.02
MET_SoftTrk_Scale	± 0.02	± 0.01	± 0.02
MUON_ID	± 0.24	± 0.20	± 0.30
MUON_MS	± 0.13	± 0.27	± 0.20
MUON_SCALE	± 0.03	± 0.01	± 0.01
MUON_SAGITTA_RHO	± 0.00	± 0.00	± 0.00
MUON_SAGITTA_RESBIAS	± 0.94	± 0.88	± 0.60
Total	± 4.30	± 3.68	± 5.26
MC Stat.	± 0.93	± 1.23	± 0.91

Table A.6: Relative experimental uncertainties in % related to the lepton, jets, and missing transverse energy scale and resolution on the NWA VBF signal with mass 600 GeV in the ggF quasi-inclusive SR (2nd column), VBF 1J SR (3rd column) and VBF 2J SR (4th column). All uncertainties have been symmetrized by taking the average up and down variation for simplicity. The "Total" row refers to the quadrature sum of all variations. The final row "MC Stat." shows for comparison the statistical uncertainty from MC samples.

Systematic	TopCRIncl	WWCRIncl	SRIncl
FT_EFF_Eigen_B_0	± 1.53	± 6.12	± 5.92
FT_EFF_Eigen_B_1	± 0.02	± 0.00	± 0.03
FT_EFF_Eigen_B_2	± 0.67	± 3.32	± 3.25
FT_EFF_Eigen_C_0	± 0.16	± 0.25	± 0.25
FT_EFF_Eigen_C_1	± 0.00	± 0.00	± 0.00
FT_EFF_Eigen_C_2	± 0.00	± 0.01	± 0.01
FT_EFF_Eigen_Light_0	± 0.49	± 0.72	± 0.71
FT_EFF_Eigen_Light_1	± 0.04	± 0.06	± 0.06
FT_EFF_Eigen_Light_2	± 0.02	± 0.02	± 0.02
FT_EFF_Eigen_Light_3	± 0.00	± 0.00	± 0.00
FT_EFF_extrapolation_from_charm	± 0.00	± 0.00	± 0.00
FT_EFF_extrapolation	± 0.00	± 0.00	± 0.01
JVT	± 0.22	± 0.08	± 0.07
EL_EFF_ID_CorrUncertaintyNP0	± 0.00	± 0.00	± 0.00
EL_EFF_ID_CorrUncertaintyNP1	± 0.00	± 0.00	± 0.00
EL_EFF_ID_CorrUncertaintyNP2	± 0.00	± 0.00	± 0.00
EL_EFF_ID_CorrUncertaintyNP3	± 0.00	± 0.00	± 0.00
EL_EFF_ID_CorrUncertaintyNP4	± 0.00	± 0.00	± 0.00
EL_EFF_ID_CorrUncertaintyNP5	± 0.00	± 0.00	± 0.00
EL_EFF_ID_CorrUncertaintyNP6	± 0.00	± 0.00	± 0.00
EL_EFF_ID_CorrUncertaintyNP7	± 0.00	± 0.00	± 0.00
EL_EFF_ID_CorrUncertaintyNP8	± 0.00	± 0.00	± 0.00
EL_EFF_ID_CorrUncertaintyNP9	± 0.04	± 0.05	± 0.04
EL_EFF_ID_CorrUncertaintyNP10	± 0.04	± 0.03	± 0.04
EL_EFF_ID_CorrUncertaintyNP11	± 0.09	± 0.10	± 0.10
EL_EFF_ID_CorrUncertaintyNP12	± 0.07	± 0.10	± 0.07
EL_EFF_ID_CorrUncertaintyNP13	± 0.02	± 0.02	± 0.02
EL_EFF_ID_CorrUncertaintyNP14	± 0.14	± 0.14	± 0.13
EL_EFF_ID_CorrUncertaintyNP15	± 0.01	± 0.01	± 0.00
EL_EFF_Iso_TOTAL_1NPCOR_PLUS_UNCOR	± 0.00	± 0.00	± 0.00
EL_EFF_Trigger_TOTAL_1NPCOR_PLUS_UNCOR	± 0.01	± 0.01	± 0.01
EL_EFF_TriggerEff_TOTAL_1NPCOR_PLUS_UNCOR	± 0.00	± 0.00	± 0.00
EL_EFF_Reco_TOTAL_1NPCOR_PLUS_UNCOR	± 0.13	± 0.13	± 0.13
EFF_ID_SIMPLIFIED_UncorrUncertaintyNP0	± 0.00	± 0.00	± 0.00
EFF_ID_SIMPLIFIED_UncorrUncertaintyNP1	± 0.00	± 0.00	± 0.00
EFF_ID_SIMPLIFIED_UncorrUncertaintyNP2	± 0.00	± 0.00	± 0.00
EFF_ID_SIMPLIFIED_UncorrUncertaintyNP3	± 0.00	± 0.00	± 0.00
EFF_ID_SIMPLIFIED_UncorrUncertaintyNP4	± 0.00	± 0.00	± 0.00
EFF_ID_SIMPLIFIED_UncorrUncertaintyNP5	± 0.00	± 0.00	± 0.00
EFF_ID_SIMPLIFIED_UncorrUncertaintyNP6	± 0.06	± 0.06	± 0.06
EFF_ID_SIMPLIFIED_UncorrUncertaintyNP7	± 0.04	± 0.04	± 0.04
EFF_ID_SIMPLIFIED_UncorrUncertaintyNP8	± 0.12	± 0.09	± 0.12
EFF_ID_SIMPLIFIED_UncorrUncertaintyNP9	± 0.00	± 0.00	± 0.00
EFF_ID_SIMPLIFIED_UncorrUncertaintyNP10	± 0.00	± 0.00	± 0.00
EFF_ID_SIMPLIFIED_UncorrUncertaintyNP11	± 0.00	± 0.00	± 0.00
EFF_ID_SIMPLIFIED_UncorrUncertaintyNP12	± 0.00	± 0.00	± 0.00
EFF_ID_SIMPLIFIED_UncorrUncertaintyNP13	± 0.00	± 0.00	± 0.00
EFF_ID_SIMPLIFIED_UncorrUncertaintyNP14	± 0.00	± 0.00	± 0.00
EFF_ID_SIMPLIFIED_UncorrUncertaintyNP15	± 0.02	± 0.05	± 0.03
EFF_ID_SIMPLIFIED_UncorrUncertaintyNP16	± 0.01	± 0.03	± 0.02
EFF_ID_SIMPLIFIED_UncorrUncertaintyNP17	± 0.04	± 0.08	± 0.06
MUON_EFF_TrigStatUncertainty	± 0.01	± 0.01	± 0.01
MUON_EFF_TrigSystUncertainty	± 0.02	± 0.02	± 0.02
MUON_ISO_STAT	± 0.01	± 0.01	± 0.02
MUON_ISO_SYS	± 0.31	± 0.32	± 0.30
MUON_RECO_STAT	± 0.10	± 0.10	± 0.10
MUON_RECO_STAT_LOWPT	± 0.00	± 0.00	± 0.00
MUON_RECO_SYS	± 0.66	± 0.65	± 0.00
MUON_RECO_SYS_LOWPT	± 0.00	± 0.00	± 0.00
MUON_TTVA_STAT	± 0.02	± 0.02	± 0.02
MUON_TTVA_SYS	± 0.00	± 0.00	± 0.00
PRW_DATASF	± 0.51	± 0.65	± 0.65
Total	± 1.99	± 7.08	± 6.84
MC Stat.	± 0.07	± 3.43	± 1.61

Table A.7: Relative experimental uncertainties in % related to the the efficiency corrections on the top quark background in the ggF top-quark CR (2nd column), ggF WW CR (3rd column) and ggF quasi-inclusive SR (4th column). All uncertainties have been symmetrized by taking the average up and down variation for simplicity. The "Total" row refers to the quadrature sum of all variations. The final row "MC Stat." shows for comparison the statistical uncertainty from MC samples.

Systematic	TopCRVBF	WWCRVBF	VBFSR1J	VBFSR2J
FT_EFF_Eigen_B_0	± 1.16	± 4.28	± 4.56	± 5.68
FT_EFF_Eigen_B_1	± 0.01	± 0.01	± 0.01	± 0.02
FT_EFF_Eigen_B_2	± 0.46	± 0.03	± 0.10	± 2.46
FT_EFF_Eigen_C_0	± 0.03	± 0.12	± 0.14	± 0.29
FT_EFF_Eigen_C_1	± 0.00	± 0.02	± 0.02	± 0.00
FT_EFF_Eigen_C_2	± 0.00	± 0.01	± 0.01	± 0.01
FT_EFF_Eigen_Light_0	± 0.30	± 0.32	± 0.30	± 0.90
FT_EFF_Eigen_Light_1	± 0.03	± 0.05	± 0.05	± 0.07
FT_EFF_Eigen_Light_2	± 0.01	± 0.03	± 0.03	± 0.02
FT_EFF_Eigen_Light_3	± 0.00	± 0.00	± 0.00	± 0.00
FT_EFF_extrapolation_from_charm	± 0.00	± 0.00	± 0.00	± 0.00
FT_EFF_extrapolation	± 0.00	± 0.00	± 0.00	± 0.00
JVT	± 0.26	± 0.52	± 0.49	± 0.00
EL_EFF_ID_CorrUncertaintyNP0	± 0.00	± 0.00	± 0.00	± 0.00
EL_EFF_ID_CorrUncertaintyNP1	± 0.00	± 0.00	± 0.00	± 0.00
EL_EFF_ID_CorrUncertaintyNP2	± 0.00	± 0.00	± 0.00	± 0.00
EL_EFF_ID_CorrUncertaintyNP3	± 0.00	± 0.00	± 0.00	± 0.00
EL_EFF_ID_CorrUncertaintyNP4	± 0.00	± 0.00	± 0.00	± 0.00
EL_EFF_ID_CorrUncertaintyNP5	± 0.00	± 0.00	± 0.00	± 0.00
EL_EFF_ID_CorrUncertaintyNP6	± 0.00	± 0.00	± 0.00	± 0.00
EL_EFF_ID_CorrUncertaintyNP7	± 0.00	± 0.00	± 0.00	± 0.00
EL_EFF_ID_CorrUncertaintyNP8	± 0.00	± 0.00	± 0.00	± 0.00
EL_EFF_ID_CorrUncertaintyNP9	± 0.04	± 0.05	± 0.03	± 0.04
EL_EFF_ID_CorrUncertaintyNP10	± 0.03	± 0.03	± 0.04	± 0.04
EL_EFF_ID_CorrUncertaintyNP11	± 0.12	± 0.14	± 0.09	± 0.10
EL_EFF_ID_CorrUncertaintyNP12	± 0.11	± 0.15	± 0.06	± 0.08
EL_EFF_ID_CorrUncertaintyNP13	± 0.04	± 0.05	± 0.02	± 0.02
EL_EFF_ID_CorrUncertaintyNP14	± 0.11	± 0.11	± 0.13	± 0.12
EL_EFF_ID_CorrUncertaintyNP15	± 0.06	± 0.12	± 0.01	± 0.00
EL_EFF_Iso_TOTAL_1NPCOR_PLUS_UNCOR	± 0.00	± 0.00	± 0.00	± 0.00
EL_EFF_Trigger_TOTAL_1NPCOR_PLUS_UNCOR	± 0.01	± 0.01	± 0.01	± 0.01
EL_EFF_TriggerEff_TOTAL_1NPCOR_PLUS_UNCOR	± 0.00	± 0.00	± 0.00	± 0.00
EL_EFF_Reco_TOTAL_1NPCOR_PLUS_UNCOR	± 0.14	± 0.15	± 0.12	± 0.13
EFF_ID_SIMPLIFIED_UncorrUncertaintyNP0	± 0.00	± 0.00	± 0.00	± 0.00
EFF_ID_SIMPLIFIED_UncorrUncertaintyNP1	± 0.00	± 0.00	± 0.00	± 0.00
EFF_ID_SIMPLIFIED_UncorrUncertaintyNP2	± 0.00	± 0.00	± 0.00	± 0.00
EFF_ID_SIMPLIFIED_UncorrUncertaintyNP3	± 0.00	± 0.00	± 0.00	± 0.00
EFF_ID_SIMPLIFIED_UncorrUncertaintyNP4	± 0.00	± 0.00	± 0.00	± 0.00
EFF_ID_SIMPLIFIED_UncorrUncertaintyNP5	± 0.02	± 0.00	± 0.00	± 0.00
EFF_ID_SIMPLIFIED_UncorrUncertaintyNP6	± 0.07	± 0.09	± 0.07	± 0.05
EFF_ID_SIMPLIFIED_UncorrUncertaintyNP7	± 0.04	± 0.02	± 0.05	± 0.04
EFF_ID_SIMPLIFIED_UncorrUncertaintyNP8	± 0.09	± 0.05	± 0.13	± 0.00
EFF_ID_SIMPLIFIED_UncorrUncertaintyNP9	± 0.00	± 0.00	± 0.00	± 0.00
EFF_ID_SIMPLIFIED_UncorrUncertaintyNP10	± 0.00	± 0.00	± 0.00	± 0.00
EFF_ID_SIMPLIFIED_UncorrUncertaintyNP11	± 0.00	± 0.00	± 0.00	± 0.00
EFF_ID_SIMPLIFIED_UncorrUncertaintyNP12	± 0.00	± 0.00	± 0.00	± 0.00
EFF_ID_SIMPLIFIED_UncorrUncertaintyNP13	± 0.00	± 0.00	± 0.00	± 0.00
EFF_ID_SIMPLIFIED_UncorrUncertaintyNP14	± 0.01	± 0.01	± 0.00	± 0.00
EFF_ID_SIMPLIFIED_UncorrUncertaintyNP15	± 0.03	± 0.03	± 0.01	± 0.03
EFF_ID_SIMPLIFIED_UncorrUncertaintyNP16	± 0.01	± 0.01	± 0.01	± 0.02
EFF_ID_SIMPLIFIED_UncorrUncertaintyNP17	± 0.04	± 0.03	± 0.03	± 0.07
MUON_EFF_TrigStatUncertainty	± 0.01	± 0.02	± 0.01	± 0.01
MUON_EFF_TrigSystUncertainty	± 0.11	± 0.18	± 0.02	± 0.00
MUON_ISO_STAT	± 0.01	± 0.02	± 0.01	± 0.01
MUON_ISO_SYS	± 0.33	± 0.39	± 0.30	± 0.30
MUON_RECO_STAT	± 0.10	± 0.10	± 0.10	± 0.09
MUON_RECO_STAT_LOWPT	± 0.00	± 0.00	± 0.00	± 0.00
MUON_RECO_SYS	± 0.66	± 0.65	± 0.67	± 0.66
MUON_RECO_SYS_LOWPT	± 0.00	± 0.00	± 0.00	± 0.00
MUON_TTVA_STAT	± 0.02	± 0.02	± 0.02	± 0.02
MUON_TTVA_SYS	± 0.00	± 0.00	± 0.00	± 0.00
PRW_DATASF	± 0.37	± 0.52	± 0.11	± 0.73
Total	± 1.58	± 4.44	± 4.67	± 6.35
MC Stat.	± 0.21	± 1.47	± 0.94	± 0.80

Table A.8: Relative experimental uncertainties in % related to the efficiency corrections on the top quark background in the VBF top-quark CR (2nd column), VBF WW CR (3rd column), VBF 1J SR (4th column), and VBF 2J SR (5th column). All uncertainties have been symmetrized by taking the average up and down variation for simplicity. The "Total" row refers to the quadrature sum of all variations. The final row "MC Stat." shows for comparison the statistical uncertainty from MC samples.

Systematic	WWCRIncl	SRIncl
FT_EFF_Eigen_B_0	± 0.03	± 0.03
FT_EFF_Eigen_B_1	± 0.00	± 0.00
FT_EFF_Eigen_B_2	± 0.00	± 0.00
FT_EFF_Eigen_C_0	± 0.20	± 0.25
FT_EFF_Eigen_C_1	± 0.01	± 0.01
FT_EFF_Eigen_C_2	± 0.00	± 0.01
FT_EFF_Eigen_Light_0	± 0.52	± 0.59
FT_EFF_Eigen_Light_1	± 0.04	± 0.04
FT_EFF_Eigen_Light_2	± 0.02	± 0.02
FT_EFF_Eigen_Light_3	± 0.00	± 0.00
FT_EFF_extrapolation_from_charm	± 0.00	± 0.00
FT_EFF_extrapolation	± 0.00	± 0.01
JVT	± 0.09	± 0.09
EL_EFF_ID_CorrUncertaintyNP0	± 0.00	± 0.00
EL_EFF_ID_CorrUncertaintyNP1	± 0.00	± 0.00
EL_EFF_ID_CorrUncertaintyNP2	± 0.00	± 0.00
EL_EFF_ID_CorrUncertaintyNP3	± 0.00	± 0.00
EL_EFF_ID_CorrUncertaintyNP4	± 0.00	± 0.00
EL_EFF_ID_CorrUncertaintyNP5	± 0.00	± 0.00
EL_EFF_ID_CorrUncertaintyNP6	± 0.00	± 0.00
EL_EFF_ID_CorrUncertaintyNP7	± 0.00	± 0.00
EL_EFF_ID_CorrUncertaintyNP8	± 0.00	± 0.00
EL_EFF_ID_CorrUncertaintyNP9	± 0.05	± 0.04
EL_EFF_ID_CorrUncertaintyNP10	± 0.03	± 0.04
EL_EFF_ID_CorrUncertaintyNP11	± 0.10	± 0.10
EL_EFF_ID_CorrUncertaintyNP12	± 0.11	± 0.08
EL_EFF_ID_CorrUncertaintyNP13	± 0.02	± 0.03
EL_EFF_ID_CorrUncertaintyNP14	± 0.16	± 0.15
EL_EFF_ID_CorrUncertaintyNP15	± 0.02	± 0.01
EL_EFF_Iso_TOTAL_1NPCOR_PLUS_UNCOR	± 0.00	± 0.00
EL_EFF_Trigger_TOTAL_1NPCOR_PLUS_UNCOR	± 0.01	± 0.01
EL_EFF_TriggerEff_TOTAL_1NPCOR_PLUS_UNCOR	± 0.00	± 0.00
EL_EFF_Reco_TOTAL_1NPCOR_PLUS_UNCOR	± 0.13	± 0.13
EFF_ID_SIMPLIFIED_UncorrUncertaintyNP0	± 0.00	± 0.00
EFF_ID_SIMPLIFIED_UncorrUncertaintyNP1	± 0.00	± 0.00
EFF_ID_SIMPLIFIED_UncorrUncertaintyNP2	± 0.00	± 0.00
EFF_ID_SIMPLIFIED_UncorrUncertaintyNP3	± 0.00	± 0.00
EFF_ID_SIMPLIFIED_UncorrUncertaintyNP4	± 0.00	± 0.00
EFF_ID_SIMPLIFIED_UncorrUncertaintyNP5	± 0.00	± 0.00
EFF_ID_SIMPLIFIED_UncorrUncertaintyNP6	± 0.06	± 0.06
EFF_ID_SIMPLIFIED_UncorrUncertaintyNP7	± 0.03	± 0.04
EFF_ID_SIMPLIFIED_UncorrUncertaintyNP8	± 0.07	± 0.00
EFF_ID_SIMPLIFIED_UncorrUncertaintyNP9	± 0.00	± 0.00
EFF_ID_SIMPLIFIED_UncorrUncertaintyNP10	± 0.00	± 0.00
EFF_ID_SIMPLIFIED_UncorrUncertaintyNP11	± 0.00	± 0.00
EFF_ID_SIMPLIFIED_UncorrUncertaintyNP12	± 0.00	± 0.00
EFF_ID_SIMPLIFIED_UncorrUncertaintyNP13	± 0.00	± 0.00
EFF_ID_SIMPLIFIED_UncorrUncertaintyNP14	± 0.00	± 0.00
EFF_ID_SIMPLIFIED_UncorrUncertaintyNP15	± 0.06	± 0.04
EFF_ID_SIMPLIFIED_UncorrUncertaintyNP16	± 0.03	± 0.02
EFF_ID_SIMPLIFIED_UncorrUncertaintyNP17	± 0.07	± 0.06
MUON_EFF_TrigStatUncertainty	± 0.01	± 0.01
MUON_EFF_TrigSystUncertainty	± 0.03	± 0.02
MUON_ISO_STAT	± 0.01	± 0.01
MUON_ISO_SYS	± 0.34	± 0.33
MUON_RECO_STAT	± 0.10	± 0.10
MUON_RECO_STAT_LOWPT	± 0.00	± 0.00
MUON_RECO_SYS	± 0.64	± 0.65
MUON_RECO_SYS_LOWPT	± 0.00	± 0.00
MUON_TTVA_STAT	± 0.02	± 0.02
MUON_TTVA_SYS	± 0.00	± 0.00
PRW_DATASF	± 0.63	± 0.63
Total	± 1.16	± 1.20
MC Stat.	± 0.34	± 0.16

Table A.9: Relative experimental uncertainties in % related to the efficiency corrections on the WW background in the ggF WW CR (2nd column) and ggF quasi-inclusive SR (3rd column). All uncertainties have been symmetrized by taking the average up and down variation for simplicity. The "Total" row refers to the quadrature sum of all variations. The final row "MC Stat." shows for comparison the statistical uncertainty from MC samples

Systematic	WWCRVBF	VBFSR1J
FT_EFF_Eigen_B_0	± 0.02	± 0.02
FT_EFF_Eigen_B_1	± 0.00	± 0.00
FT_EFF_Eigen_B_2	± 0.00	± 0.00
FT_EFF_Eigen_C_0	± 0.13	± 0.12
FT_EFF_Eigen_C_1	± 0.02	± 0.02
FT_EFF_Eigen_C_2	± 0.01	± 0.01
FT_EFF_Eigen_Light_0	± 0.26	± 0.27
FT_EFF_Eigen_Light_1	± 0.04	± 0.04
FT_EFF_Eigen_Light_2	± 0.02	± 0.02
FT_EFF_Eigen_Light_3	± 0.00	± 0.00
FT_EFF_extrapolation_from_charm	± 0.00	± 0.00
FT_EFF_extrapolation	± 0.00	± 0.00
JVT	± 0.05	± 0.07
EL_EFF_ID_CorrUncertaintyNP0	± 0.00	± 0.00
EL_EFF_ID_CorrUncertaintyNP1	± 0.00	± 0.00
EL_EFF_ID_CorrUncertaintyNP2	± 0.00	± 0.00
EL_EFF_ID_CorrUncertaintyNP3	± 0.00	± 0.00
EL_EFF_ID_CorrUncertaintyNP4	± 0.00	± 0.00
EL_EFF_ID_CorrUncertaintyNP5	± 0.00	± 0.00
EL_EFF_ID_CorrUncertaintyNP6	± 0.00	± 0.00
EL_EFF_ID_CorrUncertaintyNP7	± 0.00	± 0.00
EL_EFF_ID_CorrUncertaintyNP8	± 0.00	± 0.00
EL_EFF_ID_CorrUncertaintyNP9	± 0.06	± 0.04
EL_EFF_ID_CorrUncertaintyNP10	± 0.02	± 0.03
EL_EFF_ID_CorrUncertaintyNP11	± 0.15	± 0.09
EL_EFF_ID_CorrUncertaintyNP12	± 0.16	± 0.07
EL_EFF_ID_CorrUncertaintyNP13	± 0.06	± 0.03
EL_EFF_ID_CorrUncertaintyNP14	± 0.10	± 0.14
EL_EFF_ID_CorrUncertaintyNP15	± 0.14	± 0.01
EL_EFF_Iso_TOTAL_1NPCOR_PLUS_UNCOR	± 0.00	± 0.00
EL_EFF_Trigger_TOTAL_1NPCOR_PLUS_UNCOR	± 0.01	± 0.01
EL_EFF_TriggerEff_TOTAL_1NPCOR_PLUS_UNCOR	± 0.00	± 0.00
EL_EFF_Reco_TOTAL_1NPCOR_PLUS_UNCOR	± 0.15	± 0.12
EFF_ID_SIMPLIFIED_UncorrUncertaintyNP0	± 0.00	± 0.00
EFF_ID_SIMPLIFIED_UncorrUncertaintyNP1	± 0.00	± 0.00
EFF_ID_SIMPLIFIED_UncorrUncertaintyNP2	± 0.00	± 0.00
EFF_ID_SIMPLIFIED_UncorrUncertaintyNP3	± 0.00	± 0.00
EFF_ID_SIMPLIFIED_UncorrUncertaintyNP4	± 0.00	± 0.00
EFF_ID_SIMPLIFIED_UncorrUncertaintyNP5	± 0.05	± 0.00
EFF_ID_SIMPLIFIED_UncorrUncertaintyNP6	± 0.09	± 0.07
EFF_ID_SIMPLIFIED_UncorrUncertaintyNP7	± 0.02	± 0.05
EFF_ID_SIMPLIFIED_UncorrUncertaintyNP8	± 0.03	± 0.10
EFF_ID_SIMPLIFIED_UncorrUncertaintyNP9	± 0.00	± 0.00
EFF_ID_SIMPLIFIED_UncorrUncertaintyNP10	± 0.00	± 0.00
EFF_ID_SIMPLIFIED_UncorrUncertaintyNP11	± 0.00	± 0.00
EFF_ID_SIMPLIFIED_UncorrUncertaintyNP12	± 0.00	± 0.00
EFF_ID_SIMPLIFIED_UncorrUncertaintyNP13	± 0.00	± 0.00
EFF_ID_SIMPLIFIED_UncorrUncertaintyNP14	± 0.02	± 0.00
EFF_ID_SIMPLIFIED_UncorrUncertaintyNP15	± 0.04	± 0.02
EFF_ID_SIMPLIFIED_UncorrUncertaintyNP16	± 0.01	± 0.02
EFF_ID_SIMPLIFIED_UncorrUncertaintyNP17	± 0.02	± 0.03
MUON_EFF_TrigStatUncertainty	± 0.02	± 0.01
MUON_EFF_TrigSystUncertainty	± 0.22	± 0.02
MUON_ISO_STAT	± 0.02	± 0.01
MUON_ISO_SYS	± 0.44	± 0.32
MUON_RECO_STAT	± 0.09	± 0.10
MUON_RECO_STAT_LOWPT	± 0.00	± 0.00
MUON_RECO_SYS	± 0.65	± 0.65
MUON_RECO_SYS_LOWPT	± 0.00	± 0.00
MUON_TTVA_STAT	± 0.02	± 0.02
MUON_TTVA_SYS	± 0.00	± 0.00
PRW_DATASF	± 1.22	± 1.61
Total	± 1.54	± 1.81
MC Stat.	± 1.06	± 0.78

Table A.10: Relative experimental uncertainties in % related to the efficiency corrections on the WW background in the VBF WW 1J CR (2nd column) and VBF 1J SR (3rd column). All uncertainties have been symmetrized by taking the average up and down variation for simplicity. The "Total" row refers to the quadrature sum of all variations. The final row "MC Stat." shows for comparison the statistical uncertainty from MC samples.

Systematic	SRIncl	SRVBF1J	SRVBF2J
FT_EFF_Eigen_B_0	± 0.05	± 0.05	± 0.08
FT_EFF_Eigen_B_1	± 0.00	± 0.00	± 0.00
FT_EFF_Eigen_B_2	± 0.01	± 0.00	± 0.03
FT_EFF_Eigen_C_0	± 0.23	± 0.10	± 0.28
FT_EFF_Eigen_C_1	± 0.01	± 0.01	± 0.00
FT_EFF_Eigen_C_2	± 0.00	± 0.01	± 0.01
FT_EFF_Eigen_Light_0	± 0.78	± 0.28	± 0.98
FT_EFF_Eigen_Light_1	± 0.05	± 0.04	± 0.04
FT_EFF_Eigen_Light_2	± 0.02	± 0.03	± 0.01
FT_EFF_Eigen_Light_3	± 0.00	± 0.00	± 0.00
FT_EFF_extrapolation_from_charm	± 0.00	± 0.00	± 0.00
FT_EFF_extrapolation	± 0.00	± 0.00	± 0.01
JVT	± 0.09	± 0.09	± 0.14
EL_EFF_ID_CorrUncertaintyNP0	± 0.00	± 0.00	± 0.00
EL_EFF_ID_CorrUncertaintyNP1	± 0.00	± 0.00	± 0.00
EL_EFF_ID_CorrUncertaintyNP2	± 0.00	± 0.00	± 0.00
EL_EFF_ID_CorrUncertaintyNP3	± 0.00	± 0.00	± 0.00
EL_EFF_ID_CorrUncertaintyNP4	± 0.00	± 0.00	± 0.00
EL_EFF_ID_CorrUncertaintyNP5	± 0.00	± 0.00	± 0.00
EL_EFF_ID_CorrUncertaintyNP6	± 0.00	± 0.00	± 0.00
EL_EFF_ID_CorrUncertaintyNP7	± 0.00	± 0.00	± 0.00
EL_EFF_ID_CorrUncertaintyNP8	± 0.00	± 0.00	± 0.00
EL_EFF_ID_CorrUncertaintyNP9	± 0.04	± 0.04	± 0.05
EL_EFF_ID_CorrUncertaintyNP10	± 0.10	± 0.10	± 0.11
EL_EFF_ID_CorrUncertaintyNP11	± 0.16	± 0.15	± 0.17
EL_EFF_ID_CorrUncertaintyNP12	± 0.01	± 0.02	± 0.03
EL_EFF_ID_CorrUncertaintyNP13	± 0.04	± 0.04	± 0.07
EL_EFF_ID_CorrUncertaintyNP14	± 0.08	± 0.06	± 0.11
EL_EFF_ID_CorrUncertaintyNP15	± 0.01	± 0.02	± 0.01
EL_EFF_Iso_TOTAL_1NPCOR_PLUS_UNCOR	± 0.00	± 0.00	± 0.00
EL_EFF_Trigger_TOTAL_1NPCOR_PLUS_UNCOR	± 0.01	± 0.01	± 0.01
EL_EFF_TriggerEff_TOTAL_1NPCOR_PLUS_UNCOR	± 0.00	± 0.00	± 0.00
EL_EFF_Reco_TOTAL_1NPCOR_PLUS_UNCOR	± 0.16	± 0.15	± 0.16
EFF_ID_SIMPLIFIED_UncorrUncertaintyNP0	± 0.00	± 0.00	± 0.00
EFF_ID_SIMPLIFIED_UncorrUncertaintyNP1	± 0.00	± 0.00	± 0.00
EFF_ID_SIMPLIFIED_UncorrUncertaintyNP2	± 0.00	± 0.00	± 0.00
EFF_ID_SIMPLIFIED_UncorrUncertaintyNP3	± 0.00	± 0.00	± 0.00
EFF_ID_SIMPLIFIED_UncorrUncertaintyNP4	± 0.00	± 0.00	± 0.00
EFF_ID_SIMPLIFIED_UncorrUncertaintyNP5	± 0.00	± 0.00	± 0.00
EFF_ID_SIMPLIFIED_UncorrUncertaintyNP6	± 0.02	± 0.02	± 0.02
EFF_ID_SIMPLIFIED_UncorrUncertaintyNP7	± 0.02	± 0.02	± 0.02
EFF_ID_SIMPLIFIED_UncorrUncertaintyNP8	± 0.37	± 0.39	± 0.38
EFF_ID_SIMPLIFIED_UncorrUncertaintyNP9	± 0.00	± 0.00	± 0.00
EFF_ID_SIMPLIFIED_UncorrUncertaintyNP10	± 0.00	± 0.00	± 0.00
EFF_ID_SIMPLIFIED_UncorrUncertaintyNP11	± 0.00	± 0.00	± 0.00
EFF_ID_SIMPLIFIED_UncorrUncertaintyNP12	± 0.00	± 0.00	± 0.00
EFF_ID_SIMPLIFIED_UncorrUncertaintyNP13	± 0.00	± 0.00	± 0.00
EFF_ID_SIMPLIFIED_UncorrUncertaintyNP14	± 0.00	± 0.00	± 0.00
EFF_ID_SIMPLIFIED_UncorrUncertaintyNP15	± 0.00	± 0.00	± 0.00
EFF_ID_SIMPLIFIED_UncorrUncertaintyNP16	± 0.01	± 0.00	± 0.00
EFF_ID_SIMPLIFIED_UncorrUncertaintyNP17	± 0.10	± 0.06	± 0.11
MUON_EFF_TrigStatUncertainty	± 0.00	± 0.00	± 0.00
MUON_EFF_TrigSystUncertainty	± 0.01	± 0.01	± 0.01
MUON_ISO_STAT	± 0.01	± 0.02	± 0.02
MUON_ISO_SYS	± 0.27	± 0.25	± 0.32
MUON_RECO_STAT	± 0.10	± 0.10	± 0.09
MUON_RECO_STAT_LOWPT	± 0.00	± 0.00	± 0.00
MUON_RECO_SYS	± 0.76	± 0.76	± 0.76
MUON_RECO_SYS_LOWPT	± 0.00	± 0.00	± 0.00
MUON_TTVA_STAT	± 0.02	± 0.02	± 0.02
MUON_TTVA_SYS	± 0.00	± 0.00	± 0.00
PRW_DATASF	± 0.42	± 0.49	± 0.86
Total	± 1.32	± 1.10	± 1.70
MC Stat.	± 0.40	± 1.41	± 2.18

Table A.11: Relative experimental uncertainties in % related to the efficiency corrections on the NWA ggF signal with mass 600 GeV in the ggF quasi-inclusive SR (2nd column), VBF 1J SR (3rd column) and VBF 2J SR (4th column). All uncertainties have been symmetrized by taking the average up and down variation for simplicity. The "Total" row refers to the quadrature sum of all variations. The final row "MC Stat." shows for comparison the statistical uncertainty from MC samples.

Systematic	SRIncl	SRVBF1J	SRVBF2J
FT_EFF_Eigen_B_0	± 0.04	± 0.01	± 0.02
FT_EFF_Eigen_B_1	± 0.00	± 0.00	± 0.00
FT_EFF_Eigen_B_2	± 0.01	± 0.00	± 0.01
FT_EFF_Eigen_C_0	± 0.39	± 0.08	± 0.23
FT_EFF_Eigen_C_1	± 0.06	± 0.01	± 0.05
FT_EFF_Eigen_C_2	± 0.02	± 0.00	± 0.02
FT_EFF_Eigen_Light_0	± 0.75	± 0.15	± 0.56
FT_EFF_Eigen_Light_1	± 0.02	± 0.02	± 0.01
FT_EFF_Eigen_Light_2	± 0.01	± 0.01	± 0.00
FT_EFF_Eigen_Light_3	± 0.00	± 0.00	± 0.00
FT_EFF_extrapolation_from_charm	± 0.00	± 0.00	± 0.00
FT_EFF_extrapolation	± 0.01	± 0.00	± 0.00
JVT	± 0.04	± 0.12	± 0.06
EL_EFF_ID_CorrUncertaintyNP0	± 0.00	± 0.00	± 0.00
EL_EFF_ID_CorrUncertaintyNP1	± 0.00	± 0.00	± 0.00
EL_EFF_ID_CorrUncertaintyNP2	± 0.00	± 0.00	± 0.00
EL_EFF_ID_CorrUncertaintyNP3	± 0.00	± 0.00	± 0.00
EL_EFF_ID_CorrUncertaintyNP4	± 0.00	± 0.00	± 0.00
EL_EFF_ID_CorrUncertaintyNP5	± 0.00	± 0.00	± 0.00
EL_EFF_ID_CorrUncertaintyNP6	± 0.00	± 0.00	± 0.00
EL_EFF_ID_CorrUncertaintyNP7	± 0.00	± 0.00	± 0.00
EL_EFF_ID_CorrUncertaintyNP8	± 0.00	± 0.00	± 0.00
EL_EFF_ID_CorrUncertaintyNP9	± 0.04	± 0.04	± 0.05
EL_EFF_ID_CorrUncertaintyNP10	± 0.11	± 0.10	± 0.11
EL_EFF_ID_CorrUncertaintyNP11	± 0.16	± 0.15	± 0.17
EL_EFF_ID_CorrUncertaintyNP12	± 0.02	± 0.01	± 0.03
EL_EFF_ID_CorrUncertaintyNP13	± 0.06	± 0.03	± 0.06
EL_EFF_ID_CorrUncertaintyNP14	± 0.10	± 0.06	± 0.09
EL_EFF_ID_CorrUncertaintyNP15	± 0.01	± 0.02	± 0.02
EL_EFF_Iso_TOTAL_1NPCOR_PLUS_UNCOR	± 0.00	± 0.00	± 0.00
EL_EFF_Trigger_TOTAL_1NPCOR_PLUS_UNCOR	± 0.01	± 0.01	± 0.01
EL_EFF_TriggerEff_TOTAL_1NPCOR_PLUS_UNCOR	± 0.00	± 0.00	± 0.00
EL_EFF_Reco_TOTAL_1NPCOR_PLUS_UNCOR	± 0.16	± 0.15	± 0.15
EFF_ID_SIMPLIFIED_UncorrUncertaintyNP0	± 0.00	± 0.00	± 0.00
EFF_ID_SIMPLIFIED_UncorrUncertaintyNP1	± 0.00	± 0.00	± 0.00
EFF_ID_SIMPLIFIED_UncorrUncertaintyNP2	± 0.00	± 0.00	± 0.00
EFF_ID_SIMPLIFIED_UncorrUncertaintyNP3	± 0.00	± 0.00	± 0.00
EFF_ID_SIMPLIFIED_UncorrUncertaintyNP4	± 0.00	± 0.00	± 0.00
EFF_ID_SIMPLIFIED_UncorrUncertaintyNP5	± 0.00	± 0.00	± 0.00
EFF_ID_SIMPLIFIED_UncorrUncertaintyNP6	± 0.02	± 0.02	± 0.02
EFF_ID_SIMPLIFIED_UncorrUncertaintyNP7	± 0.02	± 0.02	± 0.02
EFF_ID_SIMPLIFIED_UncorrUncertaintyNP8	± 0.00	± 0.39	± 0.40
EFF_ID_SIMPLIFIED_UncorrUncertaintyNP9	± 0.00	± 0.00	± 0.00
EFF_ID_SIMPLIFIED_UncorrUncertaintyNP10	± 0.00	± 0.00	± 0.00
EFF_ID_SIMPLIFIED_UncorrUncertaintyNP11	± 0.00	± 0.00	± 0.00
EFF_ID_SIMPLIFIED_UncorrUncertaintyNP12	± 0.00	± 0.00	± 0.00
EFF_ID_SIMPLIFIED_UncorrUncertaintyNP13	± 0.00	± 0.00	± 0.00
EFF_ID_SIMPLIFIED_UncorrUncertaintyNP14	± 0.00	± 0.00	± 0.00
EFF_ID_SIMPLIFIED_UncorrUncertaintyNP15	± 0.01	± 0.00	± 0.00
EFF_ID_SIMPLIFIED_UncorrUncertaintyNP16	± 0.01	± 0.00	± 0.00
EFF_ID_SIMPLIFIED_UncorrUncertaintyNP17	± 0.11	± 0.06	± 0.07
MUON_EFF_TrigStatUncertainty	± 0.00	± 0.00	± 0.00
MUON_EFF_TrigSystUncertainty	± 0.01	± 0.01	± 0.01
MUON_ISO_STAT	± 0.02	± 0.02	± 0.02
MUON_ISO_SYS	± 0.29	± 0.27	± 0.31
MUON_RECO_STAT	± 0.10	± 0.10	± 0.10
MUON_RECO_STAT_LOWPT	± 0.00	± 0.00	± 0.00
MUON_RECO_SYS	± 0.76	± 0.75	± 0.77
MUON_RECO_SYS_LOWPT	± 0.00	± 0.00	± 0.00
MUON_TTVA_STAT	± 0.02	± 0.02	± 0.02
MUON_TTVA_SYS	± 0.00	± 0.00	± 0.00
PRW_DATASF	± 0.27	± 0.71	± 0.22
Total	± 1.25	± 1.25	± 1.17
MC Stat.	± 0.93	± 1.23	± 0.91

Table A.12: Relative experimental uncertainties in % related to the efficiency corrections on the NWA VBF signal with mass 600 GeV in the ggF quasi-inclusive SR (2nd column), VBF 1J SR (3rd column) and VBF 2J SR (4th column). All uncertainties have been symmetrized by taking the average up and down variation for simplicity. The "Total" row refers to the quadrature sum of all variations. The final row "MC Stat." shows for comparison the statistical uncertainty from MC samples.

Appendix B

Theory Uncertainty Shapes

The theoretical uncertainties on the major SM backgrounds are considered with both shape and norm portions. This appendix shares the full shape comparison of the individual variations for each of the three major backgrounds considered: $t\bar{t}$, Wt, and $qqWW$. The shape is compared in each of the three signal regions and also in the four control regions (even though the shape portion is not considered here in the statistical analysis) by comparing the nominal m_T distribution of the selected process and the m_T of the derived variation.

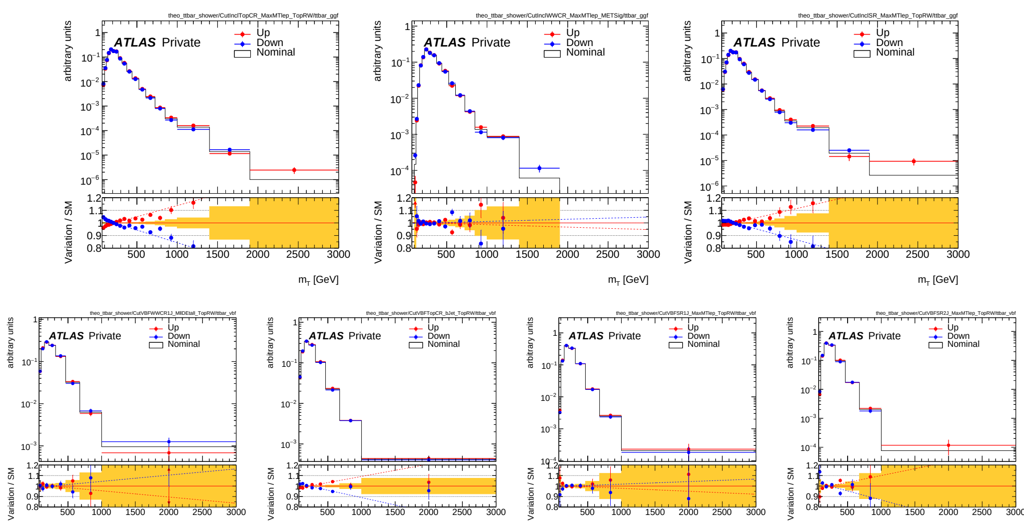

Figure B.1: Shape portion of the shower uncertainty on $t\bar{t}$ background sample for each of the control and signal regions in the ggF (top) and VBF (bottom) phase spaces.

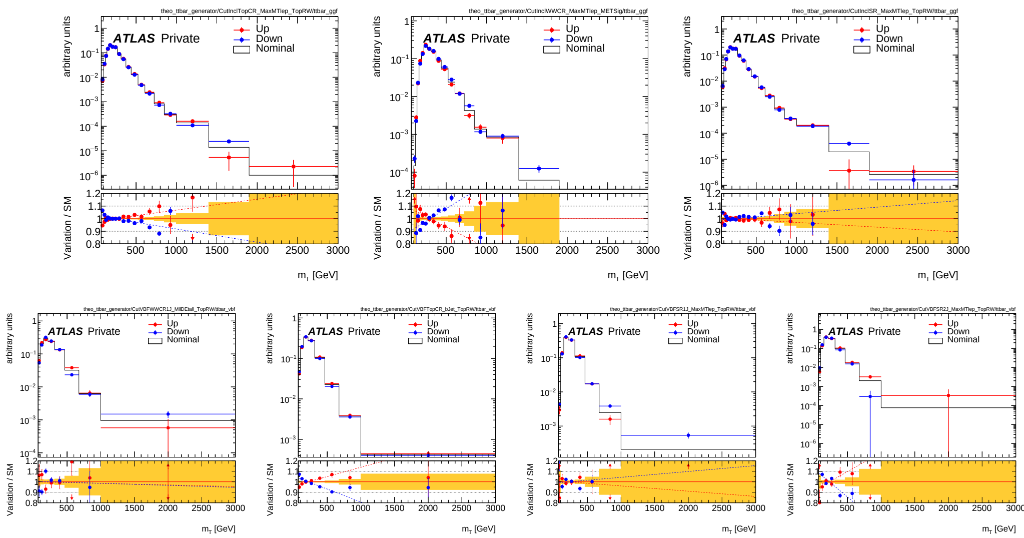

Figure B.2: Shape portion of the generator uncertainty on $t\bar{t}$ background sample for each of the control and signal regions in the ggF (top) and VBF (bottom) phase spaces.

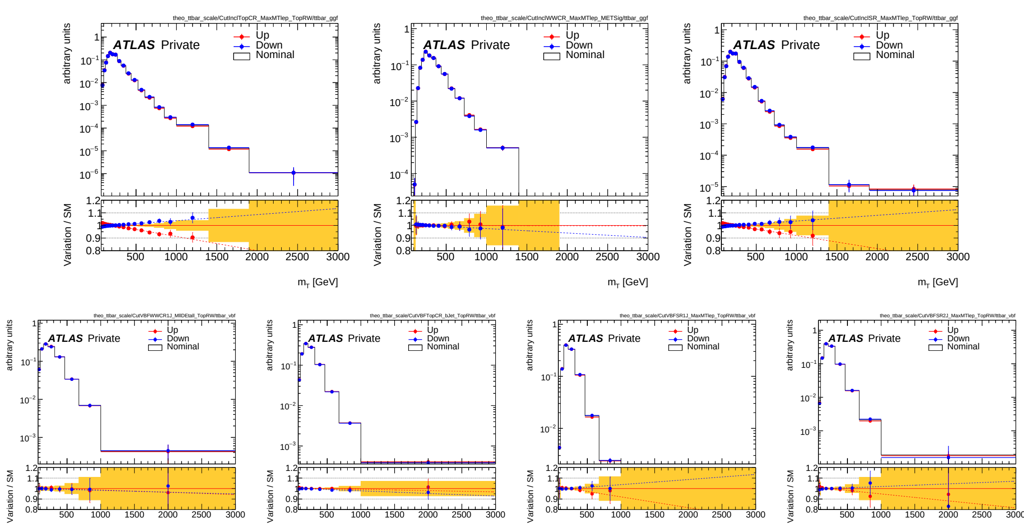

Figure B.3: Shape portion of the scale uncertainty on $t\bar{t}$ background sample for each of the control and signal regions in the ggF (top) and VBF (bottom) phase spaces.

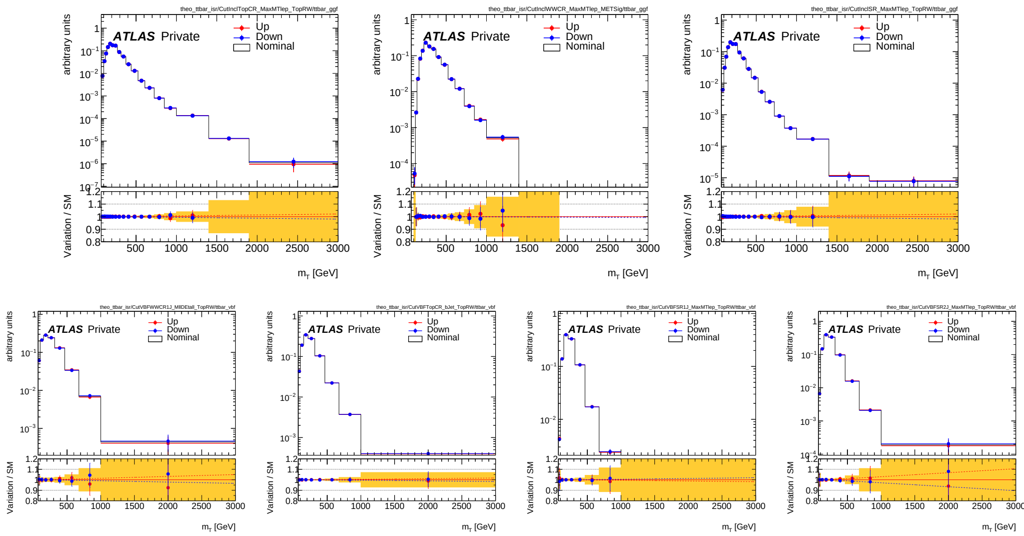

Figure B.4: Shape portion of the ISR uncertainty on $t\bar{t}$ background sample for each of the control and signal regions in the ggF (top) and VBF (bottom) phase spaces.

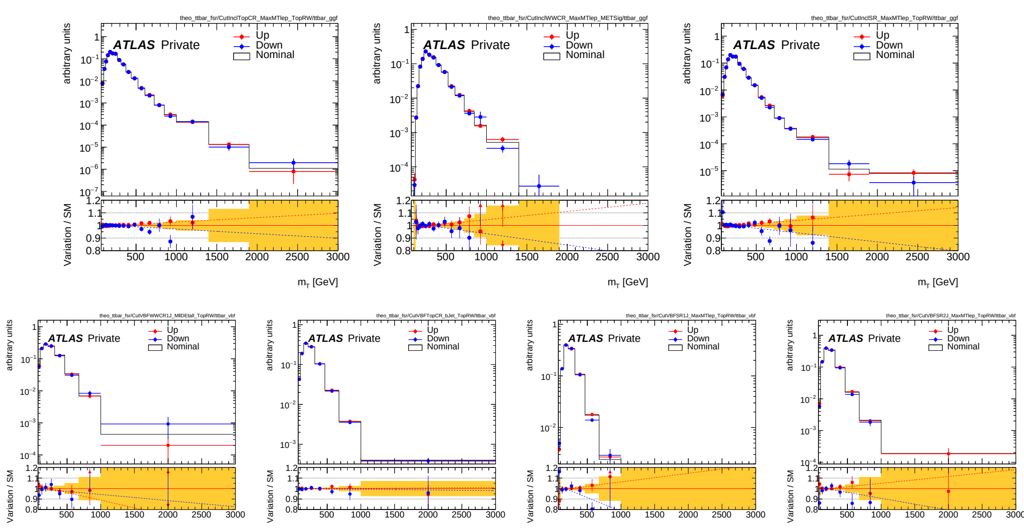

Figure B.5: Shape portion of the FSR uncertainty on $t\bar{t}$ background sample for each of the control and signal regions in the ggF (top) and VBF (bottom) phase spaces.

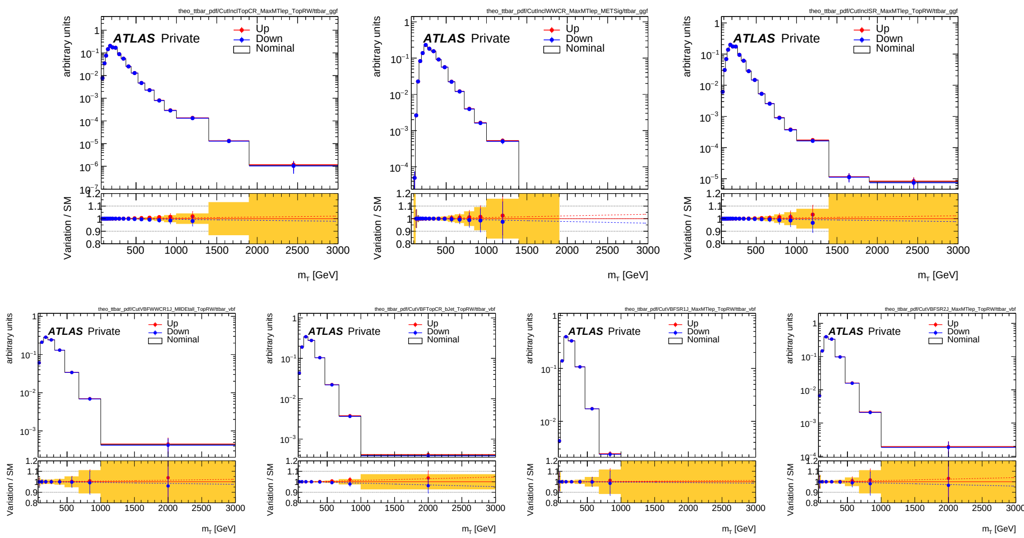

Figure B.6: Shape portion of the PDF uncertainty on $t\bar{t}$ background sample for each of the control and signal regions in the ggF (top) and VBF (bottom) phase spaces.

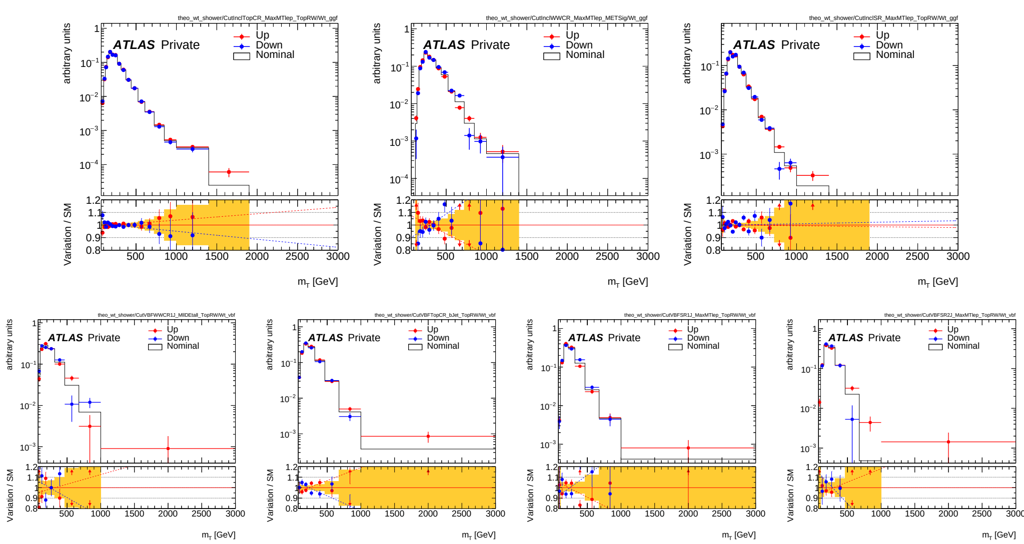

Figure B.7: Shape portion of the shower uncertainty on Wt background sample for each of the control and signal regions in the ggF (top) and VBF (bottom) phase spaces.

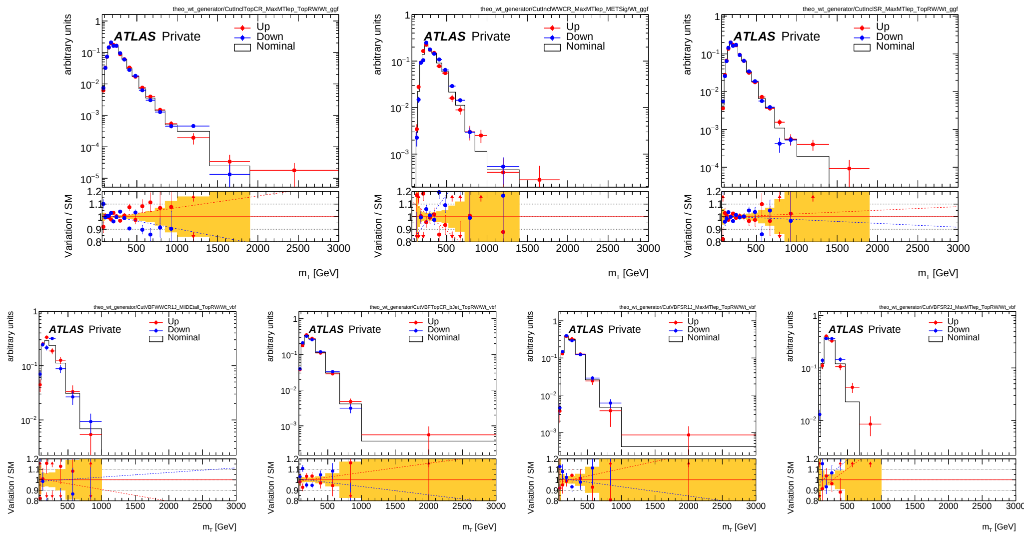

Figure B.8: Shape portion of the generator uncertainty on Wt background sample for each of the control and signal regions in the ggF (top) and VBF (bottom) phase spaces.

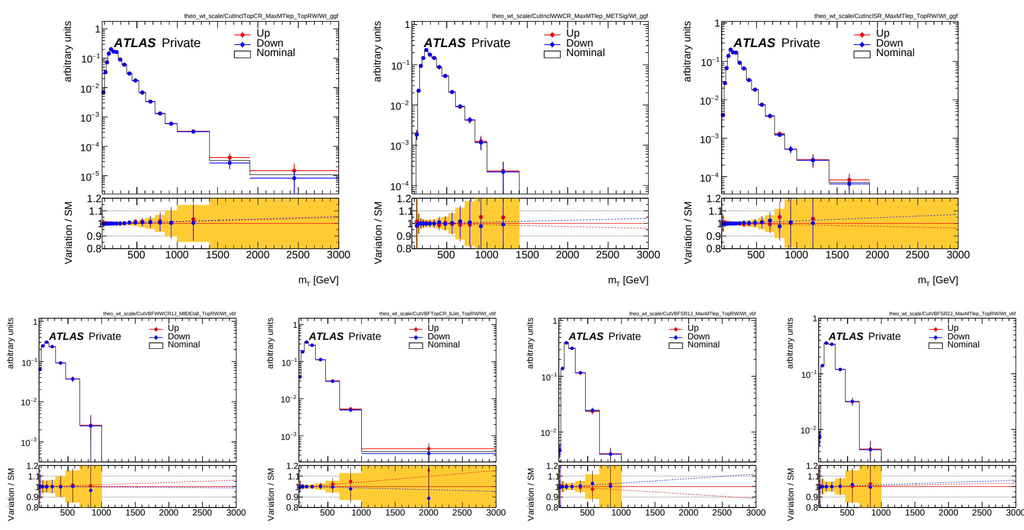

Figure B.9: Shape portion of the scale uncertainty on Wt background sample for each of the control and signal regions in the ggF (top) and VBF (bottom) phase spaces.

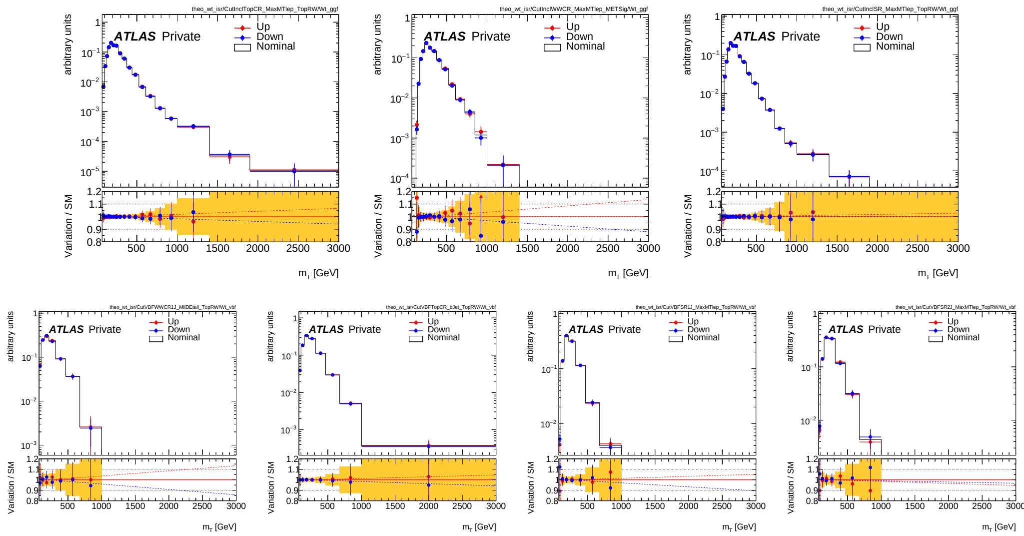

Figure B.10: Shape portion of the ISR uncertainty on Wt background sample for each of the control and signal regions in the ggF (top) and VBF (bottom) phase spaces.

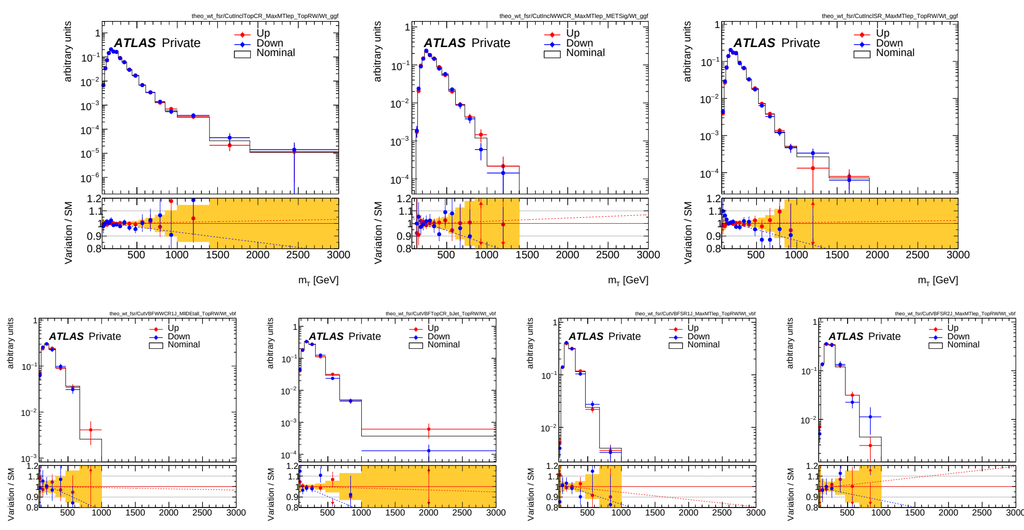

Figure B.11: Shape portion of the FSR uncertainty on Wt background sample for each of the control and signal regions in the ggF (top) and VBF (bottom) phase spaces.

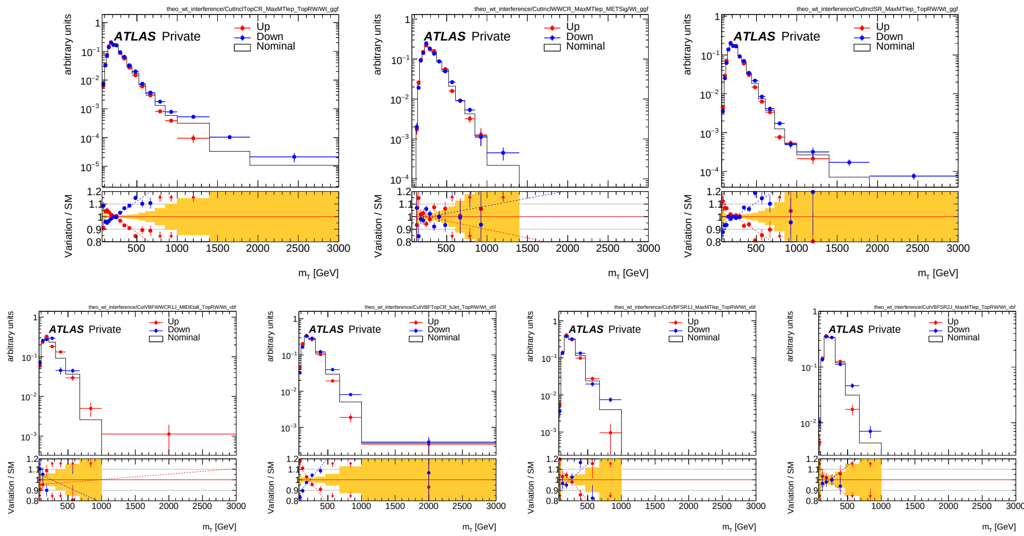

Figure B.12: Shape portion of the interference uncertainty on Wt background sample for each of the control and signal regions in the ggF (top) and VBF (bottom) phase spaces.

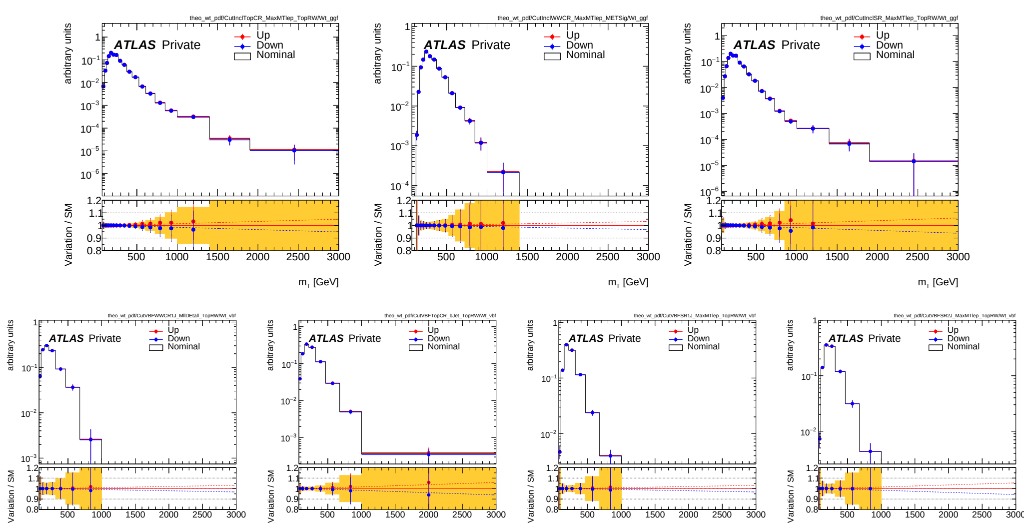

Figure B.13: Shape portion of the PDF uncertainty on Wt background sample for each of the control and signal regions in the ggF (top) and VBF (bottom) phase spaces.

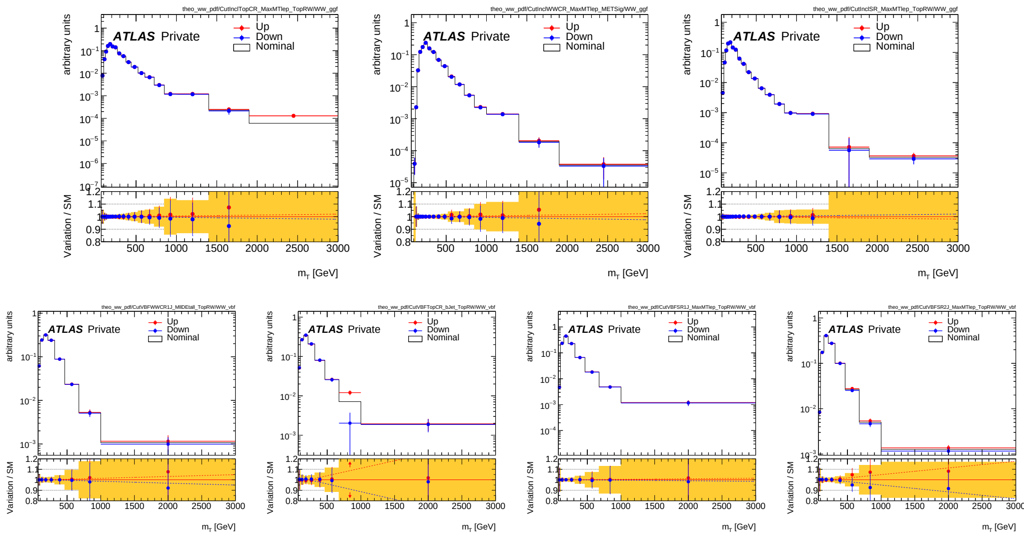

Figure B.14: Shape portion of the PDF uncertainty on $qqWW$ background sample for each of the control and signal regions in the ggF (top) and VBF (bottom) phase spaces.

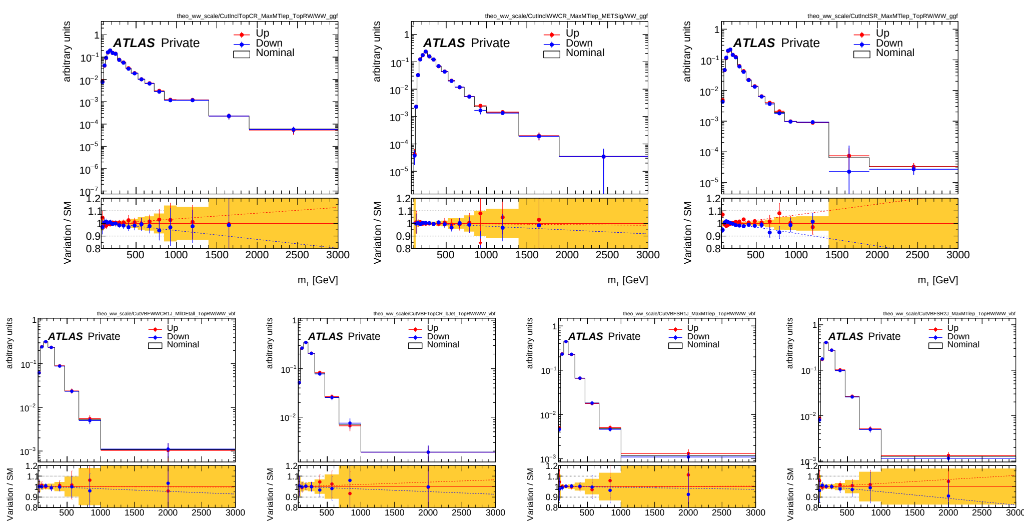

Figure B.15: Shape portion of the scale uncertainty on $qqWW$ background sample for each of the control and signal regions in the ggF (top) and VBF (bottom) phase spaces.

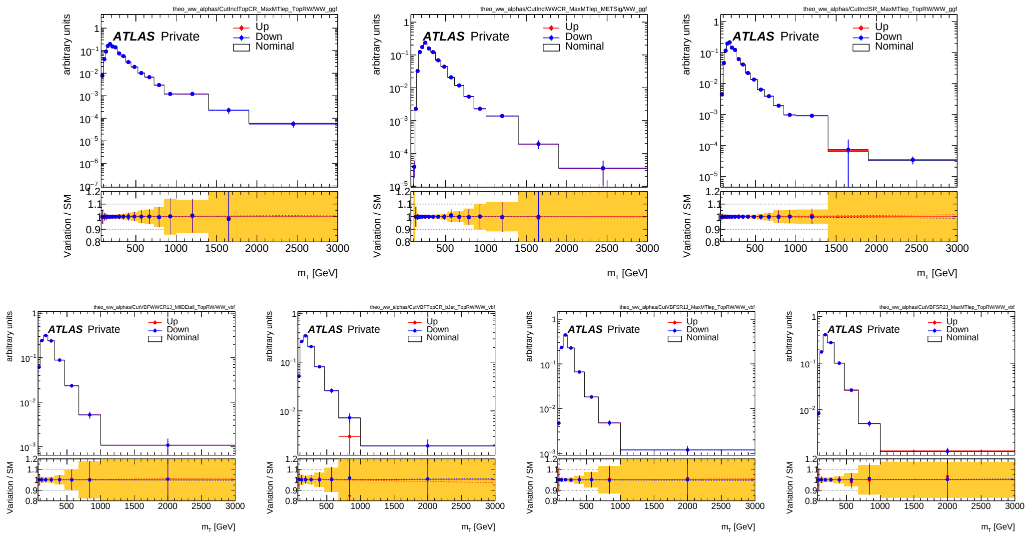

Figure B.16: Shape portion of the α_S uncertainty on $qqWW$ background sample for each of the control and signal regions in the ggF (top) and VBF (bottom) phase spaces.

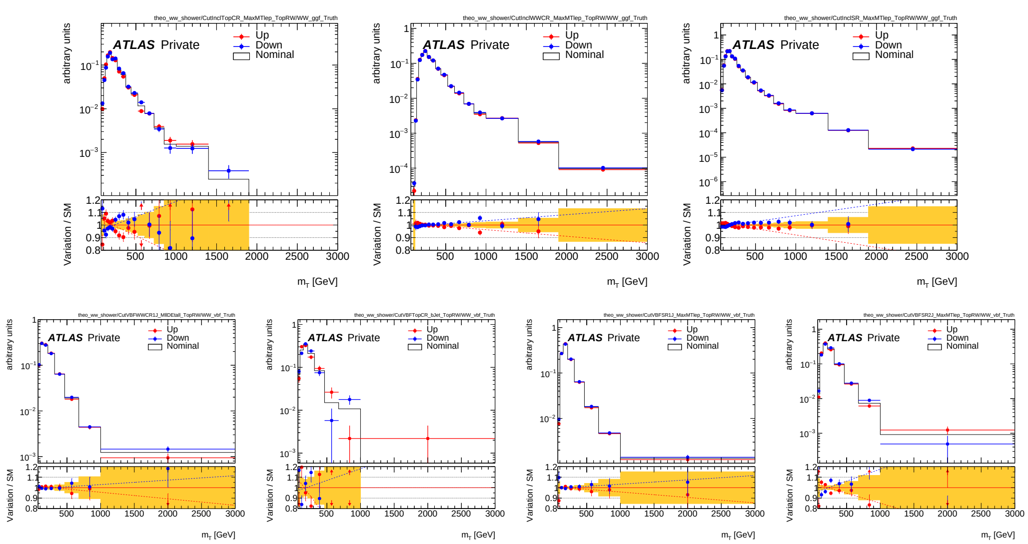

Figure B.17: Shape portion of the shower uncertainty on $qqWW$ background sample for each of the control and signal regions in the ggF (top) and VBF (bottom) phase spaces.

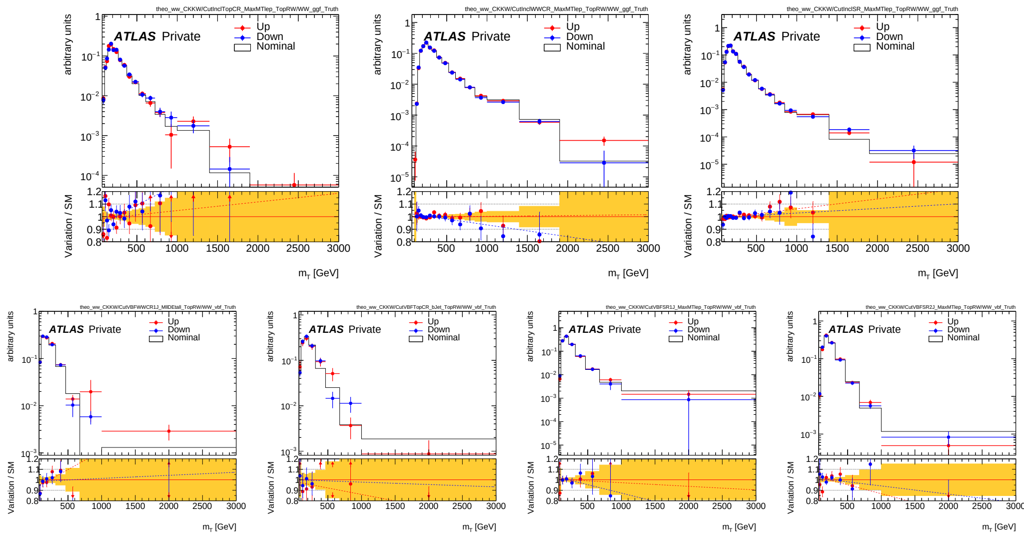

Figure B.18: Shape portion of the CKKW uncertainty on $qqWW$ background sample for each of the control and signal regions in the ggF (top) and VBF (bottom) phase spaces.

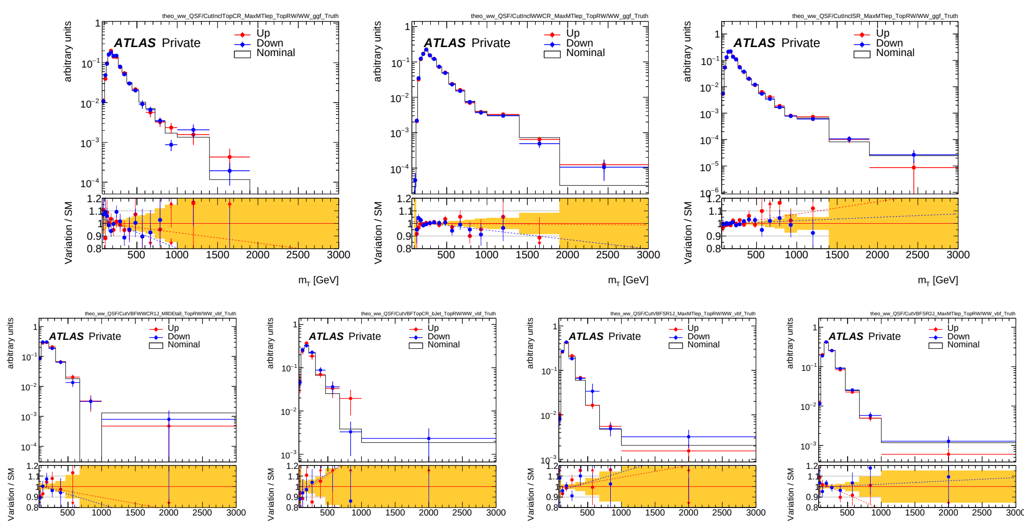

Figure B.19: Shape portion of the QSF uncertainty on $qqWW$ background sample for each of the control and signal regions in the ggF (top) and VBF (bottom) phase spaces.

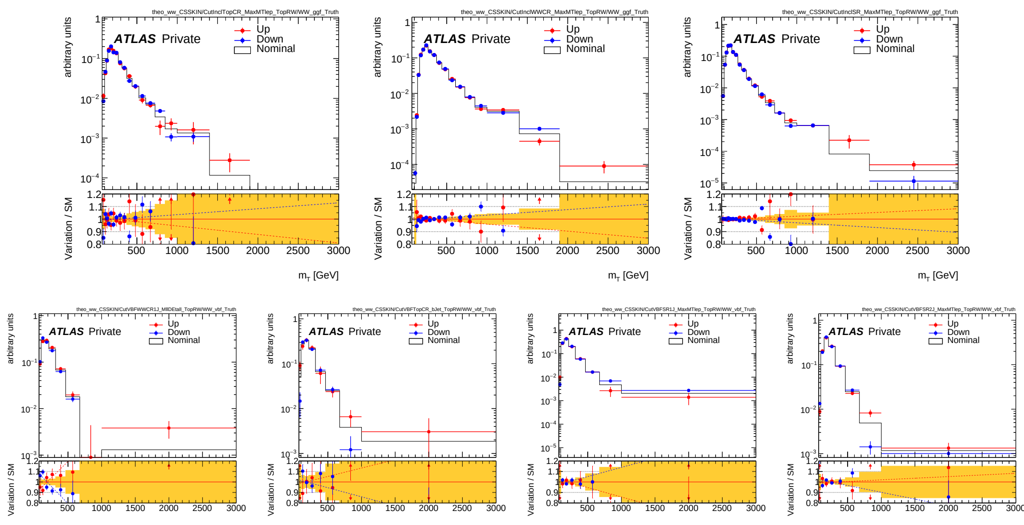

Figure B.20: Shape portion of the CSSKIN uncertainty on $qqWW$ background sample for each of the control and signal regions in the ggF (top) and VBF (bottom) phase spaces.